FOSSIL ENERGY

DOE/ET/10340-132
(DE82014462)

HIGH-TEMPERATURE TURBINE TECHNOLOGY PROGRAM HOT-GAS PATH DEVELOPMENT TEST

Part II (Testing)

Topical Report

March 1982

Work Performed Under Contract No. AC01-76ET10340

General Electric Company
Schenectady, New York

U. S. DEPARTMENT OF ENERGY

DISCLAIMER

DISCLAIMER

DOE/ET/10340-132
(DE82014462)
Distribution Category UC-90f

HIGH-TEMPERATURE TURBINE TECHNOLOGY PROGRAM HOT-GAS PATH DEVELOPMENT TEST PART II (TESTING)

TOPICAL REPORT

March 1982

M.W. HORNER

GE Program Manager
DOE-HTTT Program

Prepared by

General Electric Company
Gas Turbine Division
Schenectady, N.Y. 12345

Prepared for

United States Department of Energy
Office of Energy Technology
Under Contract No. DE-AC01-76ET10340
(Formerly Contract No. EX-76-C-01-1806)

TABLE OF CONTENTS

TABLE OF CONTENTS (Cont'd)

TABLE OF CONTENTS (Cont'd)

TABLE OF CONTENTS (Cont'd)

LIST OF ILLUSTRATIONS

LIST OF ILLUSTRATIONS (Cont'd)

LIST OF ILLUSTRATIONS (Cont'd)

LIST OF ILLUSTRATIONS (Cont'd)

LIST OF ILLUSTRATIONS (Cont'd)

LIST OF ILLUSTRATIONS (Cont'd)

LIST OF ILLUSTRATIONS (Cont'd)

LIST OF ILLUSTRATIONS (Cont'd)

LIST OF ILLUSTRATIONS (Cont'd)

LIST OF ILLUSTRATIONS (Cont'd)

LIST OF TABLES

LIST OF TABLES (Cont'd)

EXECUTIVE SUMMARY

The objective of the U.S. Department of Energy High-Temperature Turbine Technology (DOE-HTTT) program is to bring to "technology readiness" an efficient high firing temperature gas turbine for application in an Integrated Gasification Combined Cycle (IGCC) power plant. One of the tasks of Phase II of the program was to perform turbine hot section stationary components design, fabrication and testing.

This topical report of the HTTT Phase II program presents the results of testing full-scale water-cooled first-stage and second-stage turbine nozzles at design temperature and pressure to verify that the designs are adequate for operation in a full-scale turbine environment. Specifically, the steady-state tests were designed to evaluate the heat transfer and related coolant system hydraulic characteristics of water-cooled turbine nozzles, including off design and fault condition testing. Low-cycle fatigue life of the nozzles was demonstrated by subjecting cascade assemblies to several hundred simulated startup/shutdown turbine cycles. This testing was accomplished in the Hot-Gas Path Development Test Stand (HGPDTS), which is a technology development facility capable of evaluating full-scale combustion and turbine nozzle components. A description of the Hot-Gas Path Test Facility can be found in Part I* of this report. Design and fabrication details for the composite and monometallic nozzles are reported in the Phase II Final Report,** and in the Turbine Subsystem Design topical report.***

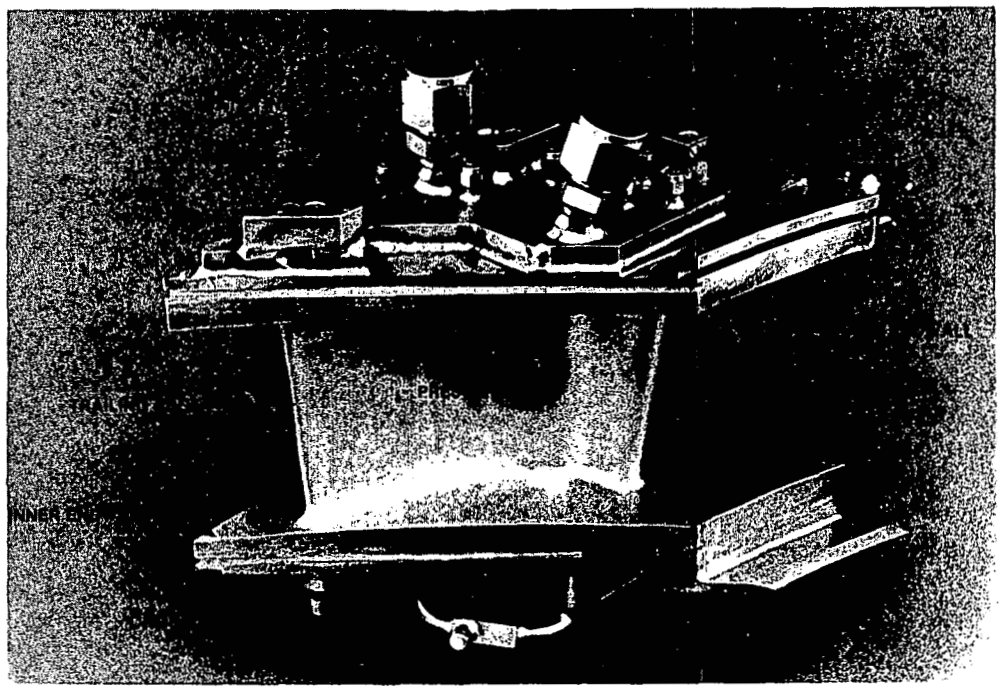

Figure S-1. First-stage nozzle

* Topical Report DOE/ET/10340-122, "Hot-Gas Path Development Test – Part I (Facility Description)," August 1981.

** Final Report DOE/ET/10340-127, "High-Temperature Turbine Technology Program – Phase II Final Report."

*** Topical Report FE-1806-95, "Turbine Subsystem Design Report – Low-Btu Gas," Dec. 1980.

The first-stage water-cooled turbine nozzle, shown in Figure S-1, is a composite structure consisting of Nitronic 50 cooling water tubes embedded in a magnesium/zirconium/chromium (MZC) copper alloy substrate. This copper alloy substrate is reinforced by Nitronic 50 spar rods in the airfoil section, Nitronic 50 endplates at the endwalls, and is encased in a highly corrosion-resistant IN617 cladding. The entire structure is hot isostatically pressed to form a composite structure.

A three-throat cascade of the first-stage turbine nozzle was successfully tested in the HGPDTS at a nozzle inlet gas temperature of 2630 °F and a nozzle inlet pressure of 11.3 atmospheres. In addition to steady-state operation at the design firing temperature, the nozzle cascade was exposed to a simulated startup/shutdown turbine cycle by varying the firing temperature. The relationships between important parameters such as coolant temperature, coolant flow rate, hot gas temperature, and hot-gas mass flow rate were determined during fired testing. A total of 42 hours at the design point and 617 thermal cycles were accumulated during the test periods.

First-stage nozzle test results show that measured metal and coolant temperatures correspond well to the predicted design values. This nozzle design has been shown to be fully satisfactory for the application (2600 °F), with growth capability to 3000 °F firing temperature. Off design and fault conditions testing has shown the design to exhibit stable operating characteristics and to be tolerant of reduced coolant flow rate, well below design levels.

A post-test metallurgical examination of sectioned portions of the tested nozzles shows a totally bonded structure, confirming the test results and attesting to the successful performance of water-cooled composite nozzle hardware.

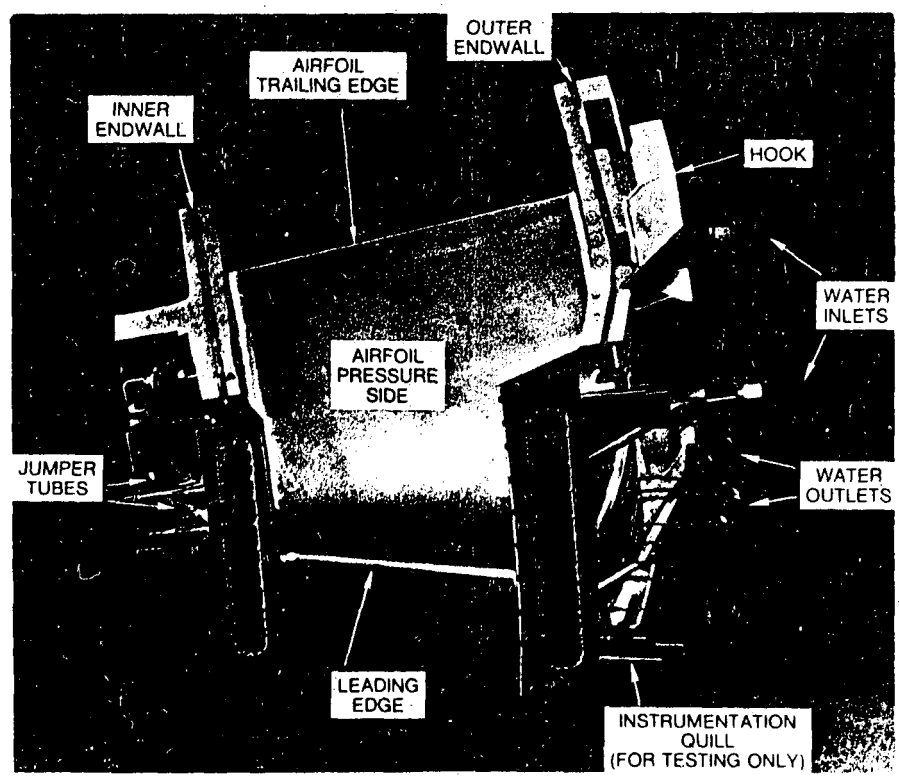

Figure S-2. Second-stage nozzle

The second-stage water-cooled turbine nozzle, shown in Figure S-2, is a monometallic construction, cast from IN718. The vane and endwalls of each nozzle segment are cooled by water in a two-pass flow network consisting of electrochemically drilled cooling passages.

A three-throat cascade of the second-stage turbine nozzle was also successfully tested in the HGPDTS at a nozzle inlet gas temperature of 2082 °F (which is the operating temperature corresponding to a firing temperature of 2600 °F) and a nozzle inlet pressure of 5.4 atmospheres. In addition to sustained steady-state operation, the nozzle cascade was exposed to a simulated startup/shutdown turbine cycle by varying the gas temperature and gas flow at the nozzle inlet. As with the first-stage nozzle test, parameter variation testing was also conducted on the second-stage nozzle. Parameters that were varied included coolant temperature, coolant flow rate, hot gas temperature, and hot-gas mass flow rate. A total of 20 hours at the design point (2082 °F) and 413 thermal cycles were accumulated during the test periods.

Second-stage nozzle test results show that measured metal and coolant temperatures correspond well to the predicted design values. This nozzle design has been shown to be fully satisfactory for application, with growth capability to 3000 °F firing temperature. Off design and fault conditions testing has shown the design to exhibit stable operating characteristics and to be tolerant of reduced coolant flow rate, well below design levels.

A post-test metallurgical examination of sectioned portions of one second stage nozzle airfoil and endwall revealed intergranular cracks emanating from several of the cooling passages. Microscopy and microprobe analyses revealed that the damage observed was the result of caustic stress corrosion cracking and not low-cycle fatigue. Conditions favorable to caustic stress corrosion cracking in IN718 material were inadvertantly created in the test nozzles by loss of water chemistry control during the extended test period. If the water chemistry control had remained within specifications, the monometallic nozzles would not have shown any significant change as a result of testing. Continuous on-line cooling water quality monitoring and the use of a volatile pH agent, such as ammonium hydroxide, will preclude caustic stress corrosion cracking in the future.

The technology readiness of water-cooled first-stage composite nozzles and second-stage monometallic nozzles has been demonstrated. In summary, the test results show that:

- Water-cooling is effective in maintaining desired nozzle metal temperatures in a high heat flux environment.
- These nozzle designs are highly resistant to low-cycle fatigue damage.
- Fabrication methods used to construct these nozzles are valid.
- These nozzles are hydraulically well balanced.
- A large margin exists to critical heat flux at reduced cooling flows.
- Both nozzle designs have growth capability to 3000 °F firing temperature.

Section 1

INTRODUCTION

1.1 BACKGROUND

The objective of the U.S. Department of Energy High-Temperature Turbine Technology (DOE-HTTT) Program is to bring to "technology readiness,"* within 6 to 10 years, a high-temperature gas turbine for use in a combined-cycle power plant, with coal-derived fuel at a firing temperature** of 2600 °F and with growth capability to 3000 °F. This program has been divided into three phases:

Phase I - Program and System Definition
Phase II - Technology Testing and Test Support Studies
Phase III - Technology Readiness Verification Test Program

The three phases of the program encompass the design, development, manufacture, and test of a GE-TRV gas turbine system† at a DOE facility. Phase I is completed, and Phase II commenced on August 1, 1977.

The objectives of Phase II are to:

- Perform component design and technology testing in critical areas
- Perform system design and trade-off analyses in sufficient depth to support the component design and test tasks
- Update the Phase I combined-cycle studies to evaluate the commercial viability of a GE-TRV gas turbine system.

As a separate task of the HTTT Phase II program, a simplified water-cooled composite nozzle segment was tested in the turbine simulator facility under simulated Integrated Gasification Combined Cycle (IGCC) conditions at 2600 °F firing temperature, 12:1 pressure ratio, with coal-derived low-Btu gas fuel. This first composite water-cooled nozzle segment was successfully tested for approximately 71 fired hours, of which 54 hours were at 2600 °F firing temperature. Post-test examination of the nozzle segment revealed a totally bonded structure with no indication of gas-path

---

* "Technology readiness" is defined as "that stage of system, subsystem, or component development where all major problems associated with the performance specification goals have been solved, and where the solutions to these problems have been demonstrated successfully. At that stage, no major risks remain for an agency or contractor in scaling up the technology (if full-scale demonstration has not been performed) and in proceeding with mission (or commercial) development of the system, subsystem, or component."

** Firing temperature is defined by the General Electric Gas Turbine Division as the inlet temperature to the first-stage buckets after all of the first-stage nozzle cooling flows and seal leakages have mixed with the combustor discharge flows.

† GE-TRV (General Electric Technology Readiness Vehicle) approximates the GE MS6000 gas turbine in size.

corrosion attack. Details of this test are documented in the Turbine Simulator topical report.*

1.2 TASK OBJECTIVES AND SCOPE

This task of the HTTT Phase II program was to test full-scale (GE-TRV) water-cooled first-stage and second-stage turbine nozzles at design temperature and pressure to verify that the designs are adequate for satisfactory operation in a GE-TRV turbine environment. Specifically, the tests were designed to evaluate the heat transfer and temperature distribution characteristics of water-cooled turbine nozzles. Low-cycle fatigue life of the nozzles was demonstrated by subjecting cascade assemblies to several hundred simulated startup/shutdown turbine cycles. This testing was accomplished in the Hot-Gas Path Development Test Stand (HGPDTS), which is a technology development facility capable of evaluating full-scale combustion and turbine nozzle components. A description of the Hot-Gas Path Test Facility can be found in Part I** of this topical report.

1.3 DESCRIPTION OF DESIGN OPERATING CONDITIONS

1.3.1 First-Stage Nozzle

The first-stage composite nozzle is located immediately downstream of the combustors and in front of the first-stage buckets as shown in Figures 1-1 and 1-2. The TRV design operating conditions for this nozzle at a 2600 °F firing temperature are an average inlet gas temperature of 2656 °F, an inlet gas pressure of 166 psia, and a gas flow of 6.37 lbm/sec/throat.

During turbine operation, the stresses due to aerodynamic loading are not significant because the first-stage nozzle is supported axially at both endwalls. Creep of a composite nozzle is of little concern due to the relatively low metal temperature. The dominant failure mode for a water-cooled nozzle is low cycle fatigue, and the principal contributor is strain due to thermal gradients in the nozzle components. Design goals are 83,000 hours life at full load, 3350 start/stop cycles, and a nozzle surface temperature $\leqslant$ 1000 °F at high (2600 to 3000 °F) turbine firing temperatures. The design and fabrication details for this nozzle are found in the Turbine Subsystem Design Topical Report (FE-1806-95, December 1980).

Mechanical, thermal, and hydraulic behavior of the composite nozzle was evaluated using a test arrangement, which allowed the composite nozzle to be exposed to the TRV operating environment. The composite nozzle was tested, as a three-throat cascade consisting of two test nozzles, and pressure and suction slave vanes, in the Hot-Gas Path Development Test Stand (HGPDTS).

Testing was performed at a measured average nozzle inlet gas temperature of 2730 °F, a nozzle gas inlet pressure of 11.3 atmospheres (166 psia), and a gas flow rate of 6.37 lbm/sec/throat.

---

* Topical Report FE-1806-92, "Turbine Simulator Tests with Coal-Derived Low-Btu Gas Fuel," Nov. 1980.

** Topical Report DOE/ET/10340-122, "Hot Gas Path Development Test – Part I (Facility Description)," August 1981.

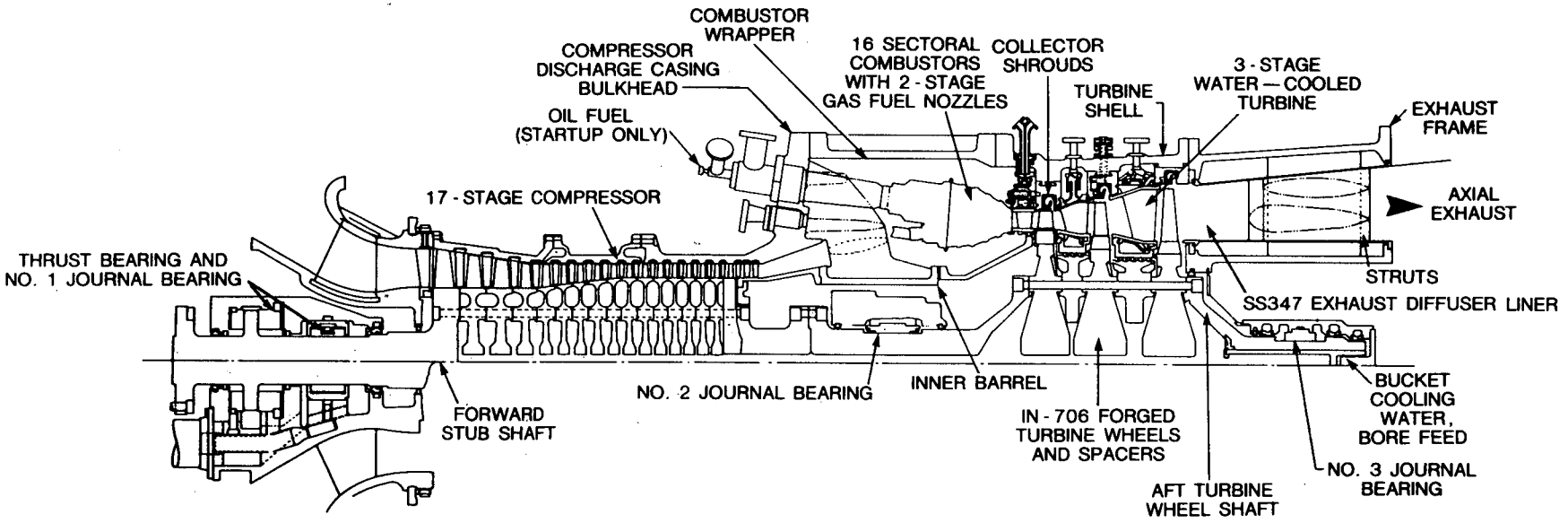

Figure 1-1. Technology Readiness Vehicle (TRV) configuration status

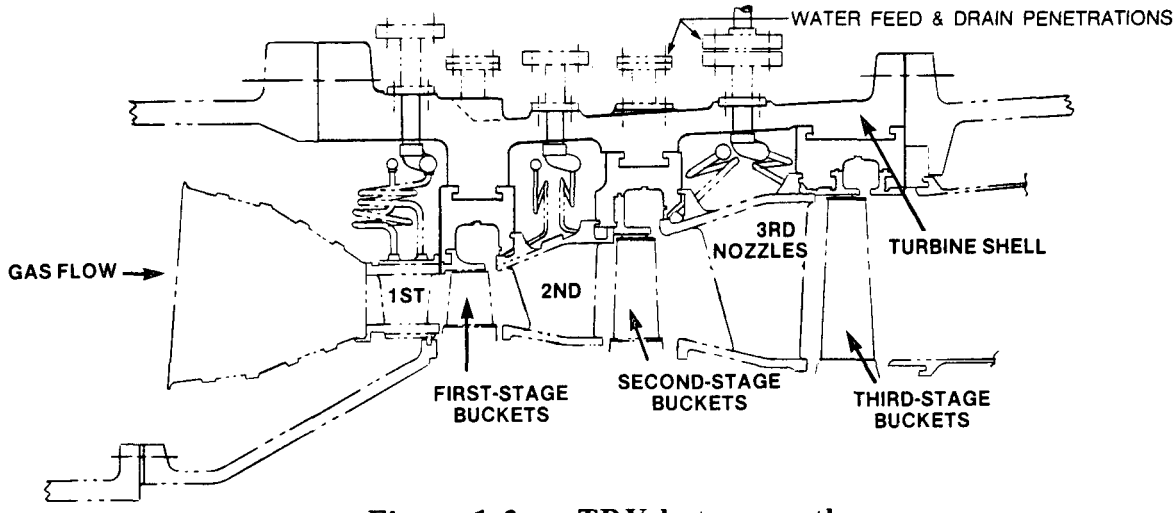

Figure 1-2. TRV hot-gas path

1.3.2 Second-Stage Nozzle

The second-stage monometallic nozzle is cantilevered from casing shroud blocks at the nozzle outer endwall, as shown in Figures 1-1 and 1-2. The TRV design operating conditions for this nozzle at a 2600 °F firing temperature are an average inlet gas temperature of 2082 °F, an inlet gas pressure of 79 psia, and a gas flow of 8.09 lbm/sec/throat.

During turbine operation, the nozzle is subjected to thermal gradients and aerodynamic loads. The hooks on the outer endwall transmit the aerodynamic bending load on the nozzle airfoils directly to the casing shroud blocks without loading the nozzle endwalls. The forward hooks provide radial support and the aft hooks provide both radial and axial support for the nozzle. As with the first-stage nozzle, the dominant failure mode is low-cycle fatigue as a result of high thermal strains due to thermal gradients in the nozzle. Design goals are 83,000 hours of life at full load, 3350 start/stop cycles, and a nozzle surface temperature $\leqslant$ 1000 °F at high (2600 to 3000 °F) turbine firing temperatures. The design and fabrication details for this nozzle are found in the Turbine Subsystem Design Topical Report (FE-1806-95, December 1980).

Mechanical, thermal, and hydraulic behavior of the monometallic nozzle was evaluated using a test arrangement, which allowed the nozzle to be exposed to the TRV operating environment. The monometallic second-stage nozzle was tested as a three-throat cascade consisting of two test nozzles, and pressure and suction slave segments, in the Hot-Gas Path Development Test Stand (HGPDTS).

Testing was performed at an average nozzle inlet gas temperature of 2082 °F, a nozzle gas inlet pressure of 5.4 atmospheres (79 psia), and a gas flow rate of 8.07 lbm/sec/throat.

1.4 REPORT CONTENTS

This report describes test results and the conclusions reached as a result of the successful completion of the water-cooled nozzle test program.

Section 2

WATER-COOLED COMPOSITE NOZZLE TEST

2.1 OBJECTIVES

The primary objective of the HTTT Water-Cooled Composite Nozzle Test was to verify that the design and fabrication of the TRV first stage nozzle are adequate for satisfactory operation in the turbine environment. Secondary objectives were to accumulate data to develop an understanding of nozzle performance as a function of the various turbine system parameters, and to validate the nozzle design analysis.

Specifically the test was designed to accomplish the following objectives:

- Demonstrate that the heat flux at the critical trailing edge and vane suction surfaces and the total heat flux agree with design values anticipated for operating conditions in the TRV.
- Demonstrate the cooling effectiveness of the water and the ability to maintain desired metal temperatures.
- Demonstrate that the thermal gradients and temperatures derived from measurements during cyclic testing fall within the bounds required to ensure the desired low-cycle fatigue (LCF) life in the TRV.
- Determine the sensitivity of the nozzle to changes in gas temperature and cooling water conditions.

2.2 TEST SPECIMEN DESCRIPTION

2.2.1 Specimen Construction

The following materials (Table 2-1) were used in the construction of the test specimen (Figure 2-1):

Table 2-1

COMPOSITE NOZZLE MATERIALS

Material	Application
Nitronic* 50 Stainless Steel	• Cooling tubes • Endwall plates • Endwall manifold covers • Airfoil spar rods
MZC† Copper	• Sublayer in which cooling tubes and spar rods are embedded
INCONEL‡ 617 (IN617)	• Skin surrounding gas path surfaces

*Trademark of Armco Steel Corporation
†Trademark of AMAX Copper, Inc.
‡Trademark of International Nickel Company

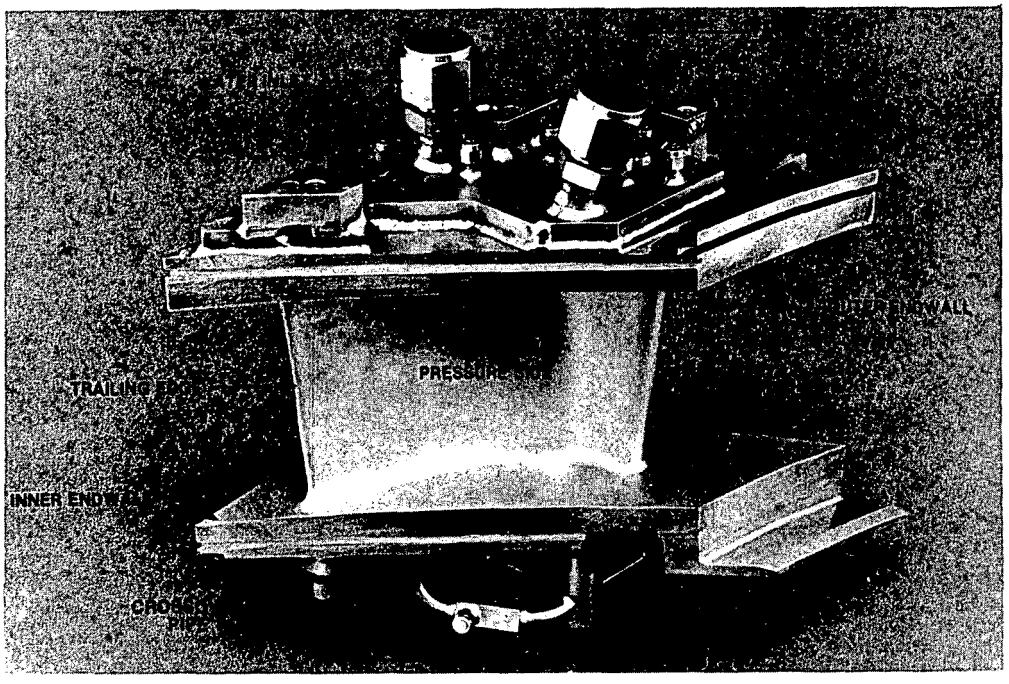

Figure 2-1. First-stage nozzle.

The gas-side surface (Figure 2-2) consists of a 0.026-inch thick skin of IN617 on both endwalls and on the airfoil vane. The corrosion-resistant skin protects the highly conductive magnesium-zirconium-chromium (MZC) copper sublayer in which the Nitronic 50 (N-50) water cooling tubes are embedded. The high thermal conductivity of the copper sublayer reduces the thermal gradients between the IN617 skin and the Nitronic 50 cooling tube wall. The structural strength of the airfoil is reinforced by six Nitronic 50 spar rods also embedded in the copper and bonded at their ends to Nitronic 50 endplates. The endplates, in addition to supporting the copper sublayer and cooling tubes on the gas side, also contain manifolds and distribution channels for the cooling water, mounting hooks, and nozzle-to-nozzle sealing grooves.

2.2.2 Specimen Cooling

Nozzle cooling is accomplished by flowing coolant (water) in tubes embedded in the copper sublayer. Water enters and leaves the nozzle at the outer endwall. It flows down the trailing edge and suction side tubes to the inner endwall and returns to the outer endwall via tubes in the leading edge and pressure side of the airfoil. Some of the water is diverted through the outer endwall by means of an orifice at the segment inlet. After cooling the outer endwall, this flow mixes with the airfoil return flow and exits the segment. Figure 2-3 shows the details of the nozzle cooling circuit and the resulting flow characteristics. The table in Figure 2-3 tabulates the cooling tube dimensions and the design coolant flow rate, temperatures, and pressures.

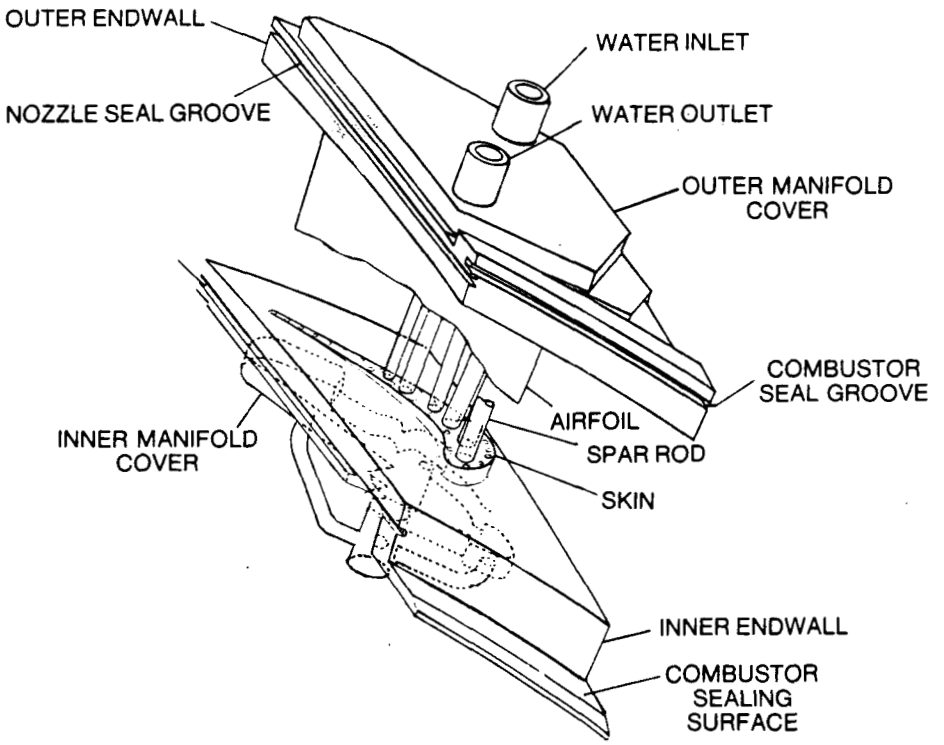

Figure 2-2. First-stage nozzle design overview

2.2.3 Pretest Inspection

Pretest inspection of the nozzles included ultrasonic inspection of the nozzle from the gas-path surfaces, and eddy current inspection of the nozzles from the internal surfaces of the airfoil cooling tubes. These inspection techniques were specifically designed to detect flaws at the following locations: the copper-to-skin interface, the copper-to-spar interface, the tube-to-copper interface, and within the copper alloy substrate. The two nozzle test specimens were serialized in fabrication as #1 and #3. Non-destructive examination (NDE) revealed that both specimens contained minor indications which were interpreted prior to testing to be tears in the endwall copper, at depths of 0.020 to 0.050 inch below the interface with the skin. The reasonably small indications of nozzle #1, were judged acceptable for the test. The larger indications of nozzle #3 were judged to require closer monitoring while under test to evaluate any change in the nature of the flaws. Refer to Section 2.8 for inspection details.

After commitment of these nozzle specimens to the test program, alternate fabrication procedures were applied to spare components to achieve fully bonded structures. These alternate procedures were demonstrated to be successful in eliminating flaw indications of the aforementioned type. These improved components were held as backups to the prime test pieces, but were not needed since the indicated flaws did not result in any detectable deterioration of the tested components.

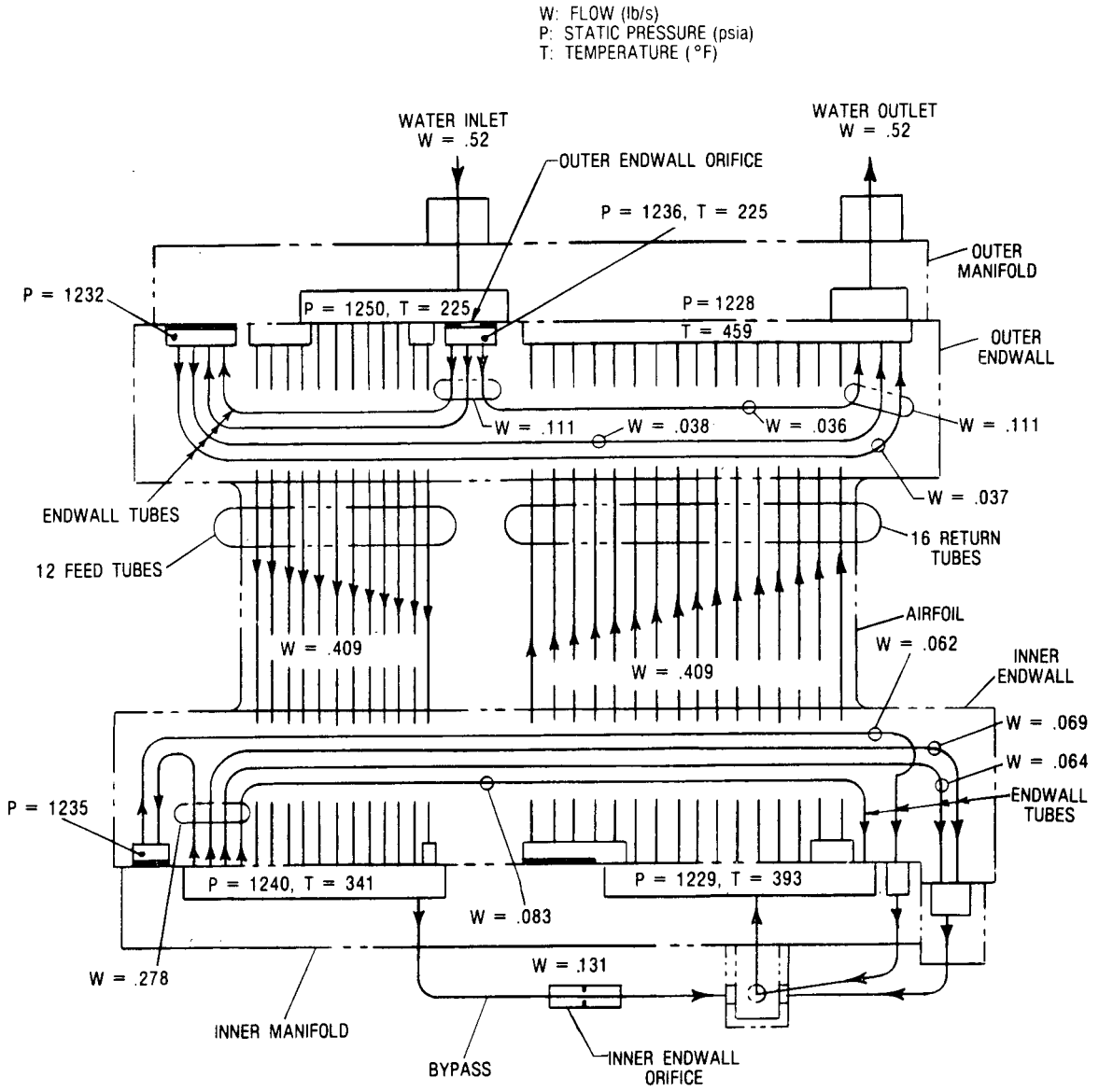

COOLING TUBE DATA				
COOLING FUNCTION	QTY.	TUBE SIZE O.D.	TUBE SIZE I.D.	MATERIAL
INNER ENDWALL COOLING	5	.125	.095	NITRONIC 50
OUTER ENDWALL COOLING	5	.125	.095	
AIRFOIL FEED COOLING	11 1*	.094 .125	.080 .105	
AIRFOIL RETURN COOLING	16	.125	.095	

*TRAILING EDGE TUBE

Figure 2-3. First-stage nozzle cooling circuit and water flows

2.3 TEST ARRANGEMENT

2.3.1 Test Specimen Installation

The composite nozzle test assembly as installed in the Hot-Gas Path Test Stand (HGPTS) is shown in Figure 2-4. The nozzle, the gas-path dimensions, and the cooling circuit are identical to the TRV first-stage nozzle. The differences between the test nozzle and the TRV nozzle are minor and only involve the mounting arrangement.

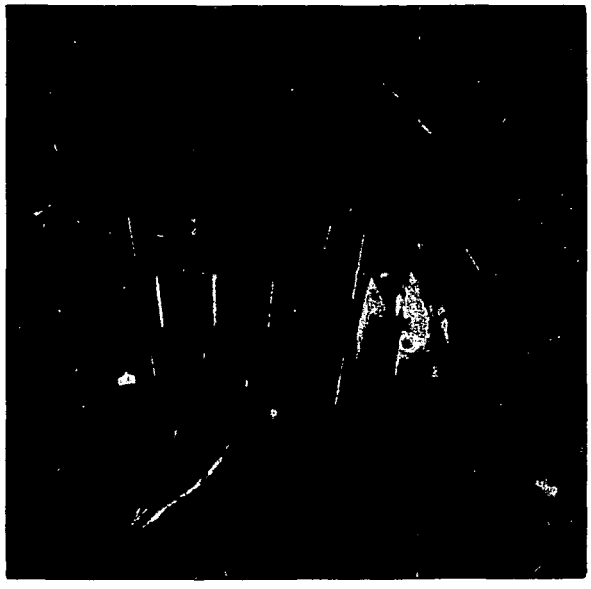

Figure 2-4. First-stage nozzle cascade mounted on heat shield in test stand

The nozzle cascade produces a fully enclosed gas path, which simulates the flow through three throats. Two test nozzle segments were interposed between two water-cooled slave segments, each of which formed one side of the cascade profile with appropriate extensions to enclose the gas path. Figures 2-4 and 2-5 show the nozzle cascade mounted on the heat shield. The heat shield transmits the nozzle cascade mechanical loads to the test stand nozzle support plate and protects the nozzle support plate from the high-temperature combustion gases. The nozzle segments contain all the essential elements required for the TRV except for attachment lugs, which will be added at both ends to support the nozzle in the turbine.

The slave segments were constructed from three copper pieces. Each segment was water-cooled through a network of holes drilled in each piece. Figures 2-6 and 2-7 illustrate the construction of the slave segments and their instrumentation.

The nozzle cascade was held together mechanically using a tie rod at each end acting through yokes at each slave segment. Spring washers were used to allow for relative expansion. An extension of the web on the suction side yoke was used for attachment to the heat shield. Axial clamping was also provided.

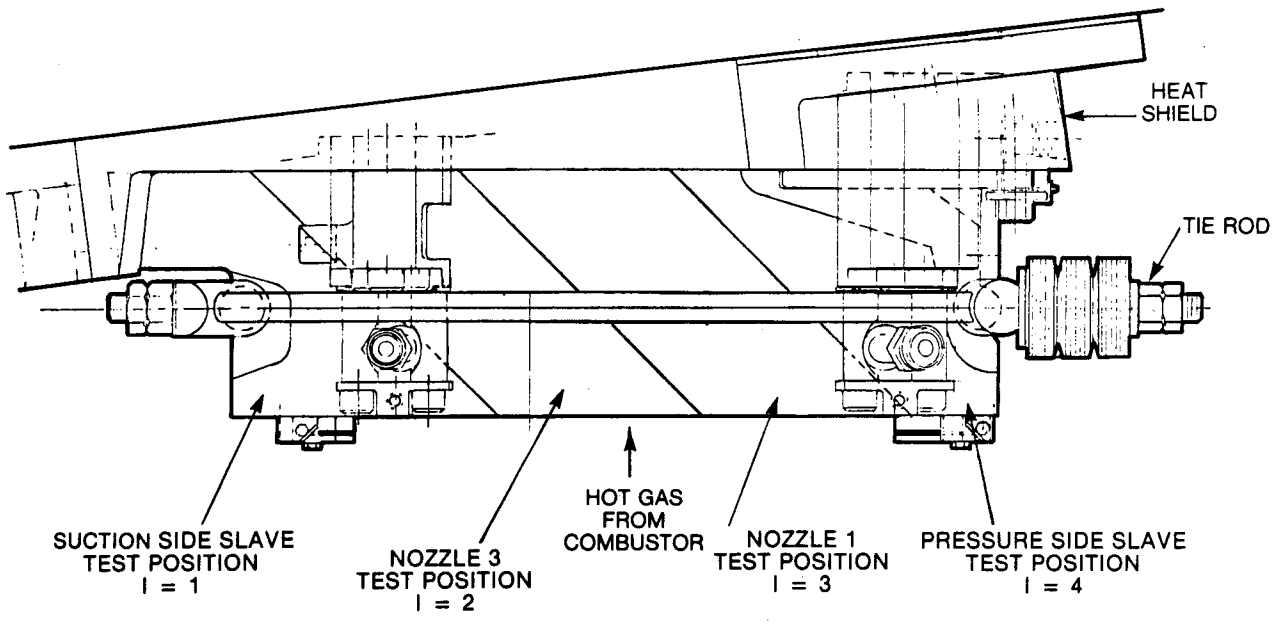

Figure 2-5. First-stage nozzle assembly (as viewed from top of HGPDTS)

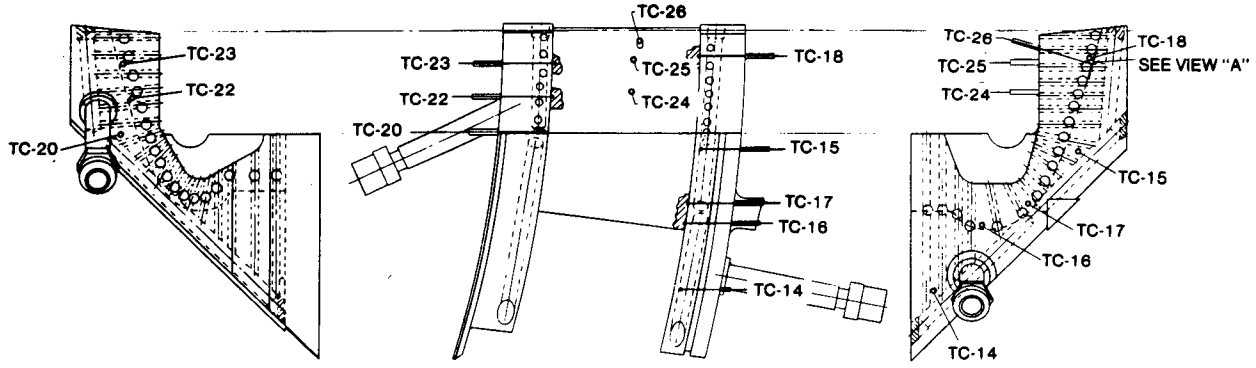

Figure 2-6. First-stage nozzle suction slave segment instrumentation

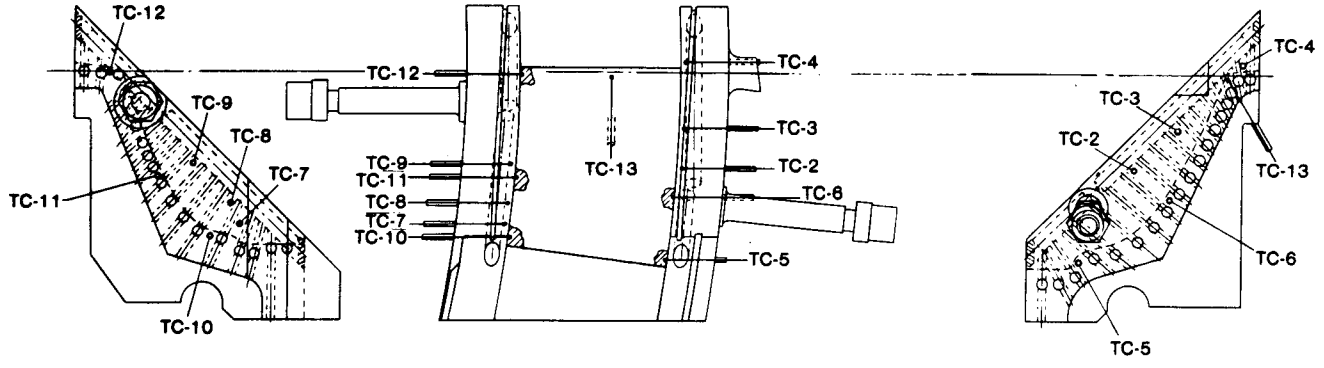

Figure 2-7. First-stage nozzle pressure slave segment instrumentation

2.3.2 Combustion System

The combustion system used for this test consisted primarily of modified General Electric product line components, and is shown in Figure 2-8. The combustion liner was a standard General Electric MS6000 liner, with the liner flow area reduced by blocking off some holes and reducing the size of others. Fuel was supplied through a gas-only fuel nozzle. The liner was surrounded by a flow sleeve. The flow sleeve and fuel nozzle were supported at the test chamber endplate by various adapter pieces, which were specifically made for this test.

A modified MS6000 transition piece was used for the test. The transition piece was shortened and the flow path modified to conform to the test nozzle. The transition piece flange was clamped to the nozzle to provide support for the transition piece, and to seal off the gas path. Four sockets were mounted on top of the transition piece to hold the gas sample probe guide tubes. The entire transition piece was surrounded by an impingement shell. The combustor air supply passed through this perforated shell and impinged on the transition piece, cooling it to an acceptable temperature. The transition piece interior surface was thermal-barrier coated to help reduce metal temperatures.

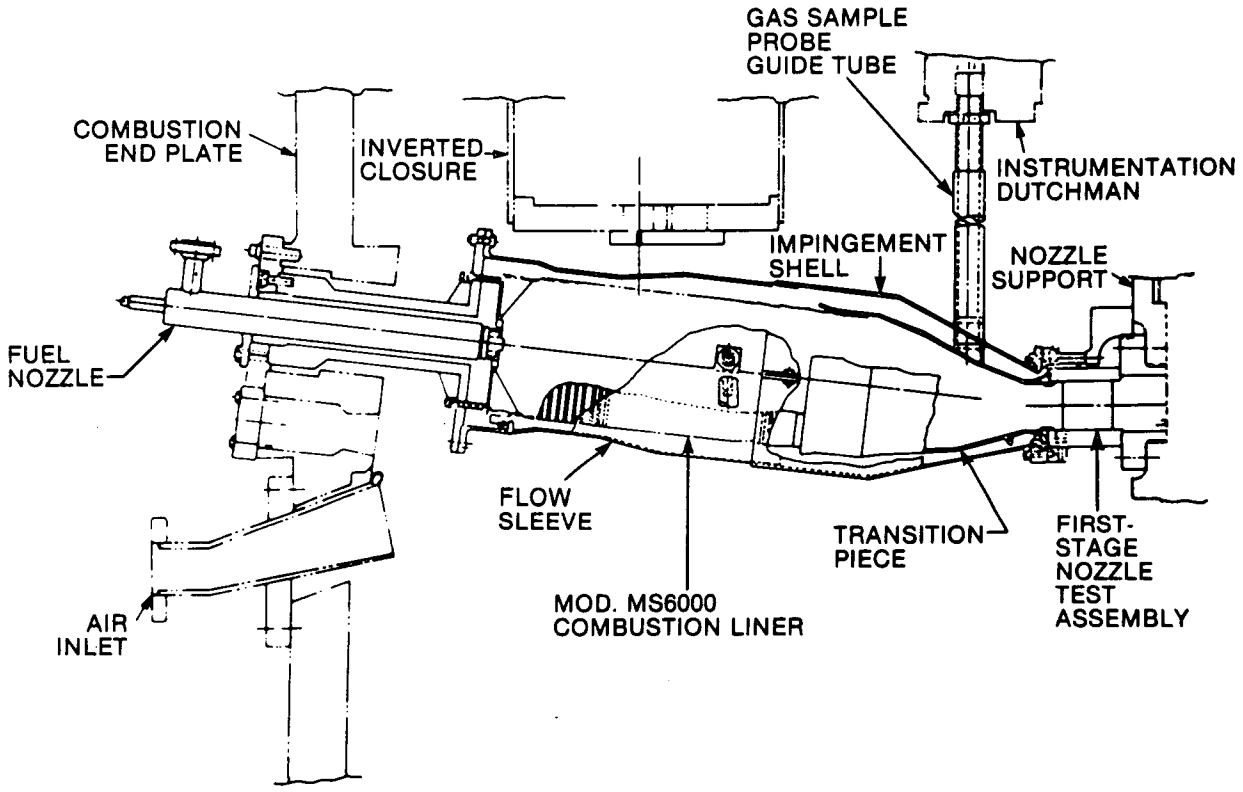

Figure 2-8. First-stage nozzle test arrangement in HGPDTS

2.4 TEST SEQUENCE

Testing was performed in the following sequence:

1. Calibration of instrumentation and checkout of the facility, test specimen, and procedures. This was accomplished by performing a cooling water flow test, a gas-path leakage test, and a hot air (unfired) flow test.
2. Fired testing at design point conditions, followed by parameter variation testing to determine the sensitivity of the test specimen to changes in inlet cooling water temperature, cooling water flow rate, gas temperature, and gas flow rate.
3. Cyclic testing to subject the test specimens to several hundred simulated turbine startup/shutdown cycles.
4. Simulated system fault testing by performance of a reduced cooling water flow rate test and an increased gas temperature test.

2.5 INSTRUMENTATION

2.5.1 Nozzle Cascade

Thermocouples were installed in strategic locations in the copper of the slave segments. The locations of these thermocouples are shown in Figures 2-6 and 2-7.

The test nozzles were each instrumented with thermocouples as shown in Figure 2-9. The thermocouples and pressure taps installed to calibrate the endwall orifices are shown in the figure. Additional thermocouples were installed on nozzle #3 to more closely monitor copper temperatures near the NDE indications. Locations of these added thermocouples are defined in Figure 2-10.

2.5.2 Combustion System

The combustion system instrumentation is summarized in Table 2-2. Liner and transition piece metal temperatures were measured with backside surface mounted thermocouples. Two accelerometers measured system vibrations. A dynamic pressure probe measured pressure variations within the system. The combustor inlet air temperature was measured by six radiation shielded thermocouples. The thermocouples were equally spaced circumferentially in the annulus between the flow sleeve and the liner near the exit plane of the liner.

Four water-cooled traversing gas sample probes were used to obtain measurements of the hot-gas path characteristics at the exit of the combustor, upstream of the first-stage nozzle. The probes were designed to measure gas temperature with an aspirated thermocouple, measure total pressure, measure static pressure, provide a quenched gas sample for combustor exhaust temperature and efficiency determination, and provide a quenched gas sample for combustor emissions compliance determination. Actuators were used to traverse each of the probes independently across the combustor exit. See Appendix E for details of the water-cooled gas sample probes.

Figure 2-11 shows the location of the transition piece instrumentation. Five thermocouples (TCCONT(I), I = 1 to 5) and a total pressure probe (PTOT) were in-

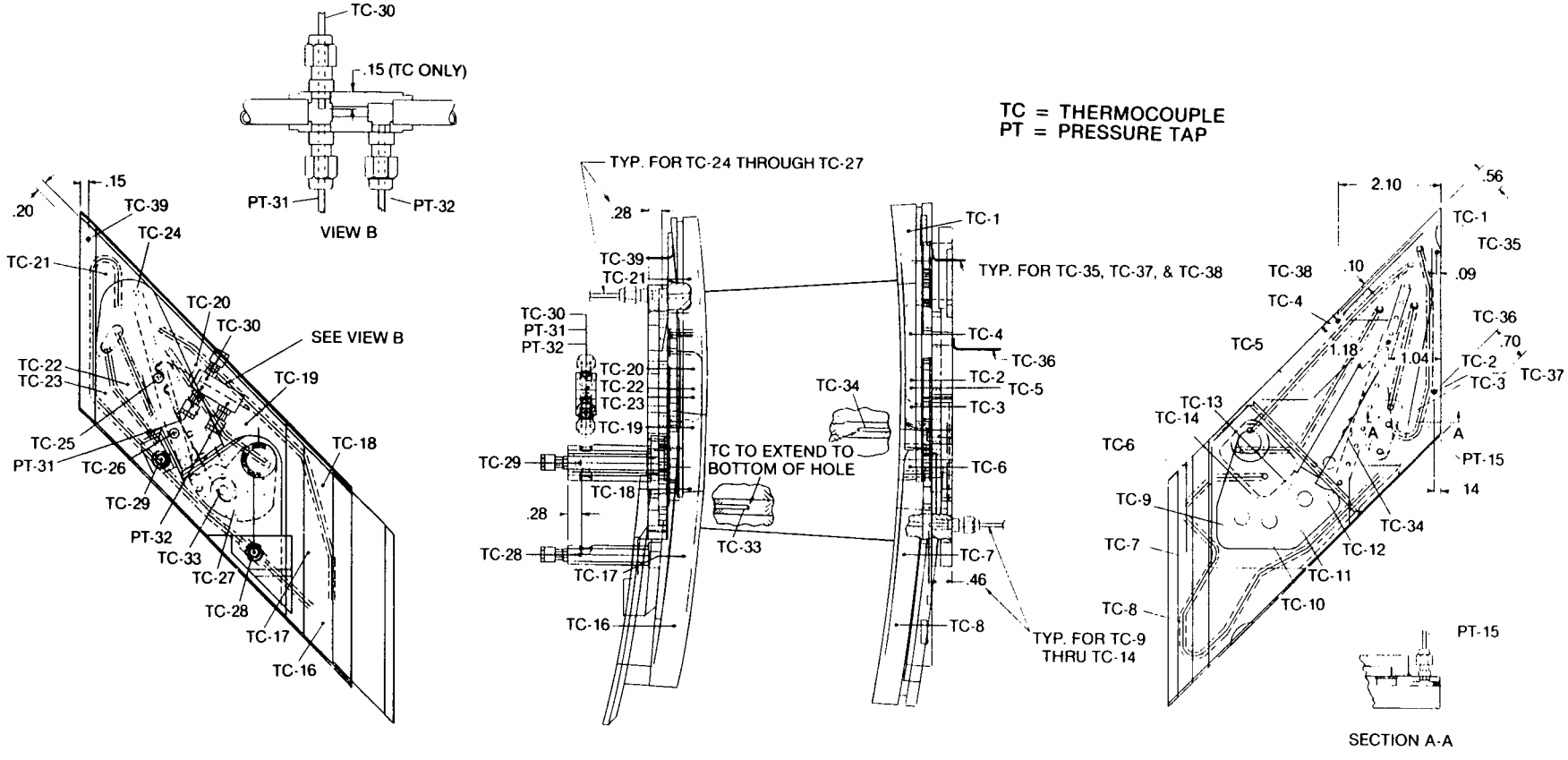

Figure 2-9. First-stage nozzle instrumentation

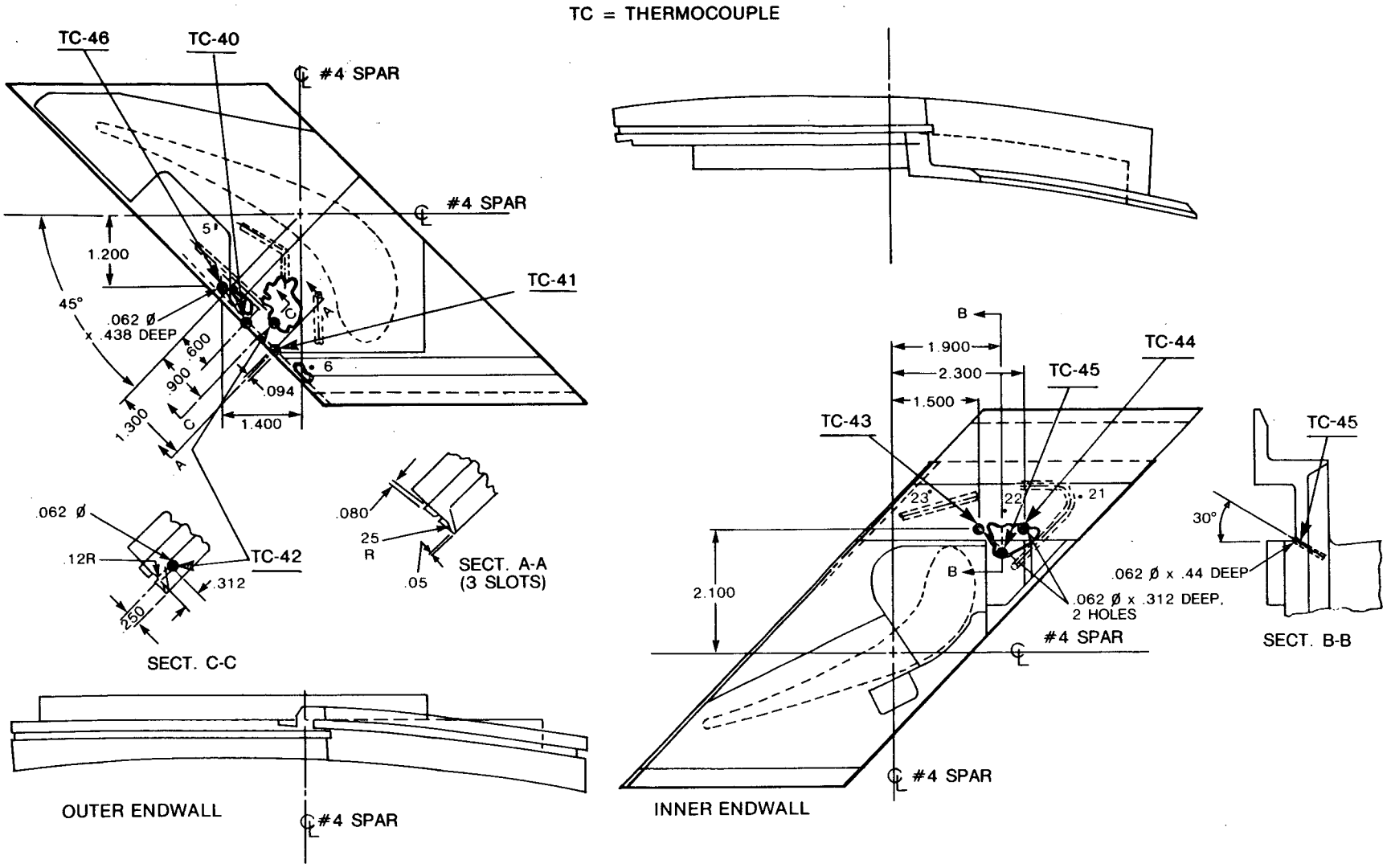

Figure 2-10. First-stage nozzle showing added thermocouples for nozzle #3

Table 2-2

COMBUSTION SYSTEM INSTRUMENTATION
FOR FIRST-STAGE NOZZLE TEST

Component	Instrumentation	Function
Liner	37 thermocouples	Monitor liner metal temperatures
Liner Flow Sleeve	6 thermocouples	Located in annulus between flow sleeve and liner (radiation shielded). Used to measure inlet air temperature
Transition Piece	38 thermocouples	Monitor transition piece metal temperature (Figure 2-11). Labeled TC (1) to TC (38).
	5 control thermocouples	Located in gas stream as shown in Figure 2-11. Used to control firing temperature. Labeled TCCONT (1) to (5), platinum-rhodium.
	4 profile thermocouples	Located as shown in Figure 2-11. Provide additional gas temperatures. Labeled PTC (1) to (4), platinum-rhodium.
	1 water-cooled total pressure probe	Provides gas total pressure. Located as shown in Figure 2-11.
	4 traversing gas sample probes	Located as shown in Figure 2-11. Each probe measures pressure, gas temperature, and emissions at five locations located radially across gas path

stalled to measure bulk gas properties at the combustion exit, and were used to control the test conditions. The four water-cooled traversing gas sample probes were located 6.017 inches upstream of the end of the transition piece. Each gas sample probe was programmed to take measurements at five radially located stations in the gas path. Each probe measures O_2 level, temperature, and pressure. Oxygen measurements were made using samples from all of the probes taken together to generate a "gang" sample, or samples were taken individually. Since the gas sample probes cannot radially traverse the entire gas path, a row of four platinum-rhodium thermo-

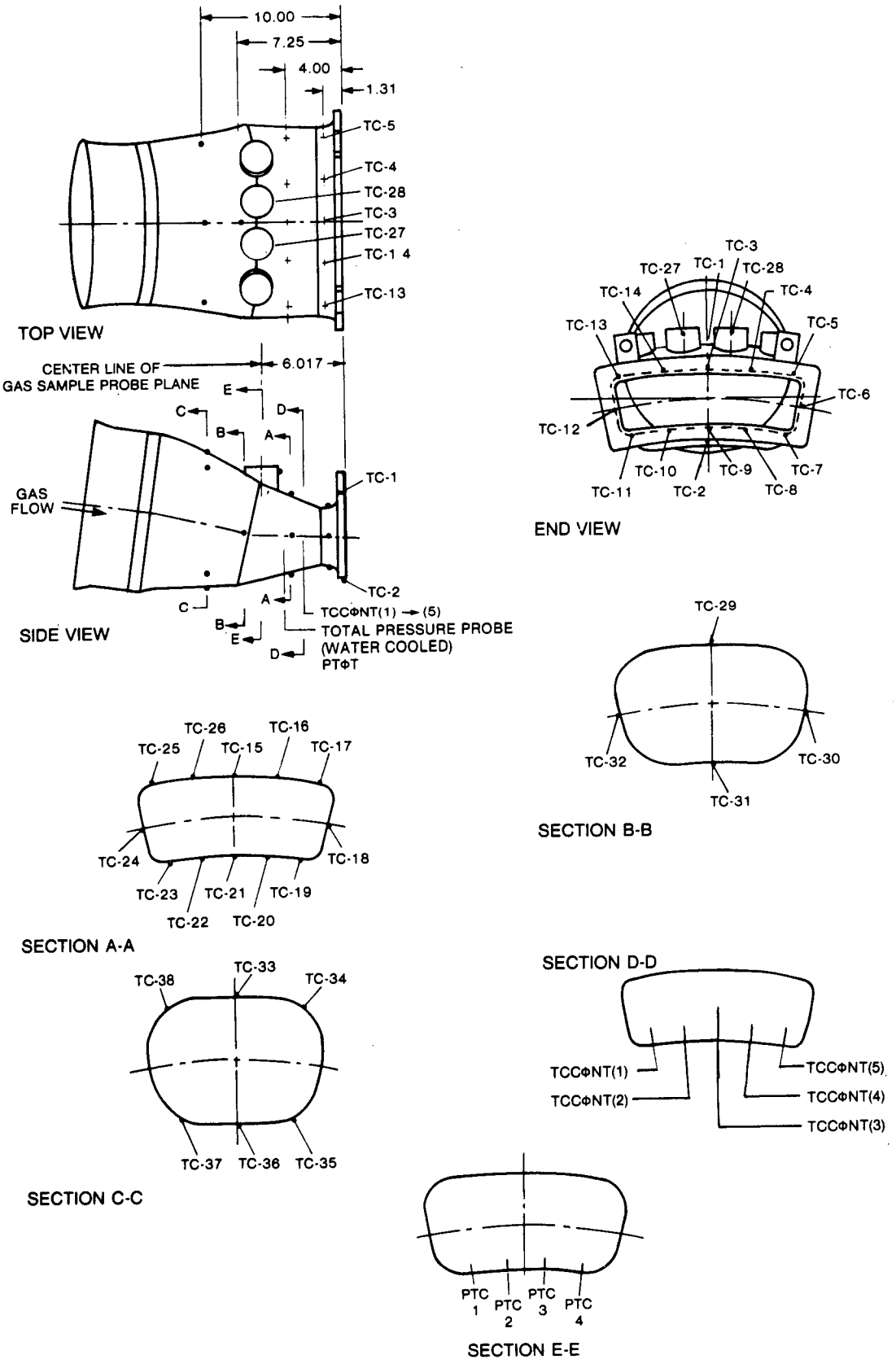

Figure 2-11. Transition piece instrumentation for first-stage nozzle test

couples were added along the transition piece innerwall in the same axial plane as the gas sample probes. The thermocouples extended into the gas path 0.65 inch (10% span). These thermocouples were used to define the temperature profile near the transition piece innerwall. The combustor exit gas temperature profile was determined using data from the traversing gas sample probes and from the transition piece innerwall thermocouples. See Appendix D for details of the gas sample probe data.

2.5.3 Special Instrumentation

An infrared pyrometer installed downstream of the nozzle cascade in the mixing chamber of the HGPDTS focused on the trailing edge portion of the suction side of the test nozzle airfoils. The pyrometer was able to scan the entire gas path height and measure the surface temperature of the airfoil. This non-contact instrument allowed temperature measurements of the airfoil to be made without disturbing the gas flow over the airfoil. Details of its design, construction, and calibration are found in Appendix A.

Instrumentation from the nozzle and test support hardware was monitored by a computer which organized the data into displays and calculated nozzle performance. The computer accomplished a complete scan of the instrumentation every thirty seconds. The computer was also programmed to trip the test, by an instantaneous shutoff of the fuel flow to the combustor, if an out-of-limits condition was detected. Trips were set on low coolant flow and pressure, high coolant temperature, and excessive combustion gas temperature.

2.5.4 Measurement Errors

Primary measurements made during the testing were water and gas pressure, temperature and flow, and metal temperature. An estimation of measurement errors is required to put the data in perspective and to complete documentation of the testing. The following are estimates of the differences between the true values and the recorded values:

Water temperature	±4°F
pressure	±3 psi
flow	±.01 pps
Gas temperature	±50°F
pressure	±2 psi
flow	±1 pps
Metal temperature	±4°F (See Appendix A for discussion of pyrometer measurement errors)

The summation of these errors does not compromise the verification of design procedures or the demonstration of technology readiness.

2.6 DATA REDUCTION PROCEDURE

A complete data reduction procedure was developed for the first-stage nozzle test. The objectives of the data reduction procedure included documenting all important test parameters, monitoring test variables during the test, expediting the calculations

which had to be made during testing, and making the information readily available in a functional format.

The data reduction procedure prints out or displays the following information groups:

- Critical parameters
- Water properties
- Air/fuel properties
- Aerodynamics
- Thermal/hydraulics
- Nozzle flow/heat splits
- Test nozzle metal temperatures
- Pressure slave segment metal temperatures
- Suction slave segment metal temperatures
- Defect temperature monitor
- Heat shield monitor
- Combustor performance data
- Liner and transition piece metal temperatures

Many of these information groups were available on a screen for immediate display and continuous monitoring as required.

The procedure used to accurately define the aerothermal information at each test point is presented below. Table 2-3 defines the nomenclature involved.

- Determine T_{BULK} from the correlation between the average of the control thermocouples, T_{FI}, and temperature indicated by O_2 levels in the combustion products. These O_2 levels were obtained by way of the probes in the gas path. Refer to Appendix D for the details of the gas temperature determination.
- Determine dilution flow, W_D, from P_{CD}, T_{IN}, and the flow function for a pressure ratio of P_{CD}/P_T. This flow is the mass of cool (~600 °F) air entering the gas path at the thermocouple support posts. Effective dilution flow area was 0.4 square inch for the initial test and 0.25 square inch for the extended test.
- Determine test stand leakage flow. $W_L = 0.532\ P_{CD}/\sqrt{T_{IN}}$ and $0.372\ P_{CD}/\sqrt{T_{IN}}$ for the initial and extended tests, respectively. These correspond to 1.0 square inch and 0.7 square inch leakage areas, respectively, for choked flow from the test stand.
- Perform flow balance to determine throat flow, $W^* = W_F + W_A - W_L$.
- Determine nozzle inlet temperature, $T_O = T_{BULK} - (W_D/W^*)(T_{BULK} - T_{IN})$
- Determine firing temperature. For the purpose of this test, firing temperature is defined as the total average temperature, T^*, at the nozzle exit. $T^* = T_O - Q/W^*C_p$
- Calculate aerodynamic flow function. $W^*\sqrt{T^*}/[P_T(A^*C_q)]$.

The above procedure was used to obtain the data presented in Section 2.7.4.2, Results of Steady-State Fired Testing.

Table 2-3

NOMENCLATURE FOR DATA REDUCTION PROCEDURE

A	Geometric area
c	Airfoil chord length
C_q	Discharge coefficient
C_p	Specific heat at constant pressure
G	Coolant flow per unit area
h	Heat transfer coefficient
k	Thermal conductivity
m	Coolant mass flow
Nu_c	Nusselt number $\frac{[hc]}{[k]}$
P	Pressure
Pr	Prandtl number $\frac{[\mu C_P]}{[k]}$
Q	Heat load for entire 3 throats
r	Recovery factor
Re_c	Reynolds number $\frac{[\rho V c]}{[\mu]}$
s	Skin thickness
T	Temperature
V	Velocity
W	Gas or air mass flow
γ	Specific heat ratio
Φ	Heat flux
μ	Absolute viscosity
ρ	Density

Superscripts

$\bar{}$	Average value (i.e. $\bar{T}$)
*	Throat

Subscripts

A	Air
BULK	Gas average at probe plane
CD	Compressor discharge (main chamber)
ci	Coolant at nozzle inlet
CHAM	Mixing chamber
cu	Copper sublayer
D	Dilution
F	Fuel
g	Gas
FI	Average of control thermocouples
IE	Inner endwall
IN	Into main chamber
L	Leakage
O	At nozzle inlet plane
OE	Outer endwall
REF	Eckert reference temperature
s	Hot gas surface
T	Total gas property upstream of nozzle
VANE	Nozzle airfoil
WATER	Cooling water
w	Cooling tube inner wall
∞	Freesteam static
as	Adiabatic surface

2.7 TESTING

2.7.1 Cooling Water Flow Test

2.7.1.1 Test Description

The cooling water flow test was run to accomplish the following:

- Determine if the nozzle orifices were distributing the flow as required
- Correlate measured water pressure drop across the test nozzles with preliminary analysis
- Provide flow versus pressure drop data as a reference for further testing
- Ensure functional operation of the water temperature thermocouples
- Calibrate the orifice and ΔP transducers metering coolant flow
- Determine if coolant leaks were present in the as-installed configuration.

The test was conducted at 450 psig water pressure. Inlet and outlet loop pressures and temperatures, and inlet flow were recorded.

Pressures were measured within each test nozzle at the following locations (refer to Figure 2-9 for locations of pressure taps and thermocouple ports):

PT 15 - Downstream of Outer Endwall Orifice (OEO)
PT 31 - Upstream of Inner Endwall Orifice (IEO)
PT 32 - Downstream of IEO
TC 12 - Outlet Manifold
TC 25 - Inner Endwall (IE) Feed Manifold
TC 27 - IE Return Manifold
TC 34 - Inlet Manifold

Inlet water temperature was maintained at 300 °F during the test, and water flows were varied from 80 to 160% of design flow (0.52 pps) for the test nozzles, and 80 to 120% of design flow (1 pps for the suction side slave and 0.72 pps for the pressure side slave) for the slave segments.

2.7.1.2 Test Results

Results from the cooling water flow test are shown in Figures 2-12 and 2-13 for the test nozzles, and in Figure 2-14 for the slave segments. Refer to Figure 2-9 for the location of the pressure taps used to get the data shown in Figures 2-12 and 2-13. For the pressure drop testing, pressure taps were installed in some thermocouple (TCxx) locations as well as pressure tap (PTxx) locations. For example, in Figure 2-12, feed tube ΔP was determined by the difference in pressure between taps located in the TC34 and TC25 locations shown in Figure 2-9.

The feed and return tube ΔP data were somewhat erratic because of measurement error (a small difference between two large numbers). However, the ΔP's appear to be the right order of magnitude. The feed ΔP is consistently higher than the return ΔP. Nozzle ΔP was measured to be 21.4 psi for nozzle #3 and 19 psi for nozzle #1 at the design total flow (0.52 pps). The predicted ΔP was 22 psi.

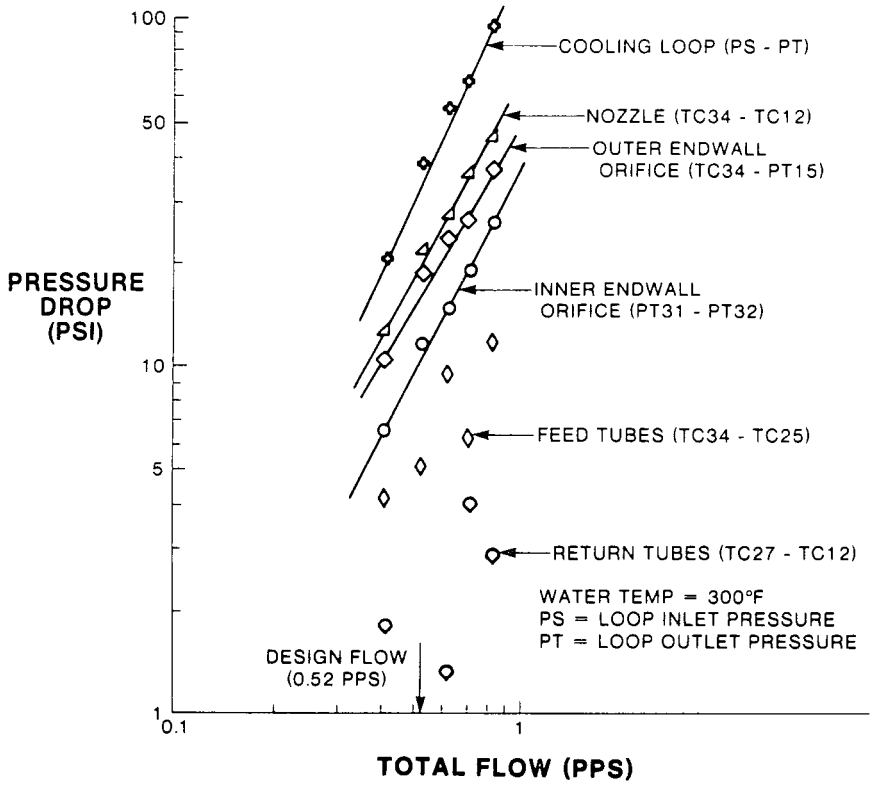

Figure 2-12. Test nozzle #3 coolant flow vs pressure drop

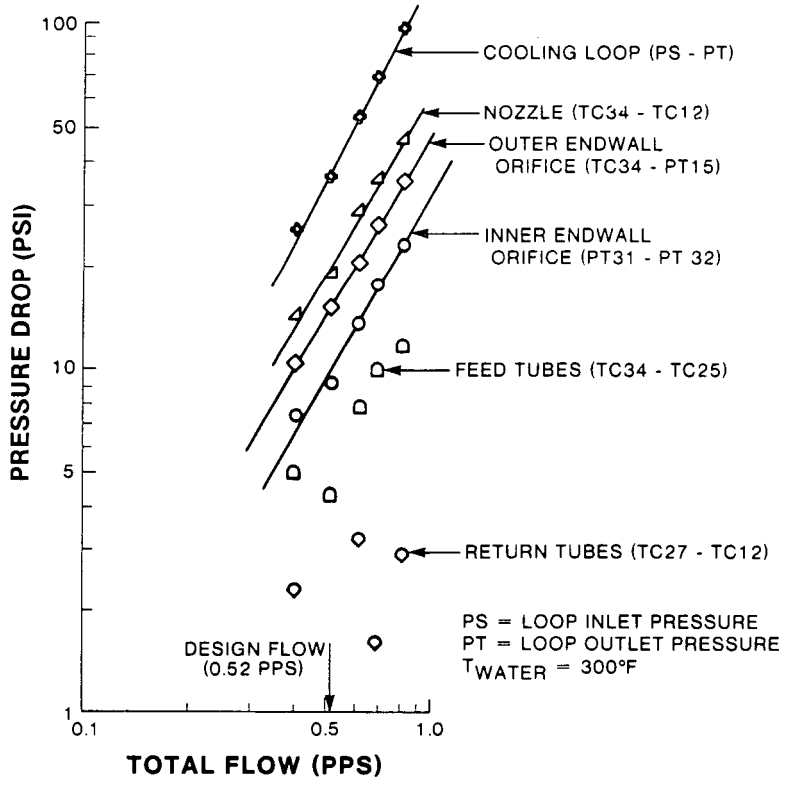

Figure 2-13. Test nozzle #1 coolant flow vs pressure drop

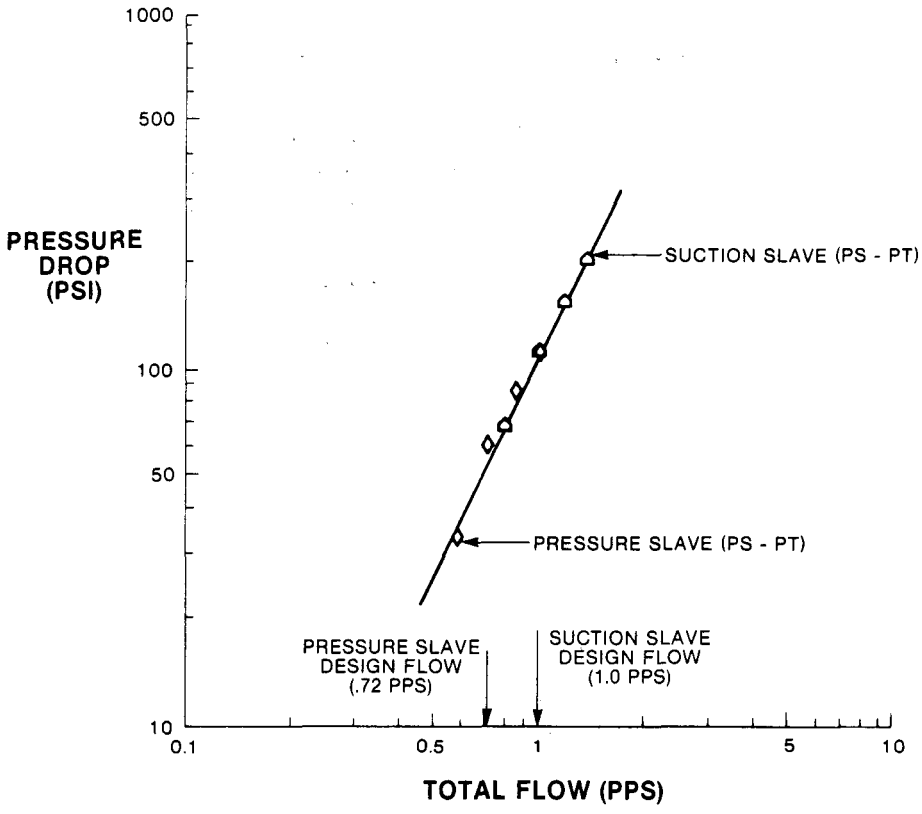

Figure 2-14. Slave segment coolant flow vs pressure drop

Leaks from a nozzle manifold weld were found during this flow test. After the test, the segment was removed from the nozzle support plate and weld repaired.

Results from the water flow test indicated that the pressure distribution within the test nozzle cooling circuit was reasonably close to what had been predicted by analysis. The following conclusions were made:

- Outer and inner endwall orifice flows are near the design value, thus assuring the desired flow to all parts of the nozzle.
- Nozzle manifold pressure drop is very close to the predicted value of 22 psi.
- Slave segment flows are near design value.

2.7.2 Gas-Path Leakage Test

2.7.2.1 Test Description

The objective of the gas-path leakage test was to determine, quantitatively, the sum of flows not going through (bypassing) the nozzle throats. The gas-path leakage test also determined the effective area of leaks that would introduce compressor discharge air into the gas path downstream of the control thermocouples.

In conducting this test, the combustion module of the HGPDTS was sealed with the cover plate and manhole covers so that it could be pressurized. The mixing chamber was open to atmospheric pressure. Transition piece inlet area was plugged, but all other instrumentation and geometry was the same as planned for fired testing.

Flow and temperature of air flow into the combustion module were measured as it was pressurized. The test was run with the compressor air line, and re-run with the atomizing air line, because the atomizing air line has a smaller measuring orifice which was more suitable for measuring the low flows in this test. Since the transition piece was plugged, the total flow leaking from the combustion module was going through the nozzle support plate seals, and/or through the intentional penetrations in the transition piece.

Table 2-4

GAS-PATH LEAKAGE TEST DATA:
FIRST STAGE NOZZLE CONFIGURATION

TEST POINT	COMPRESSOR (C) OR ATOMIZING AIR (A/A)	W_{IN} (PPS)	T_{IN} (°R)	P_{CD} (PSIA)	$W_{IN}\frac{\sqrt{T_{IN}}}{P_{CD}}$	$\frac{P_{CD}}{P_{CHAM}}$	$W_{IN}\frac{\sqrt{T_{IN}}}{P_{CD}A_LC_q}$ (ISENTROPIC)	A_LC_q (in^2)
1	C	0.170	540	17.43	0.227	1.185	0.395	0.58
2		0.204	540	18.57	0.255	1.263	0.435	0.59
3		0.242	540	21.060	0.267	1.432	0.495	0.54
4		0.288	541	22.67	0.295	1.541	0.511	0.58
5		0.300	541	24.81	0.281	1.687	0.525	0.54
6		0.335	541	27.23	0.286	1.851	0.532	0.54
7		0.337	540	28.85	0.271	1.962	0.532	0.51
8		0.359	541	30.88	0.270	2.100	0.532	0.51
9		0.381	542	32.99	0.269	2.240	0.532	0.51
10	A/A	0.099	538	16.03	0.143	1.090	0.300	0.48
11		0.135	538	16.97	0.185	1.154	0.372	0.48
12		0.235	543	21.01	0.261	1.429	0.495	0.53
13		0.270	543	22.76	0.276	1.548	0.511	0.54
14		0.304	543	24.97	0.284	1.698	0.528	0.54
15		0.335	542	27.00	0.289	1.836	0.532	0.54
16		0.173	541	18.19	0.221	1.237	0.420	0.53
17		0.332	541	27.01	0.286	1.837	0.532	0.54
18		0.364	542	28.78	0.294	1.957	0.532	0.55
19		0.396	543	30.88	0.299	2.100	0.532	0.56
20		0.419	541	33.62	0.290	2.286	0.532	0.55

Note: See Table 2-3 for nomenclature.

2.7.2.2 Test Results

Data from the gas path leakage test are tabulated in Table 2-4 and plotted in Figure 2-15. The calculated total effective area ($A_L C_q$) was determined from the test data and the isentropic flow function at the pressure ratio P_{CD}/P_{CHAM}. The total effective area represents the sum of flow areas associated with the main chamber, the control thermocouple support post cooling, the transition piece/nozzle seal leakage, and the hot-gas path probe penetrations. Other leakages were assumed negligible.

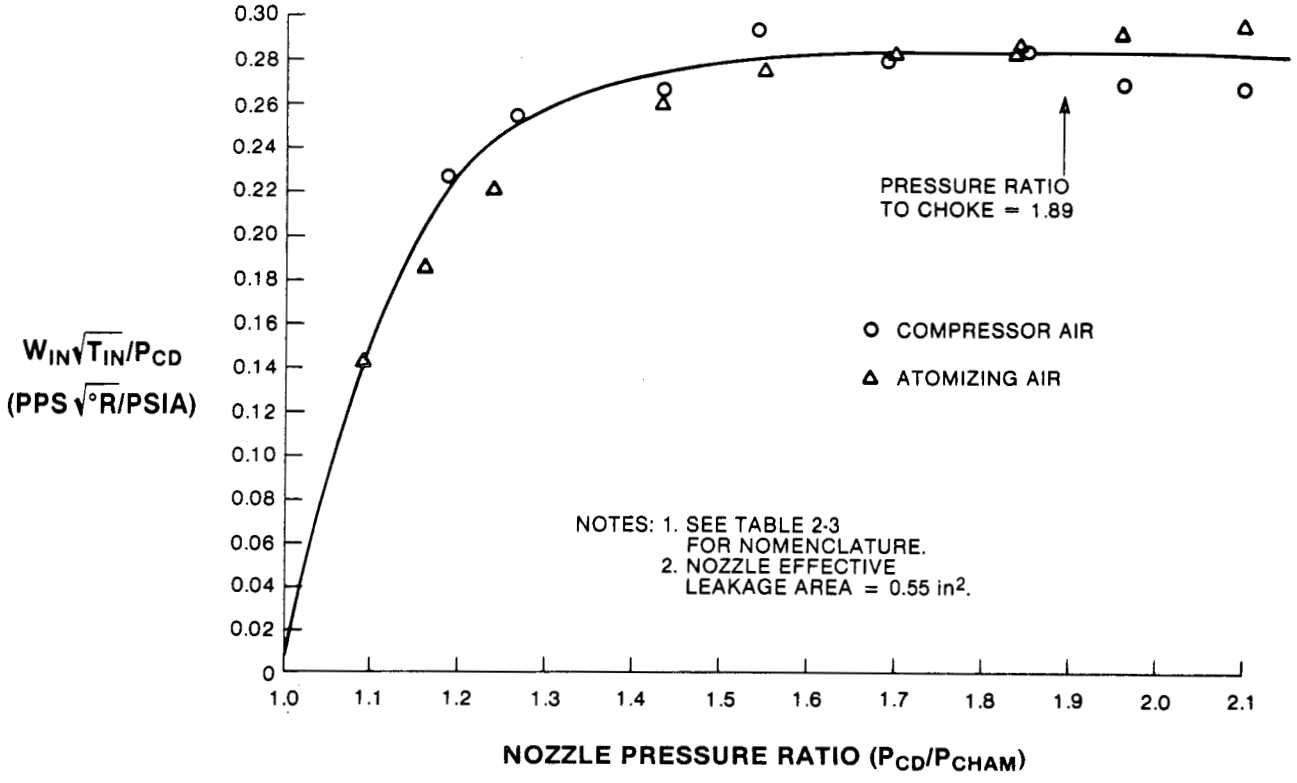

Figure 2-15. First-stage nozzle gas-path leakage test results

A total effective leakage area of 0.55 square inch was calculated from the measured data. This leakage area can easily be accounted for by the possible leakage sources. Although the results of the gas-path leakage test are correct at the pressure and temperature of the leakage test, they were not sufficient to define test stand leakage flows at full pressure and temperature operation. The test results revealed that the test stand and interface seals were intact, and that the buildup of the hardware could continue. Fired test point data were subsequently used to quantitatively determine the test stand leakage at operating pressures and temperatures.

2.7.3 Hot Air Flow Tests

2.7.3.1 Test Description

The heat flux experienced by the nozzles during fired testing is dependent upon the aerodynamic flow conditions in the nozzle gas path. A hot air flow test was run to establish aerodynamic characteristics of the nozzle cascade.

The objectives of the hot air flow test were to:

- Check out the facility under full pressure loading at elevated temperatures (600 °F).
- Check out the instrumentation and data acquisition system.
- Check out the on-line data reduction procedure.
- Determine the flow function versus nozzle pressure ratio curve over the operating pressure ratio range.

The hot air tests were conducted with the hardware assembled and readied for fired testing, with the exception of the fuel line attachment. The full data reduction procedure was activated during this test. In order to establish a range of pressure ratios across the nozzle throats, the airflow and nozzle upstream total pressures were varied. Water flow rates were set at nominal values. Water inlet temperature was varied between 225 °F and 350 °F. The upper bound on airflow was limited by the pressure drop across the combustion liner. These experimentally determined points were plotted and compared to the theoretical curve based on isentropic flow.

2.7.3.2 Test Results

The results of the hot air test are plotted in Figure 2-16. The measured value of effective throat area as determined from the data was 13 square inches. This was used as the effective area (A^*C_q) in the aerodynamic calculations. The results of the hot air test were used as a reference during fired testing.

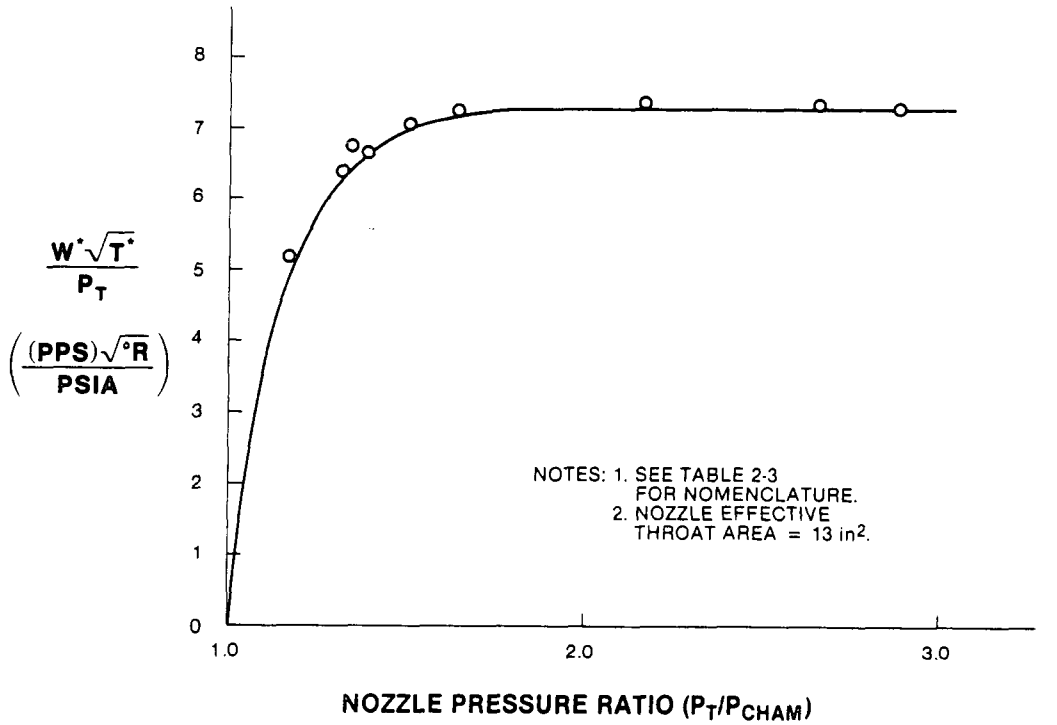

Figure 2-16. Hot air test results – first-stage nozzle configuration

2.7.4 Initial Steady-State Test

2.7.4.1 Test Description

Coolant flow to nozzle #3, installed in position #2, was maintained at 150% of design flow (0.78 lb/sec). Nozzle #1, installed in position #3, was used to acquire thermal data and will be referred to as the test nozzle. Coolant flow to the test nozzle was also set initially at 150% of design flow as a precautionary measure. Gas temperature increases were made in small steps, with data recorded for each step. The test conditions for the initial series of fired test points are summarized in Table 2-5 of Section 2.7.4.2.

A combustor gas sample probe traverse was performed at test point #17. A second traverse was performed when full firing temperature was attained. See Appendix D for details of the gas sample probe data. Testing was interrupted at the completion of test point #17A for an in-place visual examination of the nozzles.

Variations in thermal conditions were made to determine test nozzle response. These variations included coolant flow rate, coolant inlet temperature, coolant pressure, gas temperature, and gas flow rate. Parameter variation test points are summarized in Table 2-5 of Section 2.7.4.2. An in-place visual examination of the nozzles was again performed at the completion of test points #32 and #33F prior to initial cyclic testing.

2.7.4.2 Test Results

The initial steady-state fired testing results are summarized in Table 2-5 and in Figures 2-17 through 2-22. Figure 2-17 summarizes the aerodynamic flow function versus pressure ratio relationship for the range of variables covered during the initial and extended fired testing.

Variations in heat load and copper temperatures as a function of coolant flow rate, coolant inlet temperature, and gas temperature are shown in Figures 2-18, 2-19, and 2-20, respectively. Heat load, Q, is the single-nozzle heat load. The functional dependencies follow predicted trends and form a valuable data base for establishing test parameter relationships for control of subsequent steady-state and transient testing.

Gas side heat transfer coefficient (h_g) and metal surface temperature (T_s) were calculated from the available steady-state fired test data. The results of these calculated parameters are shown in Figures 2-21 and 2-22. Calculations were performed separately for each endwall and for the airfoil of the test nozzle in the following manner. Copper sublayer temperatures and gas temperatures were measured directly. The heat flux (Φ) was determined from the heat load over a known surface area of the test nozzle. The average values of h_g and T_s were calculated as follows:

$$\overline{h_g} = \frac{1}{\left[\frac{T_g - T_{cu}}{\Phi}\right] - \left[\frac{s}{k}\right]}, \text{Btu/hr-ft}^2\text{-°F}$$

$$\overline{T_s} = T_{cu} + \Phi\left[\frac{s}{k}\right], \text{°F}$$

where: T_g = gas temperature, °F
T_{cu} = copper temperature, °F
s = skin thickness, feet
k = skin thermal conductivity, Btu/hr-°F-ft
Φ = heat flux, Btu/hr-ft^2

Since an average copper temperature and gas temperature were used in this calculation, the resultant h_g and T_s can only be interpreted as average estimates over a particular area of the test nozzle.

Table 2-5

INITIAL FIRED TEST CONDITIONS
FIRST-STAGE NOZZLE TEST

TEST POINT	REMARKS	T* °F	W* PPS	P_T PSIA	Q Btu/Sec	P_T/P_{CHAM}	COPPER TEMPERATURES $\bar{T}_{OE}$[1] °F	$\bar{T}_{IE}$[2] °F	$\bar{T}_{VANE}$[3] °F
13	ADVANCING TO DESIGN POINT	1298	16.5	120.4	121.3	1.31	340	348	326
14		1438	16.2	128.8	139.6	1.26	357	367	349
15		1630	16.3	133.4	168.0	1.24	383	393	381
16A		1736	16.3	142.1	188.4	1.20	398	409	398
17A		1810	16.5	145.7	203.5	1.24	417	427	416
17		1812	16.8	141.4	204.4	1.28	420	433	421
18		1963	16.1	140.9	224.0	1.27	432	445	438
19		2244	17.0	148.6	265.5	1.29	461	481	474
19A		2486	16.5	152.4	297.0	1.28	481	502	497
20		2666	16.6	151.7	317.0	1.33	497	517	513
20B		2729	18.1	162.3	338.3	1.34	541	562	570
21	COOLANT FLOW VARIATION	2651	17.9	158.7	331.1	1.35	506	526	524
22		2668	17.9	159.0	326.7	1.36	520	543	549
23		2731	18.1	159.8	333.6	1.34	531	552	557
24		2728	17.8	159.8	332.0	1.35	542	563	576
25		2729	18.0	159.7	328.5	1.35	547	571	583
26		2730	17.7	159.8	325.0	1.34	556	581	601
27	COOLANT TEMPERATURE VARIATION	2662	18.2	160.3	328.2	1.36	562	586	601
28		2691	18.4	160.4	326.0	1.35	576	600	617
28A		2659	18.0	160.7	338.2	1.35	544	568	577
29	COOLANT PRESSURE VARIATION	2691	18.0	160.0	328.8	1.35	549	572	590
30		2731	18.3	161.1	329.3	1.36	551	573	585
31	GAS TEMPERATURE VARIATION	2312	18.4	157.3	293.1	1.36	506	527	533
32		1906	18.5	146.9	225.1	1.37	447	466	459
33	DETERMINE FLOW FUNCTION VS. PRESSURE RATIO	2690	17.9	161.5	331.4	1.34	556	568	587
33A		2738	18.7	167.8	353.4	1.39	572	581	610
33B		2730	19.0	168.3	352.8	1.40	570	579	607
33C		2733	19.1	166.0	351.3	1.46	569	576	606
33D		2731	18.6	164.3	352.5	1.55	568	578	606
33E		2750	19.1	160.6	350.4	1.99	566	586	597
33F		2763	18.8	160.4	346.8	2.32	560	587	584

Note: See Table 2-3 for nomenclature

[1]Average of Outer Endwall Measured Copper Temperatures.

[2]Average of Inner Endwall Measured Copper Temperatures.

[3]Temperature Measured by TC 34 in Spar Rod

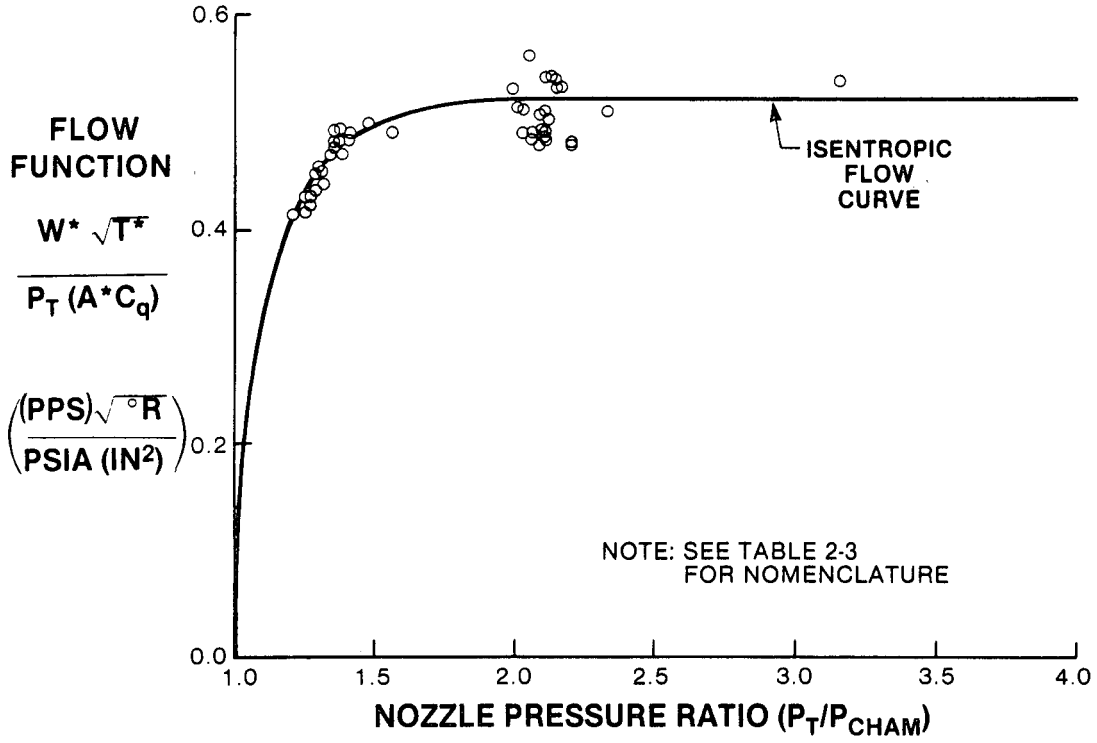

Figure 2-17. First-stage nozzle aerodynamic flow function vs nozzle pressure ratio (fired test points)

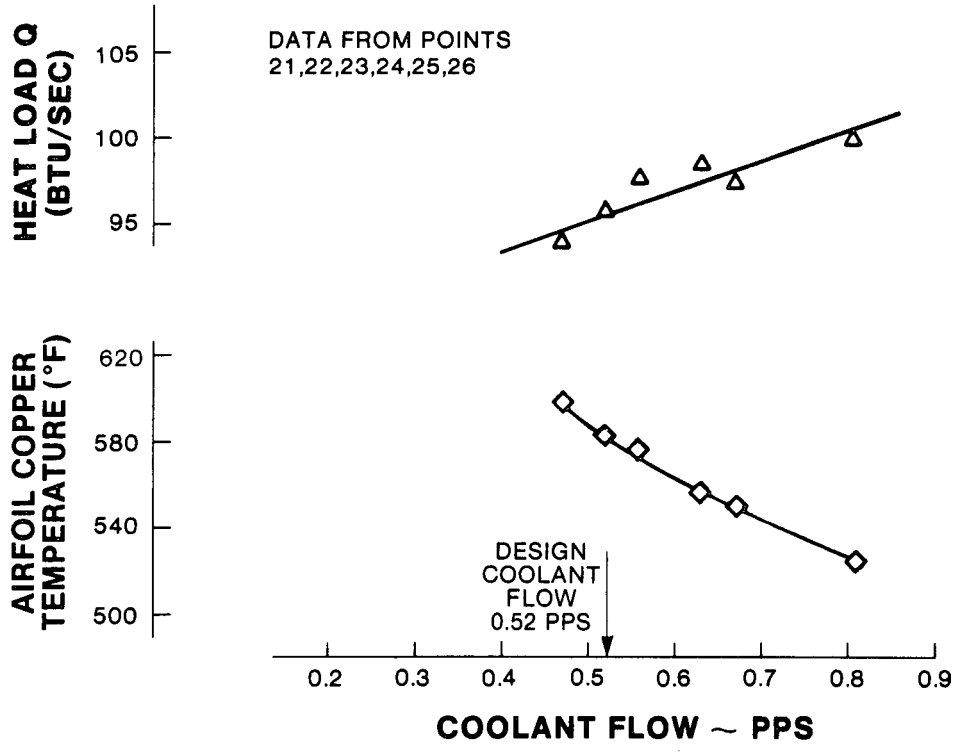

Figure 2-18. Effect of coolant flow variation on first-stage nozzle airfoil

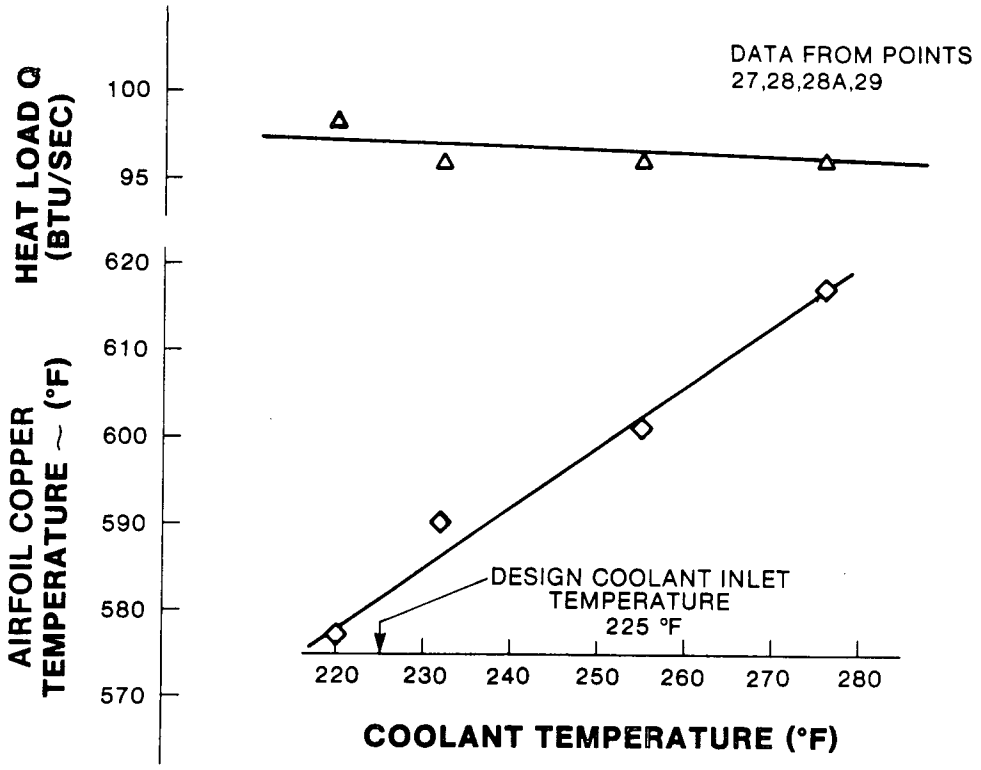

Figure 2-19. Effect of coolant temperature variation on first-stage nozzle airfoil

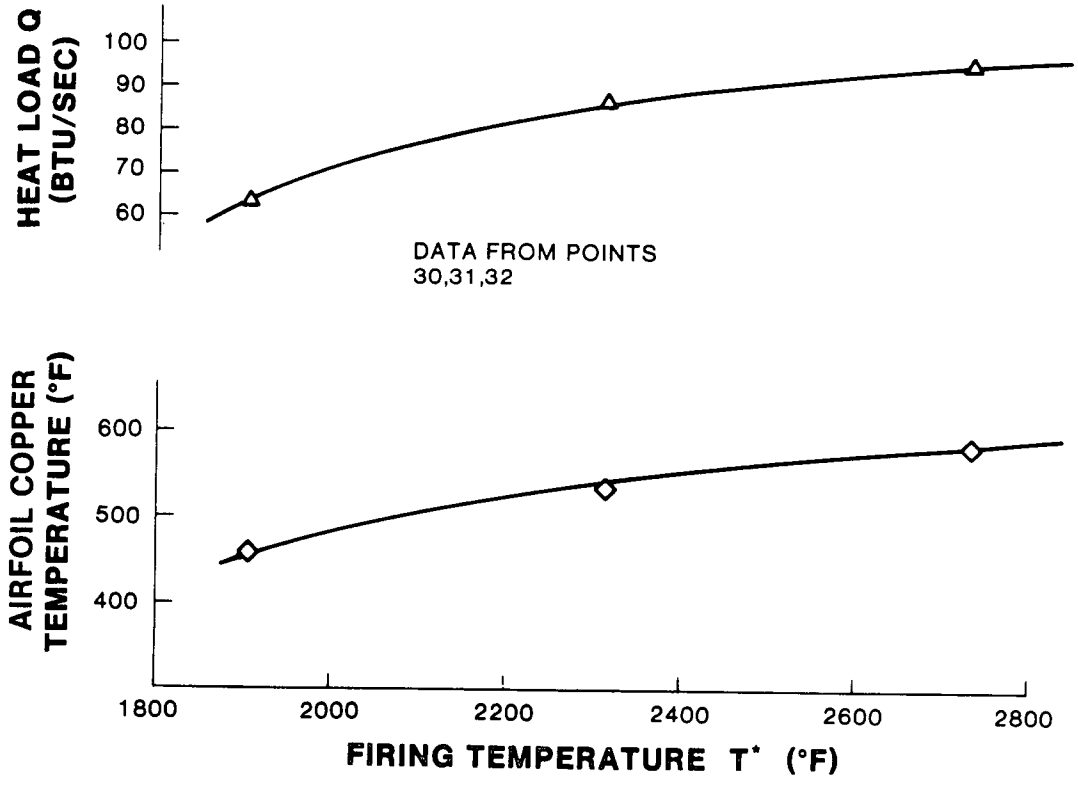

Figure 2-20. Effect of firing temperature variation on first-stage nozzle airfoil

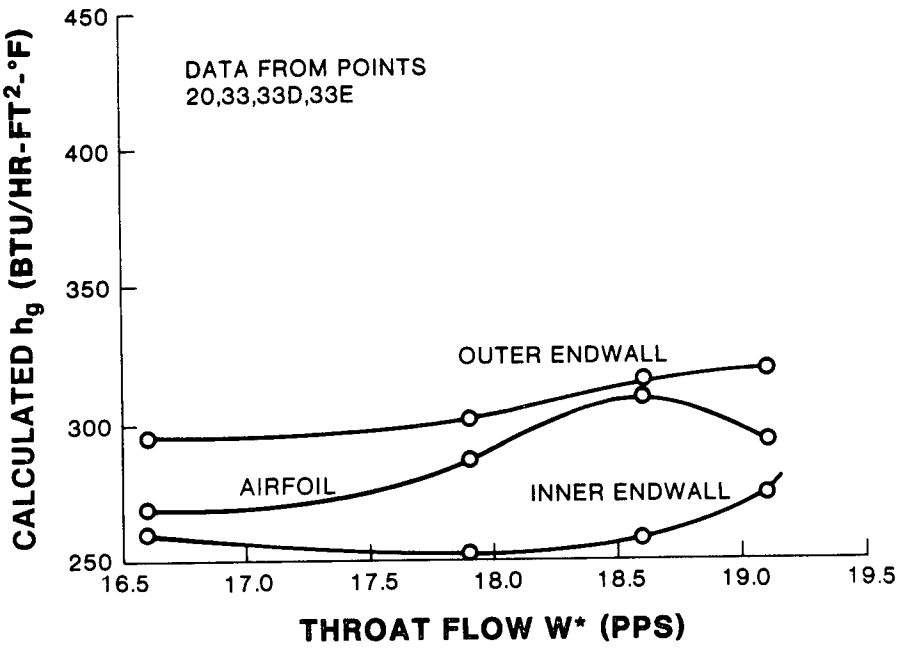

Figure 2-21. **First-stage nozzle calculated heat transfer coefficient vs throat flow**

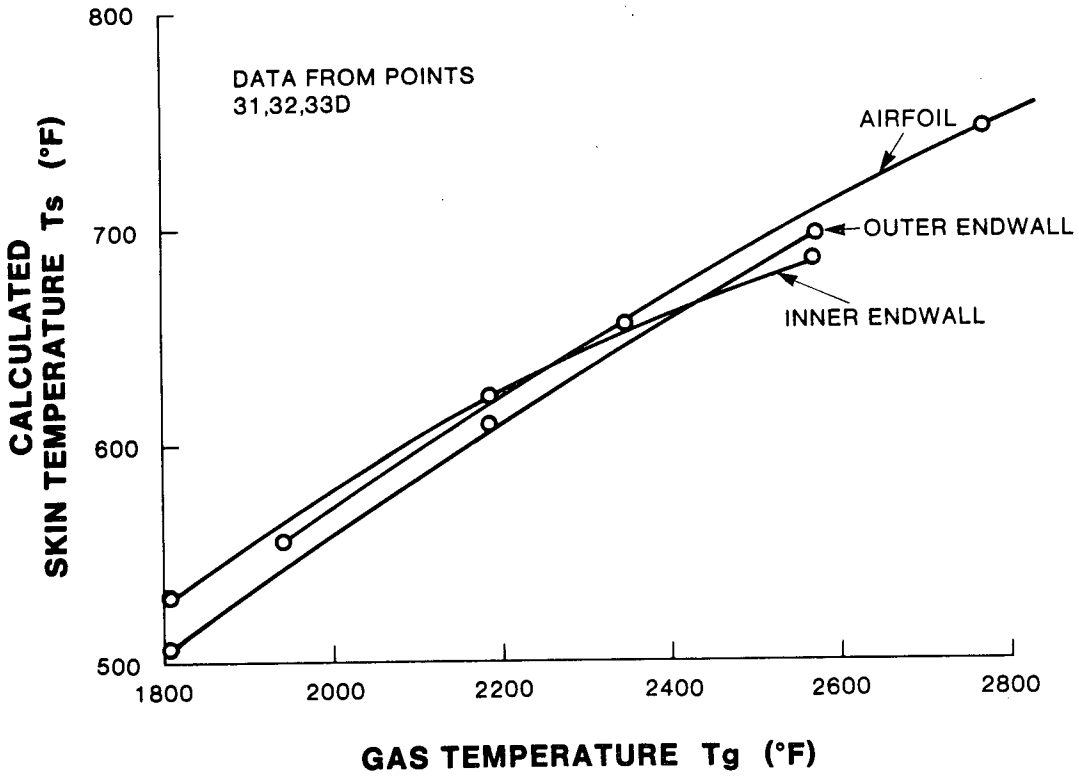

Figure 2-22. **First-stage nozzle calculated surface temperature vs gas temperature**

The water-cooled composite nozzles completed the initial test series without any visible signs of distress. Details of the in-place inspection are found in Section 2.8.2.

2.7.5 Initial Cyclic Test

2.7.5.1 Test Description

The cycle adopted for this test was designed to simulate a gas turbine startup/shutdown cycle. Figure 2-23 shows the variation of nozzle inlet gas temperature through a cycle. Airflow remained constant and fuel flow was varied manually to attain the fast start and stop slopes of the cycle. Since it was not practical to turn off the combustor between cycles, some truncation of a real cycle occurs at the low temperature end. However, this truncation occurs at a level where strain is low and the materials, particularly the copper, are at their strongest. The high temperature hold time was sufficiently long to achieve maximum creep in the copper sublayer.

2.7.5.2 Test Results

The first three cycles were accomplished as soon as initial steady-state tests were completed. Two further test periods of 46 cycles and 51 cycles completed the initial cyclic test series. Excursions from startup to design point to shutdown in the steady-state portion of the test, and inadvertent trips from the design point, brought the total number of cycles in this initial test series to 106. Visual inspection of the nozzle was performed after each test period.

Recorder traces of six thermocouple readings during the initial period of the last cycle, which included an extended duration at steady-state conditions, are shown in Figure 2-24. Response of the outer endwall leading acute corner of nozzle #3 is recorded on TC16(2) and the corresponding corner of the test nozzle #1 is TC16(3). This cycle illustrates typical behavior of TC16(2) during the period of temperature rise and initiation of steady conditions. This temperature did not stabilize until approximately one minute later than expected, and peaked at a temperature approximately 160 °F higher than expected. It then slowly returned to the expected value. A second thermocouple in the area, TC44(2), confirms this behavior, eliminating the possibility of faulty instrumentation.

It can be concluded from the response of TC18(2), which is in the opposite corner and is cooled by the same tube, that coolant conditions were steady. Two other observations tend to eliminate cooling system behavior as the cause. During some cycles the deviation from the predictable response began at copper temperatures well below that which might be expected to produce subcooled boiling. The apparent location of the hot spot away from the corner implies concentration of heat flux on the

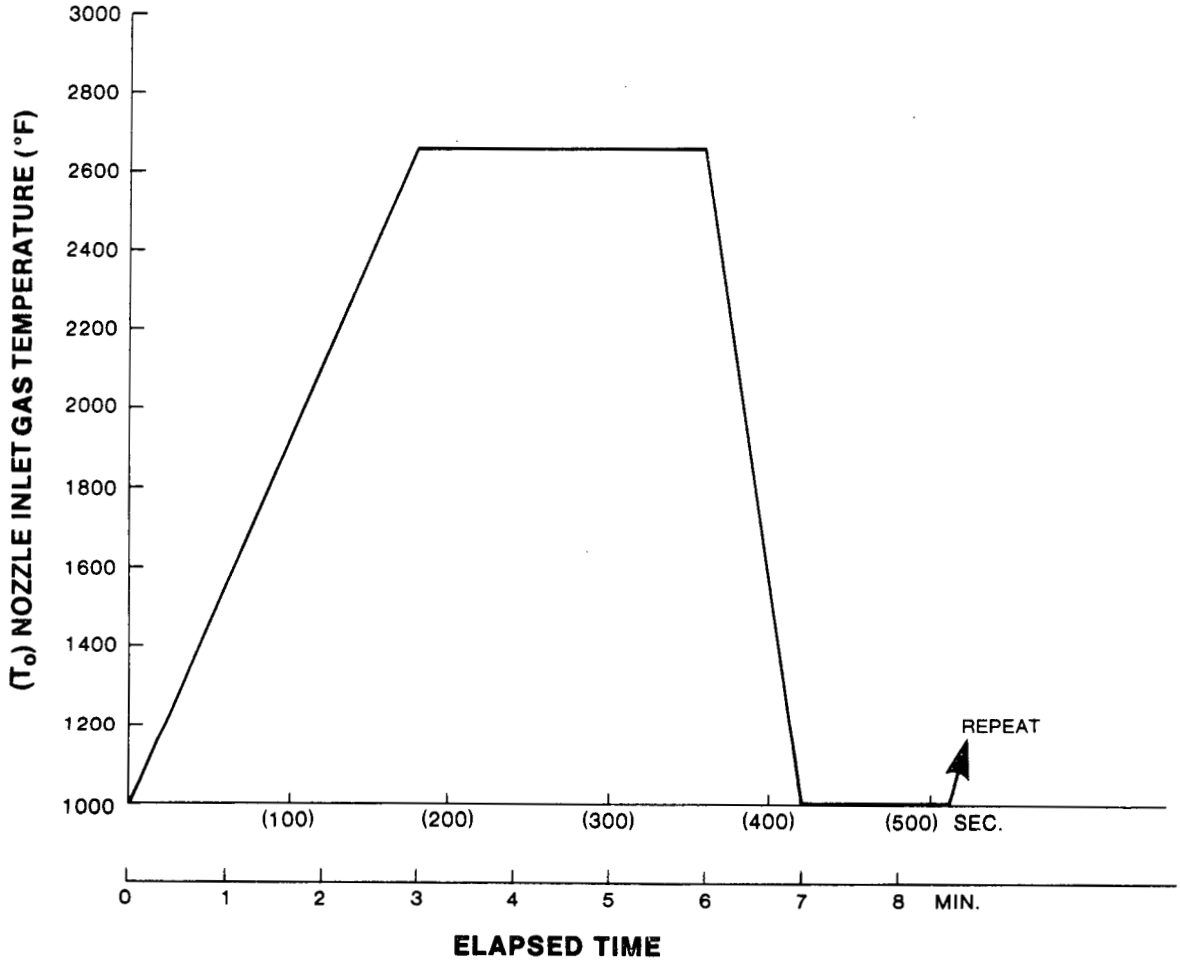

Figure 2-23. Nozzle inlet gas temperature during cyclic testing of first-stage nozzle

gas side. Direct evidence of substantial variations in the gas conditions could not be found. Nevertheless, an indirect indication of substantial variations in external conditions was found; a thermocouple on the flange of the combustion transition piece close to the hot spot recorded a similar temperature variation.

A transient response of the composite structure at the outer end of the airfoil trailing edge, which is the location of the highest thermal gradients, was recorded in one cycle where the period of temperature rise was reduced to one minute. Figure 2-25 shows that the responses of the copper TC1(3), the endplate TC35(3), and the manifold cover TC36(3), were similar and that the gradient increased monotonically despite the rapid temperature rise. Hence, inherent avoidance of transient thermal stresses higher than steady-state thermal stresses was demonstrated.

The composite nozzle completed these initial cyclic tests without visible signs of distress. Details of the in-place inspection are found in Section 2.8.2.

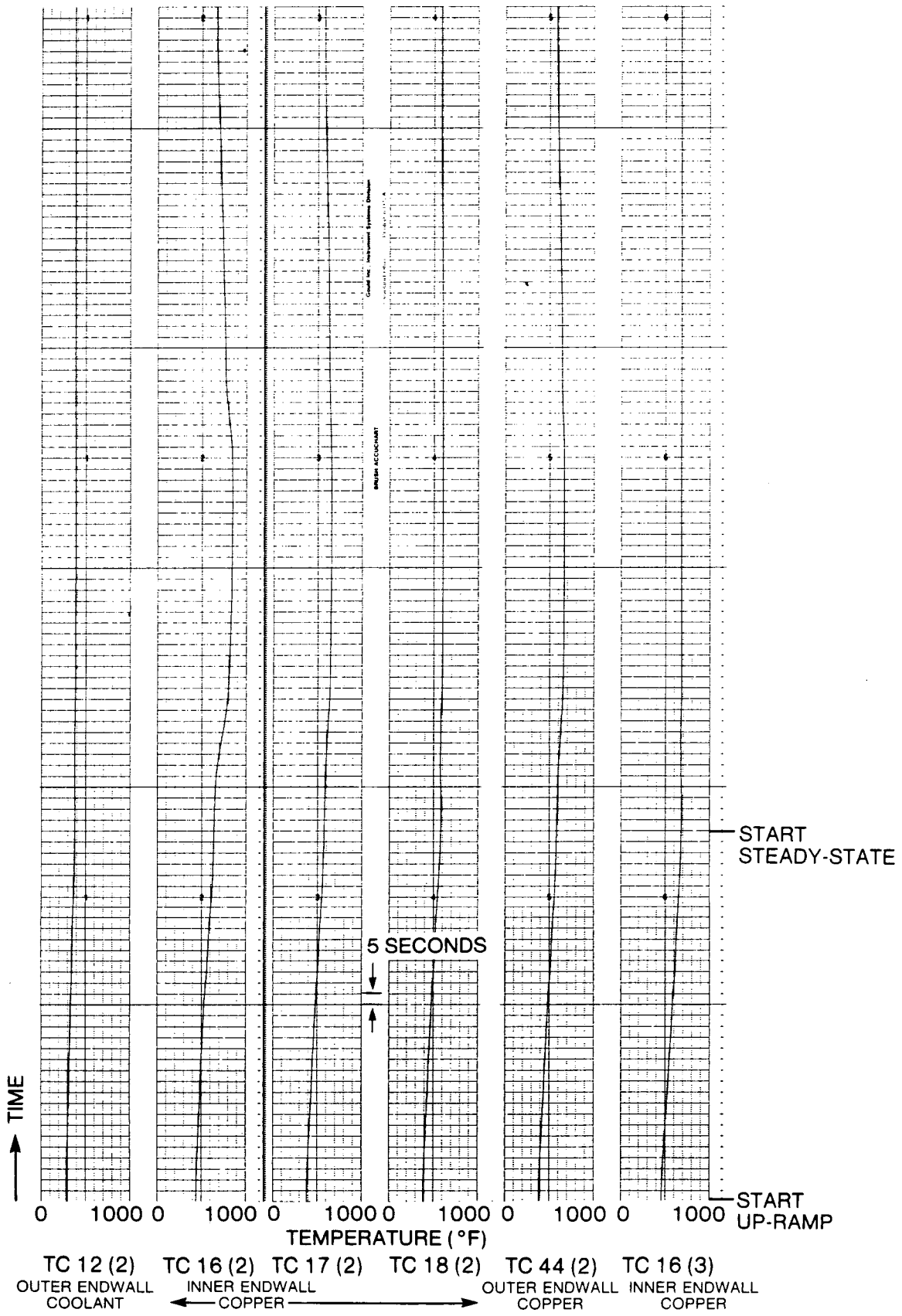

Figure 2-24. First-stage nozzle thermocouple response to normal cycle (up-ramp) and hold at steady-state conditions

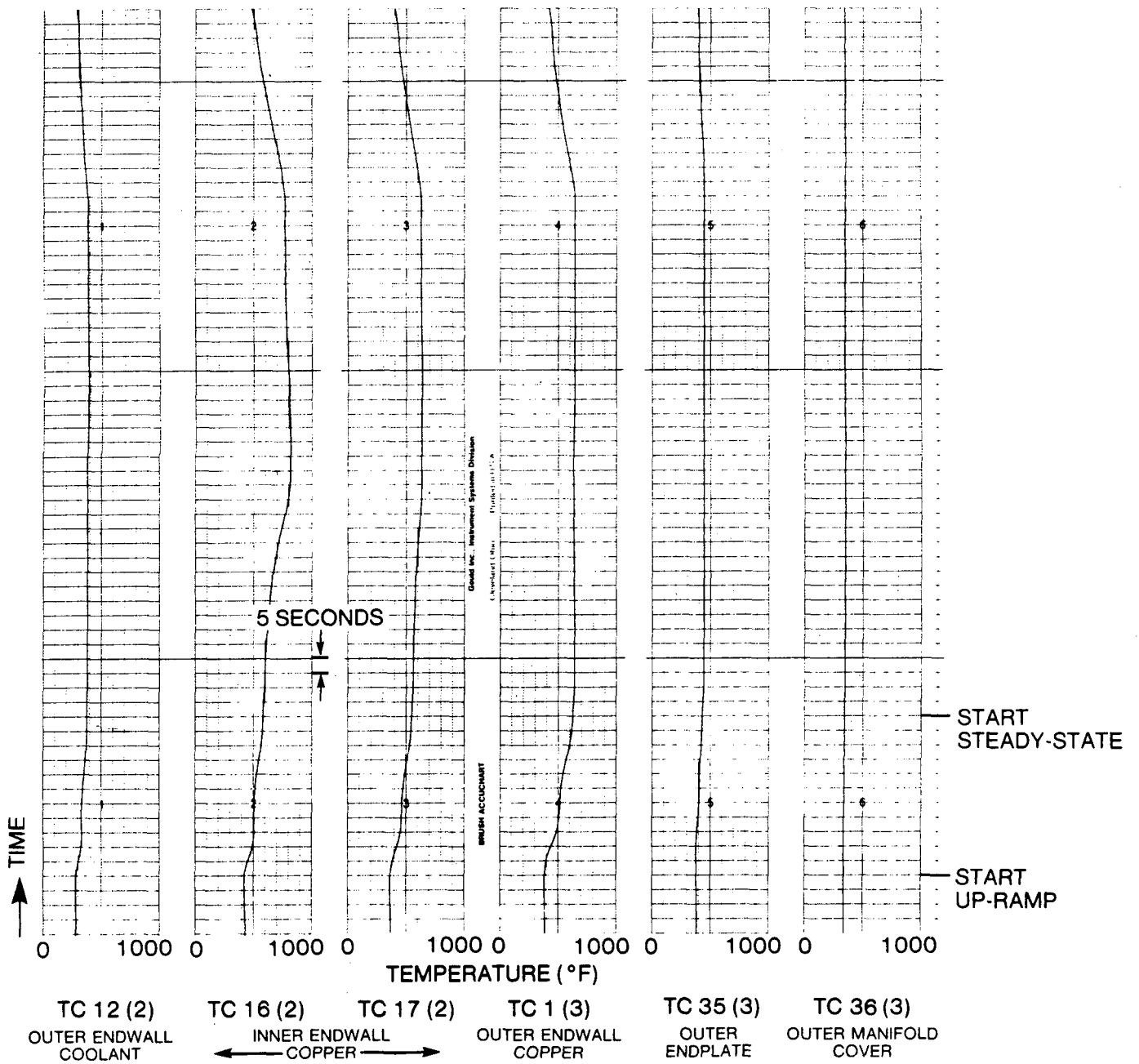

Figure 2-25. First-stage nozzle thermocouple response to rapid cycle

2.7.6 Extended Steady-State Test

2.7.6.1 Test Description

In view of the durability exhibited by nozzle #3 during the initial fired testing, its original high coolant flow was reduced to design flow (0.52 lb/sec) for extended testing at design operating conditions. The test conditions are summarized in Table 2-6 of Section 2.7.6.2. No gas sample probes were installed during this test since sufficient data were accumulated in the initial test series.

Test points #10 through #28 were completed prior to proceeding into the extended cyclic tests described in Section 2.7.7.1. Test points #29 through #34.1 were accomplished as part of the fault condition test described in Section 2.7.8.1, after completion of the extended cyclic tests.

As in the initial test series, variations in thermal conditions were made to determine test nozzle response. These variations included gas flow rate, gas pressure, and firing temperture. An in-place visual examination of the nozzles was performed at the completion of test point #28 prior to extended cyclic testing.

2.7.6.2 Test Results

The results of the extended steady-state testing are summarized in Tables 2-6 and 2-7, and in Figures 2-26 through 2-29.

Table 2-7 compares measured values at test point #29 (steady-state design conditions) with expected values for this test point condition. Extremely good agreement is shown, which establishes the validity of the composite nozzle design.

Figures 2-26 and 2-27 show the variation in heat load and airfoil copper temperature as the design point is approached. In approaching the design point, gas flow and pressure were varied as was firing temperature. The effects of varying pressure (gas density effect) and flow (flow effect) at approximately the same firing temperature are indicated on these figures. Figure 2-28 shows a plot of critical nozzle temperatures as a function of firing temperature.

Heat transfer operating points show the correlation of Nusselt number versus Reynolds number in Figure 2-29 for the airfoil (not including endwalls). The procedure for calculating these parameters is given in Appendix C. Fifty-seven fired test points and ten unfired test points are plotted in Figure 2-29. The calculated average turbulent flat plate prediction is shown for reference. The design point is that expected for choked operation, P_T = 166 psia, T^* = 2600°F.

The following conclusions can be drawn:

- The average value of the airfoil h_g used in design is about 20% higher than that which would be calculated from a line through the bulk of the test data.

Table 2-6

EXTENDED FIRED TEST CONDITIONS
FIRST-STAGE NOZZLE TEST

TEST POINT	REMARKS	T* °F	W* PPS	P_T PSIA	Q Btu/Sec	P_T/P_{CHAM}	Copper Temperatures		
							$\bar{T}_{OE}$ [1] °F	$\bar{T}_{IE}$ [2] °F	$\bar{T}_{VANE}$ [3] °F
10	ADVANCING TO DESIGN POINT	1286	14.4	85.5	95.8	3.15	325	339	321
11		1804	19.5	167.3	230.9	1.26	459	453	469
12		2424	19.9	166.7	333.7	2.09	563	546	579
13		2743	19.4	172.0	370.5	2.02	598	575	628
13A		2715	19.2	165.0	354.9	2.11	589	569	617
13B		1289	20.8	125.7	128.1	2.14	360	364	357
14		1311	20.4	116.9	115.8	2.04	331	330	327
15		1473	19.8	123.1	139.5	2.10	356	355	353
16		1629	19.9	128.6	163.2	2.12	379	377	380
17		1782	19.9	134.1	187.9	2.14	406	404	411
18		1947	19.7	139.1	213.9	2.16	429	426	443
19		2165	19.9	153.9	265.6	2.10	484	472	499
20		2370	19.9	160.3	300.9	2.08	520	500	541
21		2661	19.9	166.6	343.2	2.02	564	539	593
22	GAS FLOW VARIATION	2738	18.3	164.2	341.8	2.05	571	639	614
23		2818	19.3	173.5	374.3	2.05	600	654	659
24		2556	21.2	184.0	363.6	2.05	587	634	650
27	CYCLE HIGH AND LOW TEMPERATURE REFERENCE	2699	18.3	165.1	348.4	2.08	569	550	592
28		1183	19.7	115.2	107.8	1.98	320	323	312
29	COOLANT FLOW REDUCTION	2750	18.5	167.8	355.2	2.08	587	643	648
30		2641	18.6	165.1	344.0	2.08	588	643	649
31		2699	18.5	163.8	347.8	2.06	608	662	662
32.1		2754	18.6	166.7	353.6	2.10	638	679	703
33		1805	19.2	145.7	204.1	2.19	482	540	535
34		1795	19.0	144.5	200.7	2.19	468	528	515
34.1		2755	18.5	164.8	345.0	2.10	637	681	693

Note: See Table 2-3 for nomenclature

[1]Average of Outer Endwall Measured Copper Temperatures.

[2]Average of Inner Endwall Measured Copper Temperatures.

[3]Temperature Measured by TC34 in Spar Rod.

Table 2-7

FIRST-STAGE NOZZLE: CALCULATED VERSUS MEASURED TEST RESULTS AT STEADY STATE DESIGN CONDITIONS

Parameter	Measured**	Calculated†
Nozzle Cooling Circuit ΔP (psi)	21‡‡	22
Single Nozzle Heat Load (Btu/sec)	118	120
Nozzle Cooling Effectiveness, η††	0.78	0.76
Nozzle Airfoil		
T_{cu} (°F)	648	500-700
$\bar{T}_s$ (°F)	802‡	811
$\bar{h}_g$ (Btu/hr-ft^2-°F)	352‡	386

Note: See Table 2-3 for nomenclature.

‡‡From static pressure measurements prior to fired testing
†Expected values for $T^* = 2750$ °F
‡Calculated from test point #29
**Test point #29 data

$$\dagger\dagger \eta = \frac{\bar{T}_o - \bar{T}_s}{\bar{T}_o - T_{ci}}$$

- Firing the combustor causes the h_g to increase (at the same Reynolds number) and causes data scatter relative to the unfired test data. This effect is presumed to be due in part to the turbulence level increases.
- Outer endwall h_g calculated from the test data is close to expected values; whereas, inner endwall h_g is about 22% lower than expected.

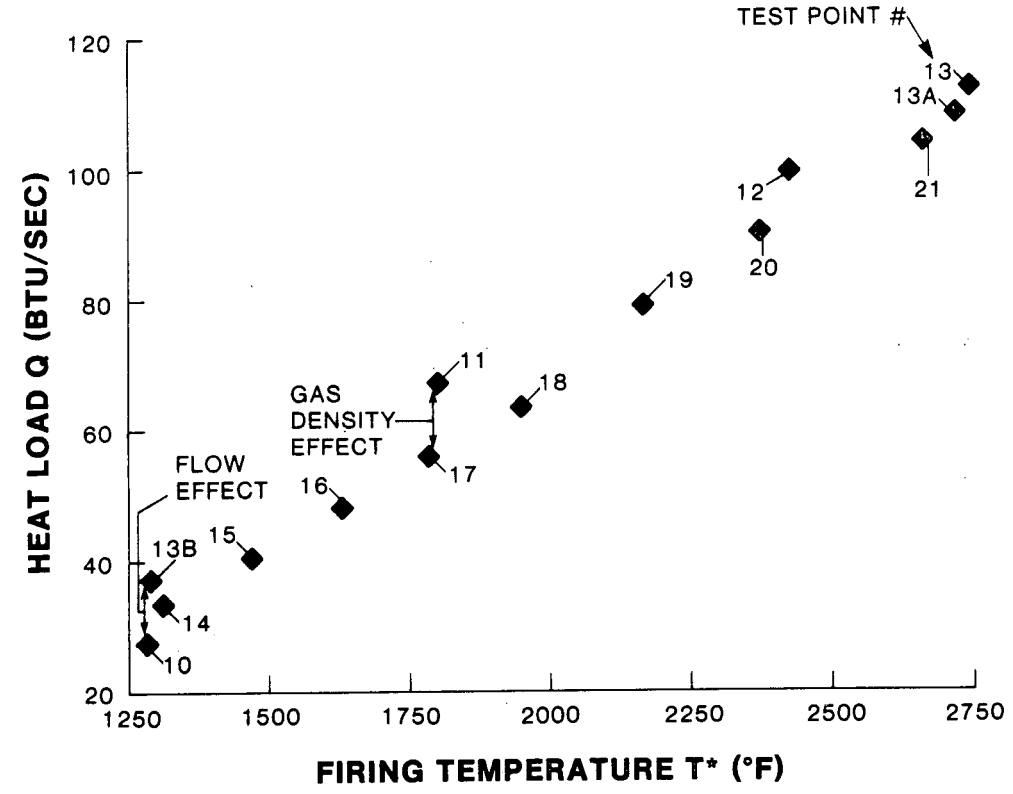

Figure 2-26. First-stage nozzle heat load

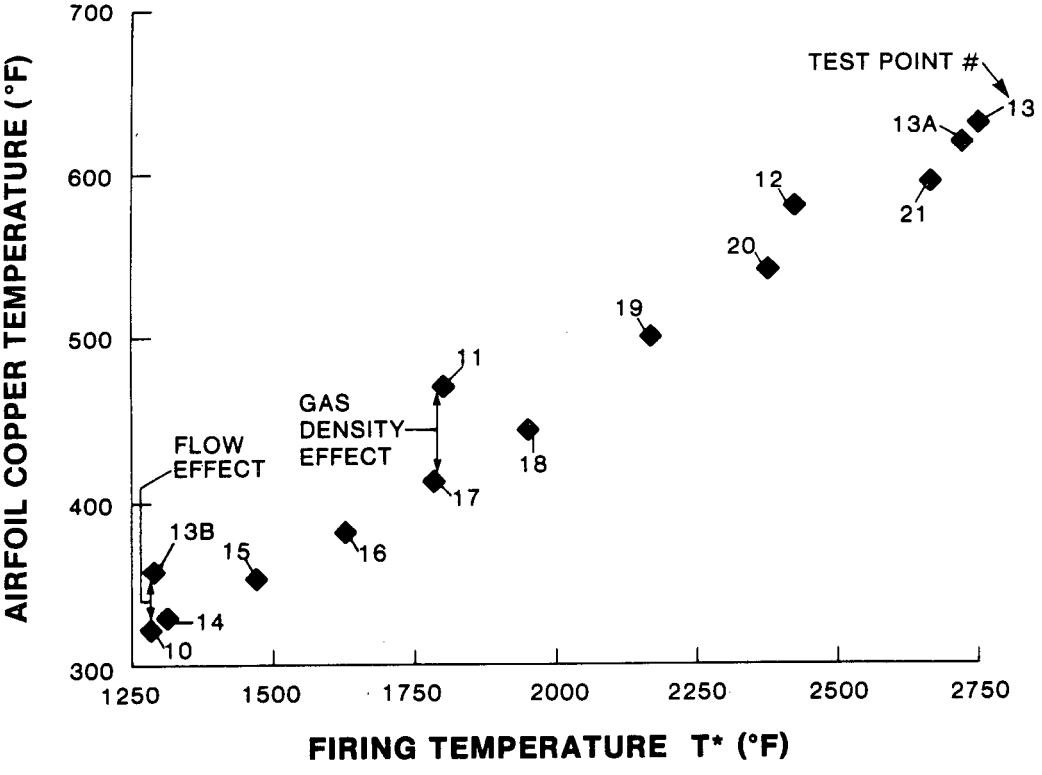

Figure 2-27. First-stage nozzle airfoil copper temperature

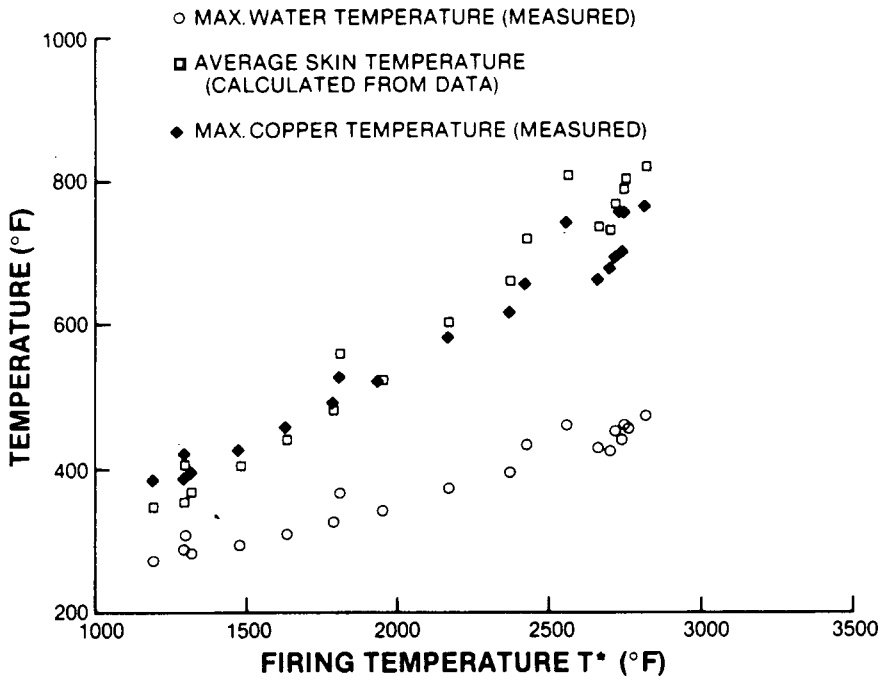

Figure 2-28. First-stage nozzle growth capability to 3000 °F

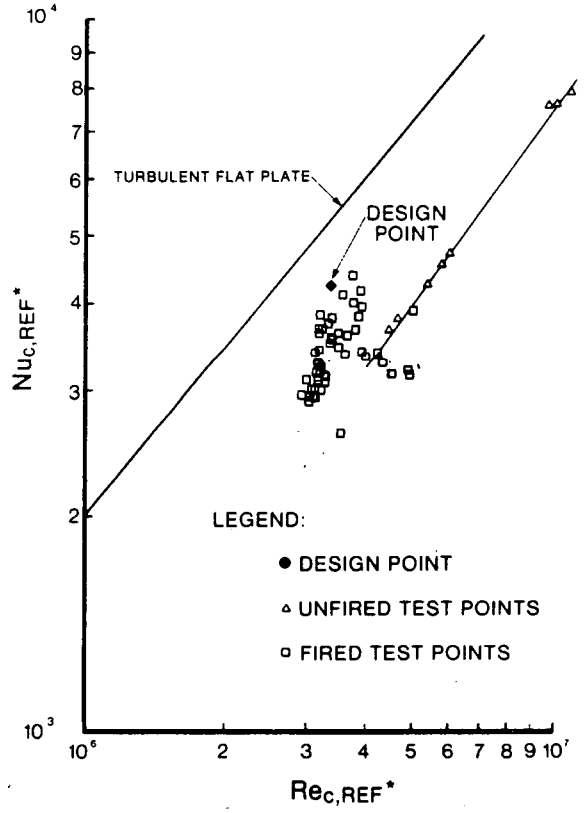

Figure 2-29. First-stage nozzle airfoil external heat transfer data

2.7.7 Extended Cyclic Test

2.7.7.1 Test Description

Cyclic testing was resumed after the extended steady-state fired testing at design conditions. Five-hundred and eleven additional cycles were attained in three series of 25, 221, and 265 cycles per series, with visual inspection between each series. The total number of cycles accumulated through both cyclic test periods on the composite nozzle test specimen was 617. This series of cyclic tests was accomplished using an automatic control system to achieve the desired combustor exit temperature.

2.7.7.2 Test Results

The conclusion from the initial cyclic test, that the sporadic overheating of the leading acute corner of nozzle #3 was associated with a concentration of heat flux on the gas side, was confirmed. The incidence of this phenomena was seen to appear regularly after each sustained pause at the low point of the cycle. Figure 2-30 shows the traces of the copper temperature and the closest transition piece metal temperture during the last cycle, when such a pause was deliberately included. The correspondence in temperature response is unmistakable. Post-test inspection revealed evidence of a hot spot in the transition piece at a location corresponding to the hot spot in the nozzle.

The composite nozzle completed the extended cyclic testing without visible signs of distress. Details of the inspection are found in Section 2.8.2.

2.7.8 System Fault Condition Test

2.7.8.1 Test Description

Test points #29 through #34.1 (see Table 2-6) were accomplished after completion of all cyclic testing. During this test series, the coolant flow rate to test nozzle #1, installed in position #3, was progressively reduced until cooling instability was registered by the temperature and pressure measurements being monitored by strip chart recorders. External conditions were held steady. The coolant flow was reduced from design flow (0.52 lb/sec) to 0.48 lb/sec and then to 0.42 lb/sec to obtain readings at test points #30 and #31, respectively. The next two test points were obtained by adjusting the coolant flow at a firing temperature of approximately 1800 °F, and then increasing the firing temperature slowly while observing the data for signs of unstable or inadequate cooling. The coolant flow was reduced to 0.37 lb/sec at test point #32.1 and then to 0.31 lb/sec when instability was encountered and steady readings were not obtained. Stable conditions were obtained at test point #34.1 with a coolant flow of 0.33 lb/sec.

2.7.8.2 Test Results

The majority of the data reduction involved calculating and plotting the variation in important variables (wall heat fluxes and copper temperatures) as flow was reduced. Figures 2-31 through 2-41 graphically document these results. Test points correspond-

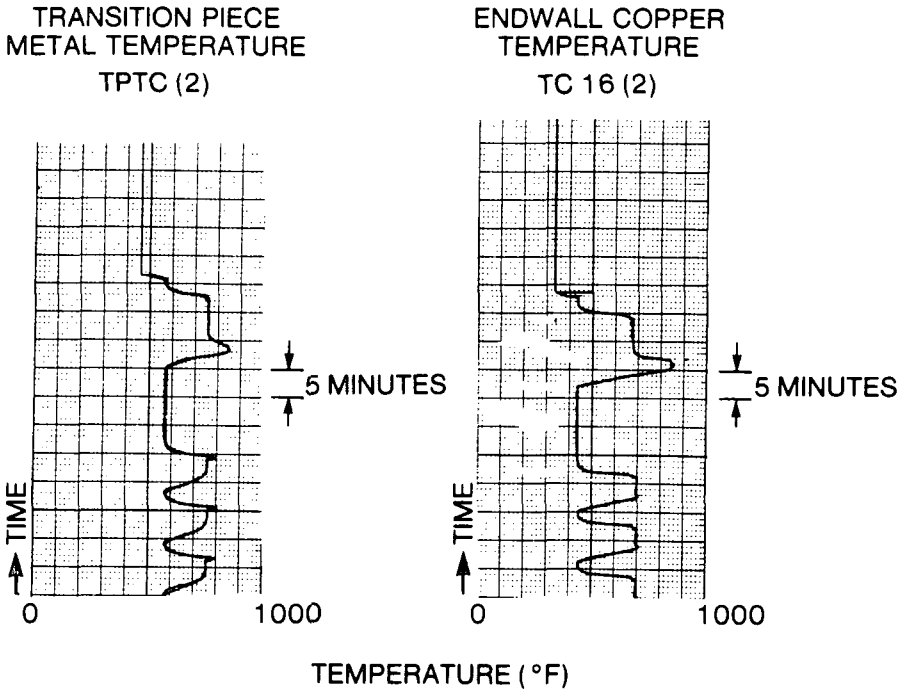

Figure 2-30. First-stage nozzle thermocouple response to normal cycle

ing to the coolant flow rates are as follows:

Test Points	Nozzle #1 Coolant Flow
29	0.53 pps
30	0.48 pps
31	0.42 pps
32.1	0.37 pps
34.1	0.33 pps

Nozzle copper temperatures as a function of coolant flow reduction are shown in Figures 2-31 through 2-33, 2-36, and 2-37. The noteworthy effect is that the temperatures level off between the last two data points (32.1 and 34.1). Gas flow, pressure, and temperature were essentially the same for these points. This behavior indicates the onset of nucleate boiling. See Appendix B for a discussion of the boiling phenomena in water-cooled gas turbine nozzles.

The variation in water temperature at various locations throughout the nozzle cooling circuit is shown in Figures 2-34 and 2-35 At the lowest coolant flow, several of the outlet coolant temperatures (TC9 and TC13, Figure 2-35) level off near saturation temperature (572 °F at 1250 psia), indicating that saturated nucleate (bulk) boiling is occurring at or near the exit of these tubes. The saturated nucleate boiling in the return tubes is accompanied by vigorous net vapor formation. This causes a dynamic, non-equilibrium situation with not all the coolant at saturation. Therefore, the thermocouples read about 25 °F below saturation.

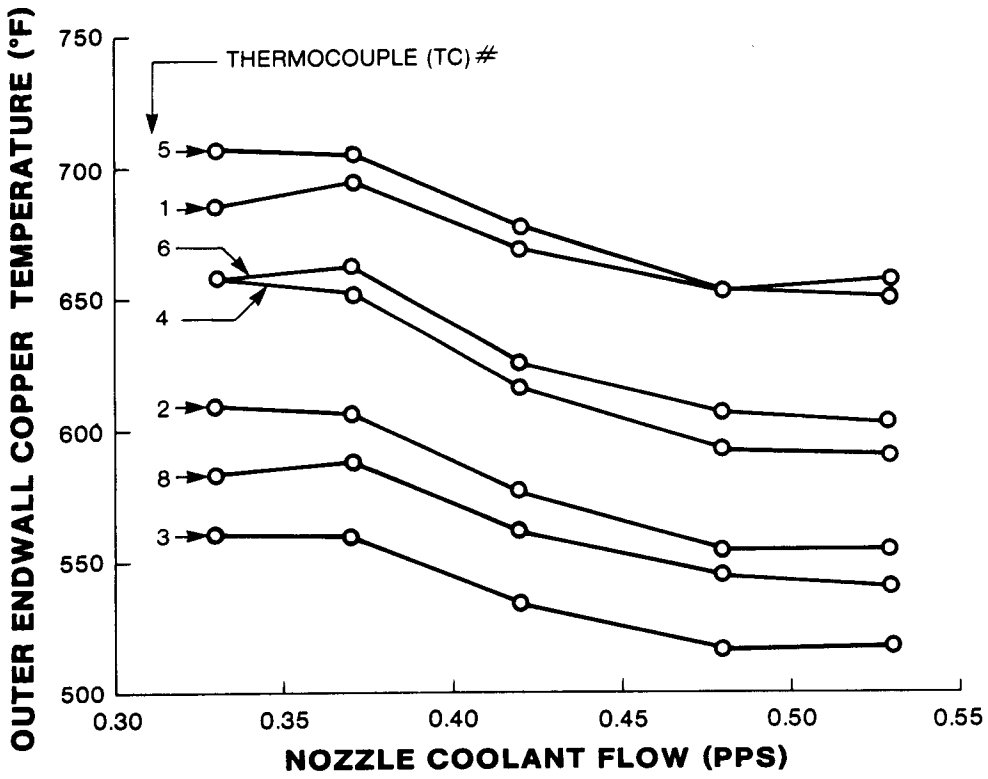

Figure 2-31. Outer endwall copper temperature vs coolant flow – first-stage nozzle test

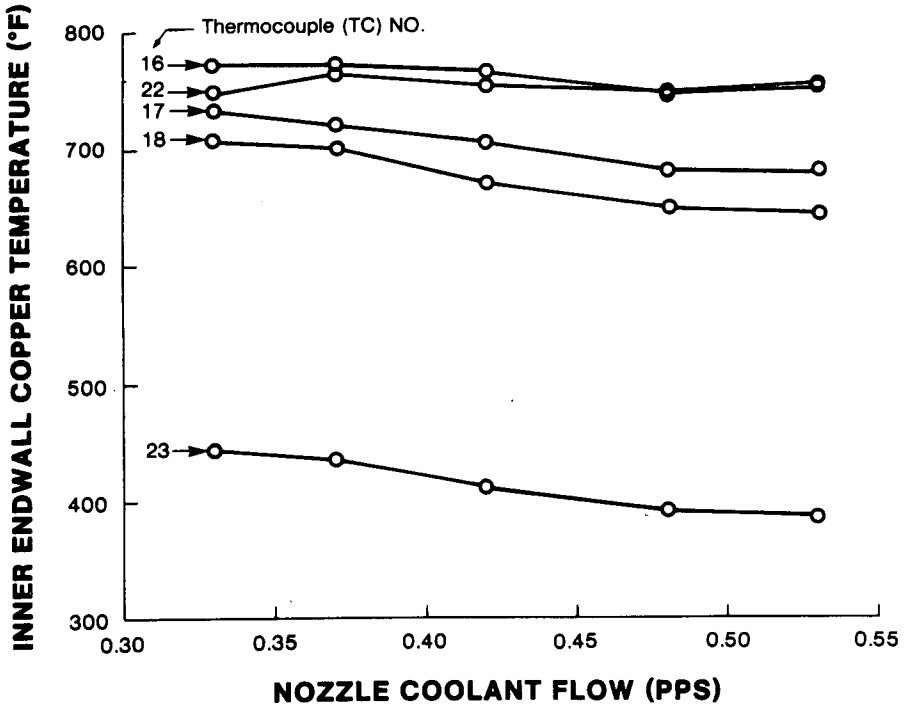

Figure 2-32. Inner endwall copper temperature vs coolant flow – first-stage nozzle test

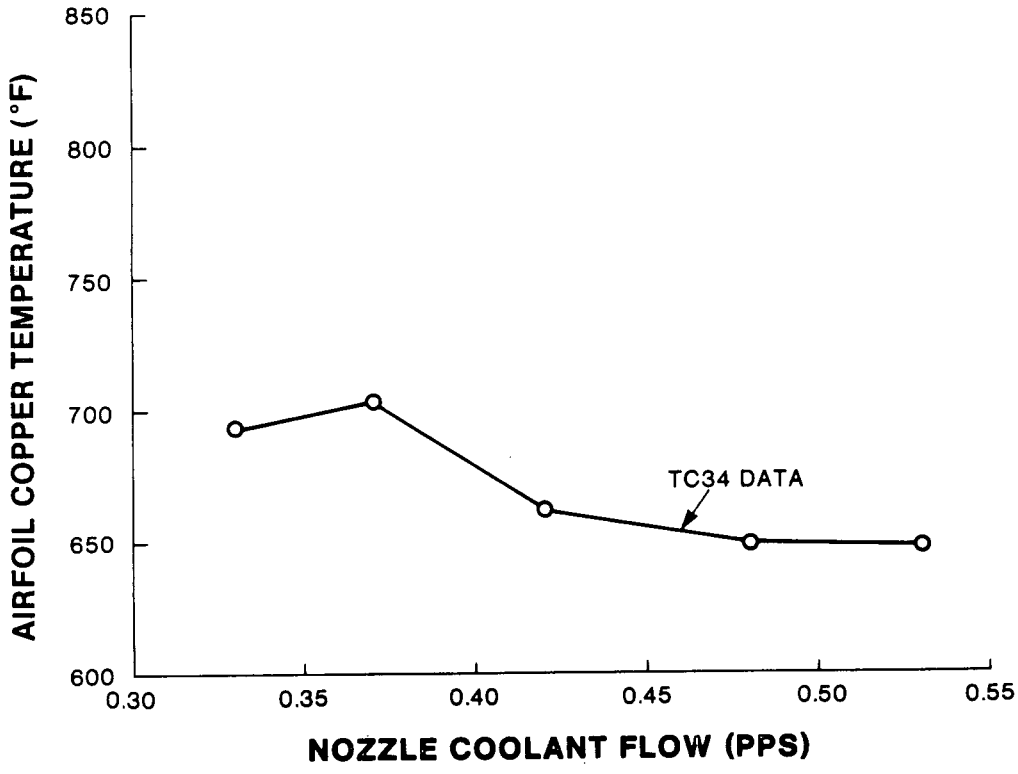

Figure 2-33. Airfoil copper temperature vs coolant flow – first-stage nozzle test

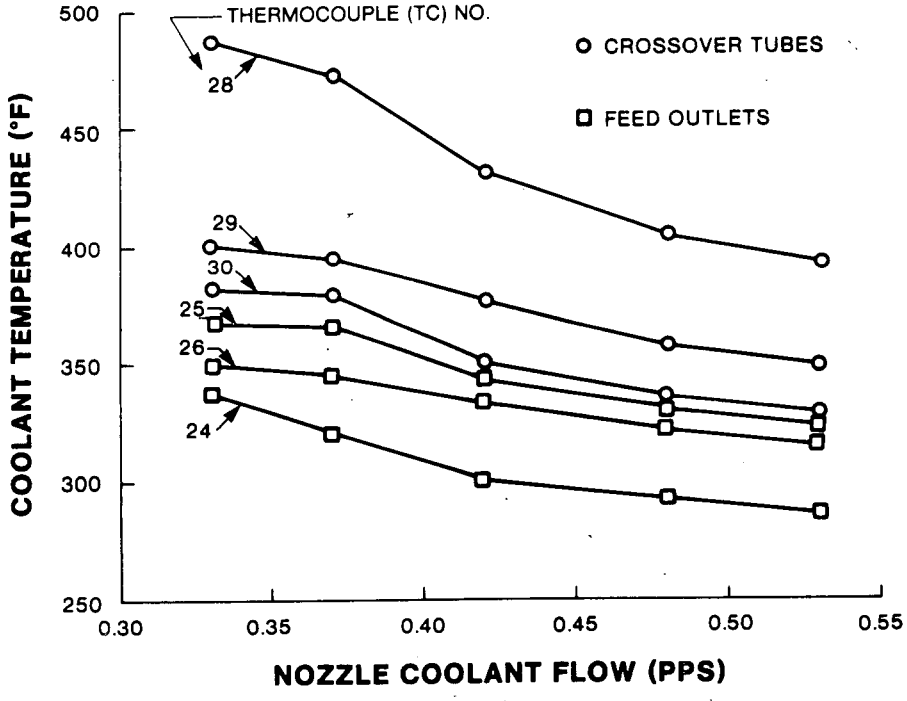

Figure 2-34. Coolant temperature vs coolant flow – first-stage nozzle feed and crossover tubes

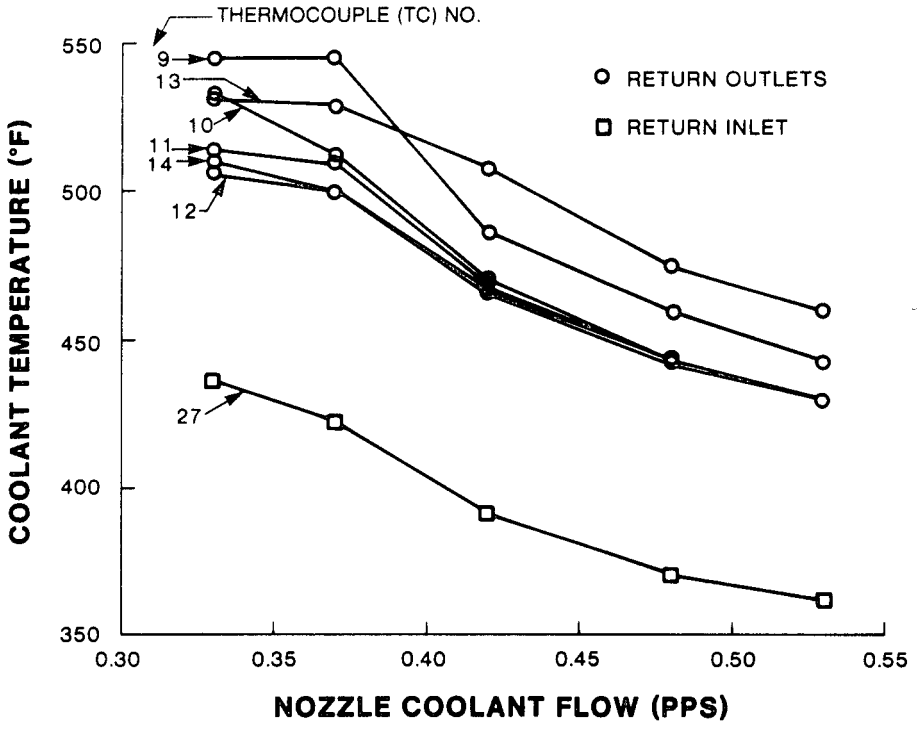

Figure 2-35. Coolant temperature vs coolant flow – first-stage nozzle return tubes

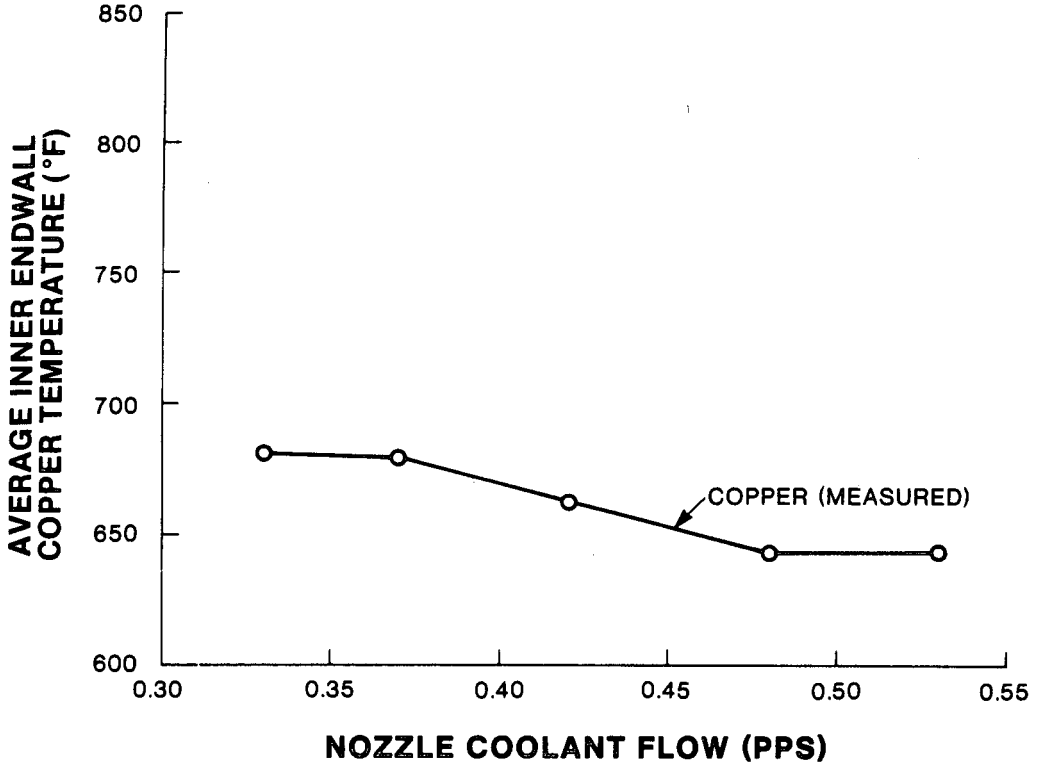

Figure 2-36. Inner endwall copper temperature vs coolant flow – first-stage nozzle test

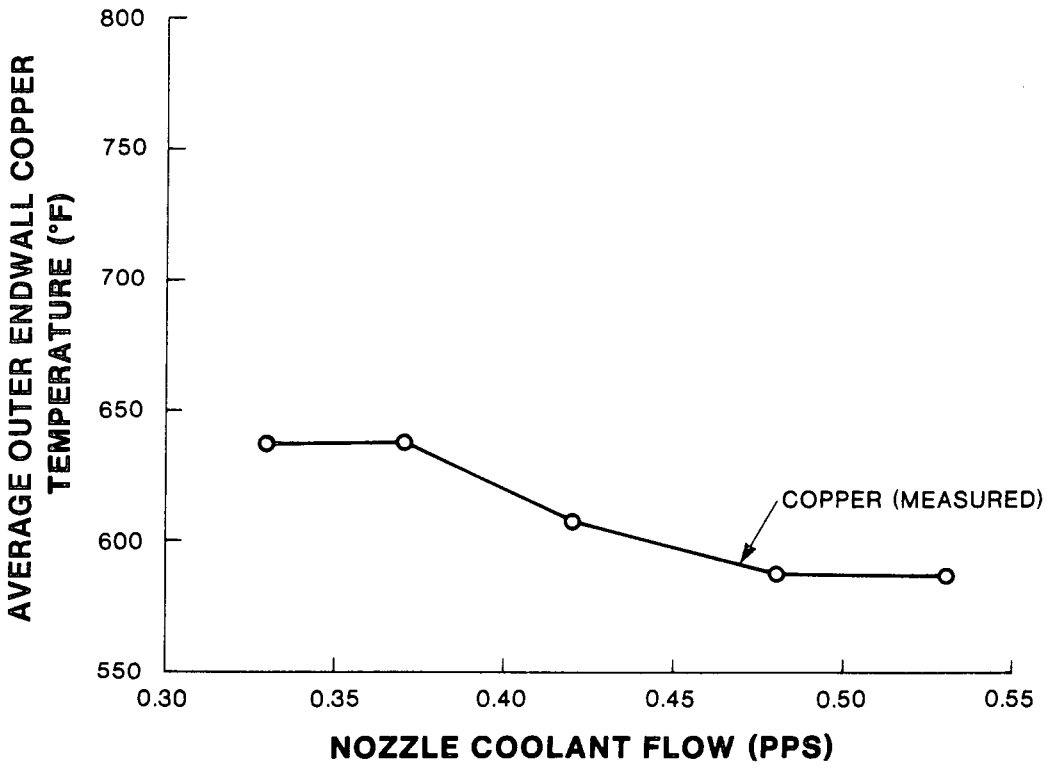

Figure 2-37. Outer endwall copper temperature vs coolant flow – first-stage nozzle test

Calculated airfoil average skin temperature based on measured copper temperature is plotted on Figure 2-38. This skin temperature agreed reasonably with the expected temperatures. During the flow reduction test, the infared pyrometer was used to monitor the trailing edge surface temperature of nozzle #1. Local skin temperatures measured by the pyrometer are plotted versus the coolant flow on Figure 2-38.

A summary of the performance of representative cooling tubes relative to a critical heat flux (CHF) curve and an onset of nucleate boiling (ONB) curve is shown in Figures 2-39, 2-40, and 2-41.

Examination of these curves leads to the following conclusions:

- During the flow reduction test, subcooled nucleate boiling occurred in the trailing edge feed tube and the return tubes. It is also very likely that it occurred in the other feed tubes as well.
- Throughout the flow reduction test, there was at least a 2/1 margin in heat flux to CHF.

Data was recorded on strip chart recorders during the period of reduced cooling between test points 32.1 and 34.1. The strip chart data through this period are reproduced in Figures 2-42, 2-43, and 2-44.

The first sign of temperature fluctuation was at test point 32.1 as shown on TC24 (Figure 2-43) at the outlet from the trailing edge tube. Although this fluctuation in

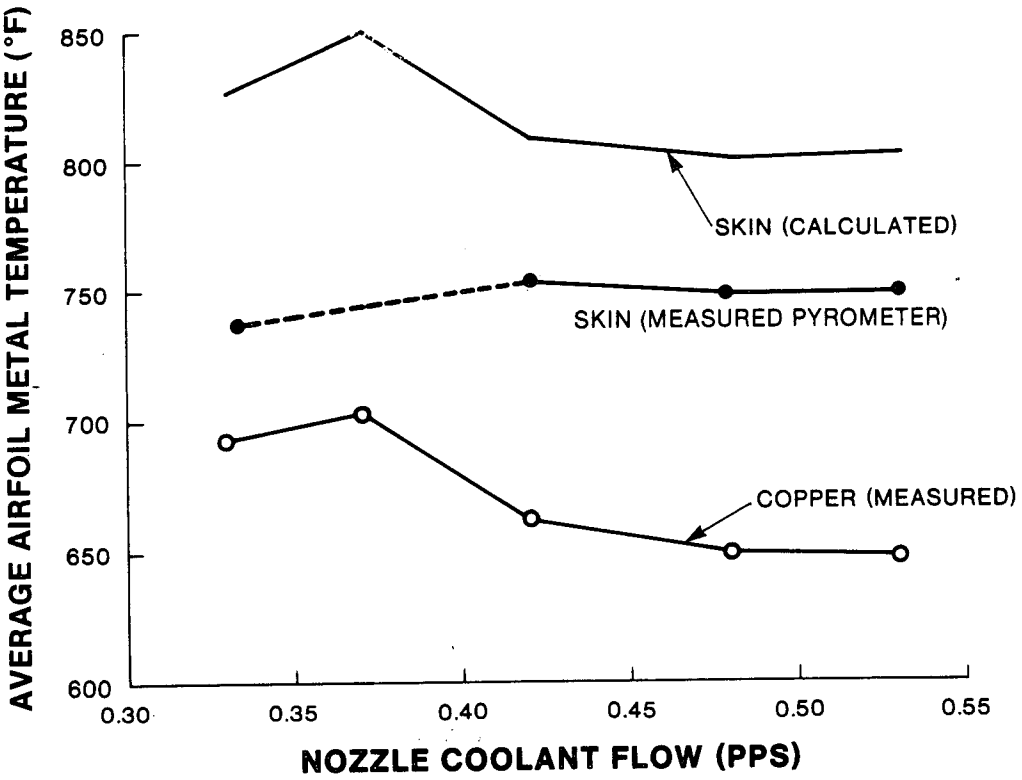

Figure 2-38. Airfoil metal temperature vs coolant flow – first-stage nozzle test

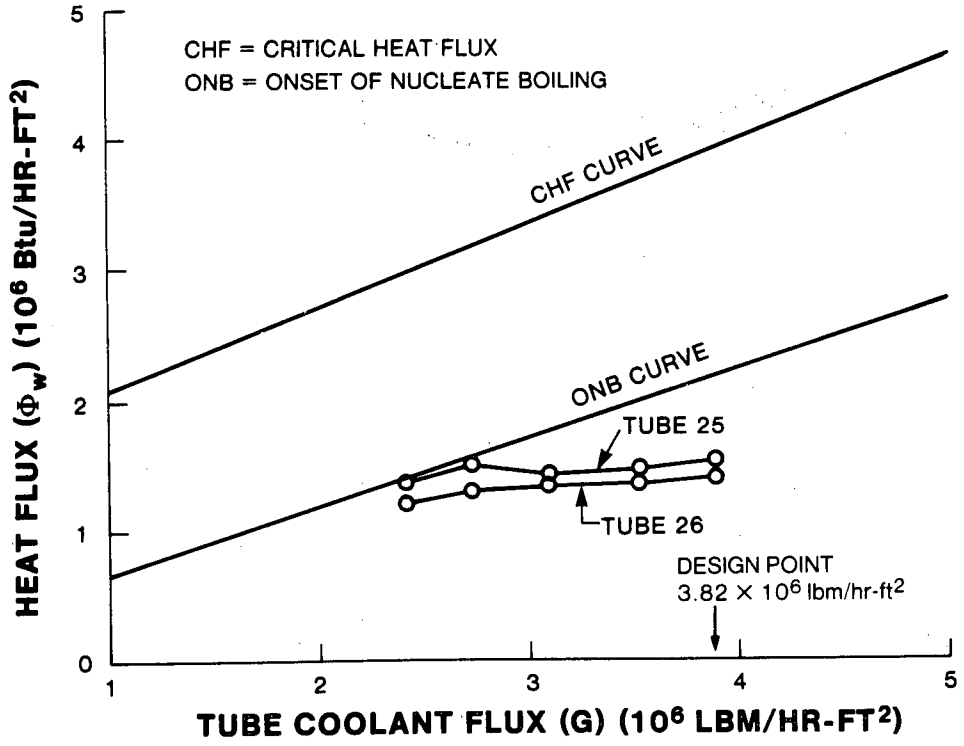

Figure 2-39. Feed tube heat flux vs coolant flux – first-stage nozzle test

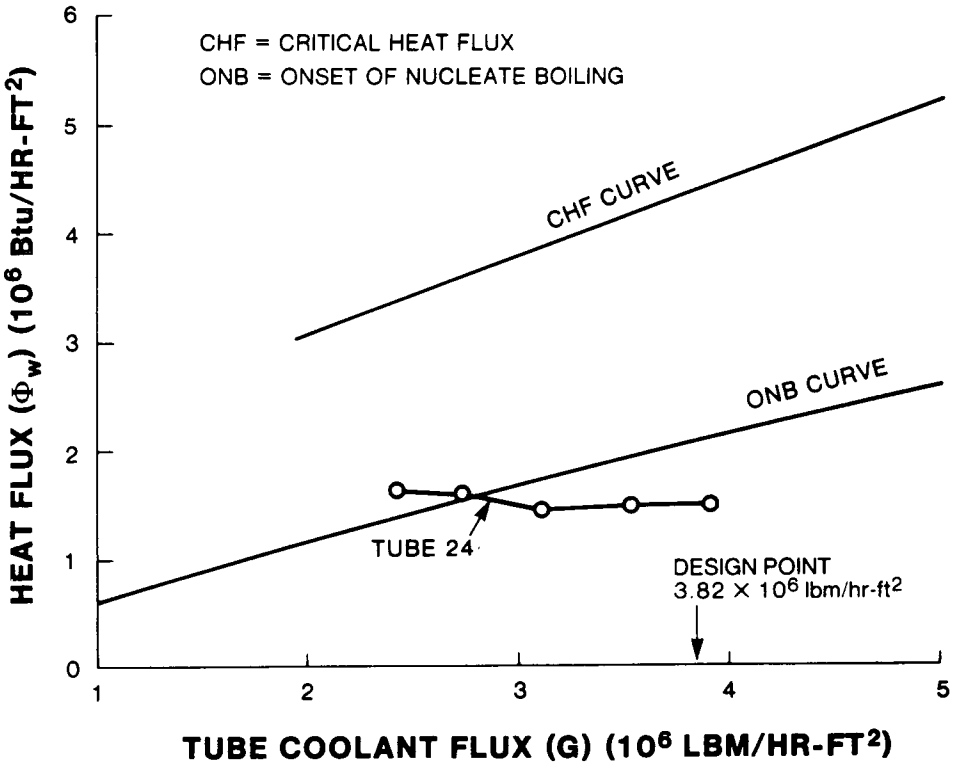

Figure 2-40. Trailing edge tube heat flux vs coolant flux – first-stage nozzle test

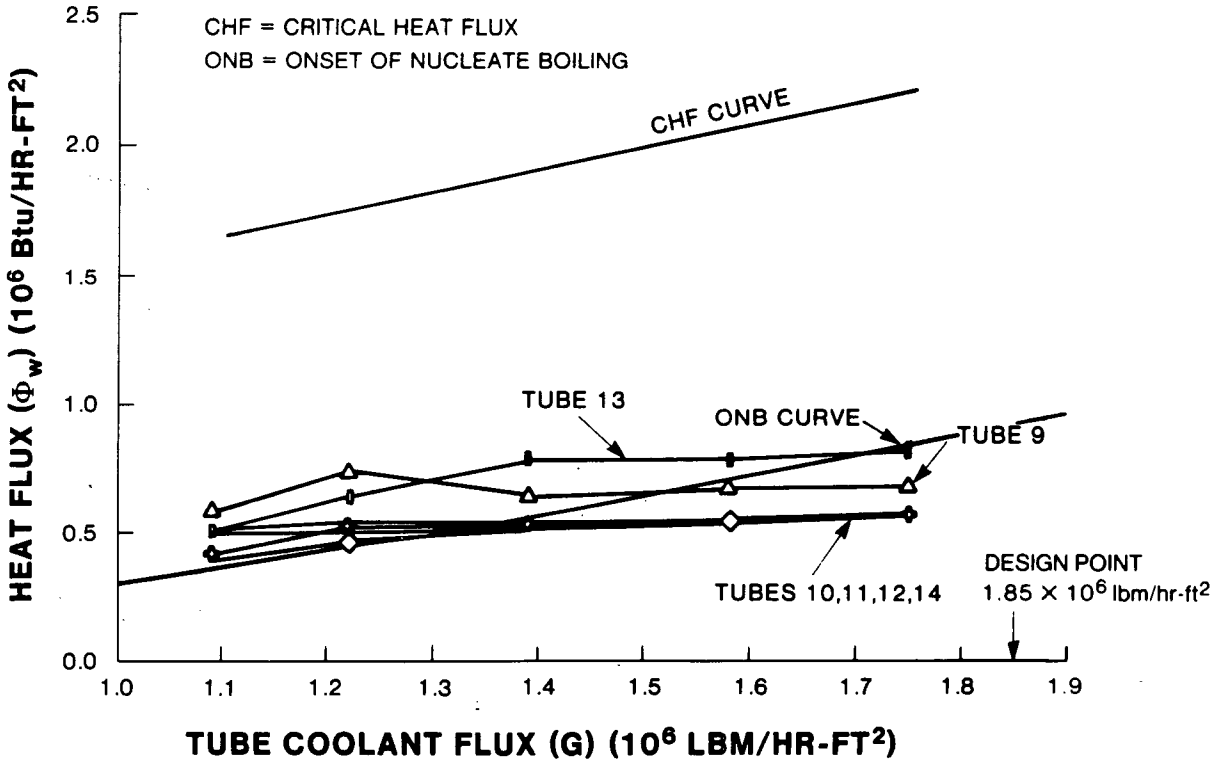

Figure 2-41. Return tube heat flux vs coolant flux – first-stage nozzle test

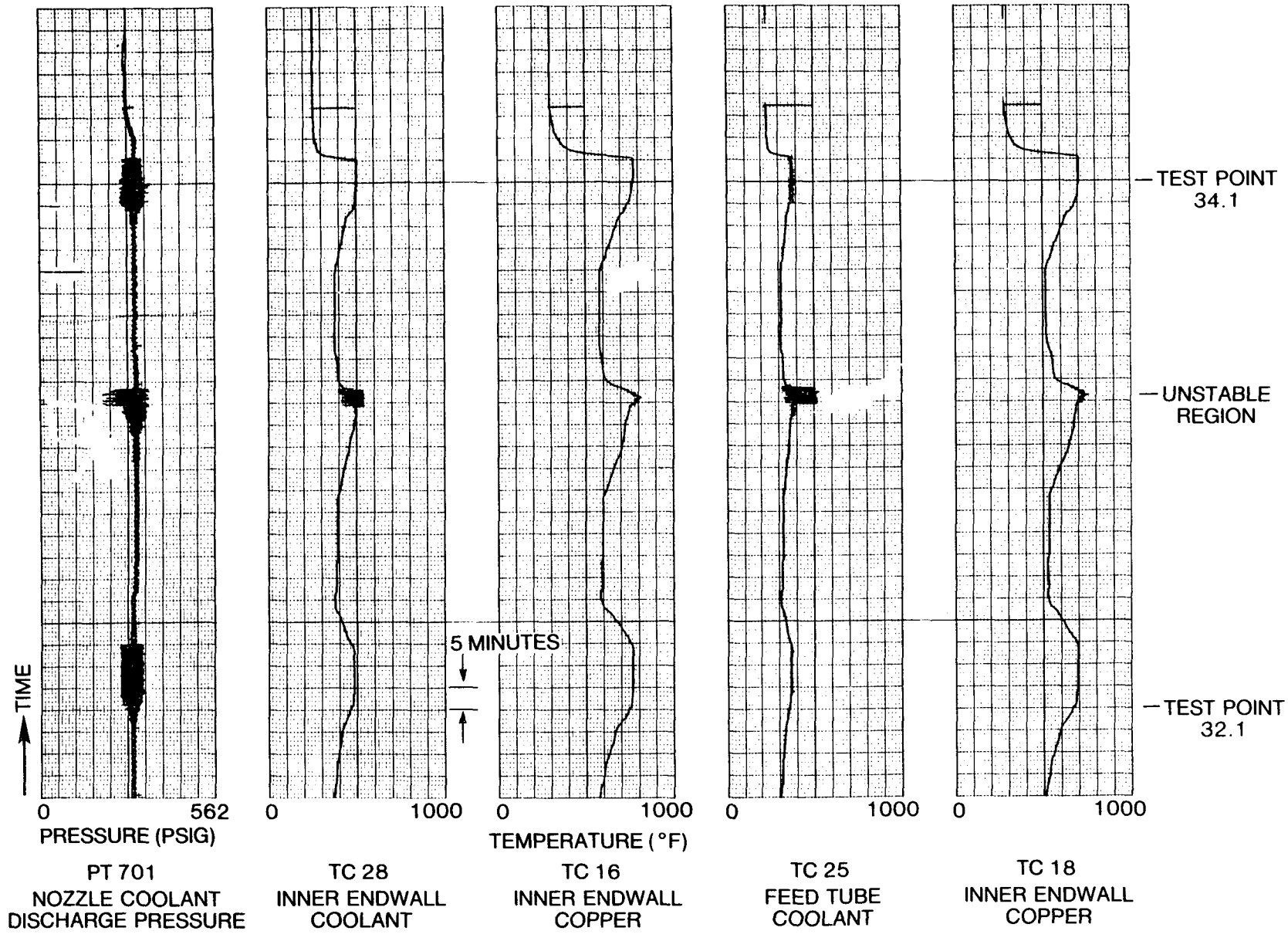

Figure 2-42. Coolant pressure and temperature – metal temperature response to reduction of coolant flow – first-stage nozzle test

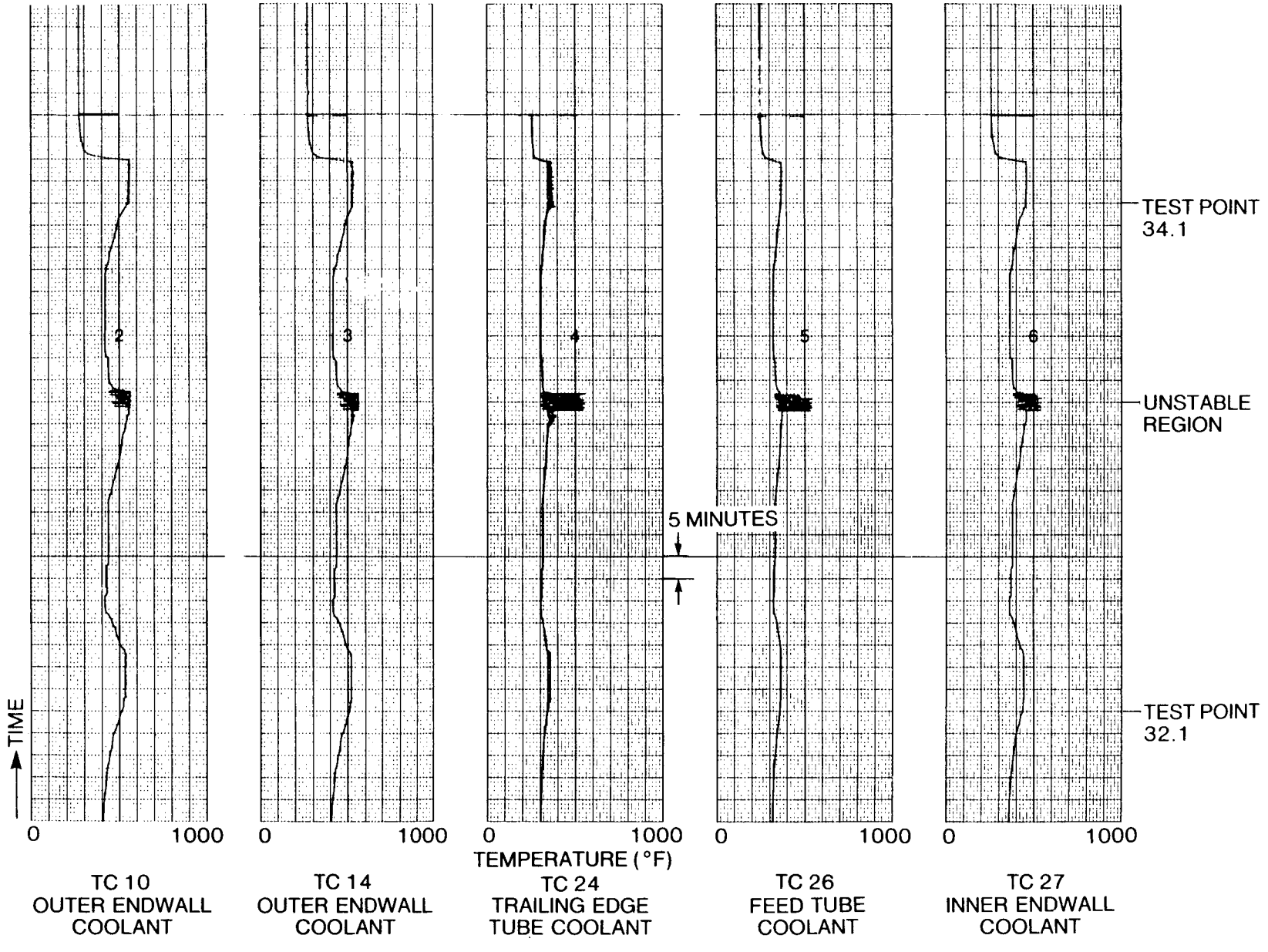

Figure 2-43. Coolant temperature response to reduction of coolant flow – first-stage nozzle test

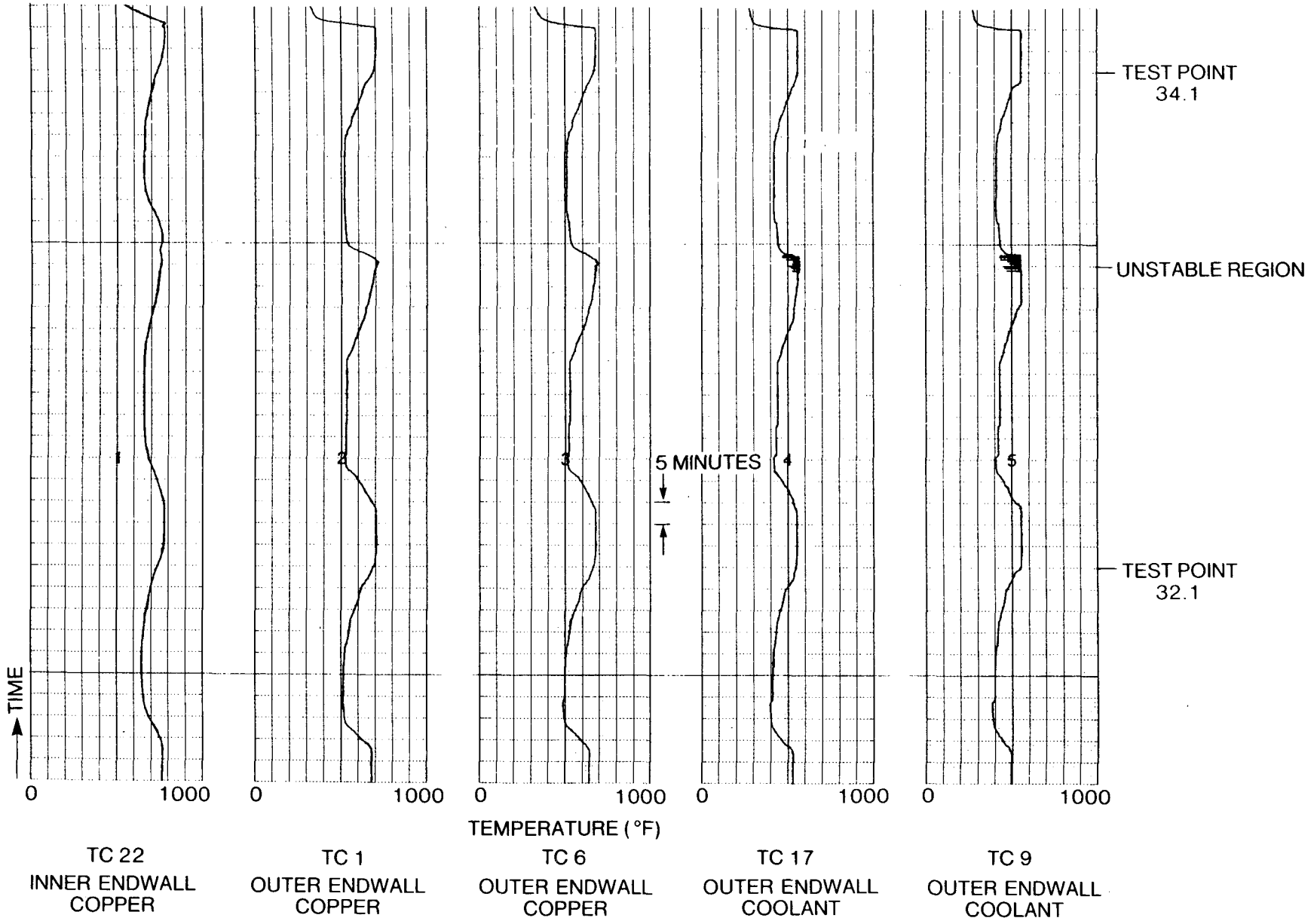

Figure 2-44. Thermocouple response to reduction of coolant flow – first-stage nozzle test

temperature was slight, a 60 psi pressure fluctuation was detected on PT701 (Figure 2-42) which then jumped to 120 psi at onset of unsteady coolant temperature. This fluctuation indicates that saturated (bulk) boiling occurred at the nozzle exit at 60% design flow ($G = 2.4 \times 10^6$ lbm/hr-ft^2). Flow instability caused by bulk boiling indicates the flow reduction limit of this design. Therefore, it is clear that a coolant pressure fluctuation precedes, by a significant margin, any possible cooling instability. This signal should be easily detected during actual turbine operation.

During approach to the unstable region, TC24 and TC25, two of the three highly loaded feed tubes showed temperature fluctuations well before the full water system became unstable. This condition arose despite the high subcooling, particularly in the trailing edge tube. One of the return tubes as shown on TC9 reached its saturation temperature, but did not begin to fluctuate until the transition to full water system instability. As explained earlier, full water system saturation temperature is approximately 25 °F lower than the ideal saturation temperature for assumed equilibrium.

During the unstable period feed tubes TC24, TC25, and TC26, with high subcooling, also displayed a temperature fluctuation to an upper limit, which was near the saturation temperature of the return tubes. One might conclude that flow interruptions caused the average temperature to rise. However, the coolant temperature at the outlet from the two inner wall tubes (TC28) and in the manifold, after mixing, at the entrance to the return tubes (TC27) show that the bulk temperature did not rise. The small changes in copper temperature (TC16 and TC18) are also evidence that the total flow through the airfoil and inner endwall did not reduce substantially. The temperature in the outer endwall copper, and hence the flow, was nearly steady.

It may be concluded, however, that the outlet tubes (TC9, TC10, and TC11) were the primary source of cooling interruption because they registered a largely downward fluctuation in their outlet temperatures. Hence, since average discharge temperature from a tube is reduced, its cooling effectiveness is also reduced. This observation indicates that the effectiveness of the inlet tubes must have increased. Measurements to confirm these observations are not available. Qualitatively, comparison of discoloration between the two nozzles reveals that the airfoil of the nozzle in which coolant flow was reduced, particularly the leading edge, reached significantly higher temperatures.

The largest rise in airfoil copper temperature is indicated by the spar rod temperature TC34; Figure 2-45 is a magnification of this trace. The rapid changes indicate that the actual copper temperature is higher than shown. However, transient finite element analysis reveals that the airfoil copper temperature immediately surrounding the spar rod did not exceed the recorded temperature (870 °F) by more than 50 °F. Since the location of the thermocouple is under the influence of both water feed and return tubes, it was not possible to determine which tubes were more prone to the apparent interruption of cooling effectiveness.

After completion of system fault condition testing, the composite nozzles were removed from the HGPDTS and throughly inspected. Details of the post-test inspection are found in Section 2.8.3.

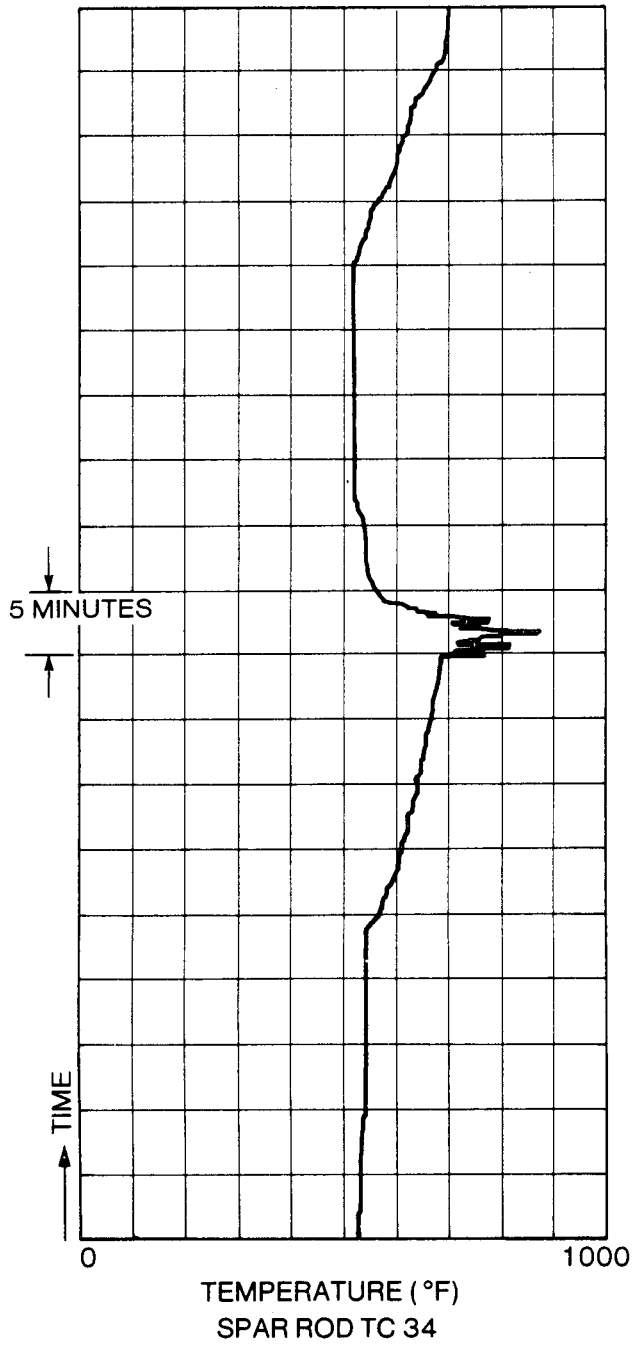

Figure 2-45. Spar rod thermocouple response to reduction of coolant flow – first-stage nozzle test

2.8 INSPECTIONS

2.8.1 Pretest Inspection

Pretest inspection of the test nozzles included ultrasonic inspection of the nozzle from the gas-path surfaces and eddy current inspection of the nozzle from the internal surfaces of the airfoil cooling tubes prior to installation of the manifold covers. Both manual and mechanized ultrasonic inspection techniques were used to inspect the test nozzles.

Results of the ultrasonic and eddy current inspection revealed no flaws in the airfoils of nozzle #1 or nozzle #3. However, ultrasonic scans did indicate anomalies at depths of 0.020 to 0.050 inch below the interface of the copper to skin in all endwalls of the test nozzles. Results of the ultrasonic inspection are shown in Figures 2-46 through 2-49.

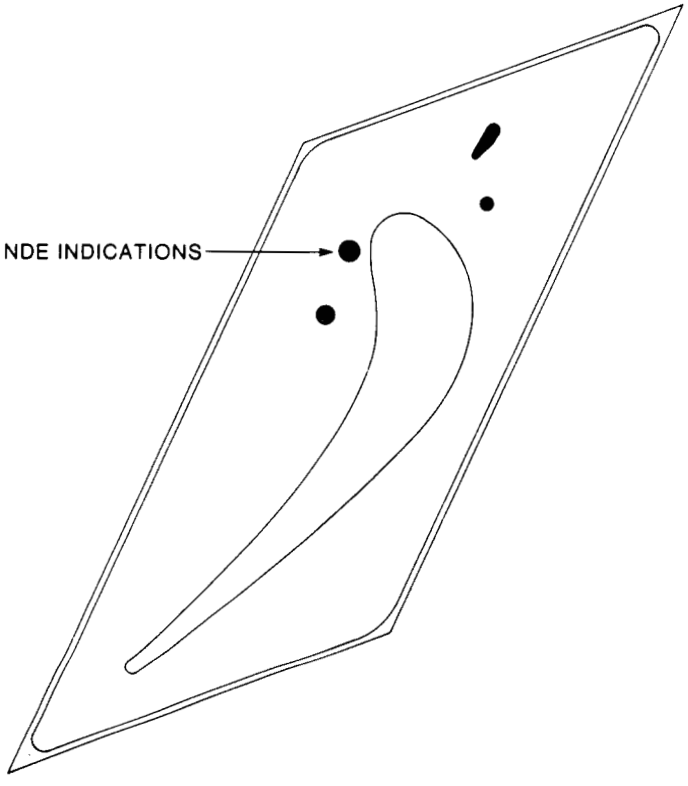

Figure 2-46. First-stage nozzle #1 outer endwall pre-test ultrasonic inspection results

2.8.2 In-Place Inspection

In-place inspections were conducted as required by the test plan. Visual inspections of the composite nozzle trailing edges were conducted by removing the mixing chamber manway cover and having an inspector enter the mixing chamber of the HGPDTS. Mirrors and high-intensity lights were used to record the surface condition of the nozzles. After completion of the initial test series, the combustion system was removed from the HGPDTS to allow a more thorough visual and ultrasonic inspection of the composite nozzle leading edges.

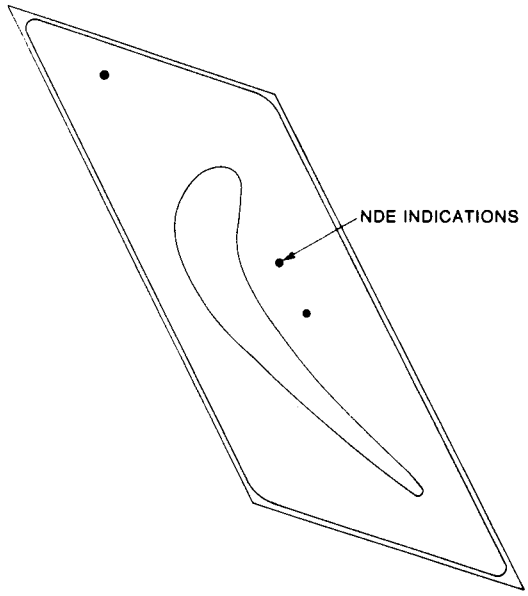

Figure 2-47. First-stage nozzle #1 inner endwall pre-test ultrasonic inspection results

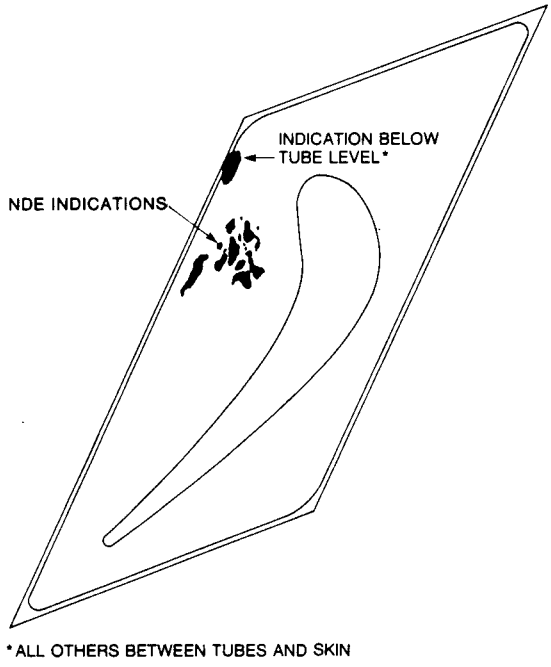

Figure 2-48. First-stage nozzle #3 outer endwall pre-test ultrasonic inspection results

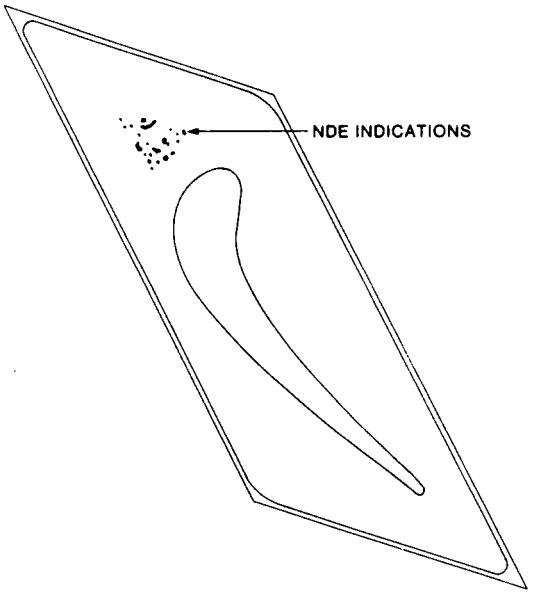

Figure 2-49. First-stage nozzle #3 inner endwall pre-test ultrasonic inspection results

Figures 2-50 and 2-51 show the nozzle cascade from each end, after completion of the initial test series (106 thermal cycles). It can be seen on Figure 2-50 that the inner endwall leading faces of nozzle #3 shows a discoloration pattern which indicates a hot spot near, but not centered on, the acute corner. During testing, the closest thermocouple to this spot, TC16(2), measured variations in temperature which were not consistent with regular cyclic response.

There were two small dark spots on the outer endwall of nozzle #3. One spot penetrated from an edge in the region of the indications recorded by pretest ultrasonic inspection. The other spot at the acute leading corner was located where no indications were recorded earlier. The spots did not show visible evidence of delamination or distortion. Test nozzle #1 did not show any such spots.

An ultrasonic examination, with the nozzle cascade mounted in the test stand and the transition piece removed, revealed no new indications. It was not possible to inspect the dark spots because they were inaccessible.

2.8.3 Post-Test Inspection

The following post-test inspections of the first-stage composite nozzles were conducted

- Visual
- Ultrasonic
- Eddy current
- Hydraulic flow check
- Metallographic

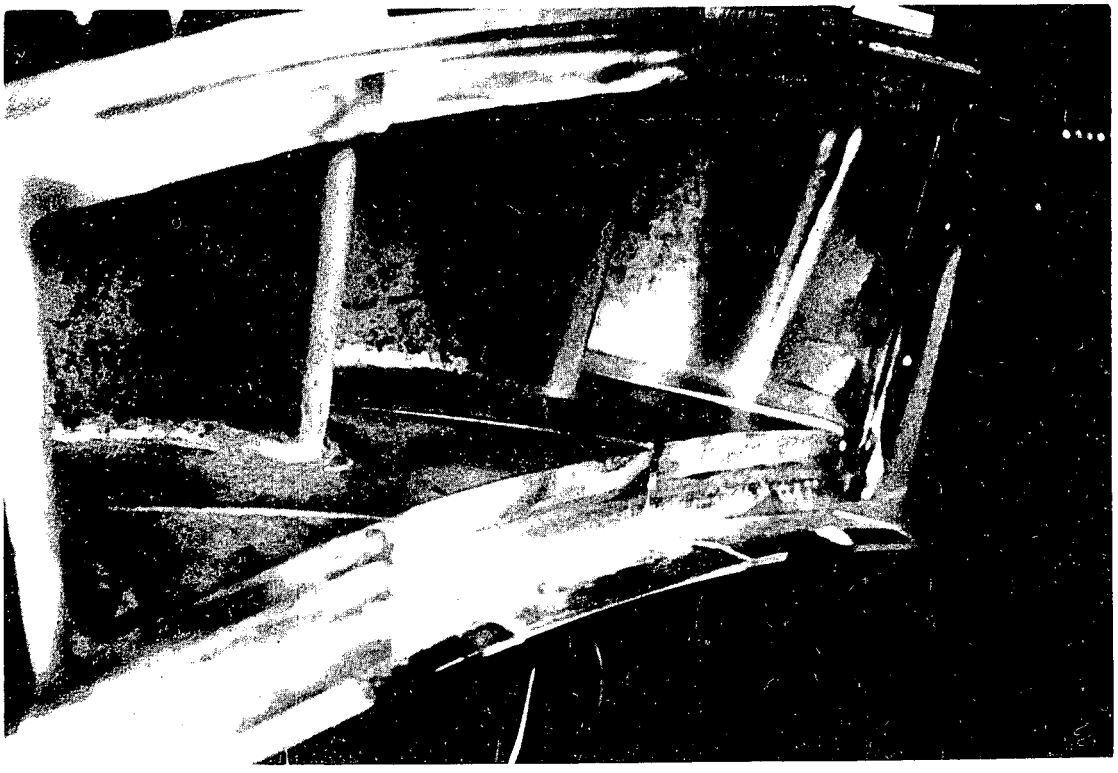

Figure 2-50. First-stage test nozzle leading edges after 106 thermal cycles

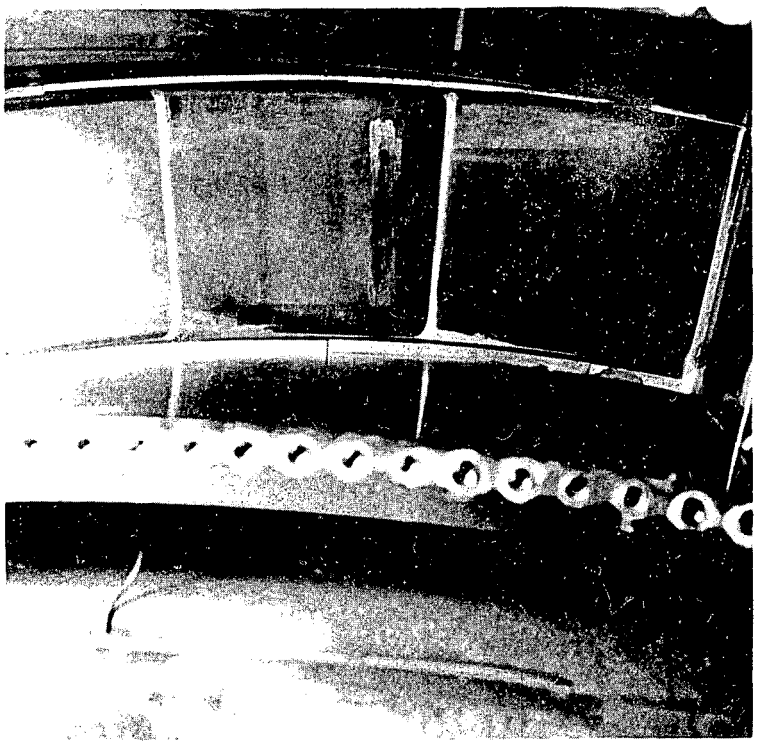

Figure 2-51. First-stage test nozzle trailing edges after 106 thermal cycles

2.8.3.1 Visual Inspection

Subsequent to testing, the nozzles were removed from the test stand. The two dark spots observed after the initial testing on nozzle #3 were visible. However, they had not grown appreciably, and no associated deterioration was evident. Figure 2-52 is a photograph showing the affected region of the outer endwall with the spots identified. The spot in the outer corner was partially obliterated by residual temperature sensitive paint. Figure 2-53 is a closer photograph showing the spot at the edge of nozzle #3. Prior to a detailed visual examination, the nozzles were cleaned with a water-alumina grit slurry at 30 psi pressure. The deposits were easily removed by this procedure.

The two key visual observations after cleaning were skin discoloration and slight skin-to-endwall separation at the acute angle corners. The shading of the skin can be seen in Figures 2-54 and 2-55. The deposits on the pressure side of nozzle #1 are from an upstream source, probably thermocouple tips, and have no apparent detrimental effect on the nozzle. Skin discoloration could not be traced to any underlying metallurgical conditions. The separation is limited to the outer 0.060 inch or less of the Nitronic 50 endwall-to-skin bond.

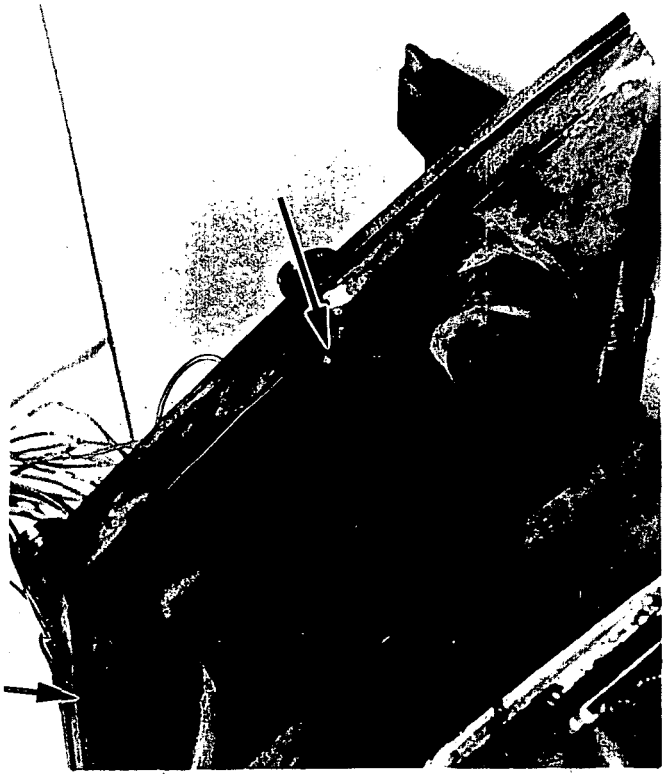

Figure 2-52. First-stage test nozzle leading edges after 617 thermal cycles

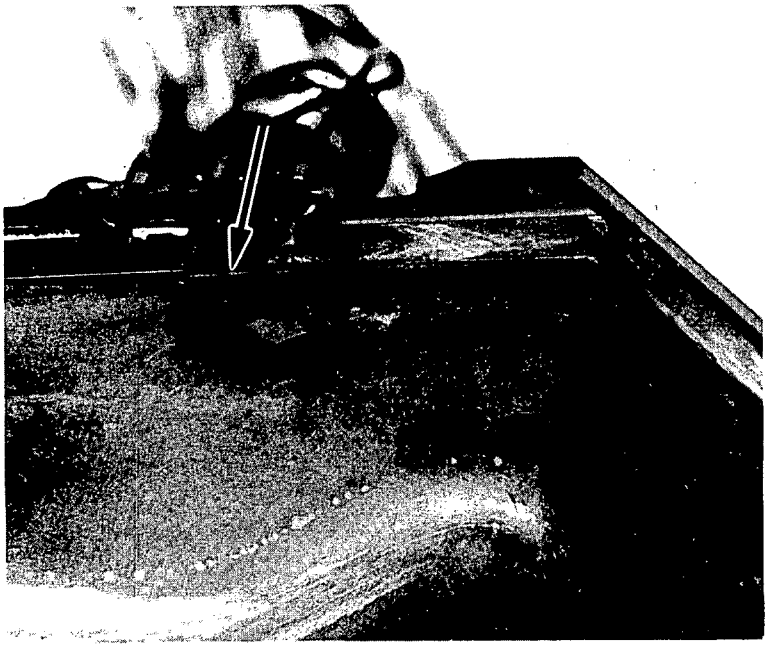

Figure 2-53. First-stage nozzle #3 outer endwall after 617 thermal cycles

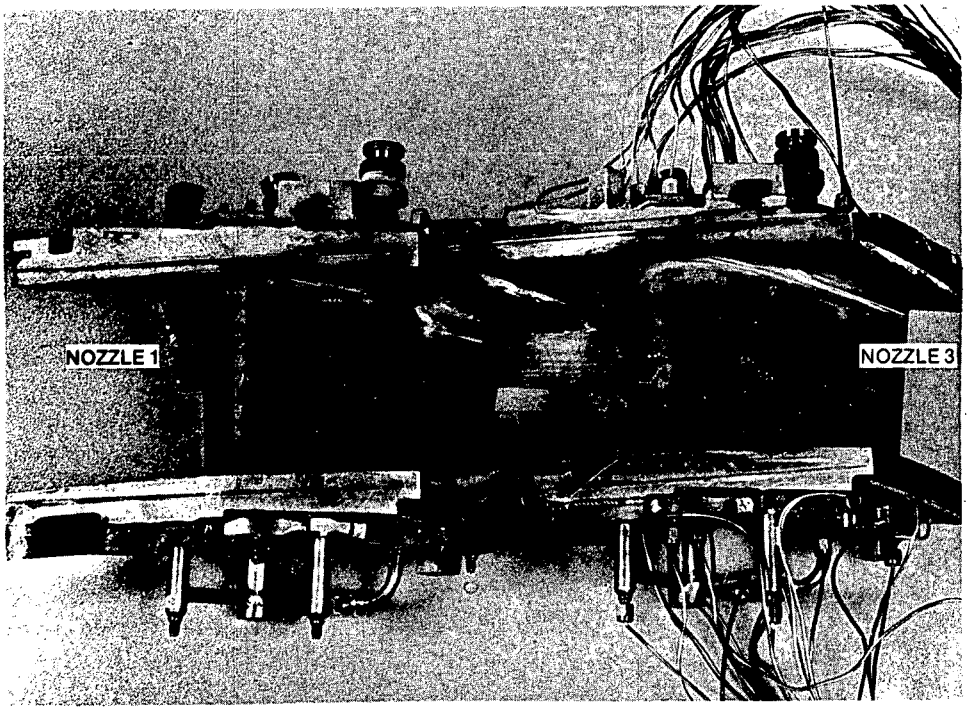

Figure 2-54. First-stage test nozzle suction sides after 617 thermal cycles

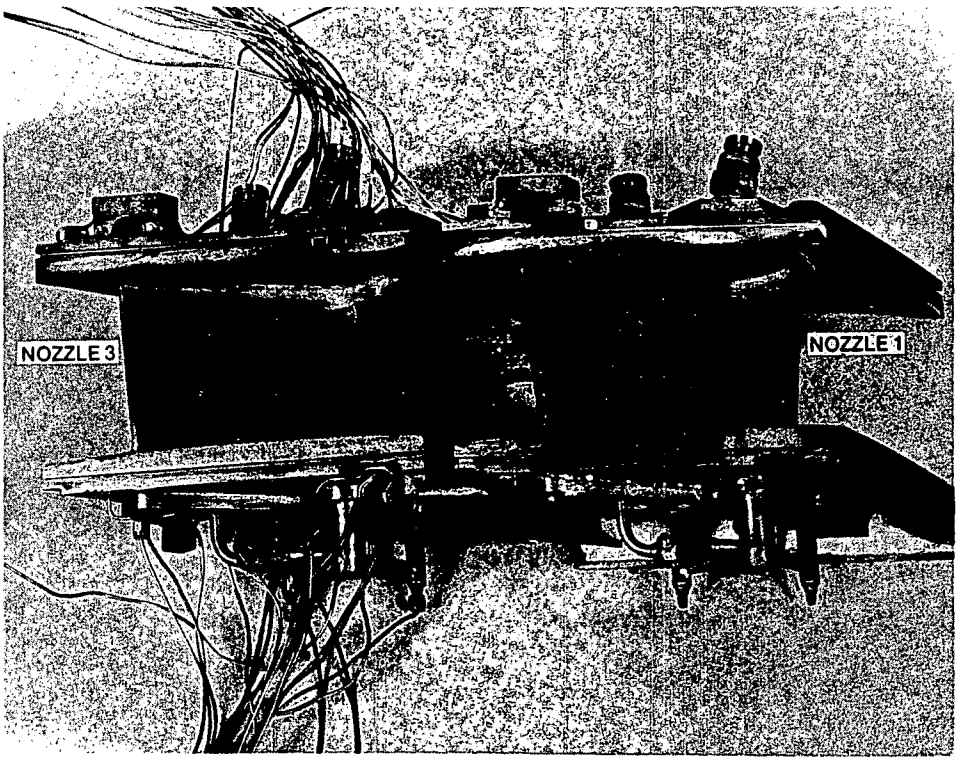

Figure 2-55. First-stage test nozzle pressure sides after 617 thermal cycles

2.8.3.2 Ultrasonic Inspection

The nozzles were inspected by a contact ultrasonic technique similar to that employed prior to testing. No indications were found in either nozzle airfoil, duplicating the pre-test results. The endwalls however, which had various indications before testing, were found after testing to be defect free with one exception: a sub-tube copper indication. All other pre-test indications appeared in the copper sublayer between the tubes and the skin. Subsequent metallography failed to substantiate the indications. Pretest ultrasonic observations are shown in Figures 2-46 thru 2-49. The only indication which repeated after testing is labeled with * in Figure 2-48.

2.8.3.3 Eddy Current Inspection

The airfoil cooling tubes were inspected internally with an eddy current probe duplicating the inspection which was performed during the pretest period. There was no significant difference between pre- and post-test results.

2.8.3.4 Hydraulic Flow Test

Post-test hydraulic flow tests were performed to assess the possibility of any tube plugging that may have occurred. As can be seen in Figures 2-56 and 2-57, the post-test inspection results repeated the pretest inspection results very well, indicating no test-related problems.

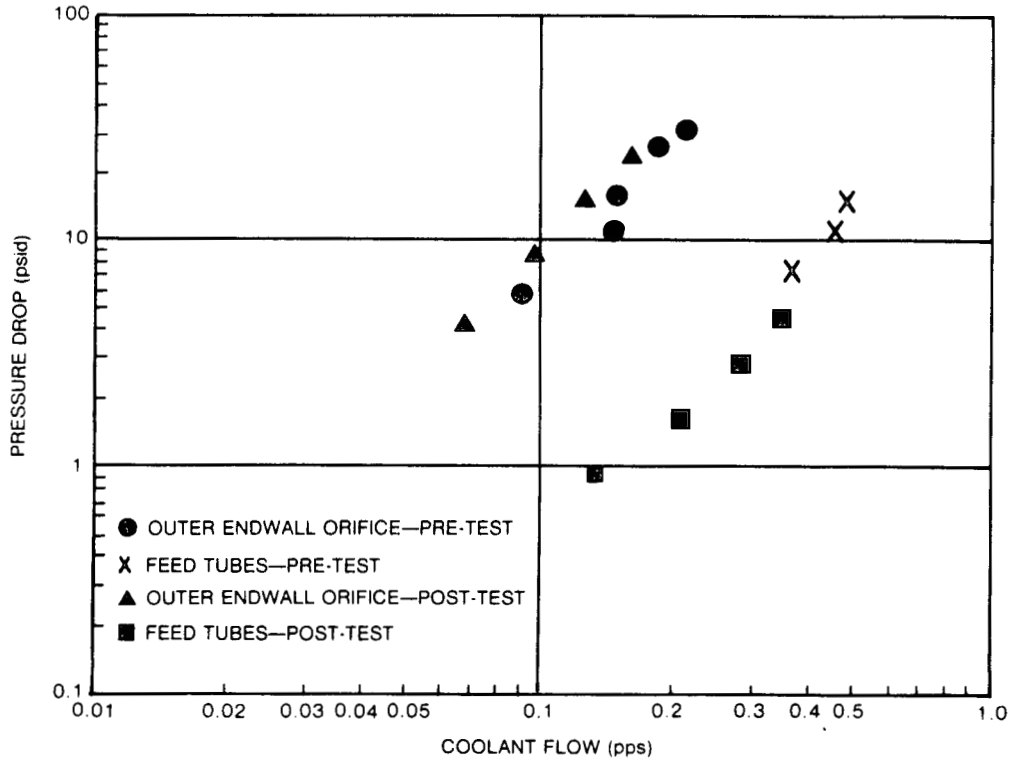

Figure 2-56. First-stage nozzle #1 post-test hydraulic flow check

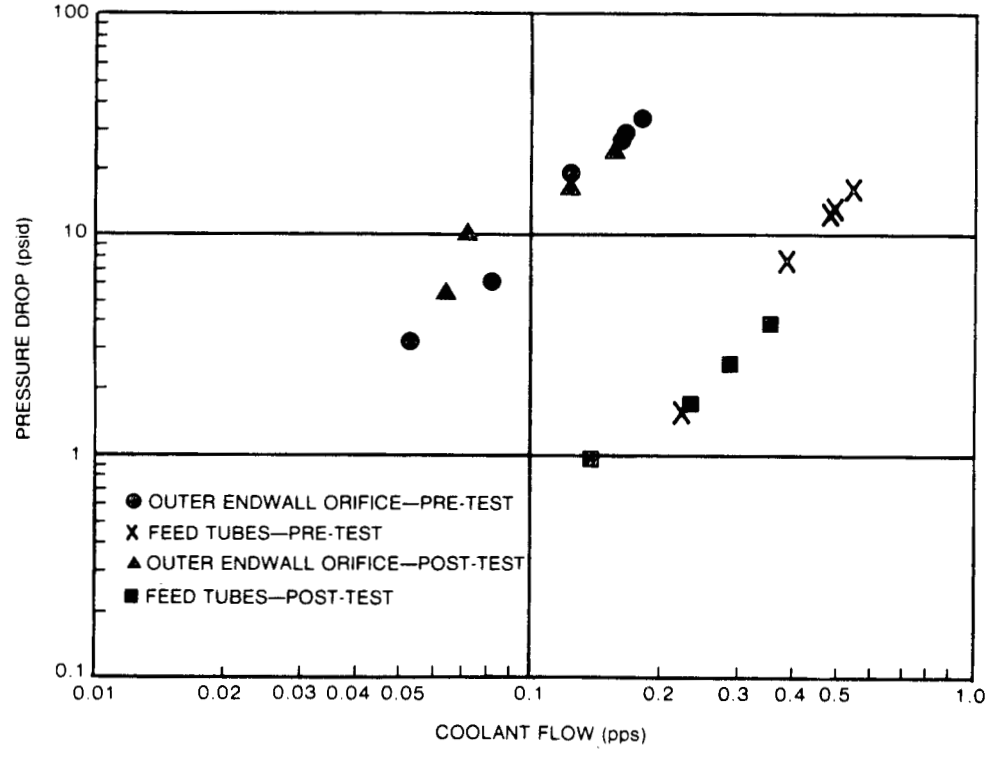

Figure 2-57. First-stage nozzle #3 post-test hydraulic flow check

2.8.3.5 Metallography

Both nozzles #1 and #3 were sectioned for metallographic inspection in accordance with Figures 2-58 and 2-59. The outer endwall of nozzle #3 was also sectioned as illustrated in Figure 2-60. All sections were mounted for metallographic examination, except for the odd-numbered airfoil sections of nozzle #3. Representative airfoil photomicrographs were taken solely on section number 8 of nozzle #3 and section number 1-2 of nozzle #1, since no differences could be detected between sections. These sections are located approximately one inch from the inner endwall.

All of the bondlines between Nitronic 50, IN617, and MZC copper were originally Ni-plated to minimize the precipitation of secondary phases at the bondline. Metallographic examination indicated some variability of Ni-plate thickness, especially for the IN617 skin; however, the plating successfully performed its function as all bondlines were essentially single-phase solid solutions. Bondlines representing the Nitronic 50 tube to MZC copper, Nitronic 50 spar rod to MZC copper, and IN617 to MZC copper are shown in Figures 2-61, 2-62 and 2-63 for nozzle #3 and on Figures 2-64 and 2-65 for nozzle #1. Electron beam microprobe line scans were made near the center of the airfoil on the adjacent section, number 7, from nozzle #3 to assess interdiffusion of key elements between the various alloys. Figures 2-66, 2-67, and 2-68 are illustrative of the bondlines shown on Figures 2-61, 2-62, and 2-63. In the case of the Nitronic 50 tube and spar, a residual Ni-plating layer of 15 to 25 microns thickness is present. However, approximately 100 microns of Ni/Cu interdiffusion occurred on the MZC copper side, and 12 to 17 microns of Ni/Fe interdiffusion was present on the Nitronic 50 side. The Cu and Fe concentration gradients extend from the Nitronic 50 through the Ni plate to the MZC copper interface.

In the case of IN617 skin, a relatively thick Ni-plate region was microprobed, indicating at least 50 microns of Ni remaining. Once again, Ni and Cu were diffused over a distance of 100 microns, while Cr from the IN617 had penetrated approximately 35 microns into the Ni. In the area of the trailing edge cooling tube, bondline precipitate was found between the IN617 skin and MZC copper for a distance of 1/2 to 3/4 inch from the trailing edge (Figure 2-69). The plating vendor had experienced difficulty depositing in this area. Probe line scans (Figure 2-70) show that both Ni and Co from IN617 interdiffuse with Cu over a 100-micron range, while Cr and Mo were involved in the bondline precipitate. X-ray images of the bondline indicate Cr, Mo, Ni, and Co enrichment in the precipitate (Figure 2-71).

The final area to be microprobed involved the bondline between the Nitronic 50 trailing edge tube and the IN617 skin (Figure 2-72). Since the tube had originally been plated and this area of the skin had little plating, a Ni interlayer of about 30-microns thickness was formed. Major elements from both alloys, including Cr, Mo, Al, and Co from IN617 and Fe, Cr, and Mo from Nitronic 50, exhibited concentration gradients into this interlayer. No intermetallic particles were found in this matrix of continuous solid solubility.

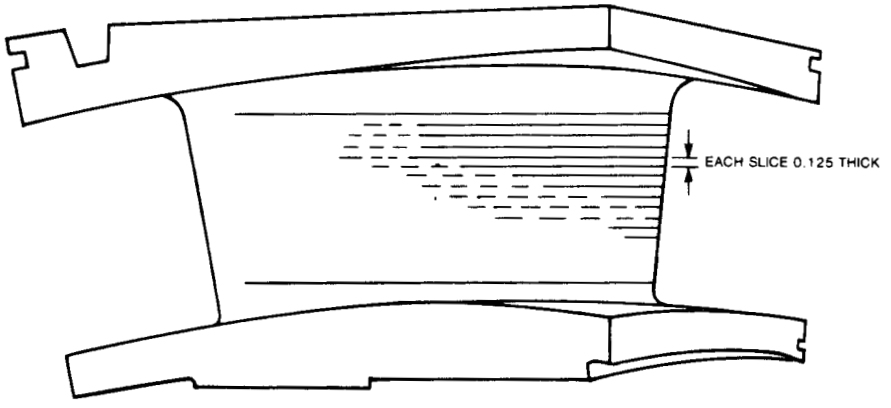

Figure 2-58. Sectioning diagram first-stage nozzle #3 airfoil

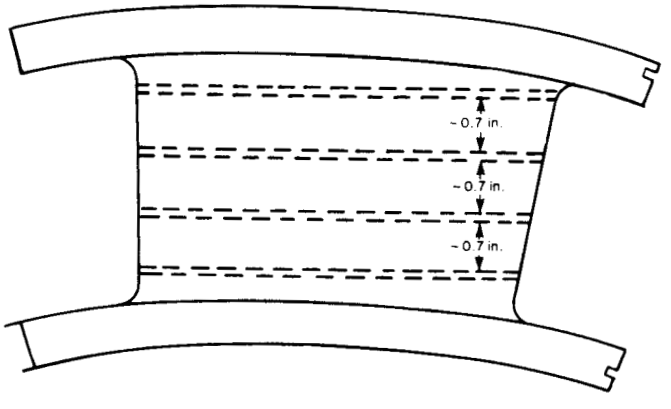

Figure 2-59. Sectioning diagram first-stage nozzle #1 airfoil

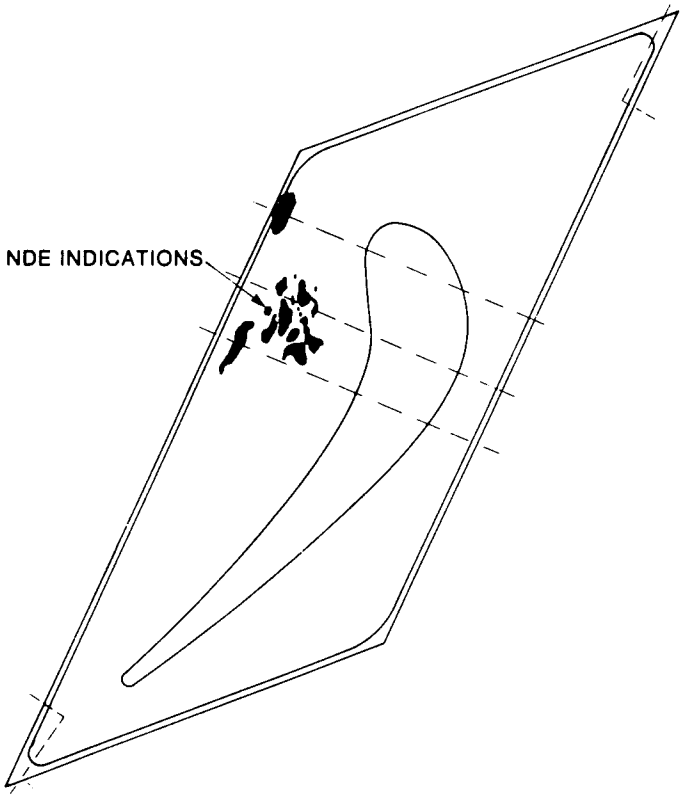

Figure 2-60. Sectioning diagram for outer endwall of first-stage nozzle #3

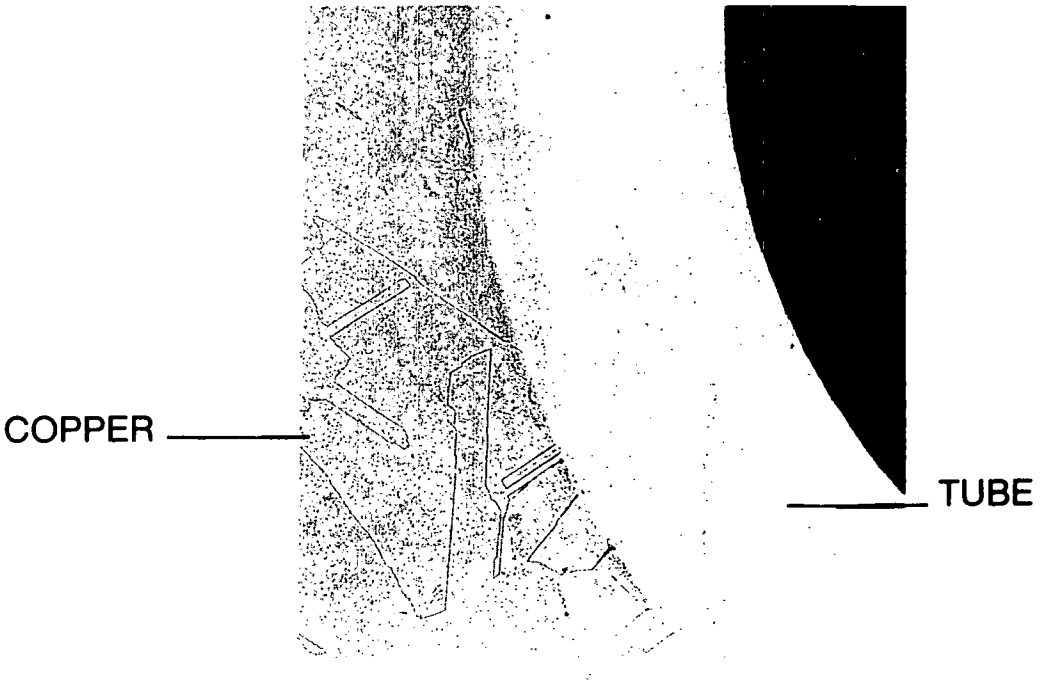

Figure 2-61. First-stage nozzle #3, Section 8, bondline Cu/N-50 tube (with plate) (magnification 90X)

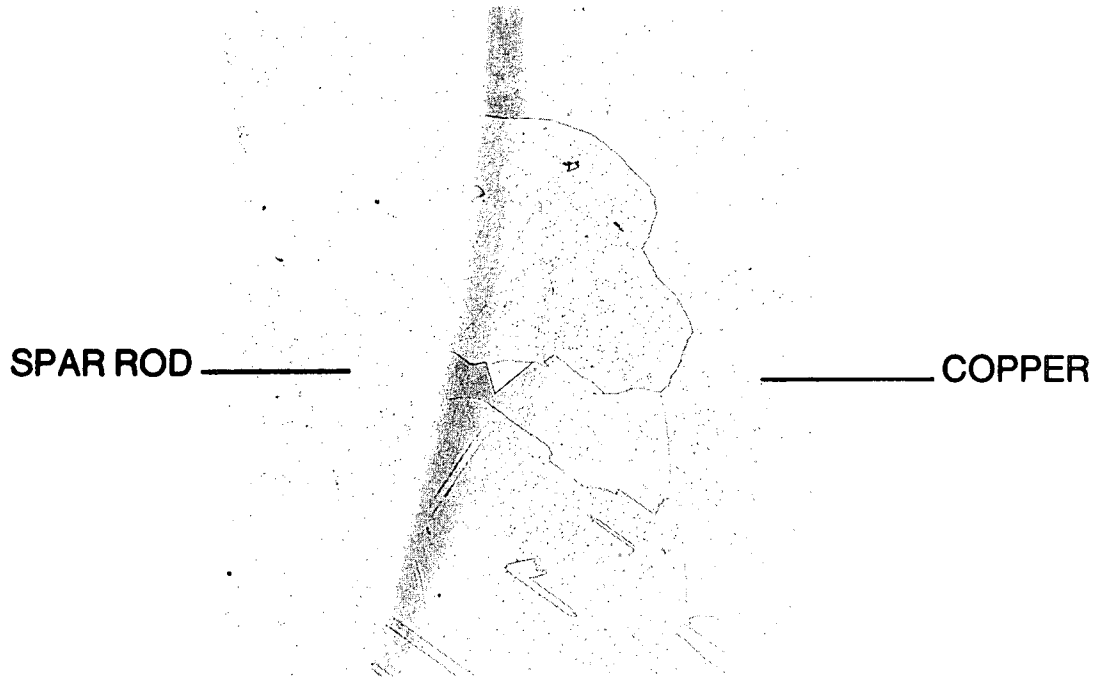

Figure 2-62. First-stage nozzle #3, Section 8, bondline Cu/N-50 spar (with plate) (magnification 90X)

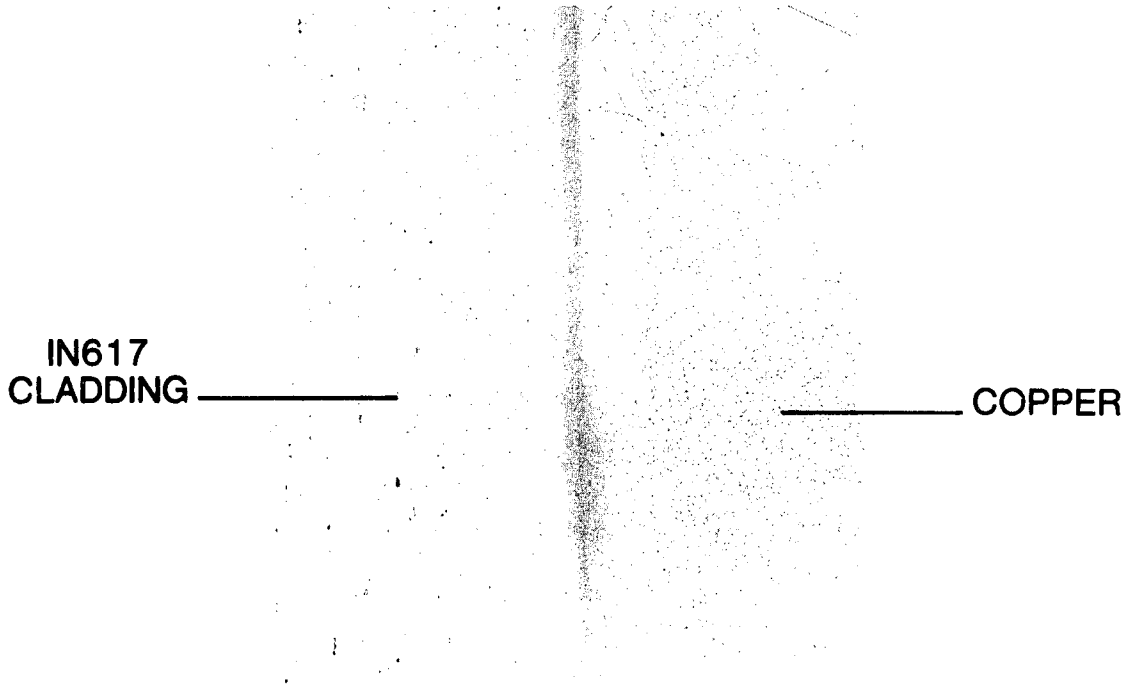

Figure 2-63. First-stage nozzle #3, Section 8, bondline IN617/Cu (with plate) (magnification 90X)

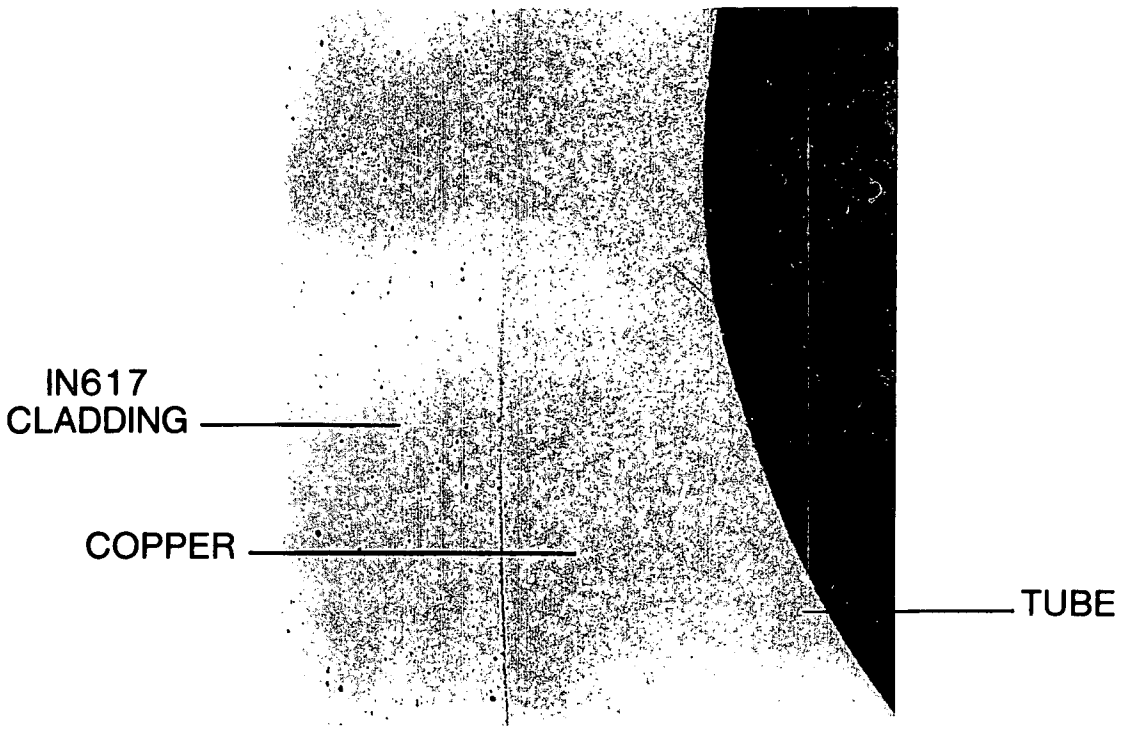

Figure 2-64. First-stage nozzle #1, Section 1-2 TE tube N-50/Cu MZC/IN617 (no plate) (magnification 90X)

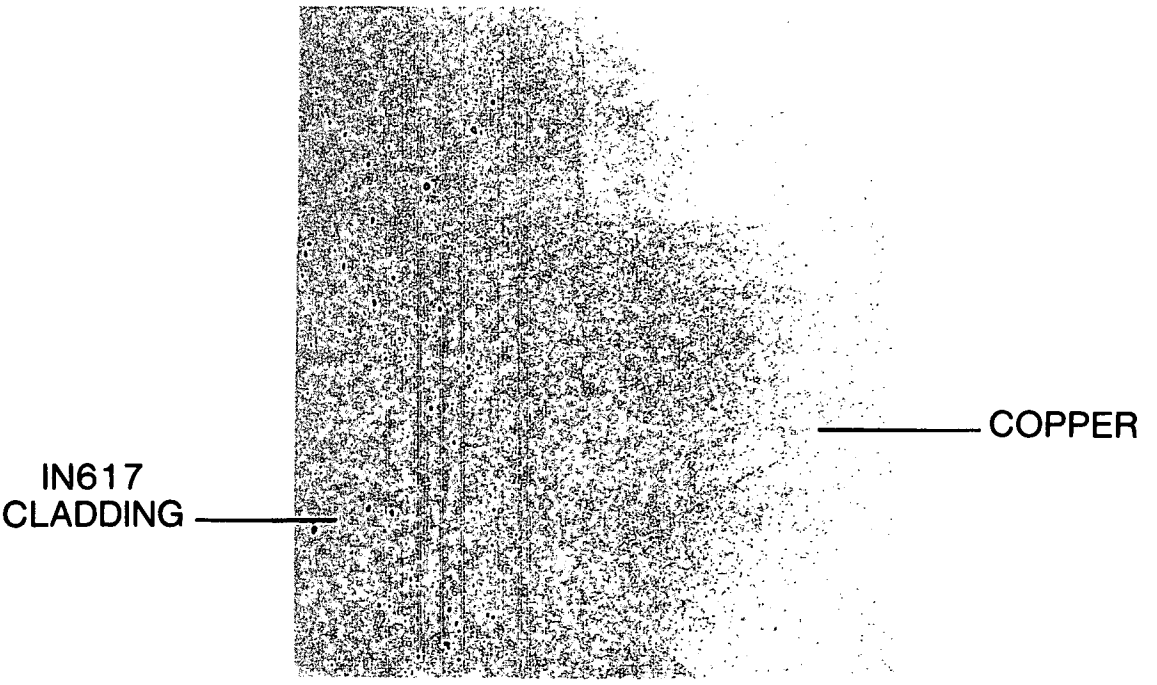

Figure 2-65. First-stage nozzle #1 Section 1-2, IN617/MZC Cu (magnification 90X)

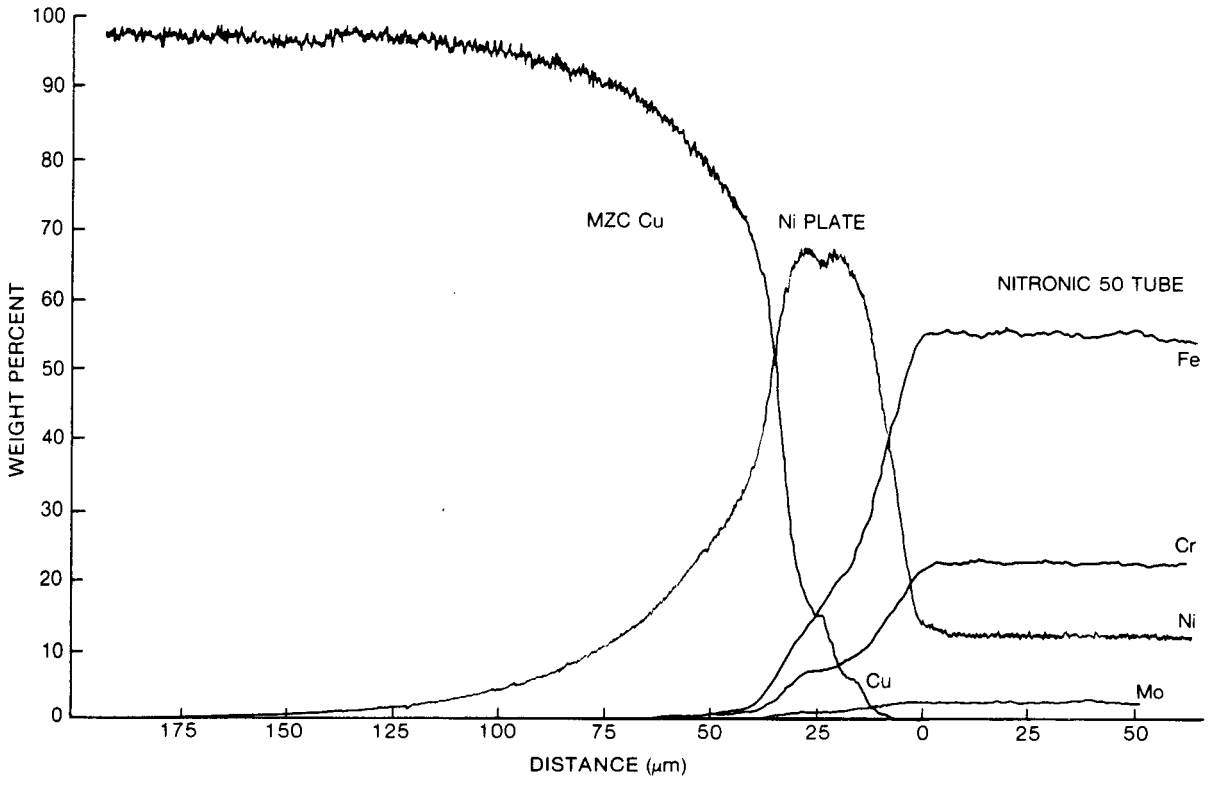

Figure 2-66. First-stage microprobe trace of tube to airfoil Cu bondline

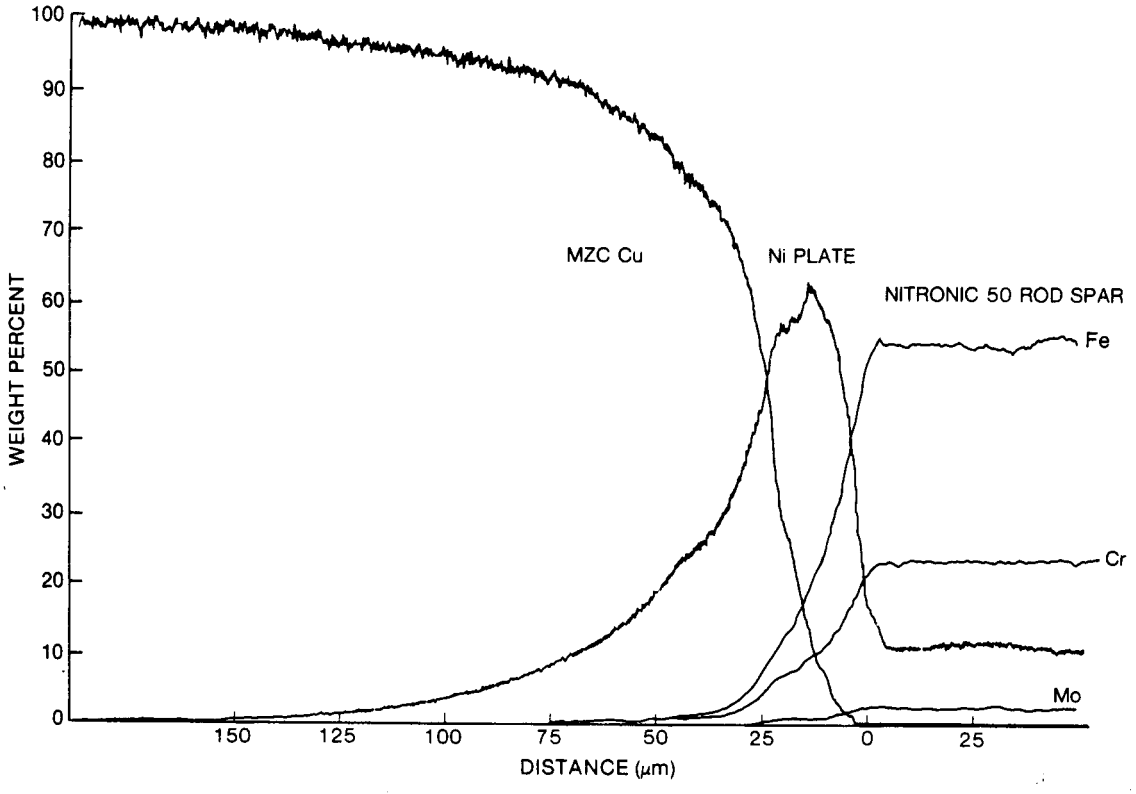

Figure 2-67. First-stage microprobe trace of spar rod to airfoil Cu bondline

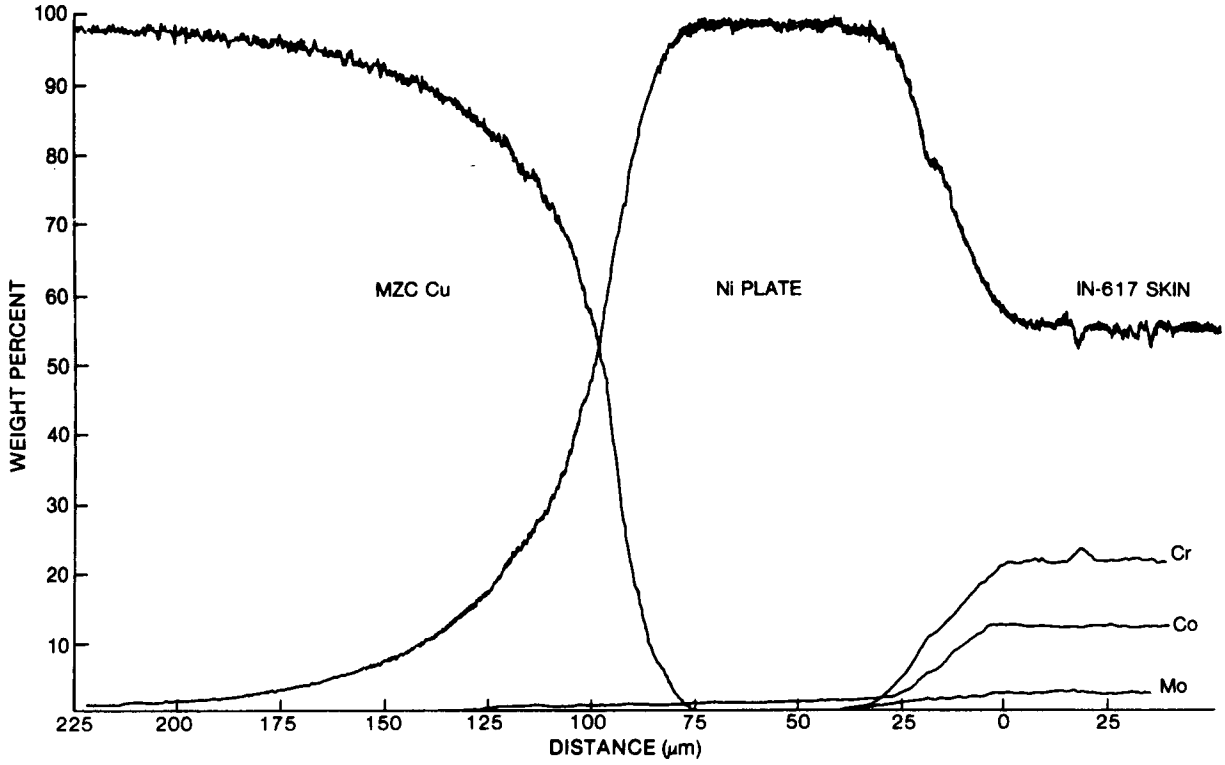

Figure 2-68. First-stage microprobe trace of skin to airfoil Cu bondline

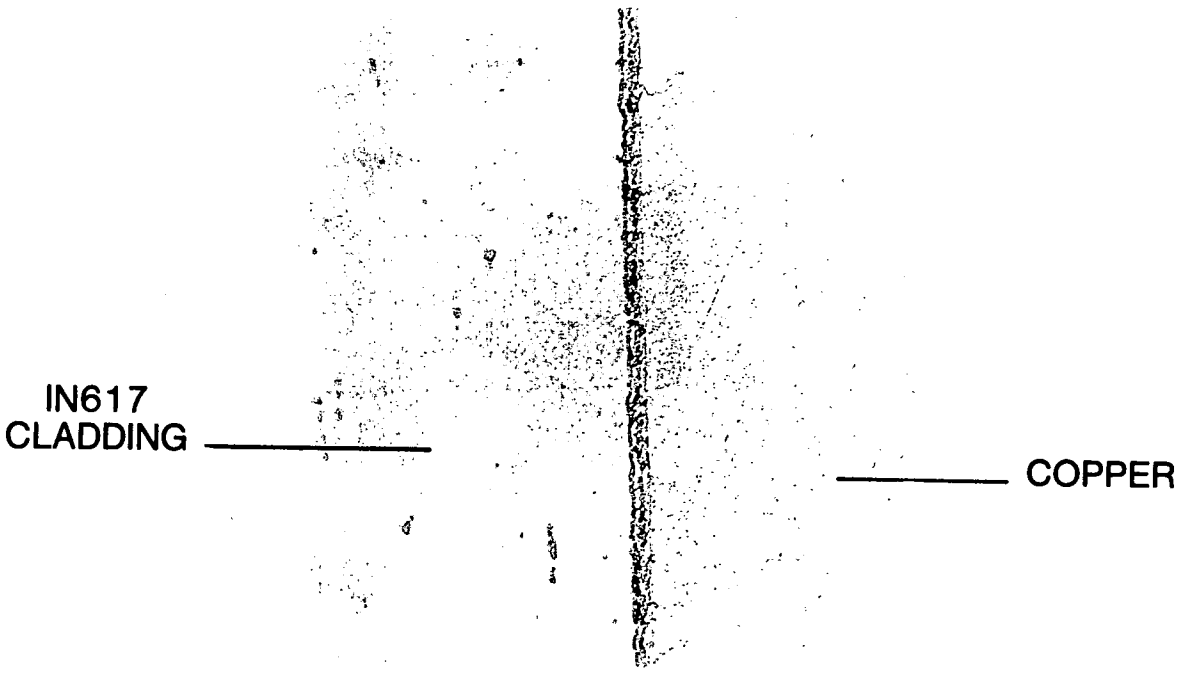

Figure 2-69. First-stage nozzle #3, Section 8, bondline Cu/IN617 at trailing edge (no plate) (magnification 180X)

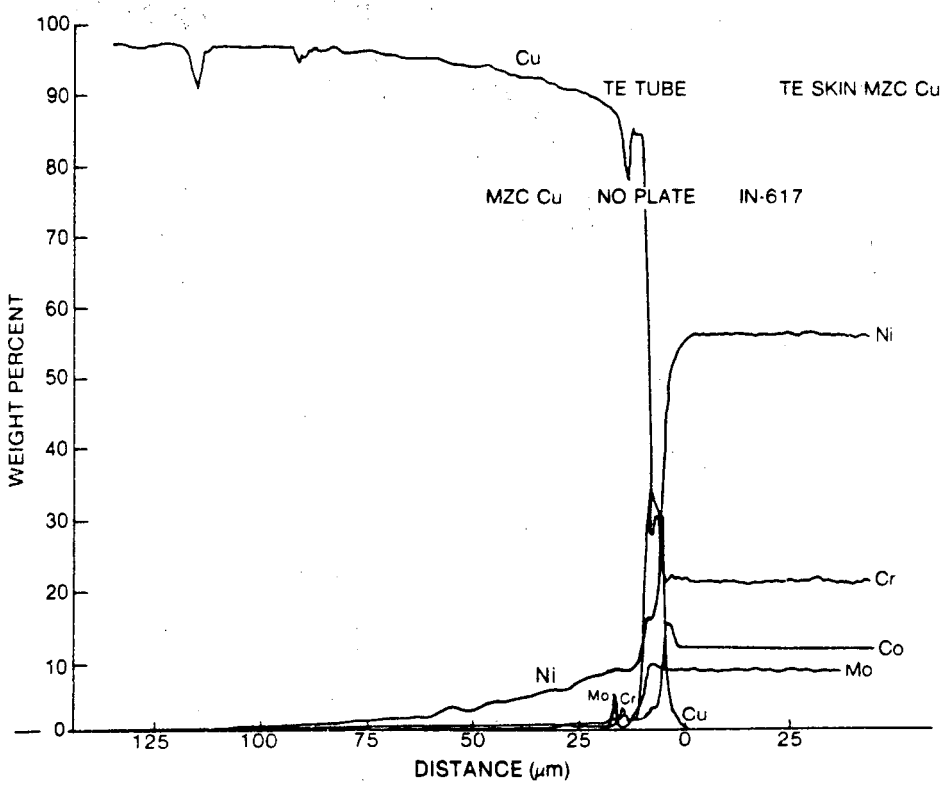

Figure 2-70. First-stage microprobe trace of skin to airfoil Cu (minimal Ni plate)

Knoop microhardness surveys were taken for the various alloy combinations (see Table 2-8). In general the baseline materials exhibited the following hardnesses:

Material	Knoop Hardness Number
MZC Copper	85 to 99
Nitronic 50	205 to 242
IN617	195 to 227
Ni plate	105

Since the only diffusion couple to retain pure Ni electroplate occurs in the case of the IN617 skin to MZC copper bondline, all of the hardness values taken in the remaining similar couples were substantially higher than either pure MZC copper or nickel (readings of 115, 118, 130, 186, and 198). Also, a value of 146 was obtained at the IN617/MZC copper interface, which exhibited the bondline precipitate near the trailing edge in an area of minimal Ni plate. The hardness values measured for MZC copper confirm that the copper sublayer was not overheated during testing.

Three additional metallographic observations of these airfoil sections are worth noting:

- The trailing edge cooling tube, by virture of its location, fabrication technique, tolerances employed in the assembly, and hot isostatic pressing (HIP) is no longer cylindrical (Figure 2-73). Deformation of the tube was apparently responsible for the generation of microcracks on the tube inner diameter (Fig-

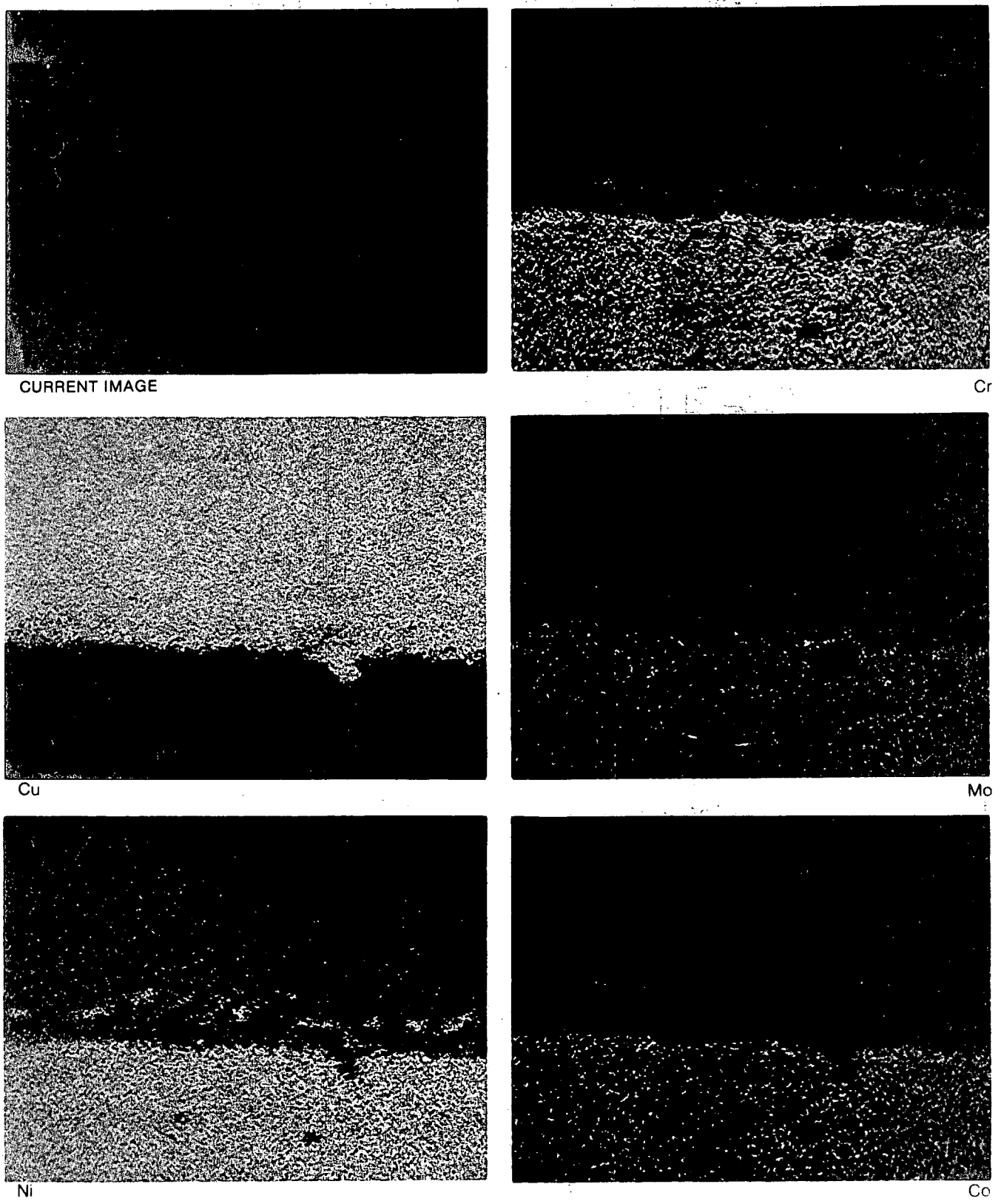

Figure 2-71. First-stage microprobe x-ray images of IN617/MZC Cu bondline without Ni plate

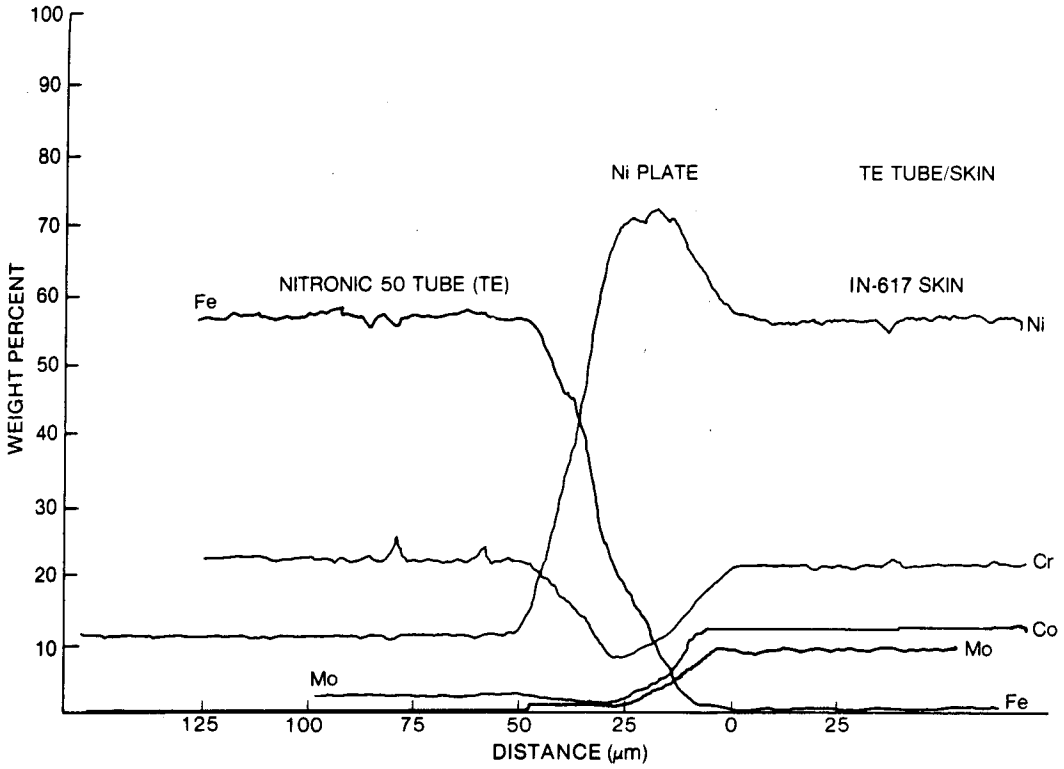

Figure 2-72. First-stage microprobe trace of trailing edge tube to skin bondline

Table 2-8

KNOOP MICROHARDNESS RESULTS

Bondline	Alloy	Hardness Number
IN617 Cladding-to-MZC Copper (with plating)	IN617 Ni Plate Ni Diffusion Zone MZC Copper	227, 218 106 115, 118 96, 95
IN617 Cladding-to-MZC Copper (no plating)	IN617 Bondline Precipitate MZC Copper	194 146 99
Nitronic 50 Tube-to-MZC Copper	Nitronic 50 Ni Diffusion Zone MZC Copper	242 186, 130 85, 89
Nitronic 50 Spar Rod-to-MZC Copper	Nitronic 50 Ni Diffusion Zone MZC Copper	213, 205 148 97, 91

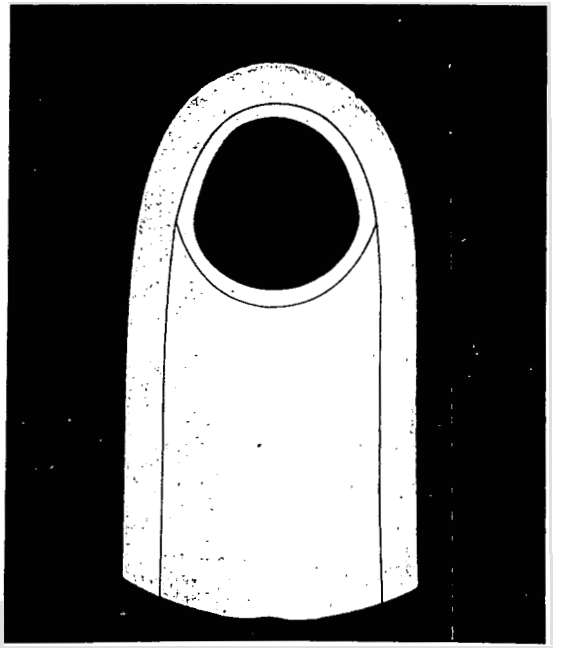

Figure 2-73. First-stage nozzle #3, Section 8, trailing edge tube deformation (magnification 9X)

ure 2-74) at the point of apparent maximum strain. Other less frequent and less severe occurrences of tube inner diameter cracking were also found. These appear to be a consequence of a carburizing HIP atmosphere. Alternate fabrication procedures applied to spare components have eliminated this processing problem.

- Surface cracking of the IN617 skin was noted in the nozzle airfoil fillet region, again as a result of the carburizing HIP atmosphere. The alternate fabrication procedures have demonstrated the elimination of this processing problem.
- There was no discernible difference between the microstructure of the various diffusion couples or the general condition of airfoil sections from nozzle #3 versus nozzle #1.

Metallographic examination of the sections taken from the outer endwall of nozzle #3 showed the following:

- None of the ultrasonic or visual indications could be identified in these cross sections.
- There was no indication of unbond between the various composite components, with the minor exception of the slight skin-to-endwall separation at the acute angle corners of the outer endwall.
- Significant bondline precipitation of a secondary phase occurred whenever Ni plate was minimal. This was especially pronounced at bondlines involving the consolidated powder metallurgy MZC copper alloy. This alloy itself contains, as a result of the higher Zr content, a eutectic grain boundary phase which is not present in the wrought product.

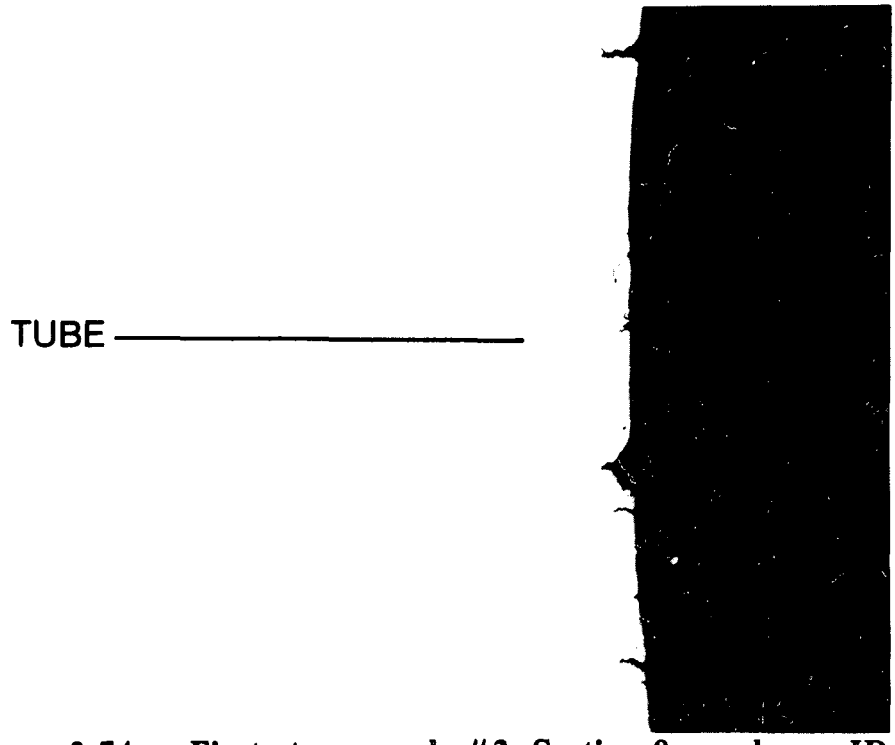

Figure 2-74. First-stage nozzle #3, Section 8, cracks on ID of N-50 tube at trailing edge (magnification 180X)

2.9 CONCLUSIONS

The major conclusion of the first-stage, water-cooled, composite nozzle testing is that the "Technology readiness"* of the nozzle design and fabrication has been demonstrated. After successful completion of steady-state, cyclic, and system fault condition tests for a total of 42 hours of fired testing at 2600 °F, and 617 thermal cycles, the following additional conclusions are drawn:

- Water cooling in conjunction with a composite structure is effective in maintaining desired nozzle metal temperatures in a high heat flux environment.
- Lack of test-related distress in the nozzles after completion of an extensive full scale test program demonstrates their mechanical resistance to low-cycle fatigue.
- Fabrication methods for constructing a composite first-stage nozzle were validated. No fabrication-related deficiencies were exposed during the tests, or during post-test inspections.
- The first-stage composite nozzle water cooling system is hydraulically well balanced. Measured flows through all portions of the nozzle cooling circuit meet design criteria.

* "Technology readiness" is defined as "that stage of system, subsystem, or component development where all major problems associated with the performance specification goals have been solved, and where the solutions to these problems have been demonstrated successfully. At that stage, no major risks remain for an agency or contractor in scaling up the technology (if full-scale demonstration has not been performed) and in proceeding with mission (or commercial) development of the system, subsystem, or component."

- Thermally, the nozzle design is limited by bulk boiling induced flow instability, rather than critical heat flux. However, it has been demonstrated that cooling water flow and cooling water inlet temperature can be adjusted to preclude operation at or near the bulk boiling regime.
- System fault condition testing has shown that a clear warning of the onset of unstable cooling conditions is provided by 60 to 120 psi oscillations of cooling water pressure in the return line. Such warning should ensure early diagnosis of cooling water problems in service.

A goal of the HTTT Program is to demonstrate the growth capability to 3000 °F firing temperature. Figure 2-28 shows a plot of critical nozzle temperatures as a function of firing temperature. Extrapolation of these results shows that, at 3000 °F firing temperature, water temperature remains less than saturated, average skin temperature is less than 1000 °F, and maximum copper temperature remains less than 800 °F. These temperatures show that the present design can survive at a 3000 °F firing temperature, and if required, cooler metal temperatures and an added margin to the onset of nucleate boiling can be obtained by reducing the coolant inlet temperature and/or by increasing the coolant flowrate. This extrapolation demonstrates that the required growth capability has been achieved.

Section 3

WATER-COOLED MONOMETALLIC NOZZLE TEST

3.1 OBJECTIVES

The primary objective of the HTTT water-cooled monometallic nozzle test was to verify that the design and fabrication of the TRV second-stage nozzle are adequate for satisfactory operation in the turbine environment. Secondary objectives were to accumulate data to develop an understanding of nozzle performance as a function of the various turbine system parameters, and to validate the nozzle design analysis.

Specifically, the test was designed to accomplish the following objectives:

- Demonstrate the cooling effectiveness of the water and the ability to maintain desired metal temperatures.
- Demonstrate that the thermal gradients and temperatures derived from measurements during cyclic testing fall within the bounds required to ensure the desired low-cycle fatigue (LCF) life in the TRV.
- Determine the sensitivity of the nozzle to changes in gas temperature and cooling water conditions.

3.2 TEST SPECIMEN DESCRIPTION

3.2.1 Specimen Construction

The second-stage nozzle (Figure 3-1) is a monometallic structure, cast from IN718. The endwalls have a conical shape forward and transition to a cylindrical shape aft. The airfoil has a linear twist which facilitates drilling of the airfoil cooling passages. The maximum gas-path height is 7.164 inches. The maximum airfoil chord at the pitch radius is 8.75 inches.

The cooling passages and manifolds were sealed with covers and plugs of IN718 sheet to form a cooling circuit. The covers and plugs are brazed into recesses machined into the nozzle. The braze material used was a gold-nickel-palladium alloy. Figure 3-2 shows the machined nozzle prior to brazing.

3.2.2 Specimen Cooling

The airfoil and endwalls of each nozzle are cooled by a two-pass flow network. Each pass is a parallel circuit, consisting of 10 to 20 passages. Cooling water enters each nozzle through a manifold on the trailing edge of the outer endwall. The cooling water then flows through the downstream half of the outer endwall, the airfoil trailing edge, the inner endwall, the airfoil leading edge, the upstream half of the outer endwall, and finally to a manifold on the leading edge of the outer endwall, where it exits the nozzle.

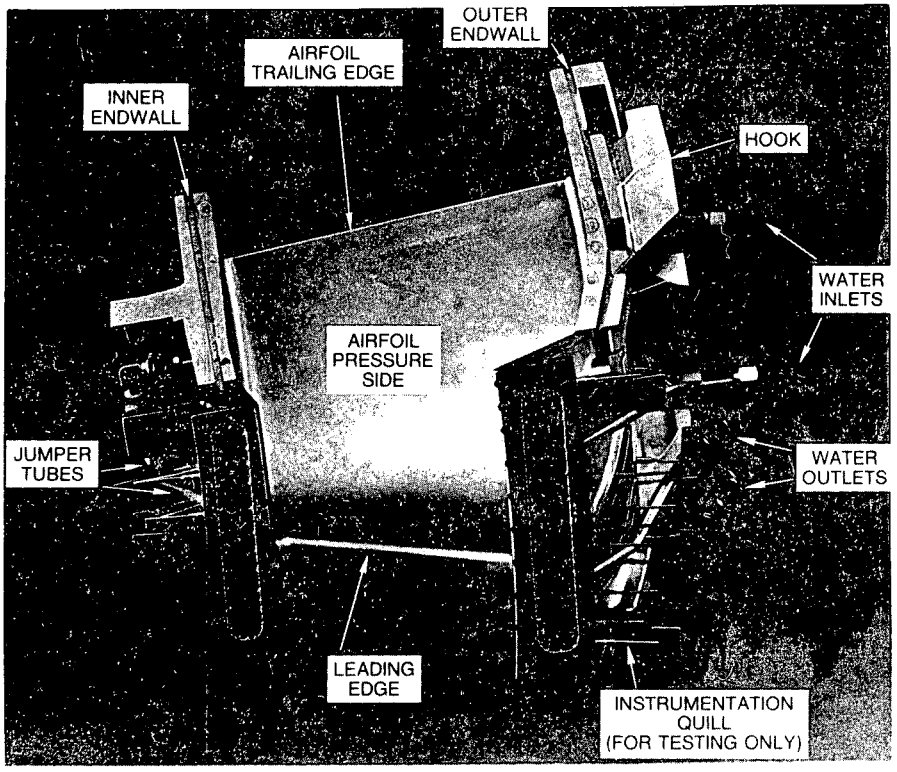

Figure 3-1. Second-stage nozzle

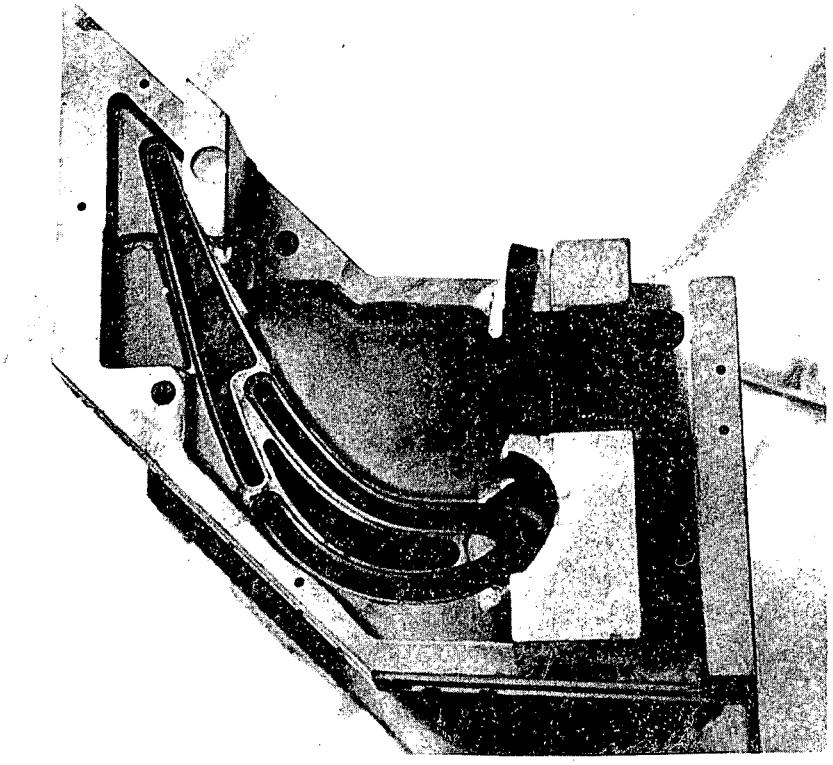

Figure 3-2. Machined second-stage nozzle prior to brazing

3.2.3 Pretest Inspection

To ensure maximum control of wall thicknesses, the majority of cooling passages in the second-stage nozzle were installed by shaped tube electrolytic machining (STEM). At the completion of drilling, the nozzles were both visually examined and x-rayed to ensure proper passage intersections and placements. All passage locations were verified and all passage intersections were determined to be within design requirements by airflow checking.

Ultrasonic inspection techniques were used to check cooling passage wall thicknesses. The two castings with the best airfoil cooling passage wall thickness readings were selected for testing and serialized in fabrication as #16 and #17. Refer to Section 3.8 for inspection details.

3.3 TEST ARRANGEMENT

3.3.1 Test Specimen Installation

The second-stage nozzle test assembly as installed in the HGPDTS is shown in Figure 3-3. The nozzle, gas-path dimensions, and cooling circuit are identical to the TRV second-stage nozzle. The major difference between the test nozzles and the ultimate TRV nozzles is in the machining of the test nozzle endwall hooks to accommodate the test stand mounting scheme.

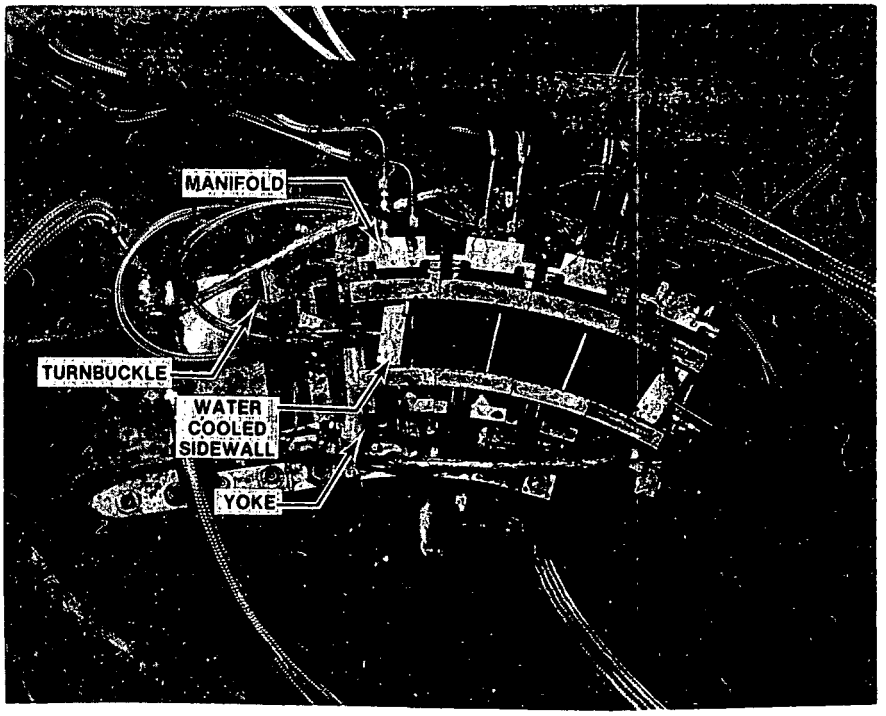

Figure 3-3. Second-stage nozzle cascade mounted on heat shield in test stand

The test configuration was a four-vane, three-throat cascade. In Figure 3-4 the cross hatching indicates the portions of the nozzles that were exposed to the hot gas stream. The two center nozzles in the cascade were the primary test nozzles. The test nozzles also carried the majority of the test instrumentation. The purpose of the end nozzles, also referred to as slave segments, was to contain the hot gas flow within the cascade. Cooling passages in the slave segments were only drilled adjacent to surfaces exposed to the hot gas. The slave segments carried only enough instrumentation to monitor them during the test. Copper water-cooled sidewalls were attached to the leading and trailing edges of the slave segments. The sidewalls help contain the hot gases within the cascade.

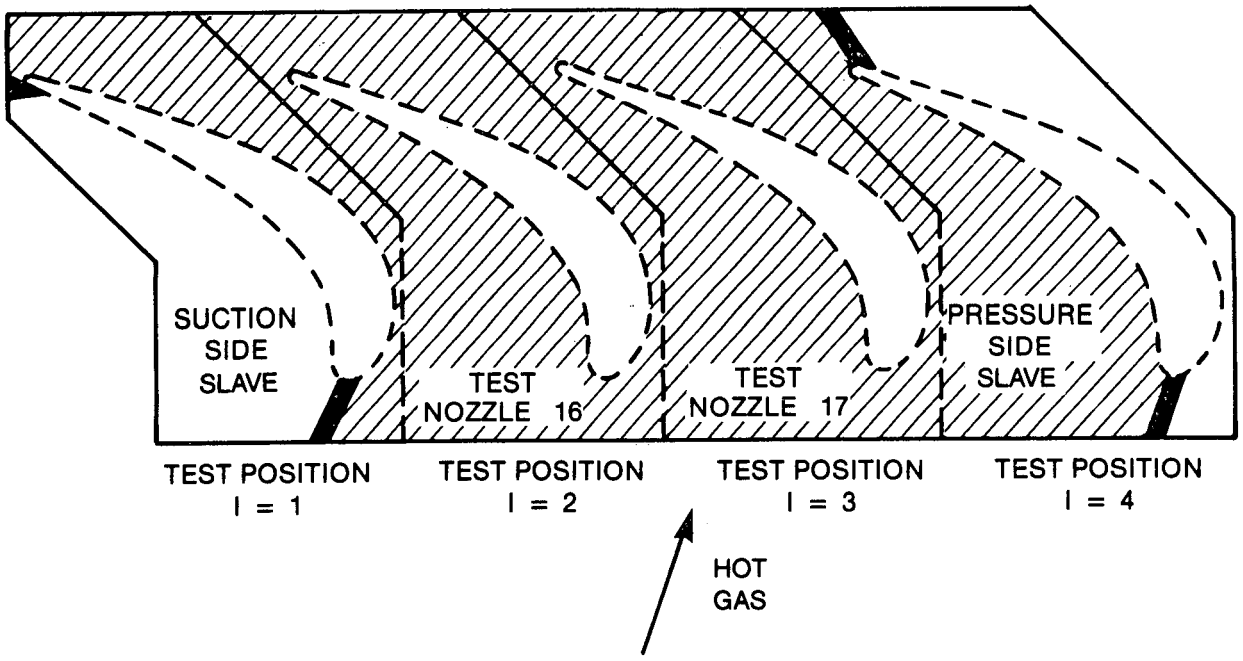

Figure 3-4. Second-stage nozzle assembly exposure to hot gas flow

The nozzle cascade was mounted on a water-cooled heat shield, which in turn was mounted to the test stand nozzle support plate. The heat shield is described in Part I* of this report. Figure 3-5 is a view of a slave segment mounted against the heat shield. The mounting arrangement and plumbing depicted were similar for the test nozzles. All segments were supported in the axial direction. A clamp at the outer endwall provided axial and radial support for the segment. Another clamp at the inner endwall provided only axial support. A manifold mounted on each nozzle distributed cooling water to the nozzles and to the copper sidewalls on the slave segments. Four nozzles were clamped together with a spring-loaded yoke. This yoke was attached to a turnbuckle which allowed adjustments of the circumferential position of the cascade and also transmitted the tangential aerodynamic load from the nozzles to the heat shield.

* Topical Report DOE/ET/10340-122, "Hot Gas Path Development Test – Part I (Facility Description)," August 1981.

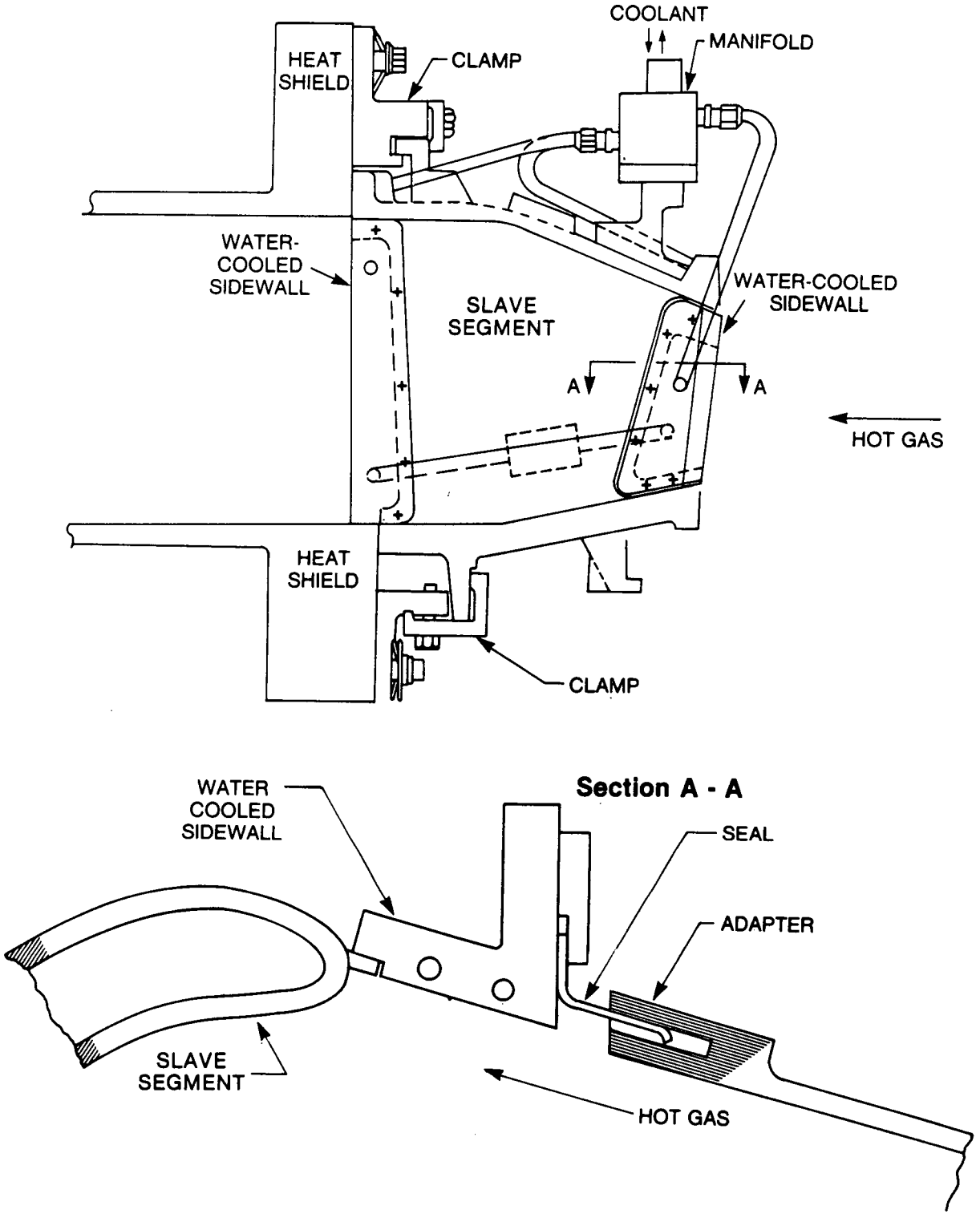

Figure 3-5. Second-stage nozzle slave segment mounting scheme

3.3.2 Combustion System

The combustion gas generator used for the test was a standard General Electric MS7000E turbine combustor. The combustor was coupled to an MS7000E transition piece. An adapter, bolted to the downstream end of the transition piece, was necessary to narrow the flow path to match the entrance to the nozzle cascade and to provide the proper gas entrance angle into the cascade. The seal configuration between the nozzle and the adapter is shown in Figure 3-5. The adapter was impingement cooled except for its downstream flange, which was film cooled. Impingement cooling was accomplished by supplying compressor discharge air to impingement shrouds which surrounded the adapter. The adapter, impingement shrouds, and transition piece are shown in Figure 3-6 mounted in the test stand upstream of the nozzle cascade. Cooling of the transition piece was accomplished by enclosing it in a plenum. The plenum, shown in Figure 3-7, creates the same airflow characteristics around the transition piece as would be experienced in the MS7000E turbine.

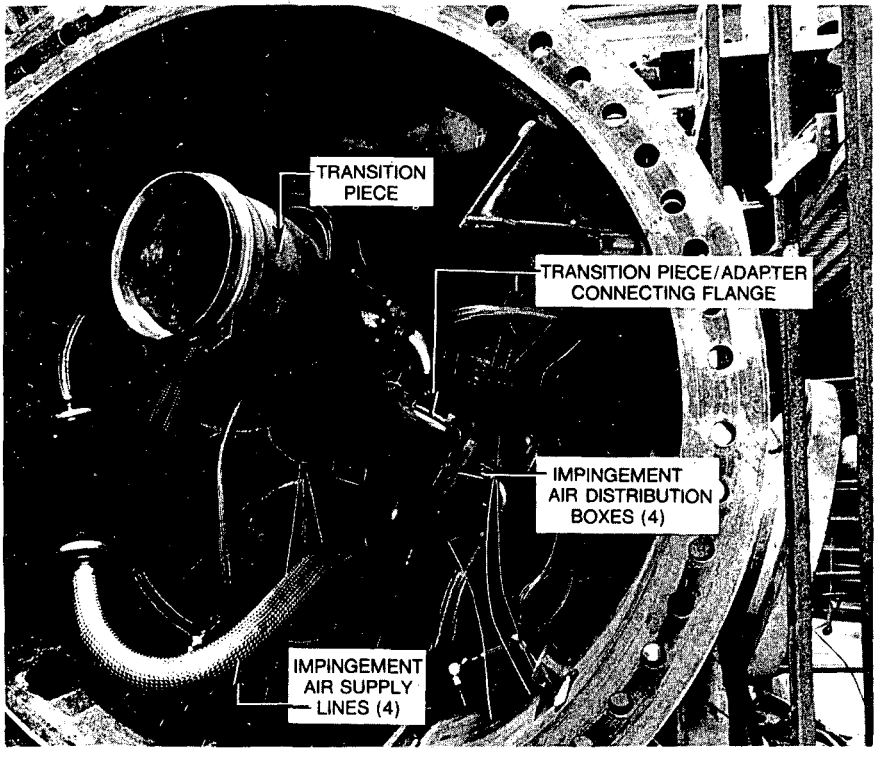

Figure 3-6. Second-stage nozzle test combustion transition piece and adapter

The test stand, ready for operation, is shown in Figure 3-8. The combustor casing and the compressor discharge air inlet are noted on the figure.

3.4 TEST SEQUENCE

Testing was performed in the following sequence:

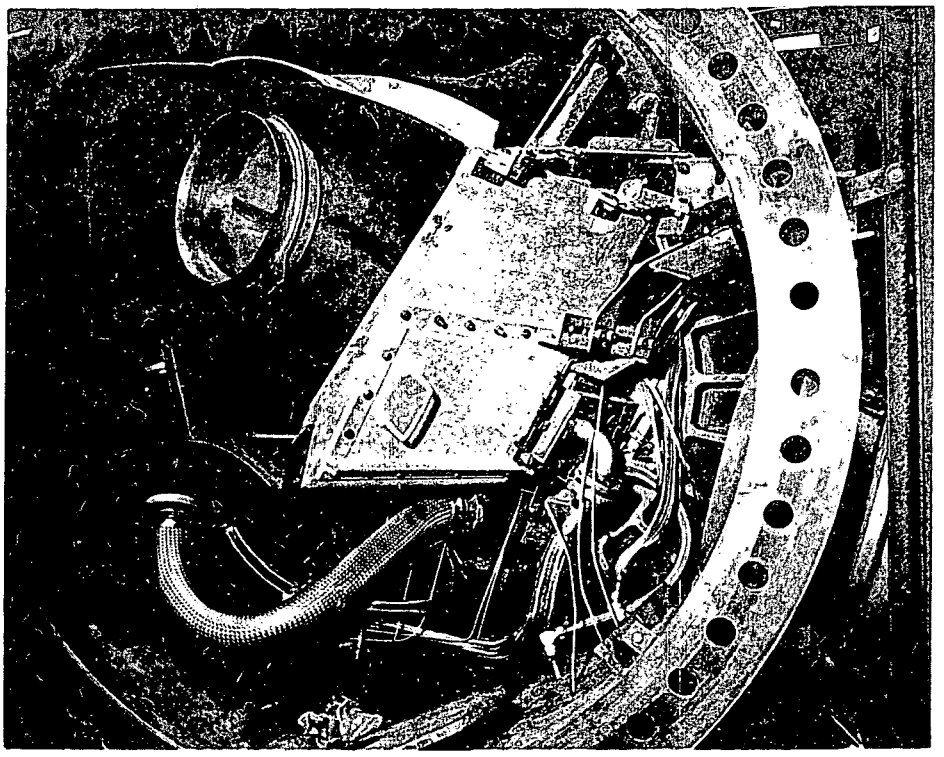

Figure 3-7. Second-stage nozzle test plenum

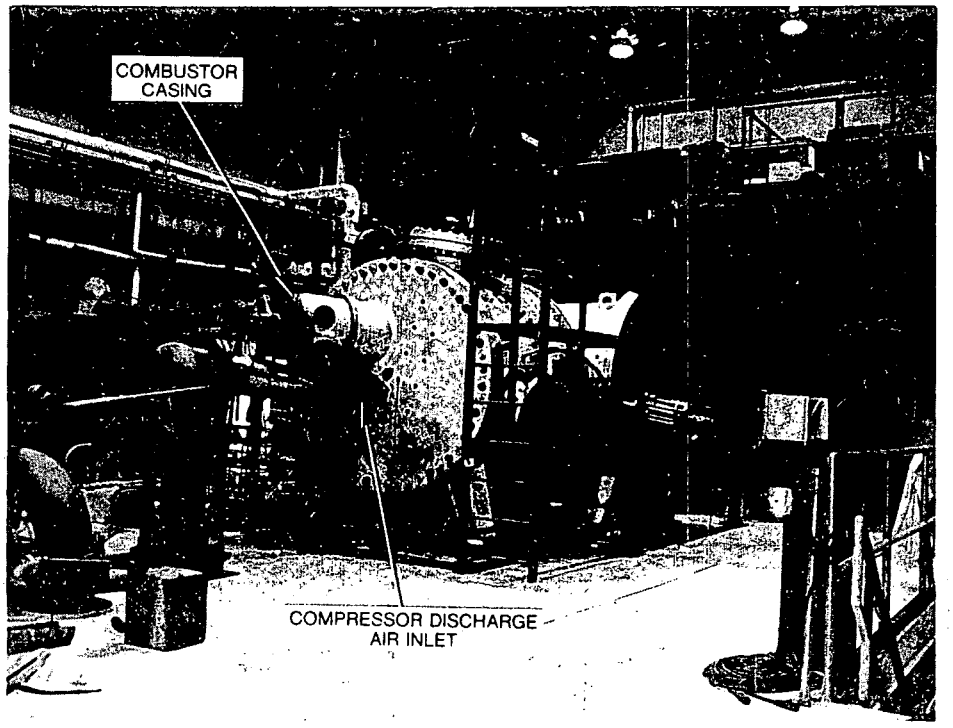

Figure 3-8. Hot-gas path development test stand assembled for the second-stage nozzle test

1. Calibration of instrumentation and checkout of the facility, test specimen, and procedures. This was accomplished by performing a cooling water flow test, a gas-path leakage test, and a hot air (unfired) flow test.
2. Fired testing at design point conditions, followed by parameter variation testing to determine the sensitivity of the test specimen to changes in inlet cooling water temperature, cooling water flow rate, gas temperature, and gas flow rate.
3. Cyclic testing to subject the test specimen to several hundred simulated turbine startup/shutdown cycles.
4. Simulated system fault testing by reducing cooling water flow rate increasing gas temperature and by a severe transient test in which the rate of change of gas temperature is three times as great as the normal startup/shutdown cycle.

3.5 INSTRUMENTATION

Instrumentation for the second-stage nozzle test was planned on the premise that a maximum of data would be obtained while maintaining structural integrity of the test nozzles.

3.5.1 Nozzle Cascade

The nozzle instrumentation consisted of thermocouples and pressure taps inserted into the manifolds and passages of the cooling circuit. Thermocouples were also located on the inner core metal surface and on the outer surfaces of the endwalls. Orifices at the inner endwall also allowed determination of the coolant flow distribution between the suction and pressure sides of the endwall. The locations of the thermocouples and pressure taps are shown in Figures 3-9, 3-10, and 3-11.

At the conclusion of the initial test series, a significant amount of confidence had been established in the durability of the nozzle. The most significant uncertainty remaining about nozzle performance was the gas-path surface temperature. At this point, gas-path surface temperature thermocouples were installed in one nozzle. Surface temperature thermocouples were installed on the suction and pressure sides of the airfoil (pitchline) and on the inner and outer endwalls of nozzle #17. The locations of the surface temperature thermocouples are indicated in Figure 3-12.

The surface temperature thermocouples were embedded in a nugget of high-conductivity alloy near the gas-path surface. Analysis showed that the nugget would attain a temperature very close to the average surface temperature between cooling holes.

Cooling water flow entering each nozzle was measured with a turbine flow meter. Water exiting the nozzle was measured with an orifice and ΔP transducer calibrated against its corresponding turbine flow meter. Loss of coolant flow from any of the nozzles could be determined by comparing inlet and outlet flows. Inlet and outlet flows were continuously monitored throughout the test as an indicator of leakage in the test nozzle.

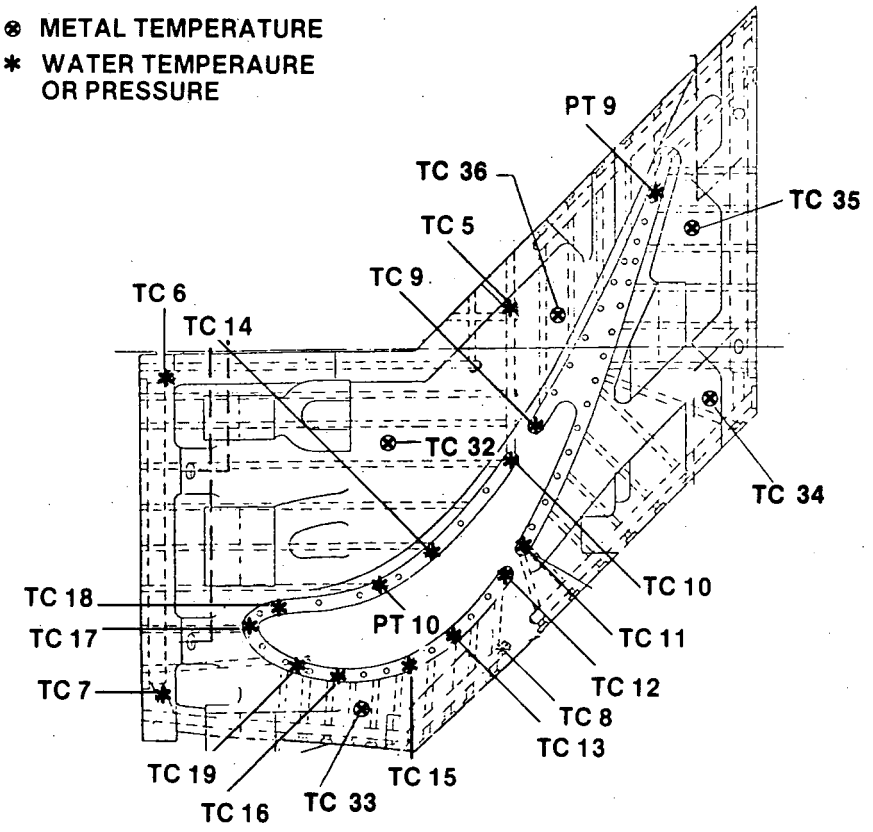

Figure 3-9. Second-stage nozzle outer endwall instrumentation

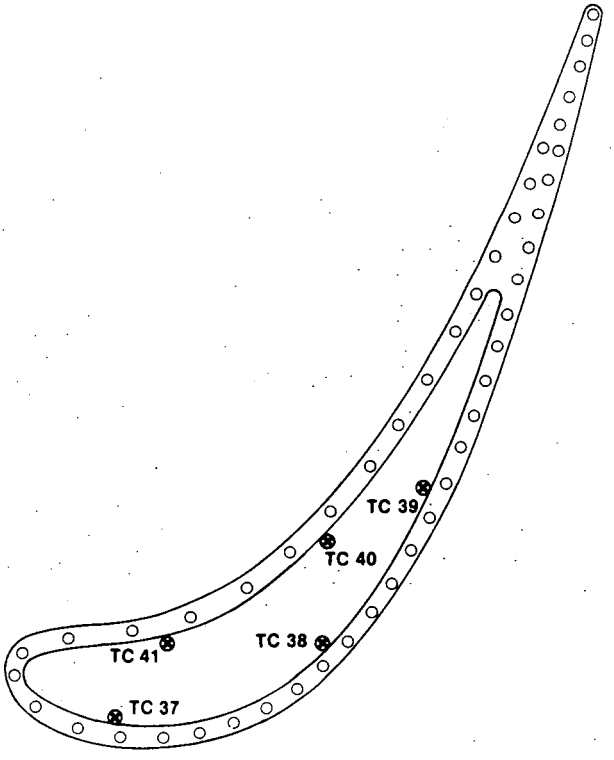

Figure 3-10. Second-stage nozzle pitch airfoil core thermocouples

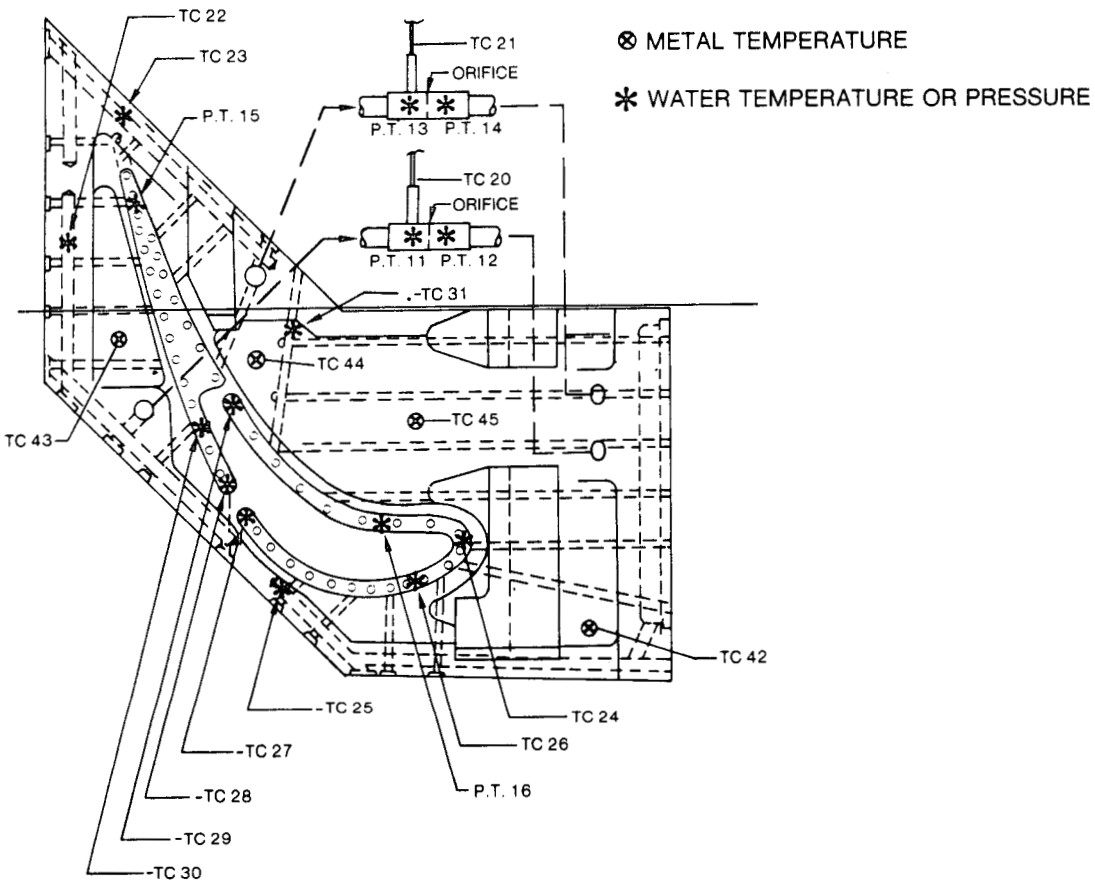

Figure 3-11. Second-stage nozzle inner endwall instrumentation

3.5.2 Combustion System

A five-by-five matrix of thermocouples was located on rakes in the flow path adapter, just upstream of the nozzle. The rake thermocouples were used to determine the average gas temperature and gas temperature profile entering the nozzle. Five control thermocouples in the transition piece were also used to measure the gas temperature. The control thermocouples were calibrated against the average temperature measured by the rake thermocouples. During fired testing, average gas temperature was set with reference to the control thermocouples. The rake thermocouples were removed from the test installation once the combustion pattern factor had been determined and the control thermocouples had been calibrated.

The average gas temperature at the inlet to the nozzle cascade was determined by applying corrections to the rake and control thermocouple readings to account for the cooling of the gas stream by air leakage at the adapter-nozzle interface, and by the loss of heat from the thermocouples to the cooler adapter walls by thermal radiation. The leakage included the flange film cooling air and the thermocouple cooling air.

Total and static pressure probes were installed in the gas stream ahead of the nozzle. A static pressure probe was located downstream of the nozzles.

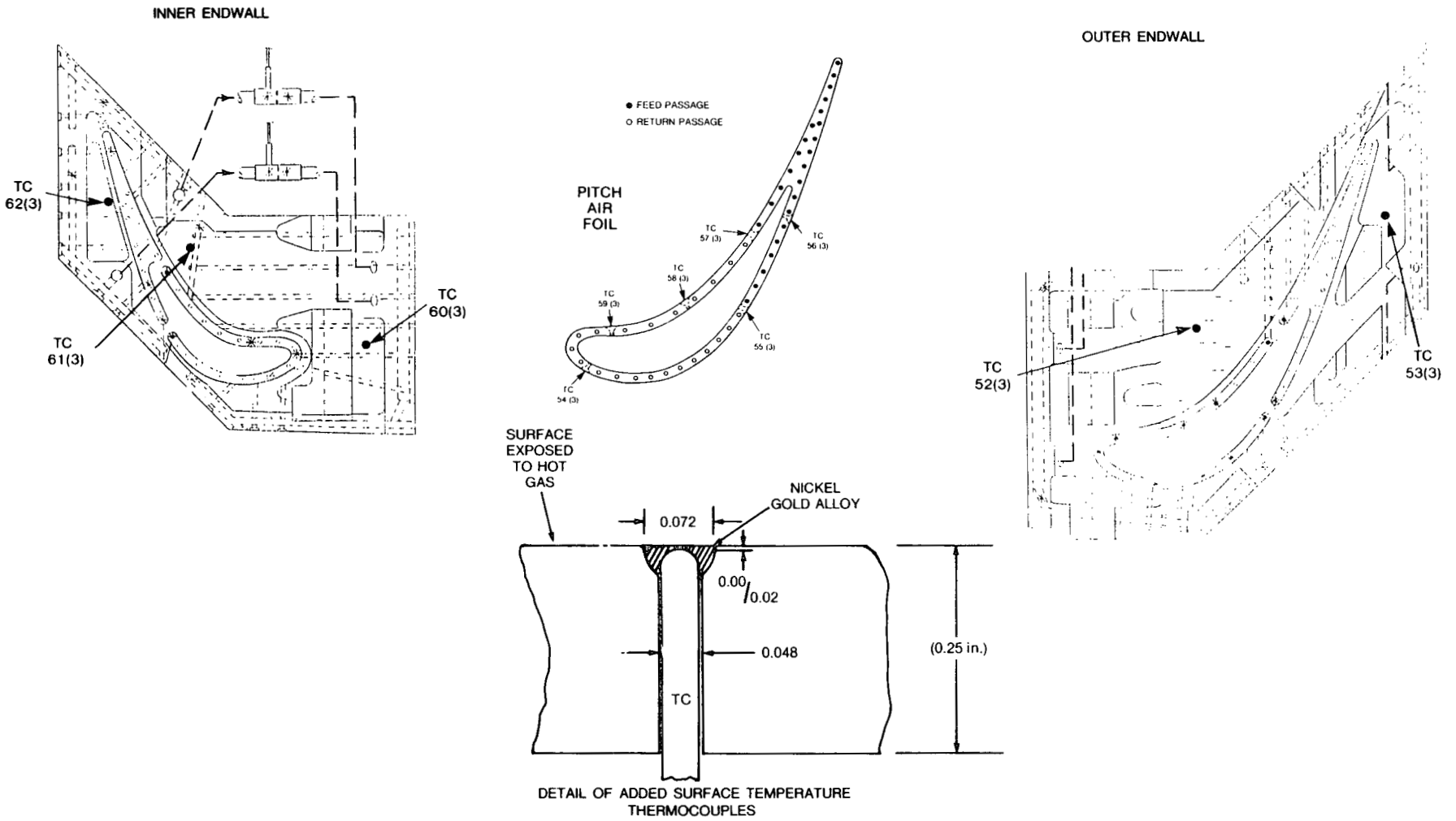

Figure 3-12. Second-stage nozzle surface thermocouple locations

3.5.3 Special Instrumentation

An infrared pyrometer was installed downstream of the nozzle assembly in the mixing chamber of the HGPDTS, focused on the trailing edge portion of the suction side of the test nozzle airfoils. The pyrometer was able to scan the entire gas-path height and measure the surface temperature of the airfoil. This non-contact instrument allowed temperature measurements of the airfoil to be made without disturbing the gas flow over the airfoil. Details of its design, construction, and calibration are found in Appendix A.

Instrumentation from the nozzle and test support hardware was monitored by a computer which organized the data into displays and calculated nozzle performance. The computer accomplished a complete scan of the instrumentation every thirty seconds. The computer was also programmed to trip the test, by an instantaneous shutoff of the fuel flow to the combustor, if an out-of-limits condition was detected. Trips were set on low coolant flow and pressure, high coolant temperature, and excessive combustion gas temperature.

3.5.4 Measurement Errors

Primary measurements made during the testing were water and gas pressure, temperature and flow, and metal temperature. An estimation of measurement errors is required to put the data in perspective and to complete documentation of the testing. The following are estimates of the differences between the true values and the recorded values:

Water temperature	±4°F
pressure	±3 psi
flow	±.01 pps
Gas temperature	±50°F
pressure	±2 psi
flow	±1 pps
Metal temperature	±4°F (See Appendix A for discussion of pyrometer measurement errors)

The summation of these errors does not compromise the verification of design procedures or the demonstration of technology readiness.

3.6 DATA REDUCTION PROCEDURE

The objectives of the data reduction procedure included documenting all important test parameters, monitoring test variables during the test, expediting the calculations which had to be made during testing, and making the information readily available in a functional format.

The data reduction procedure prints out or displays the

- Critical parameters
- Water properties
- Air/fuel properties

- Aerodynamics
- Thermal/hydraulic
- Nozzle flow/heat splits
- Test nozzle metal temperatures
- Slave segment metal temperatures
- Heat shield monitor
- Combustor performance data
- Liner and transition piece metal temperatures

Many of these information groups were available for immediate display on a screen for continuous monitoring as required. The procedure used to develop the aerothermal data is described in Section 2.6.

3.7 TESTING

3.7.1 Cooling Water Flow Test

3.7.1.1 Test Description

The cooling water flow test was run to accomplish the following:

- Determine if the flow distribution to the nozzles and water-cooled sidewalls is satisfactory.
- Investigate the pressure distribution within the nozzle cooling circuit.
- Establish the effect of water flow rate and water temperature on the static pressure drop across the nozzle cooling circuit.
- Ensure that the water temperature thermocouples are functional.
- Calibrate the orifices and ΔP transducers measuring the flow exiting the nozzles.
- Determine if leaks are present in the as-installed configuration.

All of the nozzle pressure taps were scanned at each test point to determine the pressure distribution in the cooling circuits. All of the water temperature thermocouples were scanned at each test point. The rate of cooling water loss from the high-pressure water system was measured at the 1263 psig test point to serve as a pretest base leakage rate.

The combinations of water inlet temperatures, flow rates, and pressures that were run are shown in Table 3-1.

3.7.1.2 Test Results

The results of the cooling water flow test indicated that the pressure distribution within the test nozzle cooling circuit was reasonably close to what had been predicted by analysis. It was also determined that the flow splits between the slave segments and the water-cooled sidewalls were adequate to cool both components. Figure 3-13 depicts the flow division of the nozzle cooling circuit. Table 3-2 compares the predicted and measured pressure drops through portions of the test nozzle's cooling circuit at design flow rate.

Table 3-1

COOLING WATER TEST CONDITIONS

Inlet Water Temp (°F)	Inlet Water Pressure (psig)	Water Flow Rate (lb/sec)			
		Slave Segment Position 1	Test Noz. #16 Position 2	Test Noz. #17 Position 3	Slave Segment Position 4
99	454	0.31	0.44	0.44	0.32
202	459	0.33	0.47	0.46	0.33
305	462	0.34	0.48	0.48	0.35
93	456	0.44	0.62	0.62	0.45
205	461	0.46	0.64	0.64	0.46
321	458	0.49	0.66	0.67	0.49
299	458	0.48	0.66	0.66	0.47
301	461	0.62	0.77	0.78	0.63
298	1263	0.49	0.65	0.65	0.48

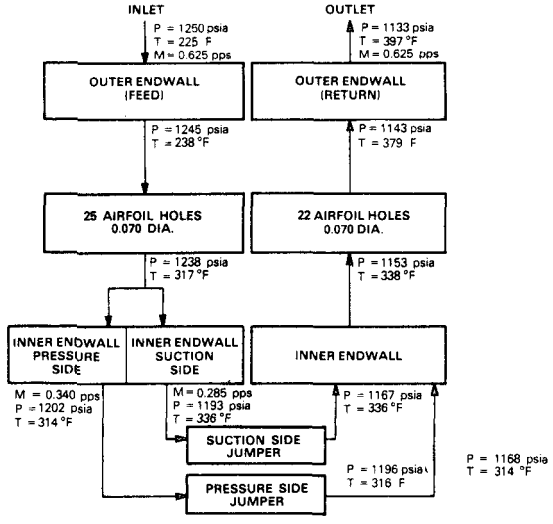

Figure 3-13. Second-stage nozzle test cooling circuit

Table 3-2

COMPARISON OF MEASURED AND PREDICTED PRESSURE DROPS IN SECOND-STAGE NOZZLE COOLING WATER CIRCUIT

Location	ΔP Measured	ΔP Predicted
Airfoil Feed Holes	6	7
Internal	99	102
Airfoil Return Holes	11	10

Figure 3-14 presents the variation in nozzle cooling circuit pressure drop as a function of mass flow rate. The data plots linearly on a log-log scale with a slope of two. This reflects the theoretically predicted pressure variation, i.e., proportional to mass flow rate squared.

The total nozzle cooling system leakage rate measured at design pressure, and prior to fired testing, was 0.0007 lb/sec. This leakage was insignificant and confined to fittings rather than the nozzles.

3.7.2 Gas-Path Leakage Test

3.7.2.1 Test Description

The gas-path leakage test was performed to determine the effective area of leaks that would introduce compressor discharge air into the gas path downstream of the thermocouple rakes. The test was conducted by sealing off the entrance to the transition piece and leaving the nozzle exit open to atmospheric pressure. The pressure in the combustion section of the test stand was controlled and the air mass flow rate into the stand was measured for each pressure ratio. An effective area was calculated. Known leakage areas which allowed air to flow into the gas path upstream of the rakes were subtracted from the calculated area. The remainder was the leakage area that permitted reduction of the average gas temperature downstream of the thermocouple rake.

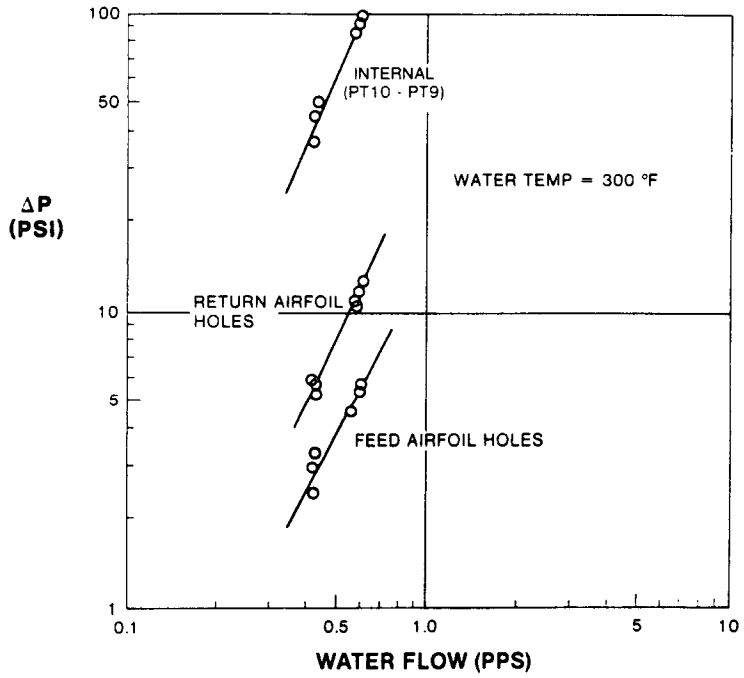

Figure 3-14. Second-stage nozzle test Position 3 cooling circuit pressure drop vs flow

The gas-path leakage test was repeated prior to the extended test series, because the test nozzles were removed from the test stand for inspection after the initial test series and there was the potential for some change in the gas-path leakage area. The

removal of the air-cooled thermocouple rakes after the initial test series also reduced the gas-path leakage area.

3.7.2.2 Test Results

Table 3-3 presents the results of the initial gas-path leakage test.

The total effective leakage area ($A_L C_q$) was determined from the test data and the isentropic flow gas tables by the application of Equation (1). The 3.49-square inch effective area calculated from Test Point (e) was chosen as the most accurate value of the leakage area, since this point was closest to a choked pressure ratio. At choked flow, the assumption of throat static pressure being equal to atmospheric pressure is most accurate. The calculated effective area of gas-path leaks upstream of the thermocouple rakes was determined to be 1.44-square inches. This was subtracted from the experimentally determined total leakage area to obtain the leakage area downstream of the rakes (2.05-square inches). This is the leakage area used in correcting average gas temperature as measured by the rakes.

Table 3-4 presents the results of the gas-path leakage test subsequent to removal of the air-cooled thermocouple rakes.

The lower calculated leakage area relative to Table 3-3 reflects the removal of the thermocouple rakes. The rakes contained approximately a 0.30-square inch leakage area for cooling.

Table 3-3

SECOND-STAGE NOZZLE GAS-PATH LEAKAGE TEST RESULTS

Test Point	W_{IN} (lb/sec)	T_{IN} (°R)	P_T (psia)	P_T/P_{CHAM}	$A_L C_q$ [(1)] (in.^{2})
a.	0.53	634	15.65	1.07	3.22
b.	0.95	634	17.51	1.19	3.42
c.	1.28	640	19.78	1.35	3.48
d.	1.69	656	24.02	1.63	3.47
e.	1.88	656	26.05	1.77	3.49

(1) $$A_L C_q = \frac{(W_{IN}\sqrt{T_{IN}}/P_T)}{(W_{IN}\sqrt{T_{IN}}/P_T A_L C_q)}$$

NOTES: 1. Numerator from Test Data
2. Denominator from Isentropic Flow Tables

3.7.3 Hot Air Flow Test

3.7.3.1 Test Description

The heat flux experienced by the nozzles during fired testing is dependent upon the aerodynamic flow conditions in the nozzle gas path. A hot air flow test was run to establish the aerodynamic characteristics of the nozzle cascade.

Table 3-4

SECOND-STAGE NOZZLE GAS-PATH
LEAKAGE TEST RESULTS
WITH THERMOCOUPLE RAKES REMOVED

Test Point	W_{IN} (lb/sec)	T_{IN} (°R)	P_T (psia)	P_T/P_{CHAM}	$A_L C_q$ (in.^{2})
a.	1.16	568	19.2	1.31	2.89
b.	1.49	572	22.1	1.51	3.19
c.	2.15	588	31.6	2.15	3.19

The objectives of the hot air flow test were to:

- Checkout the facility under full pressure loading at elevated temperatures (600 °F).
- Checkout the instrumentation and data acquisition system.
- Checkout the on-line data reduction procedure.
- Determine the flow function versus nozzle pressure ratio curve over the operating pressure ratio range.

The hot air tests were conducted with hardware assembled and ready for fired testing with the exception of the fuel line attachment. The full data reduction procedure was activated during this test. In order to establish different pressure ratios across the nozzle throats, the airflow and nozzle upstream total pressures were varied. Water flow rates were set at nominal values. Water inlet temperature was varied between 225 °F and 350 °F. The upper bound on airflow was limited by the pressure drop across the combustion liner.

These experimentally determined points are summarized in Table 3-5. The discharge coefficient for the cascade was determined from this data.

Table 3-5

RESULTS OF SECOND-STAGE NOZZLE HOT AIR FLOW TEST

W_{IN} (lb/sec)	T_{IN} (°R)	P_T (psia)	P_T/P_{CHAM}	A^*C_q (in.^{2})
9.29	1022	77.92	1.05	17.32
25.42	1040	77.29	1.18	27.19
35.19	1047	79.29	1.42	29.31
38.93	1023	78.62	1.88	29.77
35.86	1021	78.98	1.46	29.02

3.7.3.2 Test Results

Table 3-5 presents the results of the hot air flow test. The effective throat area

(A^*C_q) of the nozzle test assembly was calculated in the same fashion as in the gas-path leakage test. The effective throat area of the nozzle test assembly, at a pressure ratio approaching the choked pressure ratio, is 29.77 square inches. The nozzle area was physically measured to be 31.65-square inches. This results in a discharge flow coefficient, C_q = 0.94, which is reasonable for this test arrangement.

3.7.4 Initial Steady-State Test

3.7.4.1 Test Description

Fired testing was conducted by approaching the nozzle design conditions in a series of test points that increased the heat flux in relatively equal steps. This was accomplished by simultaneously increasing gas temperature and mass flow rate and decreasing cooling water temperature. Instrumentation data scans were evaluated at each test point before moving on to the next point. Steady-state operation at the conditions corresponding to a 2600 °F turbine firing temperature was maintained for four hours to ensure that no thermal instabilities developed. A 2600 °F turbine firing temperature corresponds to an average gas temperature of 2082 °F at the inlet of the second-stage nozzle. The test points used in approaching the design conditions are given in Table 3-6. Combustor emission data was taken for Test Points 1 through 5. Testing

Table 3-6

SECOND-STAGE NOZZLE INITIAL FIRED TEST CONDITIONS

Test Point	Remarks	Average Gas Temperature (°F)		Gas Flow (pps)		Nozzle Inlet Water Temperature (°F)	Heat Load Per Nozzle (Btu/sec)
		Measured	Corrected	Measured	Corrected		
1	Advancing	1273	1187	9.2	8.5	290	21
2	to	1590	1505	16.3	15.5	242	47
3	Design	1844	1844	20.9	20.1	172	77
4	Point	2096	2102	24.8	24.0	152	102
5*	↓	2097	2102	24.8	24.0	223	100

*Approximate design point

was interrupted at the completion of Test Point 5 for an in-place visual examination of the nozzles. Nozzle #17, installed in position #3, was used to acquire thermal data and will be referred to as the test nozzle.

After accumulating four hours at the design point, parameter variation testing was conducted. This portion of the test was designed to evaluate the nozzles' sensitivity to individual changes in the test parameters. The parameters that were varied were cooling water temperature and flow rate, hot gas temperature and mass flow rate. The test points that were run during parameter variation testing are given in Table 3-8 of Section 3.7.4.2. An in-place visual examination of the nozzles was again performed at the completion of Test Point 15, prior to initial cyclic testing.

3.7.4.2 Test Results

The test points set for the initial approach to steady-state design conditions are shown in Table 3-6. At Test Point 3, the temperature correction for gas-path leakage is equal to the correction for thermocouple radiation.

The peak and average gas temperature profiles measured at the thermocouple rakes for the design condition (Test Point 5) are presented in Figure 3-15. The profiles reflect the thermocouple radiation correction, but not the air leakage correction. The pattern factor, as defined by Equation (2), was 0.03.

$$PF = \frac{T_{PITCH} - \bar{T}}{\bar{T} - T_{CD}} \tag{2}$$

The measured gas temperature profile was flatter than the design profile, which assumed a pattern factor of 0.15. This was taken into account when comparing measured data with the design analysis. The procedure for correcting the gas temperatures was verified by measuring concentrations of O_2 in the exhaust gas for Test Points 1 through 5. The NASA equilibrium computer program† was used to convert the O_2 concentrations into corresponding gas temperatures. Temperatures determined by emissions measurement corresponded well with the measured and radiation corrected temperatures.

Metal temperature data at the design point are compared with predicted values in Table 3-7.

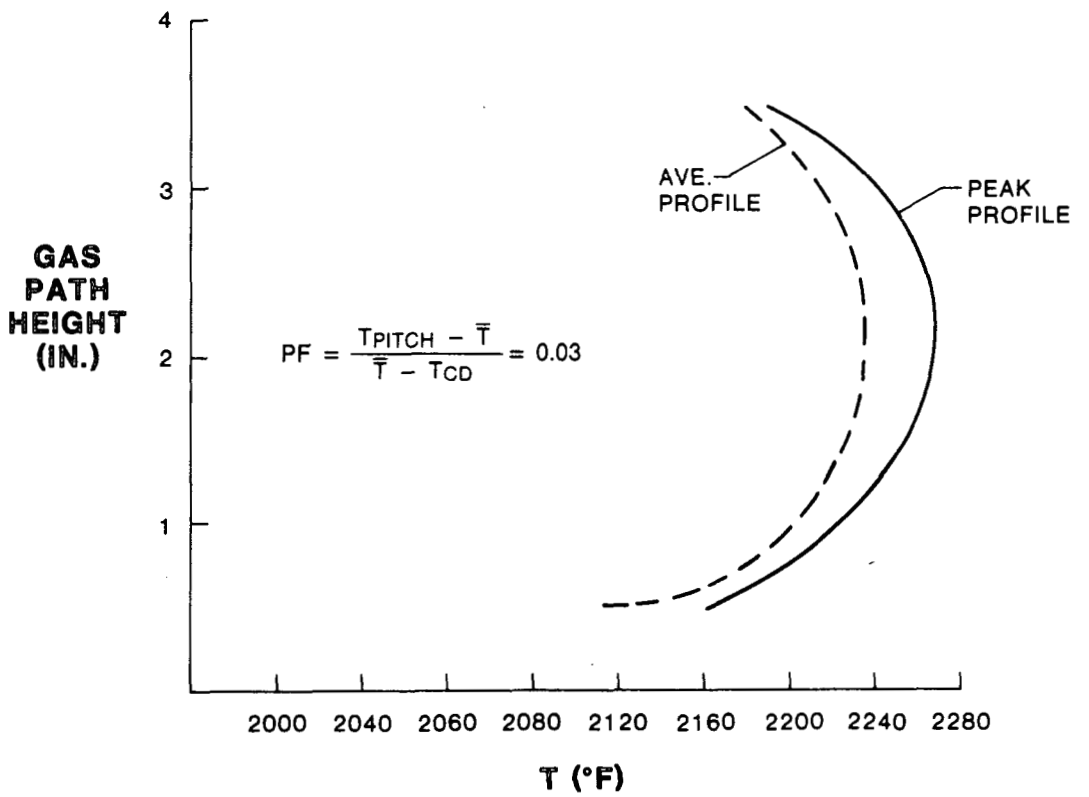

Figure 3-15. Second-stage nozzle test gas temperature profile

† NASA Mass Equilibrium Program (NASA SP-273)

Table 3-7

COMPARISON OF MEASURED AND CALCULATED TEMPERATURES – SECOND-STAGE NOZZLE

Location	Measured Temperature (°F)	Calculated Temperature (°F)
Airfoil Suction Surface Pyrometer Measurement		
Trailing Edge (TE)	700	680
2 inches forward of TE	690	815
Core		
TC 37	462	507
TC 38	444	455
TC 39	477	469
TC 40	585	524
TC 41	555	567
Outer Endwall		
TC 32	586	602
TC 34	537	459
TC 35	405	375

Generally, good correlation was obtained between the measured temperature data and the design analysis. Overall nozzle heat load, obtained from the total coolant temperature rise was within 2% of the predicted value. However, the water temperature rise in some individual cooling passages of the nozzle cooling network differed from the design analysis. One possible reason for this discrepancy is that the gas-path leakage did not mix thoroughly with the hot gas flow, thereby altering the temperature profile downstream of the rakes. Another explanation is that the actual gas heat transfer coefficient distribution may also have differed from the predicted distribution.

The airfoil surface temperature, as measured by the infrared pyrometer, corresponded well with the predicted temperature at the trailing edge, but differed substantially upstream of the trailing edge.

The test points set for parameter variation testing are shown in Table 3-8.

Figures 3-16 through 3-19 show the heat load for one nozzle as a function of each of the test variables. As expected, heat load is a strong function of gas temperature. The variation of heat load with gas mass flow rate is also significant, since the convective heat transfer coefficients are a function of mass flow rate. The variation of heat load with water flow rate is minimal, since the water cooling passage interface is the smallest portion of the total thermal resistance between the hot-gas-path and the coolant. For a constant gas temperature, heat load varied linearly with the water temperature.

Table 3-8

SECOND-STAGE NOZZLE PARAMETER VARIATION TEST CONDITIONS

Test Point	Remarks	Average Gas Temperature (°F)		Gas Flow (pps)		Nozzle Inlet Water Temperature (°F)	Nozzle Water Flow Rate (pps)
		Measured	Corrected[1]	Measured	Corrected[2]		
6	Coolant	2092	2094	24.6	23.8	153	0.63
7	Temp.	2087	2094	24.6	23.8	187	0.63
8	Variation	2098	2105	24.9	24.1	223	0.63
9	Coolant	2097	2100	24.8	24.0	223	0.55
10	Flow Variation	2097	2100	24.8	24.0	223	0.48
11	Gas Temp.	1701	1684	24.5	23.7	223	0.63
12	Variation	1904	1909	24.7	23.9	223	0.63
13	Gas Mass Flow	2081	2094	21.3	20.5	223	0.63
14	Rate	2087	2115	17.9	17.1	223	0.63
15	Variation	2087	2100	15.0	14.2	223	0.63

[1] Corrected for radiation and leakage
[2] Corrected for test stand leakage

Figure 3-20 shows the water temperature rise in each portion of the nozzle cooling circuit as a function of heat load. Heat load was controlled by changing gas temperature and gas flow rate. The variation of metal temperature in the airfoil core and on the outer surfaces of the endwalls as a function of heat load is shown in Figures 3-21 and 3-22. For these plots, gas temperature and flow rate were changed individually.

A phenomena observed in the inner endwall of nozzle #16 (Test Position 2) is displayed in Figure 3-23. Thermocouple 31 measured water temperature at the intersection of two cooling holes. A rapid rise in water temperature measured by this thermocouple was noted as total nozzle heat load increased at low values of heat load. At

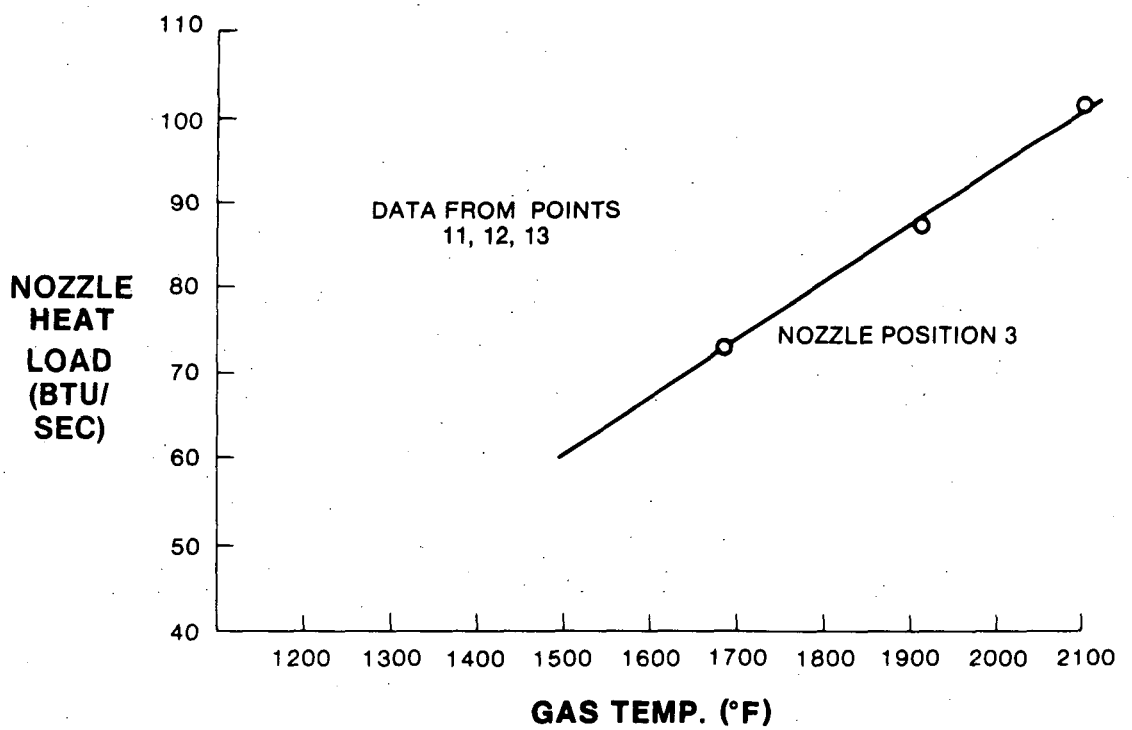

Figure 3-16. Second-stage nozzle heat load vs gas temperature

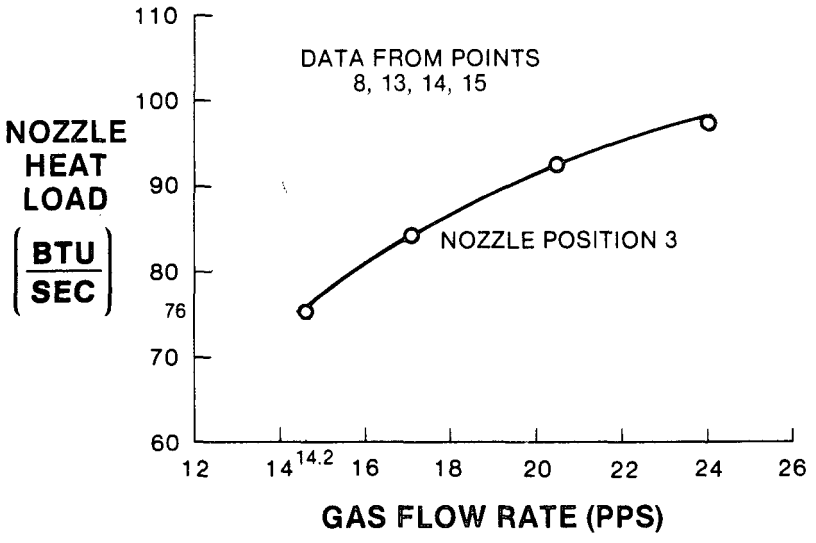

Figure 3-17. Second-stage nozzle heat load vs gas flow rate

higher values of total heat load, there was little change in measured water temperature with heat load. The phenomena was repetitive in nozzle #16 but was not duplicated in nozzle #17 (Test Position 3). Since water temperature leveled off near the saturation temperature of 572 °F for the 1250 psia cooling circuit inlet pressure, the phenomena was attributed to localized boiling at the cooling hole intersection. Water temperature did not rise because there was a continuous supply of water which could be vaporized at the boiling site. The phenomena remained localized throughout the test and did not adversely affect the overall nozzle performance.

The water-cooled monometallic nozzles completed the initial steady-state test series without any visible signs of distress. Details of the in-place inspection are found in Section 3.8.2.

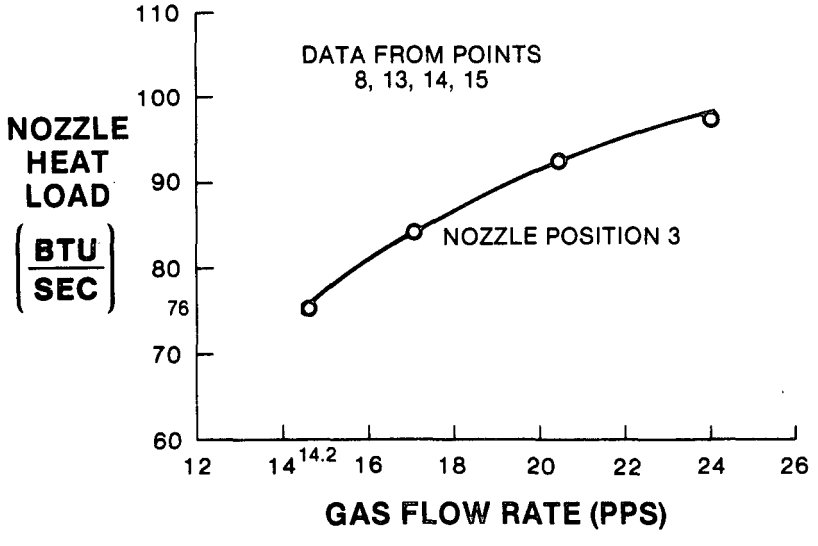

Figure 3-18. Second-stage nozzle heat load vs water flow rate

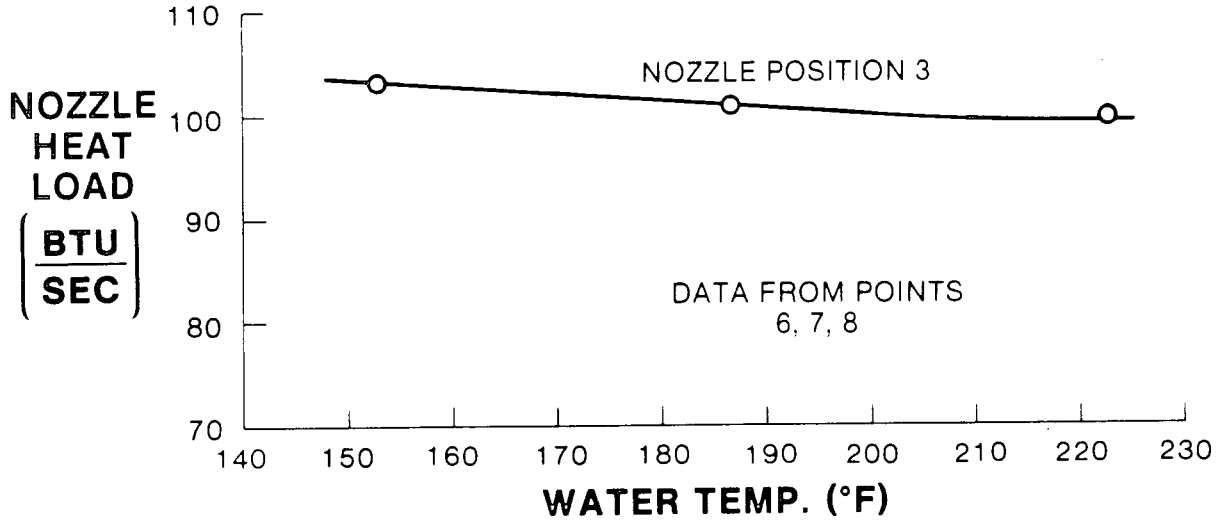

Figure 3-19. Second-stage nozzle heat load vs water temperature

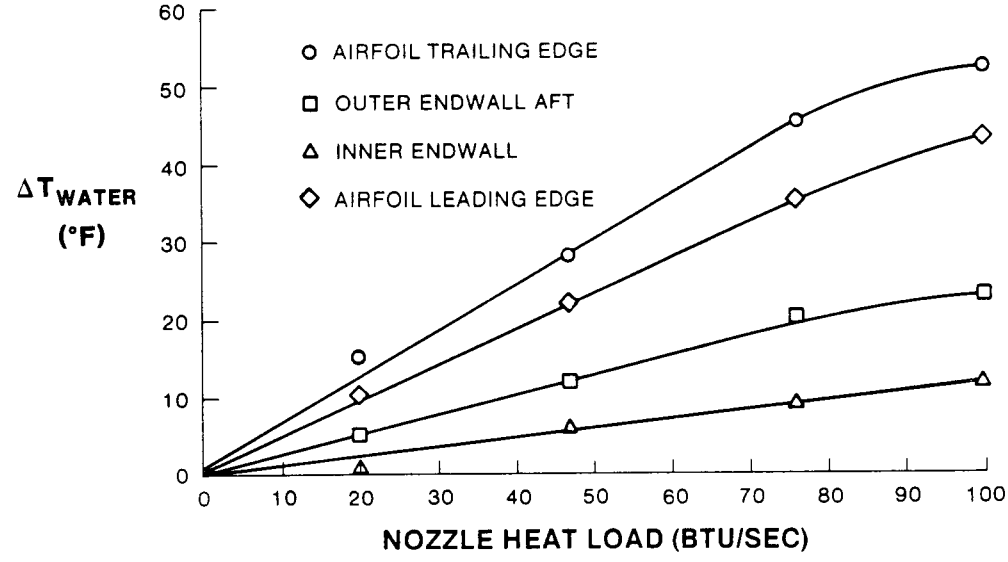

Figure 3-20. Second-stage nozzle water temperature rise vs heat load

3.7.5 Initial Cyclic Test

3.7.5.1 Test Description

The simulated turbine startup/shutdown sequence used is shown in Figure 3-24. All the major events in the actual startup/shutdown sequence are represented in the cycle. However, the change of gas temperature and flow rate with time was linearized for operational simplification. Each cycle included three minutes of steady-state operation at the design operating point.

3.7.5.2 Test Results

In an air-cooled nozzle, fatigue life is a strong function of response to transient conditions. Figure 3-25 shows a pyrometer trace of the temperature response of the

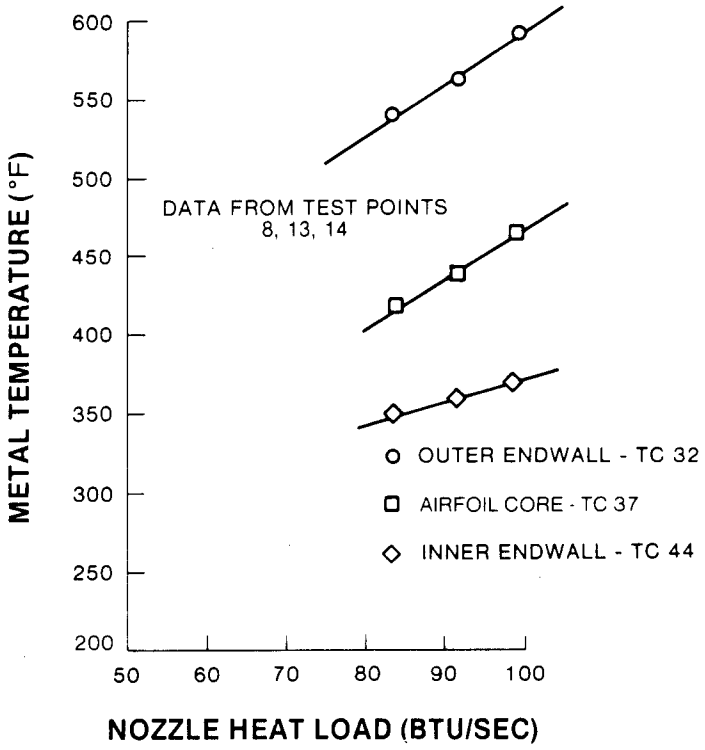

Figure 3-21. Second-stage nozzle metal temperature vs heat load (gas temperature constant, gas mass flow varied)

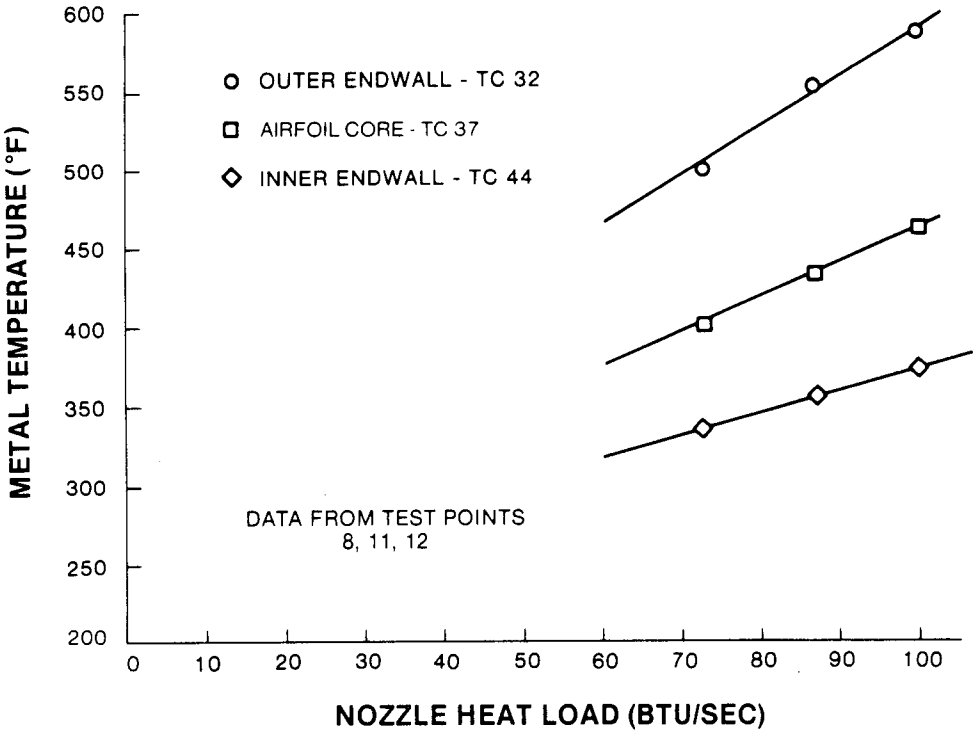

Figure 3-22. Second-stage nozzle metal temperature vs heat load (gas temperature varied, gas mass flow constant)

pitchline airfoil trailing edge surface and the thermocouple data of the pitch airfoil core temperature response to the simulated startup/shutdown sequence. The trailing edge response was typical for the other points on the airfoil surface.

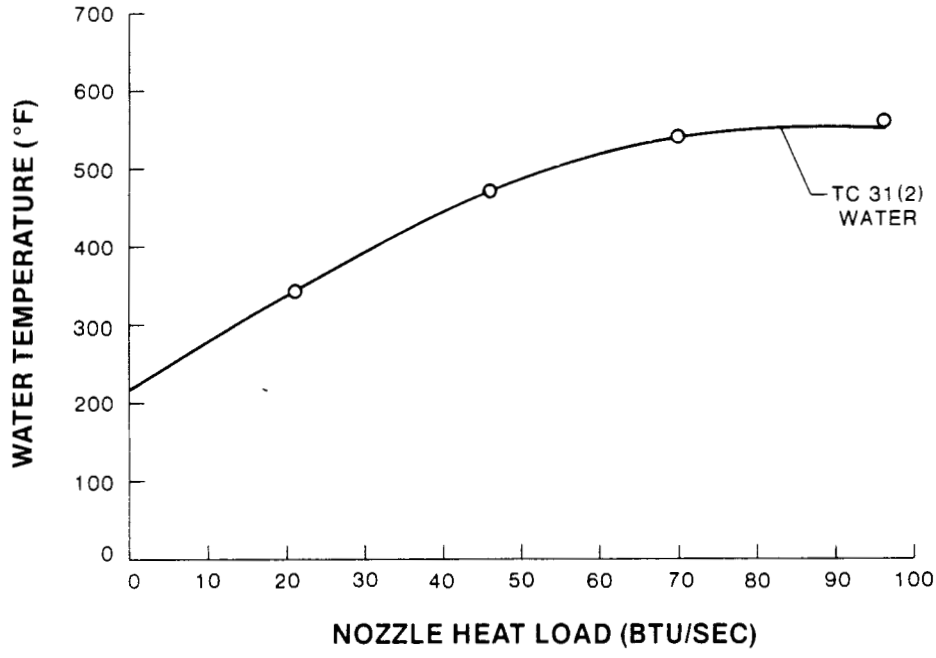

Figure 3-23. Second-stage nozzle (Position 2) thermocouple 31(2) vs heat load

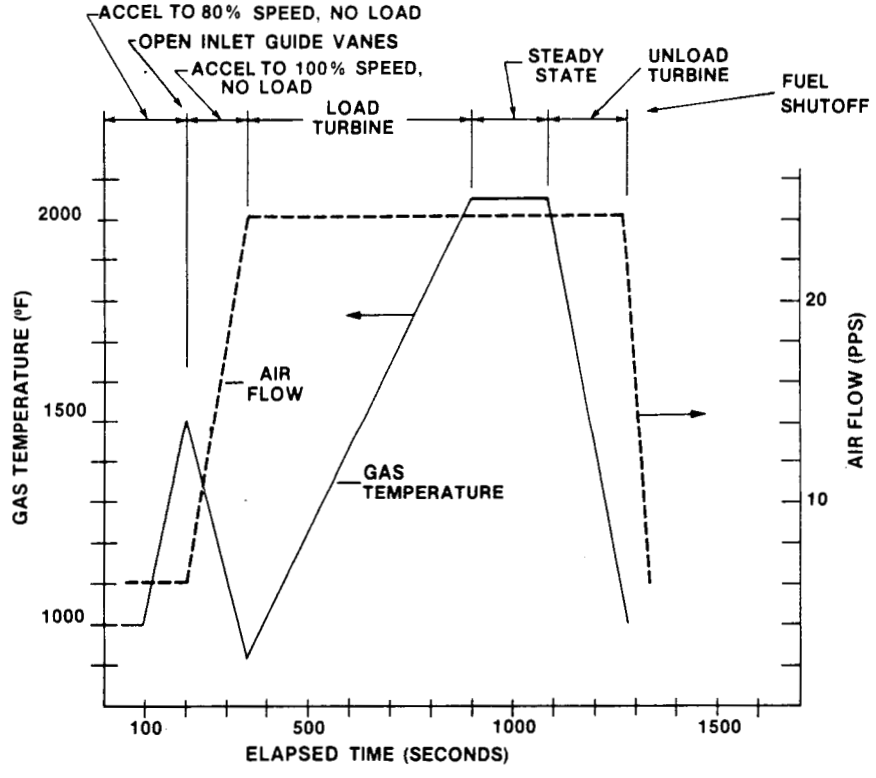

Figure 3-24. Second-stage nozzle test simulated startup/shutdown cycle

An important feature of the nozzle response was that neither the nozzle surface temperature nor the nozzle core surface temperature lagged the gas temperature during the cycle. This implies that the temperature gradients and resulting thermal stresses reach a maximum at steady-state rather than during the transient. Therefore,

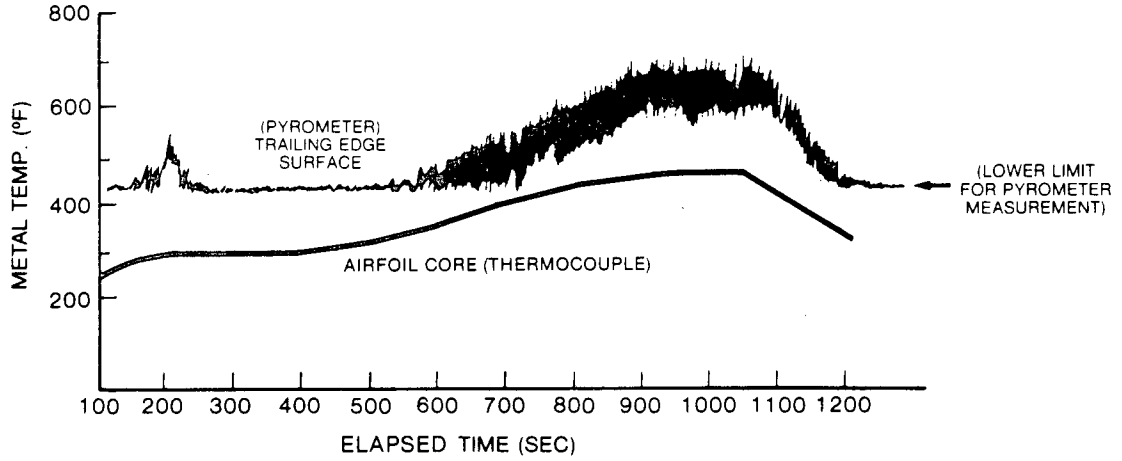

Figure 3-25. Second-stage nozzle response to initial thermal cycle

a water-cooled turbine may be able to tolerate a more rapid startup sequence than an air-cooled turbine, and might also be far less affected by trips.

Forty-seven (47) repetitions of this cycle were accumulated during the initial cyclic test series. This brought the total time at the design operating point to over eight hours. Excursions from startup to design point to shutdown in the steady-state portion of the test, and inadvertent trips from the design point, brought the total number of cycles to 52.

The monometallic nozzles completed the initial cyclic test with no visible sign of distress. The nozzles were removed from the test stand for a detailed non-destructive examination. Details of this inspection are found in Section 3.8.3.

3.7.6 Extended Steady-State Test

3.7.6.1 Test Description

Steady-state fired testing was resumed after surface thermocouples were added to nozzle #17 (Test Position 3). Modifications (see Appendix A) were also made to the infrared pyrometer to improve its utility. Test parameters were subsequently varied over a wider range than had been done previously. No thermocouple rakes were installed because sufficient data was accumulated in the initial test series. The test conditions for the parameter variation tests are summarized in Table 3-9. The parameters that were varied during this test series were gas temperature and gas mass flow rate.

3.7.6.2 Test Results

The variation of nozzle surface temperature with hot-gas temperature is shown in Figures 3-26 and 3-27. The functional dependencies follow predicted trends.

The variation of nozzle surface temperature with gas mass flow rate is shown in Figures 3-28 and 3-29. The functional dependencies also follow predicted trends. The gas mass flow variation test points were run after the completion of 312 additional thermal cycles. A comparison of the measured and the analytically predicted temperatures for the design point is presented in Table 3-10.

Table 3-9

SECOND-STAGE NOZZLE TEST CONDITIONS FOR PARAMETER VARIATION TESTING

Test Point	Remarks	Gas[1] Temp. (°F)	Gas Mass[2] Flow Rate (lb/sec)	Inlet Water Temperature (°F)	Water Flow Rate (lb/sec)
1	Gas Temp.	1192	24.02	235	0.62
2	Variation	1484	24.05	233	0.62
3		1836	24.20	235	0.62
4		2113	24.20	235	0.62
5		2113	19.80	228	0.59
6	Gas Mass	2104	15.70	229	0.59
7	Flow Rate	2133	11.90	229	0.59
8	Variation	2109	7.90	229	0.60

[1]Corrected for radiation and leakage
[2]Corrected for test stand leakage

The measured temperatures are, in all cases, lower than the predicted values. The reason for this is that the actual gas side convective heat transfer coefficients experienced by the test nozzles were lower than the values used in performing the nozzle heat transfer analysis. The gas side heat transfer coefficients used to analyze the nozzle were determined by application of turbulent flat plate theory to the predicted airfoil velocity distribution.

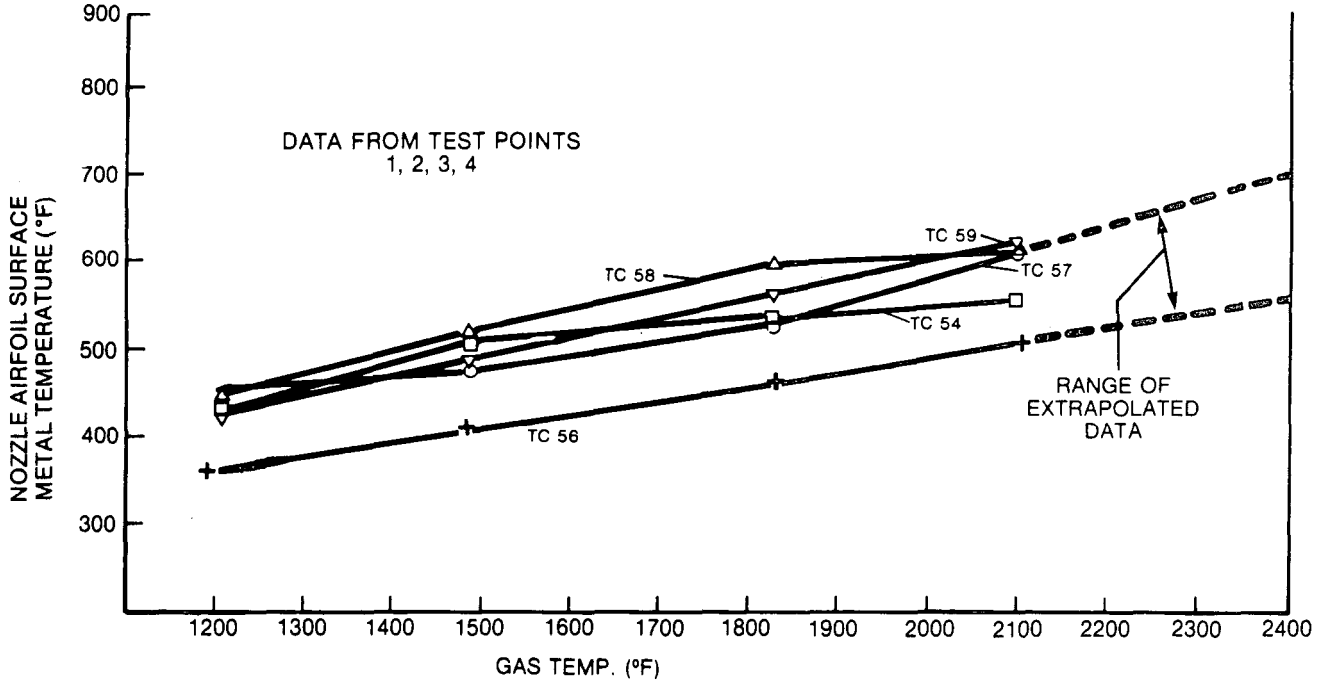

Figure 3-26. Second-stage nozzle airfoil pitchline metal temperature vs gas temperature

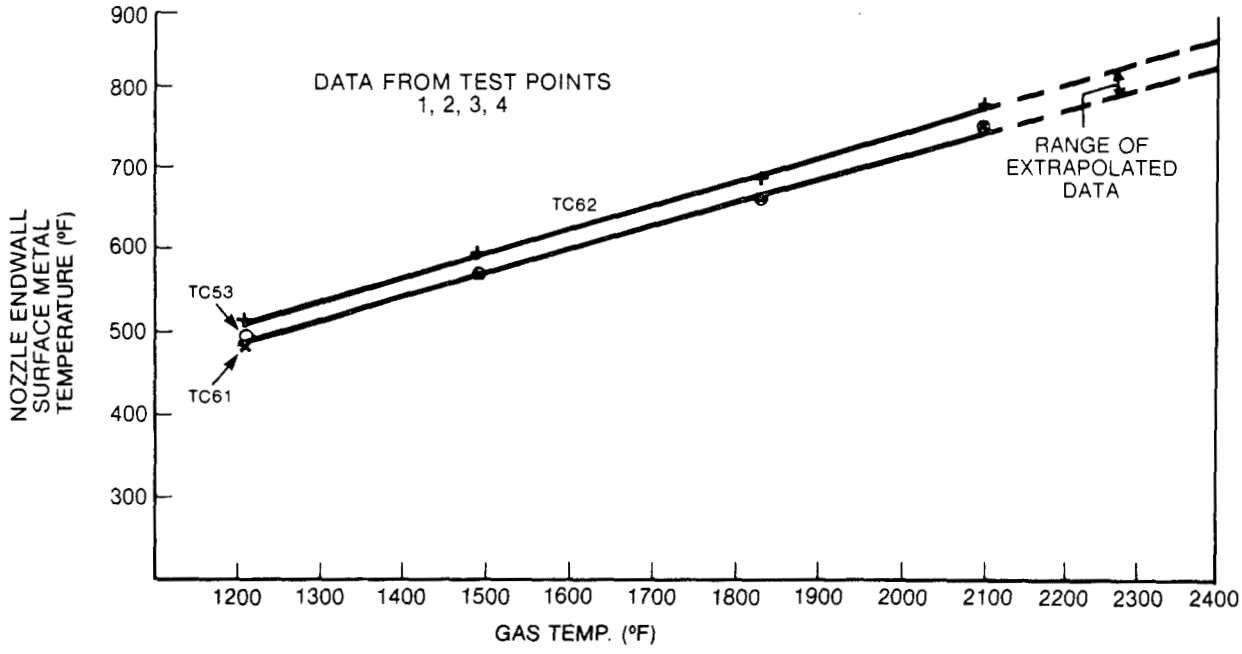

Figure 3-27. Second-stage nozzle endwall metal temperature vs gas temperature

The actual gas side heat transfer coefficients seen by the nozzle during testing at the airfoil pitchline have been calculated using measured surface temperatures and cooling water temperatures. The thermal conductance of the nozzle vane used in these calculations was determined by use of a finite element heat transfer model. These gas side heat transfer coefficients are compared to the gas side heat transfer coefficients predicted by turbulent flat plate theory in Table 3-11.

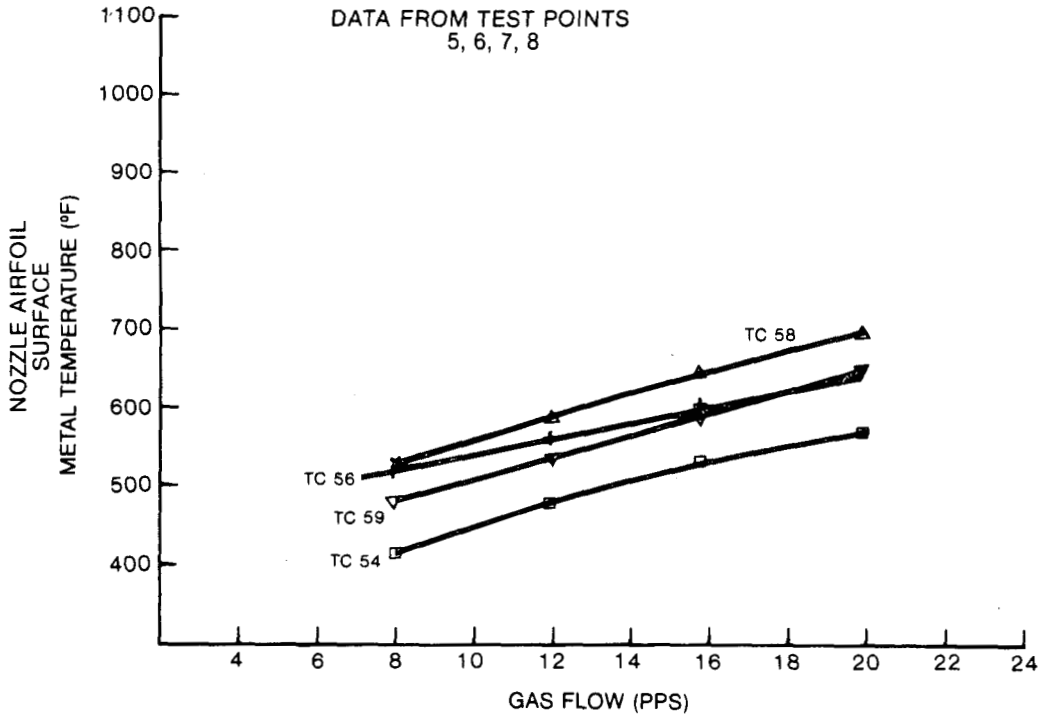

Figure 3-28. Second-stage nozzle airfoil pitchline metal temperature vs gas flow

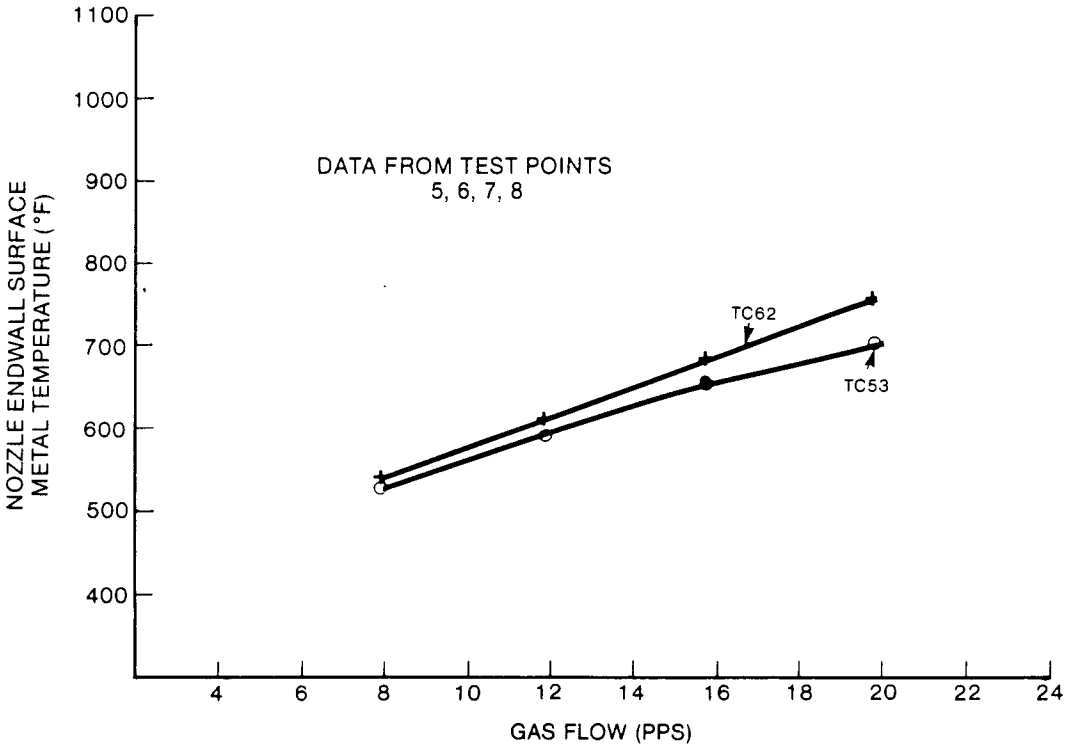

Figure 3-29. Second-stage nozzle endwall metal temperature vs gas flow

Table 3-10

SECOND-STAGE NOZZLE TEST COMPARISON OF MEASURED AIRFOIL SURFACE TEMPERATURES WITH PREDICTED VALUES, T = 2082 °F, W = 24.2 lb/sec

TC No.	Predicted Temperature (°F)	Measured Temperature (°F)
54	770	560
55	769	497
56	755	510
57	709	610
58	651	605
59	744	621

The variation in heat load with gas temperature and gas flow rate is presented in Figures 3-30 and 3-31. The measured heat load is about 8% less at the design test point than was measured in the initial test (Figures 3-16 and 3-17). This difference is the result of a 15 °F lower measured temperature differential between the inlet and exit cooling water than was measured during the initial test. The accuracy tolerance on this measured differential is ±8 °F. Therefore, some of the variance noted in heat load between initial and extended testing may be due to instrumentation accuracy. It should also be noted that during the initial testing, thermocouple rakes were located

Table 3-11

SECOND-STAGE NOZZLE TEST – COMPARISON OF MEASURED AND PREDICTED PITCHLINE AIRFOIL CONVECTIVE HEAT TRANSFER COEFFICIENTS

Thermocouple	H_g (Btu/hr-ft^2-°F)	
	Calculated from Measured Data	Predicted†
54	71	168
55	80	249
56	98	269
57	97	148
58	81	107
59	86	135

†Based on turbulent flat plate theory modified according to results obtained from cascade testing.

upstream of the nozzle leading edges. These were removed prior to the extended testing. The increased turbulence generated by these rakes would cause increased heat transfer and, hence, increased heat load. The magnitude of such an increase is very difficult to determine, but it is reasonable to assume that a portion of the higher heat load measured during the initial testing was due to the presence of the rakes.

3.7.7 Extended Cyclic Test

3.7.7.1 Test Description

Cyclic testing was resumed after the extended steady-state fired testing. For this test series, the startup/shutdown cycle was simplified and abbreviated from the cycle used in the initial test series. This was done in order to increase the number of ther-

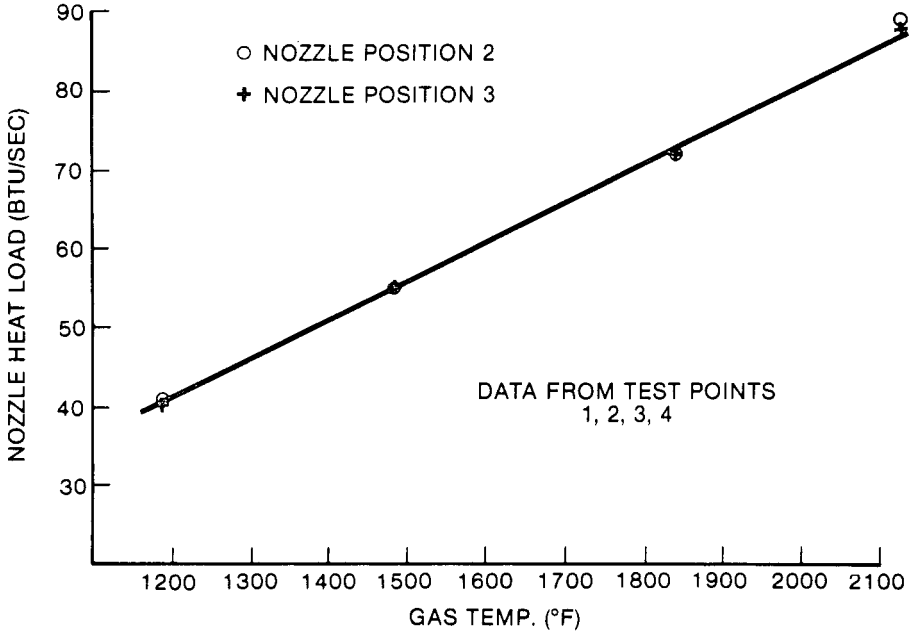

Figure 3-30. Second-stage nozzle heat load vs gas temperature

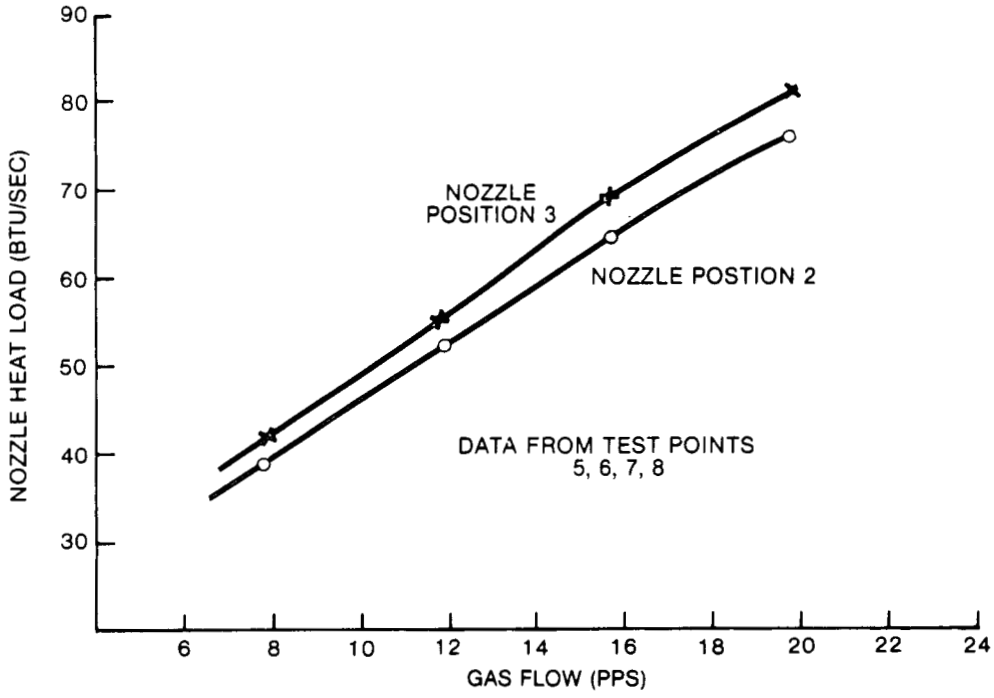

Figure 3-31. Second-stage nozzle heat load vs gas flow

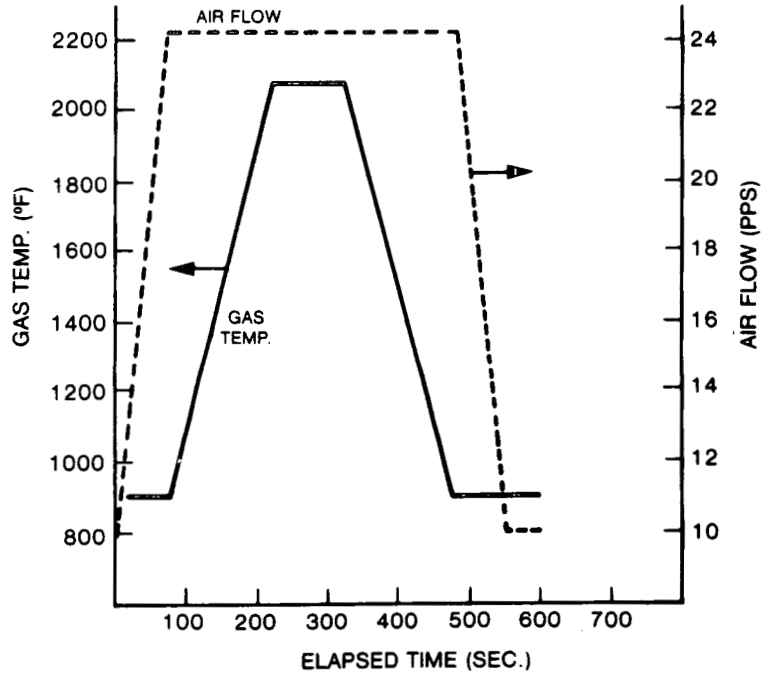

Figure 3-32. Second-stage nozzle test simplified startup/shutdown cycle

mal cycles that could be accumulated during the allotted test time. Figure 3-32 shows the startup/shutdown sequence used for this test. Since the maximum and minimum heat load points were the same for both cycles, the thermal strain range and, therefore, the fatigue damage per cycle were similar for both the initial and the extended cycle tests.

Each of these later cycles included 100 seconds of steady-state operation at the design point. This allowed sufficient time for the nozzles to reach steady-state conditions and for all data to be recorded.

Subsequent to the initial test series, the facility was improved by the addition of an automatic controller. This modification allowed the thermal cycles to be run precisely and automatically. Eighteen strip chart recorder channels were available for monitoring nozzle thermocouples. All of the nozzle surface temperature thermocouples, and other thermocouples of interest, were monitored on the strip chart recorder for a minimum of 50 cycles.

Three hundred twenty-three (323) additional thermal cycles were attained in two series of 160 and 163 cycles per series, with a visual inspection of the nozzles between each series. The total number of cycles accumulated through both the initial and extended cyclic test periods was 375.

3.7.7.2 Test Results

The temperature response of the nozzle is shown in Figures 3-33, 3-34, and 3-35. As can be seen from these figures, the maximum difference in temperature between the inner and outer surface always occurs at the peak steady-state point of the cycle. All of the metal temperatures monitored on the strip chart recorders followed the cycle precisely, despite the fact that the rate of change of heat load was greater than would be experienced in a normal turbine startup/shutdown cycle. This can be attributed to the high efficiency of water cooling in this application, and the absence of thick metal sections in the nozzle.

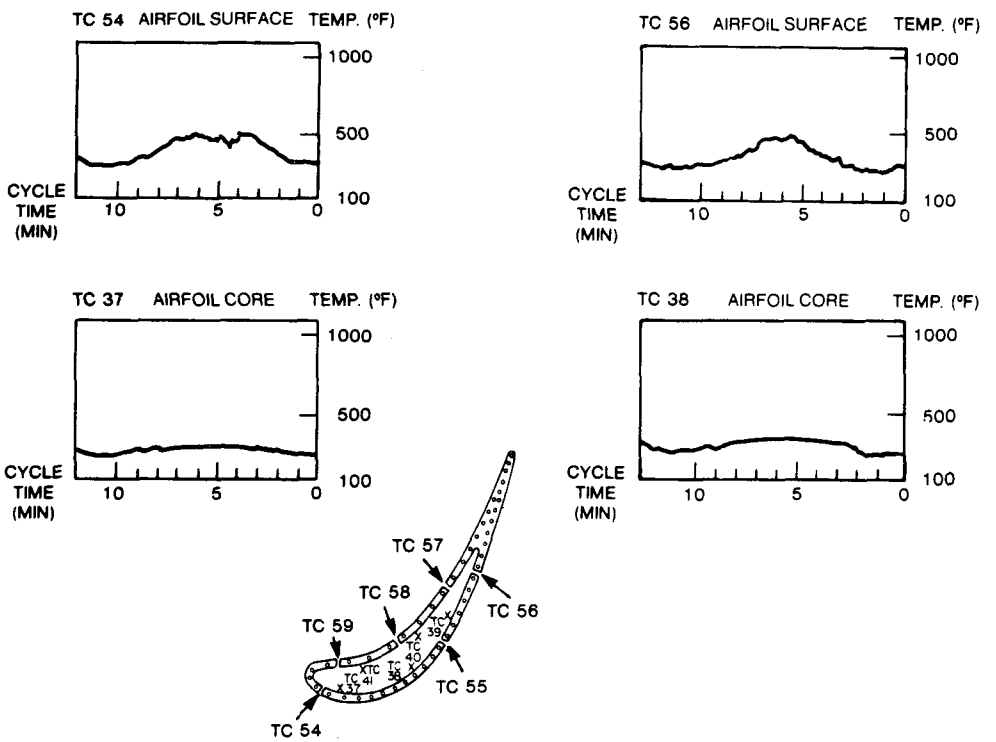

Figure 3-33. Second-stage nozzle airfoil response – cycle 147

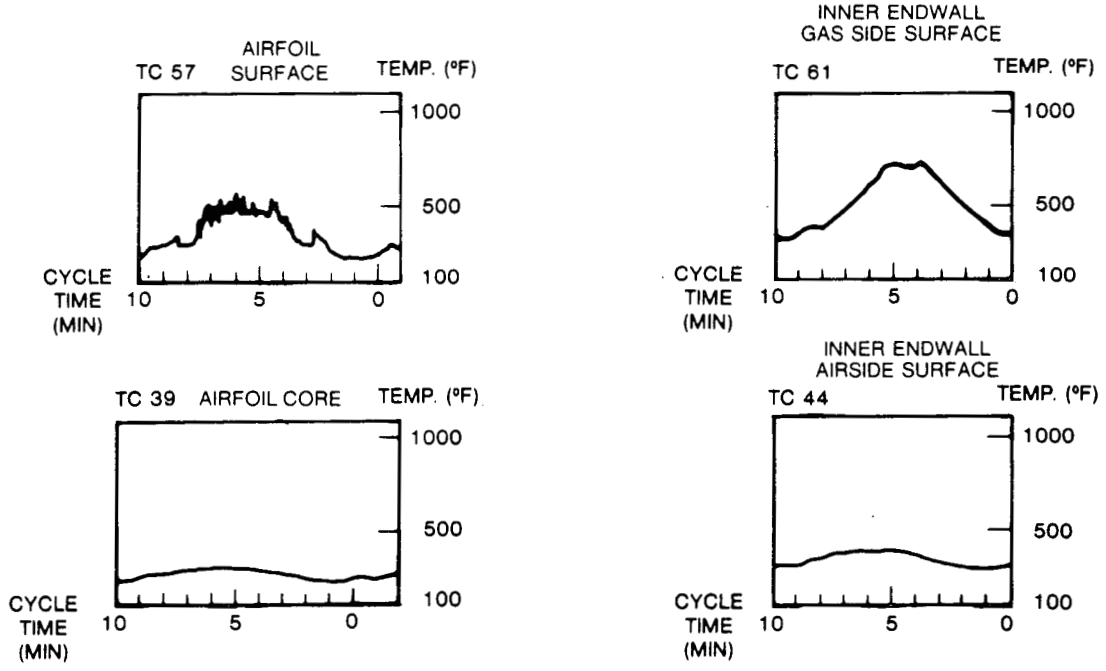

Figure 3-34. Second-stage nozzle response – cycle 201

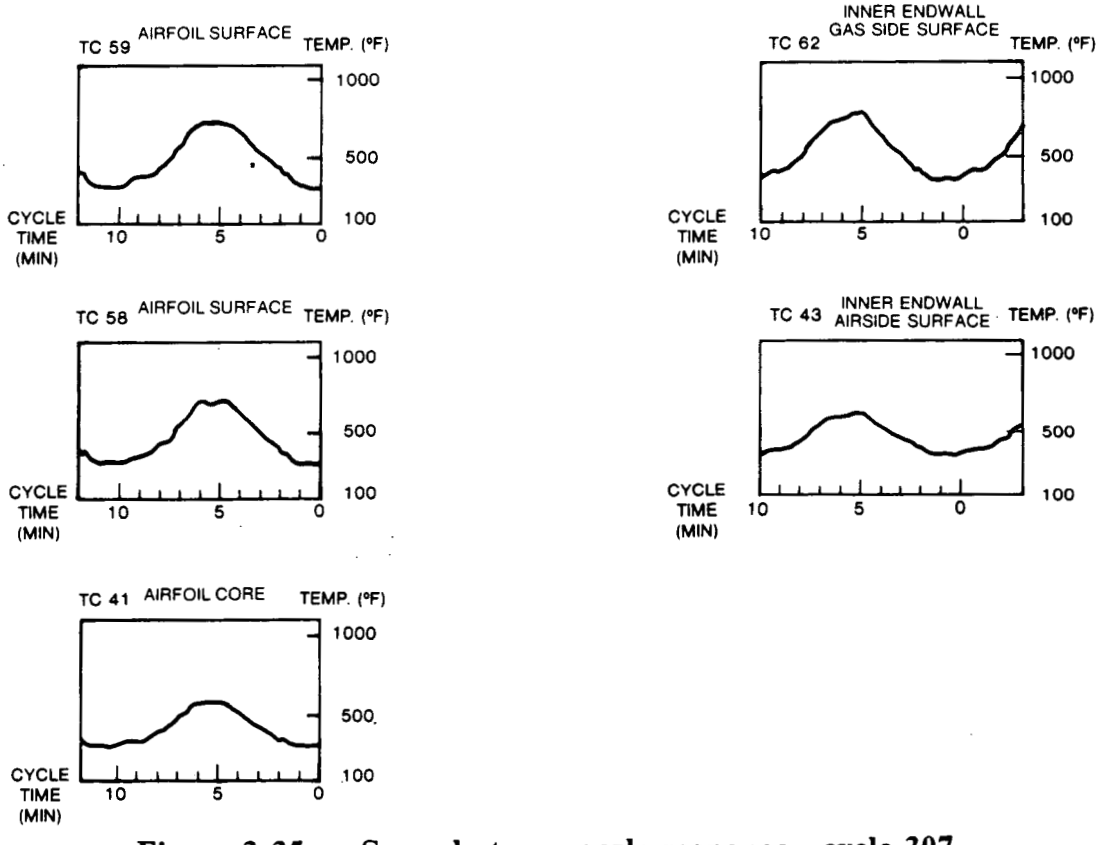

Figure 3-35. Second-stage nozzle response – cycle 307

At the completion of cycle 304, a system trip occurred due to a surge tank level alarm. When cycling was resumed, the peak indicated temperatures of both the airfoil

surface thermocouples (TC 54 through TC 59) and the airfoil core thermocouples (TC 37 through TC 41) had increased by 100 to 300 °F. The increase could not be accounted for by either a change in combustor operation or in the cooling water temperature. Since the overall heat load remained approximately the same, and water temperature rise across the various portions of the cooling circuit also remained about the same, testing was continued. This phenomena is illustrated in Figure 3-36.

3.7.8 System Fault Condition Test

3.7.8.1 Test Description

System fault condition testing entailed a reduction of the cooling water flow in nozzle #17 (Test Position 3) to 50% of the design value at the design gas temperature and gas flow rate. The reduction of coolant flow was carried out in steps as shown in Table 3-12.

A pitchline airfoil pyrometer scan was taken at each of the reduced cooling flow points. In addition, the nozzle cooling water exit pressure was monitored on a strip chart recorder in order to detect the possible onset of boiling. Operation at Test Point 11 was maintained for ten minutes.

The second system fault condition test consisted of operation at 110% of design gas temperature (Test Point 12). The reduced nozzle water flow rate was caused by a cool-

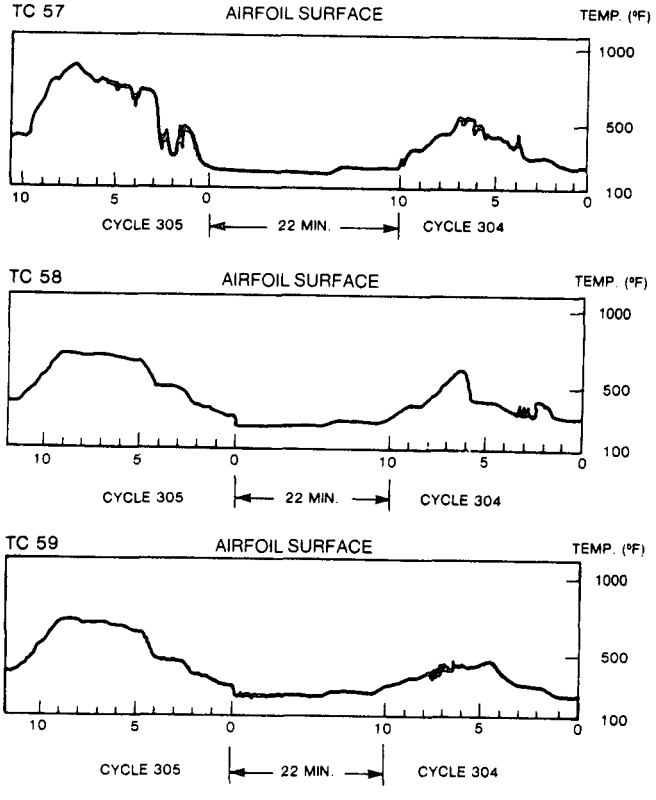

Figure 3-36. Second-stage nozzle airfoil temperature jump – cycle 305

Table 3-12

SECOND-STAGE NOZZLE –
SYSTEM FAULT TEST CONDITIONS

Test Point	Remarks	Gas[1] Temperature (°F)	Gas Mass[2] Flow Rate (lb/sec)	Nozzle Inlet Water Temperature (°F)	Nozzle Water Flow Rate (lb/sec)
8a	Coolant	2091	24.0	230	0.59
9	Flow	2113	24.0	231	0.49
10	Reduction	2090	24.1	228	0.41
11	↓	2092	24.1	233	0.31
12	Gas Temp. Increase	2288	23.9	223	0.44

[1]Corrected for radiation and leakage
[2]Corrected for test stand leakage

ing water system problem which limited the flow to 0.44 lb/sec. Operation at this point was maintained for fifteen minutes.

The third and final system fault condition test was a severe transient test in which the rate of change of gas temperature was three times as great as the normal startup/shutdown cycle. Figure 3-37 shows the severe thermal cycle to which the nozzle was exposed during this portion of the test. This cycle represents the most rapid change of heat load to which the nozzle could be subjected, given the constraints of the test facilities. Thirty-eight repetitions of this severe cycle were accumulated. This brought the total number of thermal cycles accumulated through all cyclic and fault condition testing to 413.

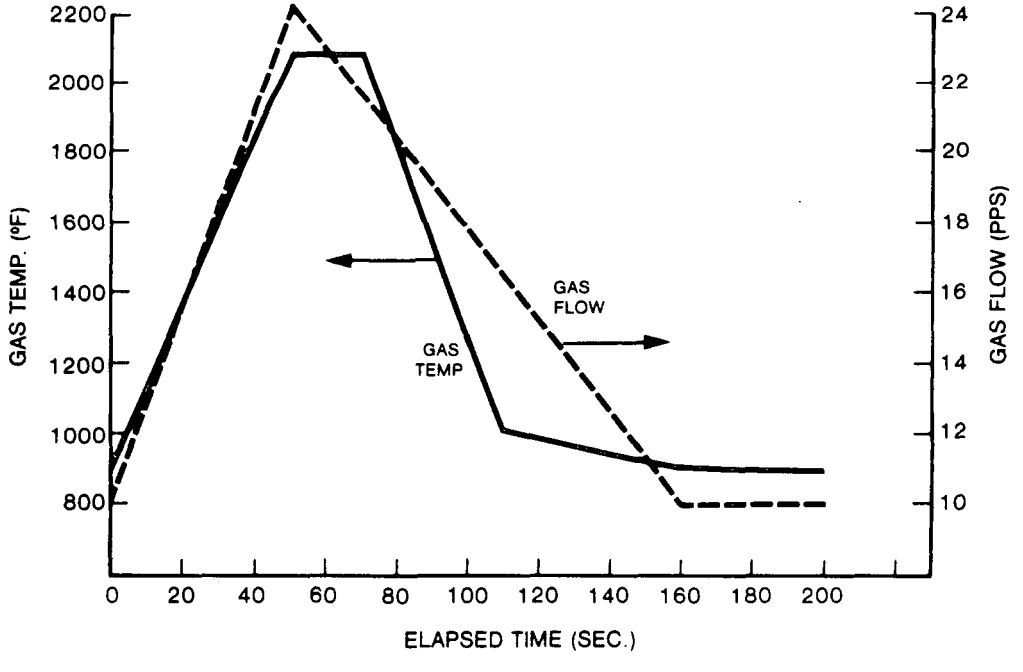

Figure 3-37. Second-stage nozzle test severe startup/shutdown cycle

3.7.8.2 Test Results

The reduced coolant flow test satisfactorily demonstrated the nozzle's ability to function adequately, despite a 50% reduction in coolant flow. The nozzle surface temperatures as a function of cooling flow are presented in Figures 3-38 and 3-39. Pyrometer results are shown in Figure A-11 of Appendix A. The relative insensitivity of surface temperature to water flow can be explained by the fact that the coolant-to-cooling-passage interface is a very small portion of the total thermal resistance between the hot gas and the cooling water. Therefore, even a large change in cooling water flow causes a small change in the total thermal resistance. As is noted in the figures, even a 50% reduction in cooling flow does not result in surface temperatures increasing to a level of concern.

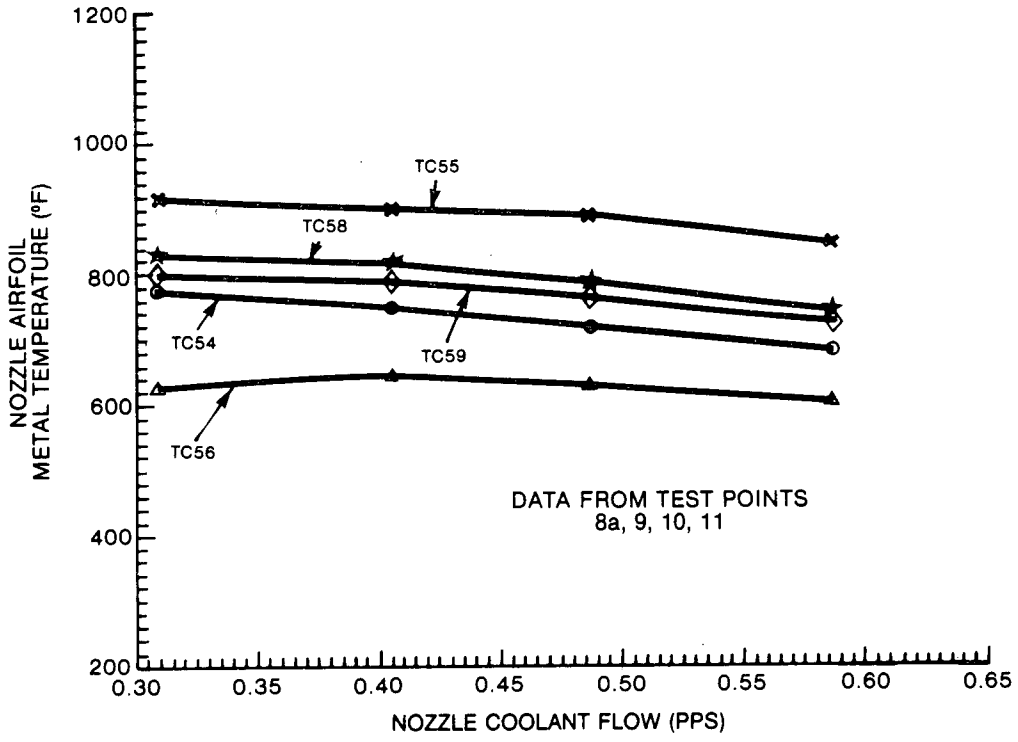

Figure 3-38. Second-stage nozzle airfoil – pitchline metal temperature vs coolant flow

The variation of water temperature, at various locations throughout the cooling water circuit, with reduced cooling flow is summarized in Figures 3-40, 3-41, and 3-42. The rate of change of coolant temperature does not level off at lower flows. This implies that saturated boiling was not reached even at the 50% flow point. No random fluctuation in coolant exit pressure was noted during the flow reduction portion of the test. Random fluctuations in pressure would be an indication of the onset of boiling as noted in the first stage nozzle test.

Coolant fluxes and heat fluxes for several cooling passages in the nozzle airfoil were calculated based on an assumed equal distribution of flow and measured water temperature changes for each of the reduced flow test points. This data is compared with the theoretical curves for the onset of nucleate boiling and critical heat flux (Fig-

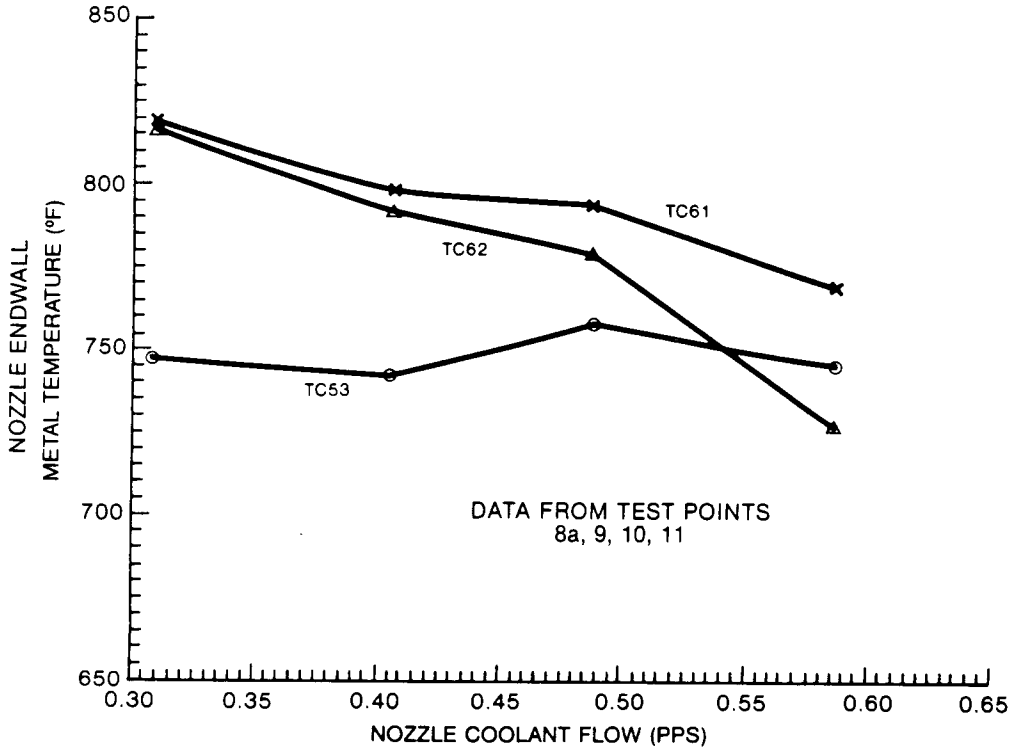

Figure 3-39. Second-stage nozzle – endwall metal temperature vs coolant flow

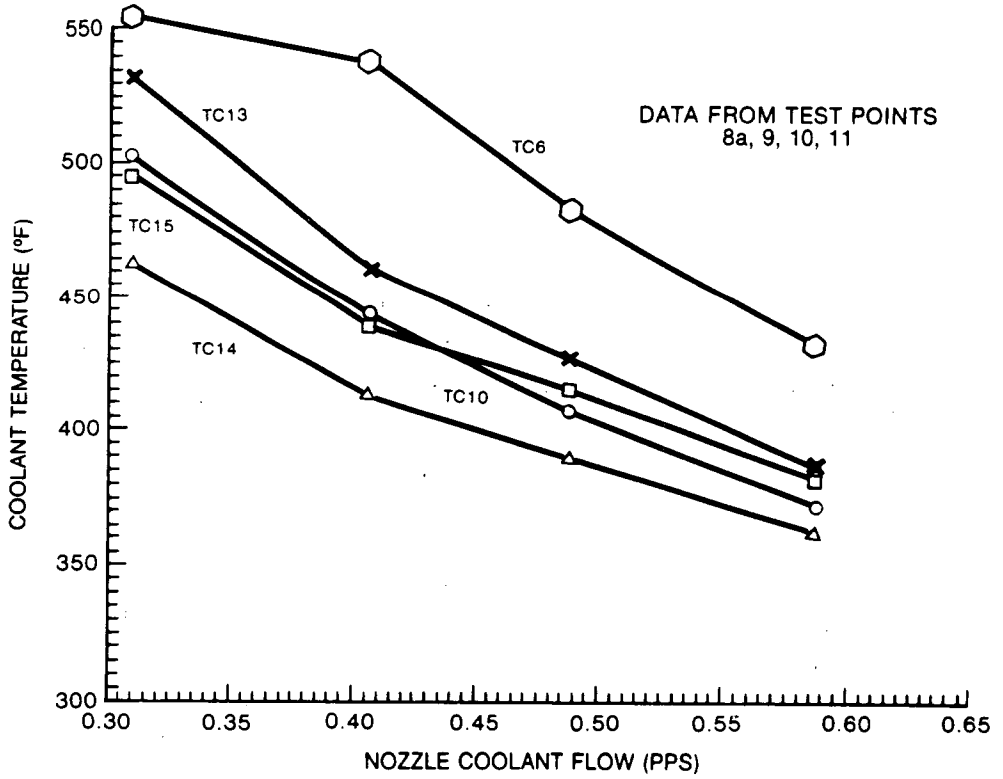

Figure 3-40. Second-stage nozzle – outer endwall coolant temperature vs coolant flow

ures 3-43 and 3-44). Passage numbers referred to in these figures were obtained from the number of the thermocouple measuring the exit water temperature. These figures indicate that a comfortable margin of safety exists to critical heat flux at all reduced flow test points. However, at the 50% coolant flow point, nucleate boiling does seem possible in some of the trailing edge passages. A thorough discussion of nucleate boiling and critical heat flux is given in Appendix B.

The nozzle airfoil surface temperatures and nozzle exit cooling water temperature measured at 110% design firing temperature are given in Table 3-13.

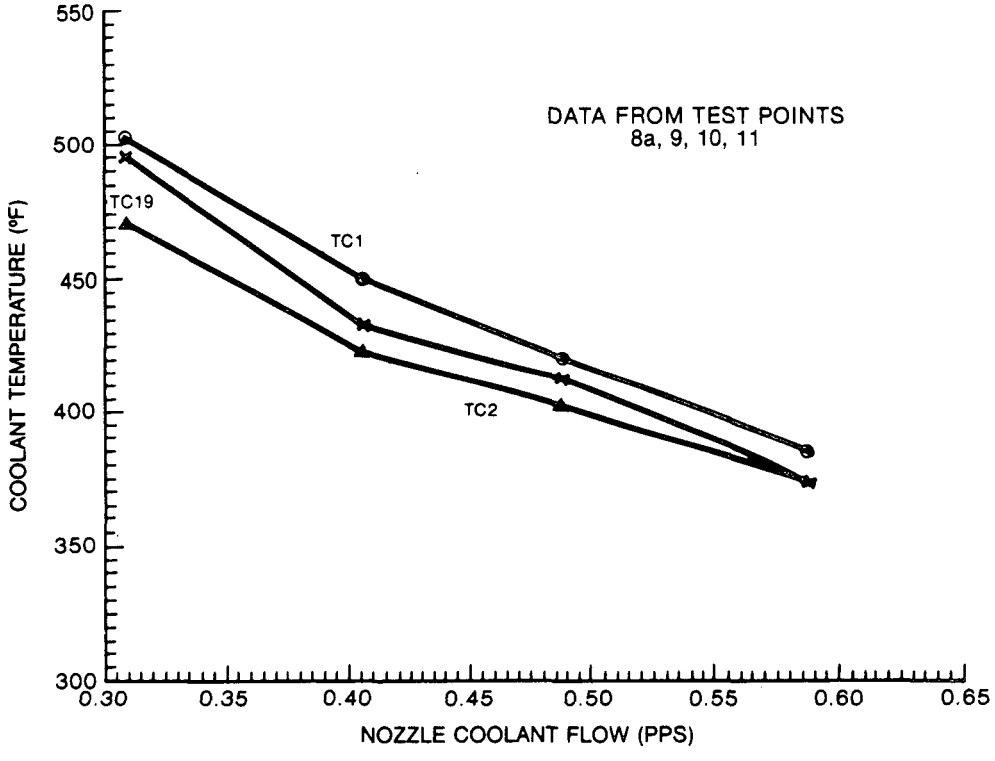

Figure 3-41. Second-stage nozzle – exit coolant temperature vs coolant flow

At Test Point 12, with coolant flow to the nozzles reduced, a 2288 °F average gas temperature was attained, which represents an equivalent firing temperature of 2860 °F, without the average gas-path surface temperature exceeding the design goal of 1000 °F. The exit cooling water temperature affords a comfortable margin of safety to bulk boiling.

The nozzle metal temperature and cooling water temperature response to the severe cycle is shown in Figure 3-45. Despite the rapid rate of change of heat load experienced by the nozzles, none of the measured temperatures lag the cycle.

After completion of system fault condition testing, the monometallic nozzles were removed from the HGPDTS and thoroughly inspected. Details of the post-test inspection are found in Section 3.8.3.

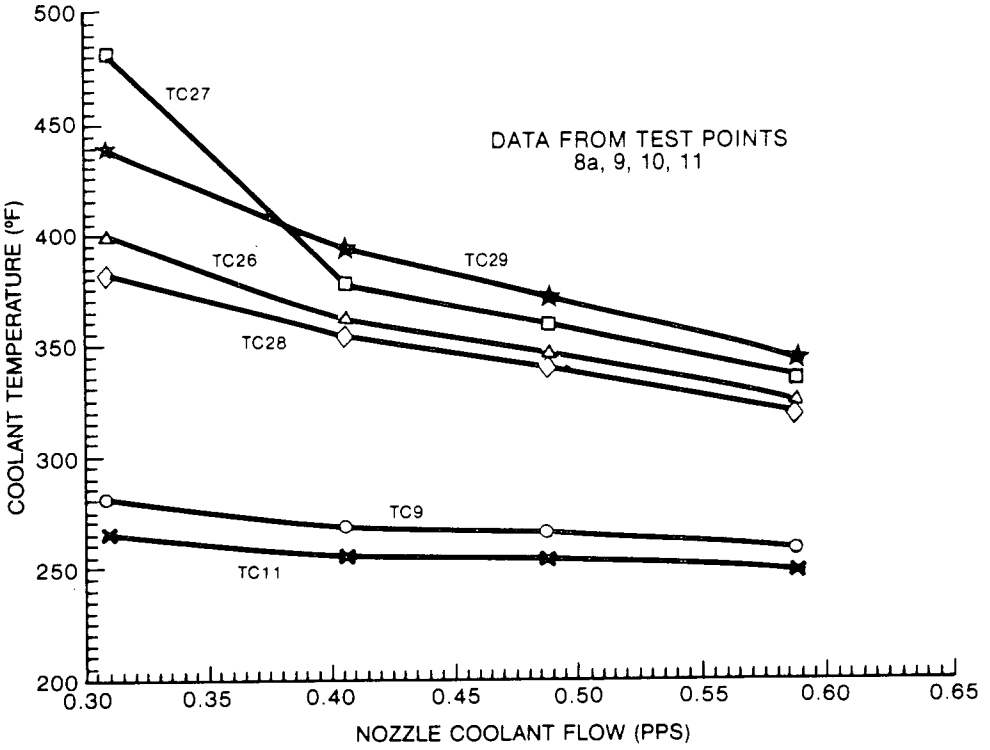

Figure 3-42. Second-stage nozzle – coolant temperature vs coolant flow

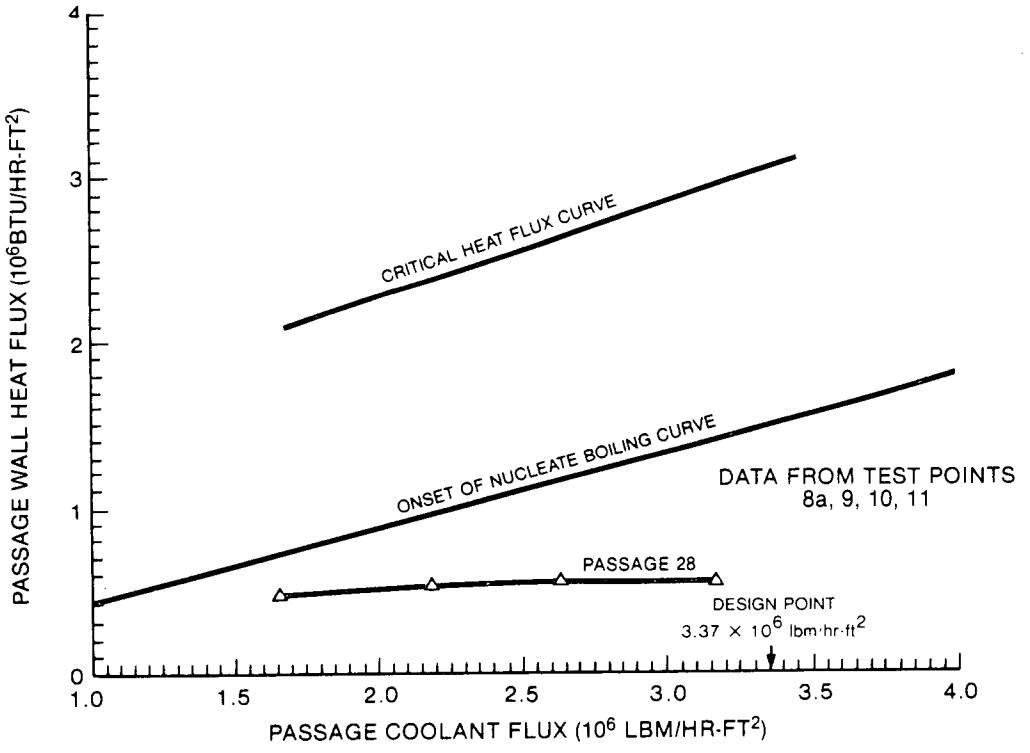

Figure 3-43. Second-stage nozzle – feed passage 28, heat flux vs coolant flux

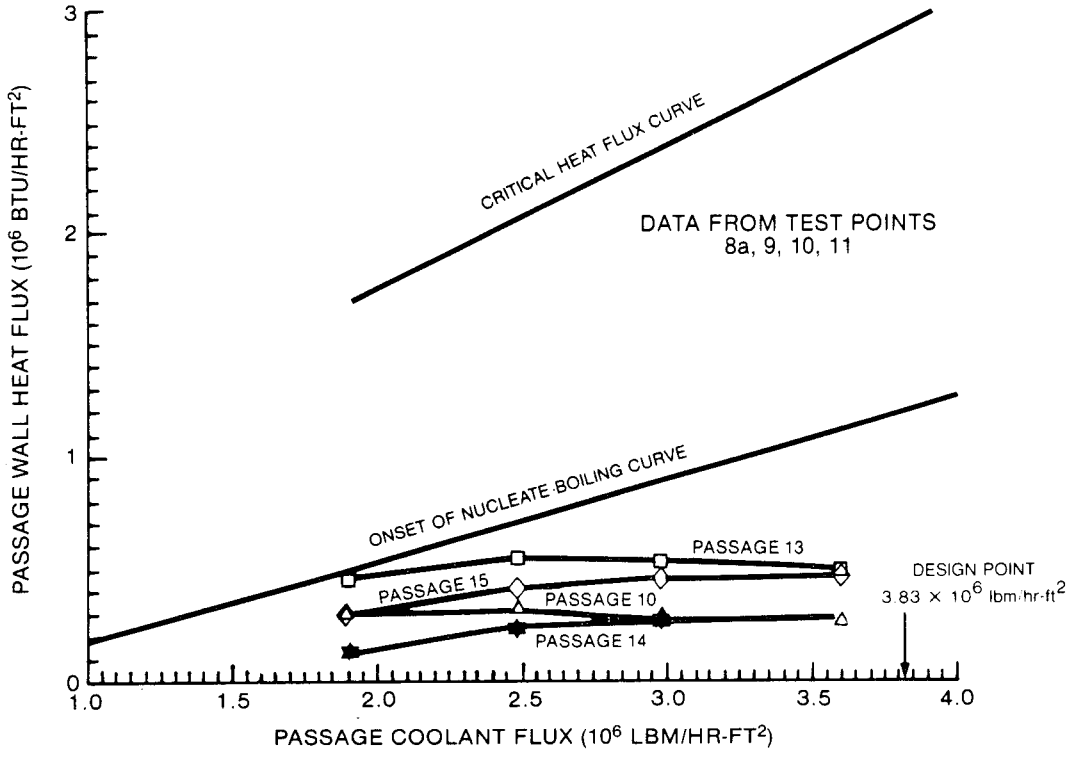

Figure 3-44. Second-stage nozzle – return passages, heat flux vs coolant flux

Table 3-13

SECOND-STAGE NOZZLE AT 110% DESIGN FIRING TEMPERATURE

Thermocouple Position	Temperature (°F)
53	809
54	903
55	1005
56	669
57	941
58	921
59	1196
61	854
62	877
1[(1)]	408

[(1)]Water temperature at exit

3.8 INSPECTIONS

3.8.1 Pretest Inspection

Hydrostatic leak checks were performed after brazing the manifold covers and plugs to the nozzles. The leak check, performed at 1500 lb/in.^{2}, showed all brazed joints to be leak-tight.

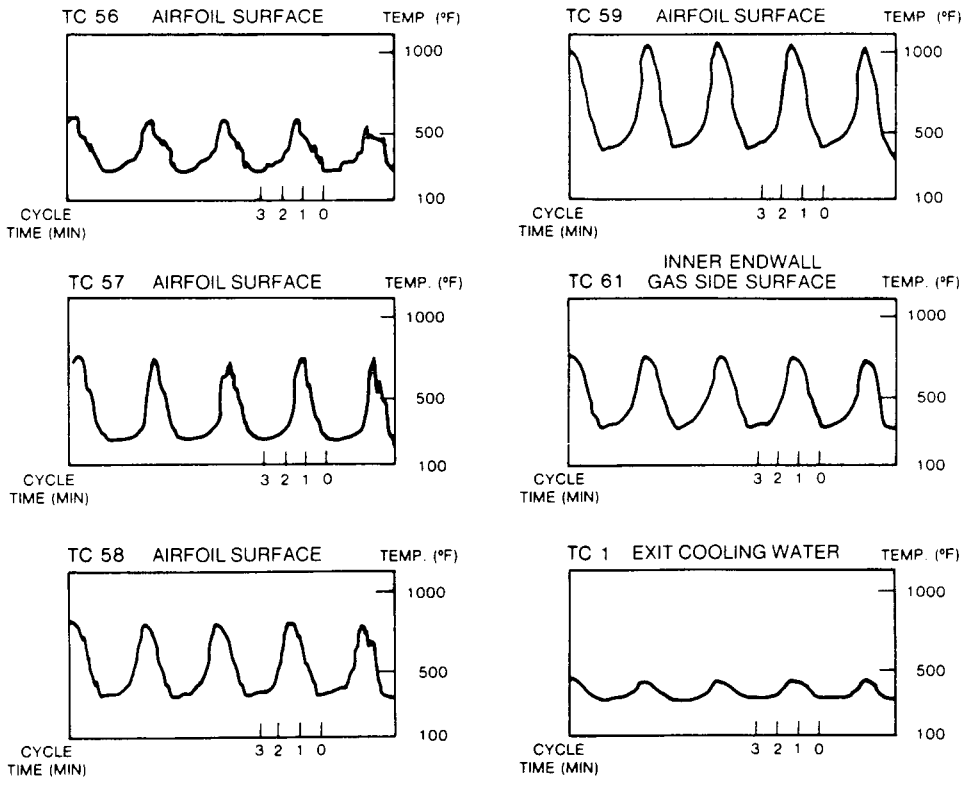

Figure 3-45. Second-stage nozzle – response to severe transient

Ultrasonic inspection techniques were used to check cooling passage wall thicknesses in the nozzle airfoil. A piece of cast IN718, with a drilled passage having a known wall thickness, was used as a calibration reference. The two nozzle castings with the best airfoil wall thickness readings were selected as test nozzles, with the remaining nozzles designated as spares.

3.8.2 In-Test Inspection

In-test inspections were conducted as required by the test plan. Visual inspections of the monometallic nozzle trailing edges were conducted by removing the mixing chamber manway cover and having an inspector enter the mixing chamber. Mirrors and high-intensity lights were used to record the surface condition of the nozzles. After completion of the initial test series, the combustion system was removed from the HGPDTS to allow removal of the nozzle assembly for a more complete inspection. A visual in-place examination after the initial steady-state and cyclic testing of the nozzles showed surface areas which were discolored between the cooling passages of the nozzles. Those markings clearly showed the pattern of cooling passages inside the nozzles (Figure 3-46). It is believed these areas were discolored as a result of a very slight oxidation of the hot surfaces between the water cooling passages.

No indications of cracking, overheating, or other distress were observed during this inspection. A total water system leakage test at 1250 lb/in.^{2} showed no change as compared to the measurement taken at the start of the testing. The nozzles were in excellent condition after the initial testing.

3.8.3 Post-Test Inspection

3.8.3.1 After Initial Testing

A post-test inspection performed after the initial test series (52 thermal cycles) included a helium leak check and an x-ray inspection of the test nozzles and slave segments. No leaks were uncovered by the helium check other than a slight porosity leak on slave segment Test Position 1, which had been identified previously. The x-ray inspection showed no indication of any cracking. The X-ray could not definitely confirm if the boiling phenomena observed in the inner endwall of nozzle #16 (Test Position 2) was caused by a brazed pin partially blocking a cooling hole.

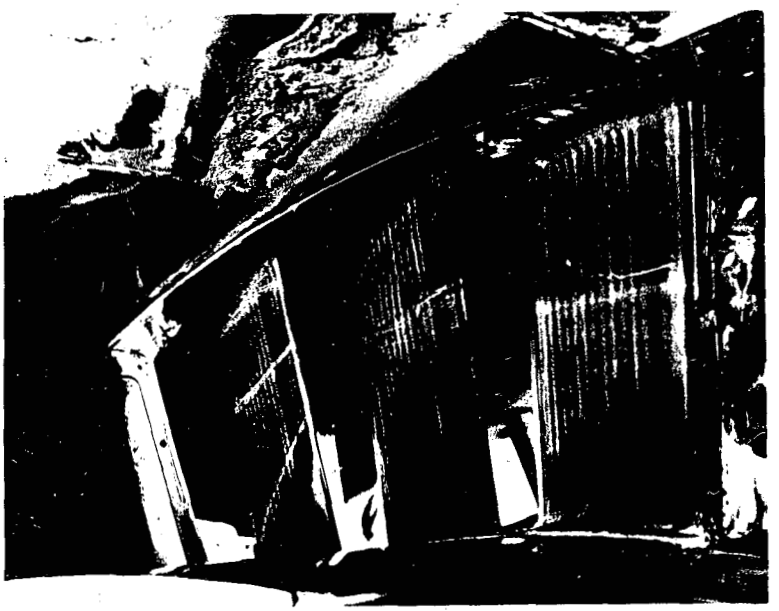

Figure 3-46. Second-stage nozzle at conclusion of initial testing (view upstream)

3.8.3.2 After Extended Testing

A post-test inspection performed after the extended test series (413 thermal cycles) consisted of the following:

- Visual
- Hydrostatic leak check
- Hydrostatic flow check
- Surface thermocouple instrumentation
- Metallographic

3.8.3.2.1 Visual Inspection. The external appearance of the nozzle gas-path surfaces did not change appreciably during extended testing from what was observed at the completion of the initial testing. The nozzle gas path, photographed from the front

Figure 3-47. Second-stage nozzle at conclusion of extended testing (view downstream)

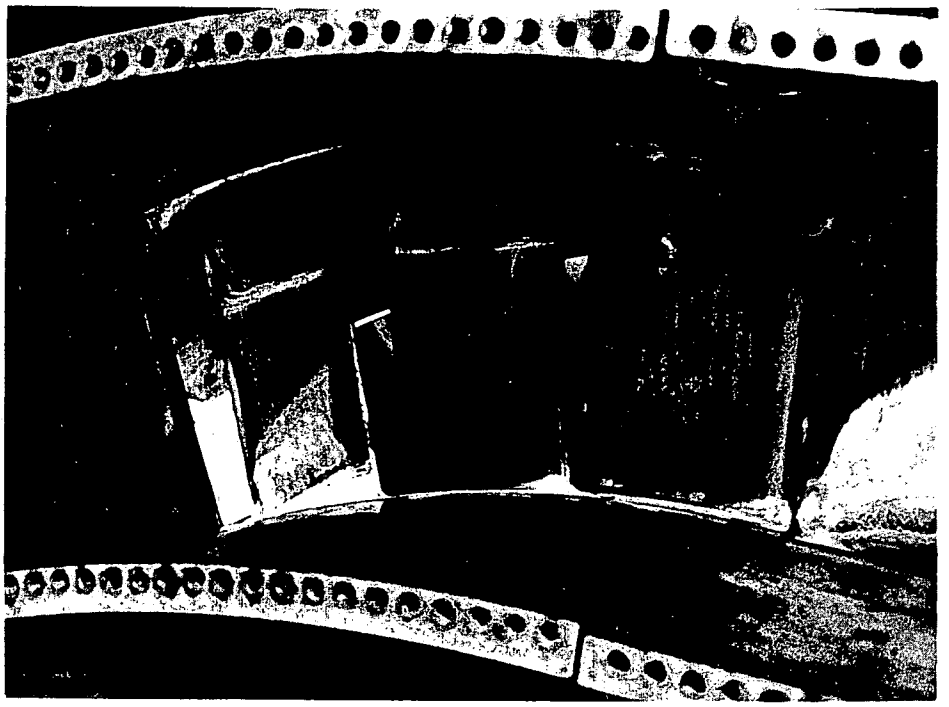

Figure 3-48. Second-stage nozzle at conclusion of extended testing (view upstream)

and rear, is shown in Figures 3-47 and 3-48. The cooling passage pattern on the airfoil near the leading edge was less pronounced than before the start of extended testing.

3.8.3.2.2 Hydrostatic Leak Check. A total water system leakage test at 1250 lb/in.^{2} was conducted prior to removal of the nozzle assembly from the HGPDTS. Small leaks were noted on the airfoil suction surface of nozzle #16, Test Position 2, and on the trailing edge of nozzle #17, Test Position 3. The leakage was measured at four grams per hour from both sources.

3.8.3.2.3 Hydraulic Flow Check. A comparison of the coolant mass flows and coolant circuit pressure drops at the beginning and end of the extended test period was made to quantify the effects of nozzle cooling passage blockage. The cooling circuit pressure drop without the test nozzles installed was also determined. This data (Table 3-14) allowed the fluid conductances of the test nozzles to be calculated from the coolant circuit pressure drop. The coolant flows measured at the end of the extended test period were the maximum attainable at that time. The data indicates a 14 % drop in the fluid conductance of nozzle position #2, and a 25% drop in the conductance of nozzle position #3.

Table 3-14

SECOND-STAGE NOZZLE TEST
HYDRAULIC FLOW CHECK

Conditions	Test Position 2 Cooling Circuit			Test Position 3 Cooling Circuit		
	Coolant Flow (lb/sec)	Pressure Drop (psi)	Test Nozzle #16 Conductance $\frac{(lb/sec)}{\sqrt{psi}}$	Coolant Flow (lb/sec)	Pressure Drop (psi)	Test Nozzle #17 Conductance $\frac{(lb/sec)}{\sqrt{psi}}$
No Nozzle In Circuit	0.61	23.9	–	0.61	30.5	–
Nozzle Installed at Beginning of Extended Test Period	0.62	244.0	0.042	0.62	232.0	0.043
Nozzle Installed at End of Extended Test Period	0.55	236.0	0.036	0.49	236.0	0.032

3.8.3.2.4 Surface Thermocouple Instrumentation Check. Due to the jump in surface temperatures indicated by the surface thermocouple during the extended cyclic testing, a thorough inspection of this instrumentation was conducted upon removal of the

nozzles from the test stand. No signs of distress were noted at the gas path thermocouple sites. In addition, a thorough check was made for secondary junctions. This was done by locally heating the thermocouple lead over its entire length while monitoring the thermocouple voltage. Voltage was generated only when the embedded junctions were heated. Therefore, it was concluded that no secondary junctions existed.

3.8.3.2.5 Metallography. Test nozzle position #3 (serial #17) was selected for detailed metallographic examination since this nozzle was equipped with surface thermocouples, it experienced the largest reduction in fluid conductance of the two test nozzles, and it developed a minor trailing edge leak (less than four grams/hr) during test.

Visual Inspection.

After removal of the test nozzles from the test stand, they were visually examined. No abnormal indications were observed. Test nozzle #17, Test Position 3, was then sectioned for metallography as shown in Figure 3-49. In addition, the surface thermocouples were cut out of areas 2 and 3 in Figure 3-49C for detailed metallographic examination.

Flourescent Penetrant Inspection.

The trailing edge airfoil section (far right in Figure 3-49C) was fluorescent penetrant inspected. Duct seal was used on both ends of the section to prevent penetrant fluids from entering the airfoil cooling passsages. The inspection revealed two pin-point indications along the trailing edge, both of which showed crater-like deposits around the pin holes when observed at 50X magnification. Another pin-point indication near the fifth cooling passage was examined and found to be a small surface depression. No other indications were observed.

Micro-Examination.

- **Internal Deposits**
  Thirteen separate pieces were mounted and polished for examination. Figures 3-50 and 3-51 show sections taken from the airfoil near the outer endwall. Figure 3-52 shows the cross sections of the surface thermocouples. Figure 3-53 shows cross sections taken through the outer endwall. White-colored deposits inside the cooling passages can be observed in all these figures. In the relatively cool water passageways near the rear (trailing edge) of the outer endwall and airfoil, the amount of deposit was relatively slight. In the hotter water passageways near the leading edge of the nozzle, extensive amounts of deposit were present. The cooling passages near the trailing edge of the nozzle receive relatively cool incoming water, whereas the cooling passages near the leading edge of the nozzle receive relatively hot water which has already flowed through the rear portion of the nozzle picking up heat.

- **Surface Thermocouples**
  The surface thermocouple cross section in area 3 of Figure 3-49C is shown again in Figure 3-54. Some cracking is evident in the junction; however, no other defects or abnormalities in these thermocouples could be found which would

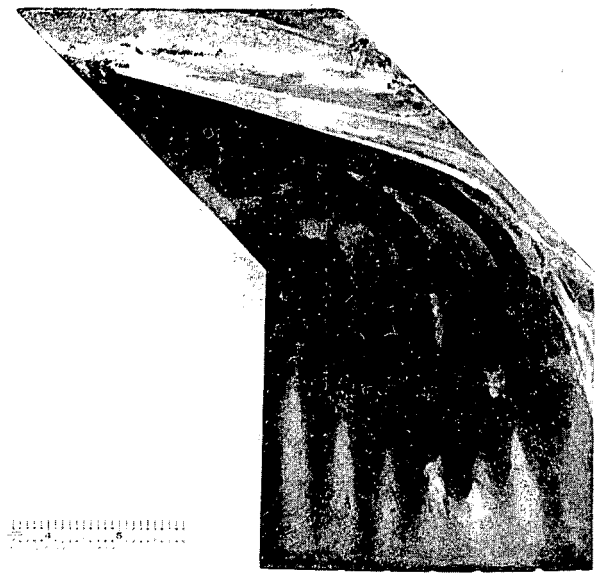

(a)

(b)

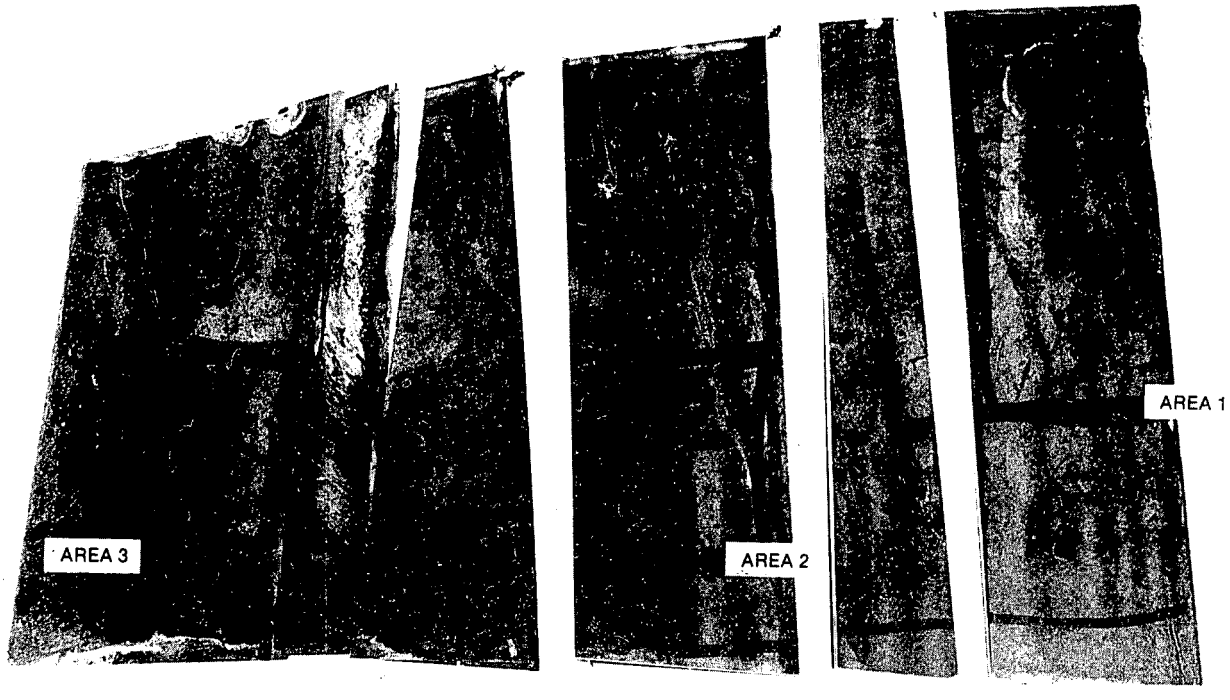

(c)

Figure 3-49. **(a) Outer endwall second-stage nozzle#3 as sectioned**
(b) Inner endwall second-stage nozzle#3 as sectioned
(c) Airfoil of second-stage nozzle #3 as sectioned

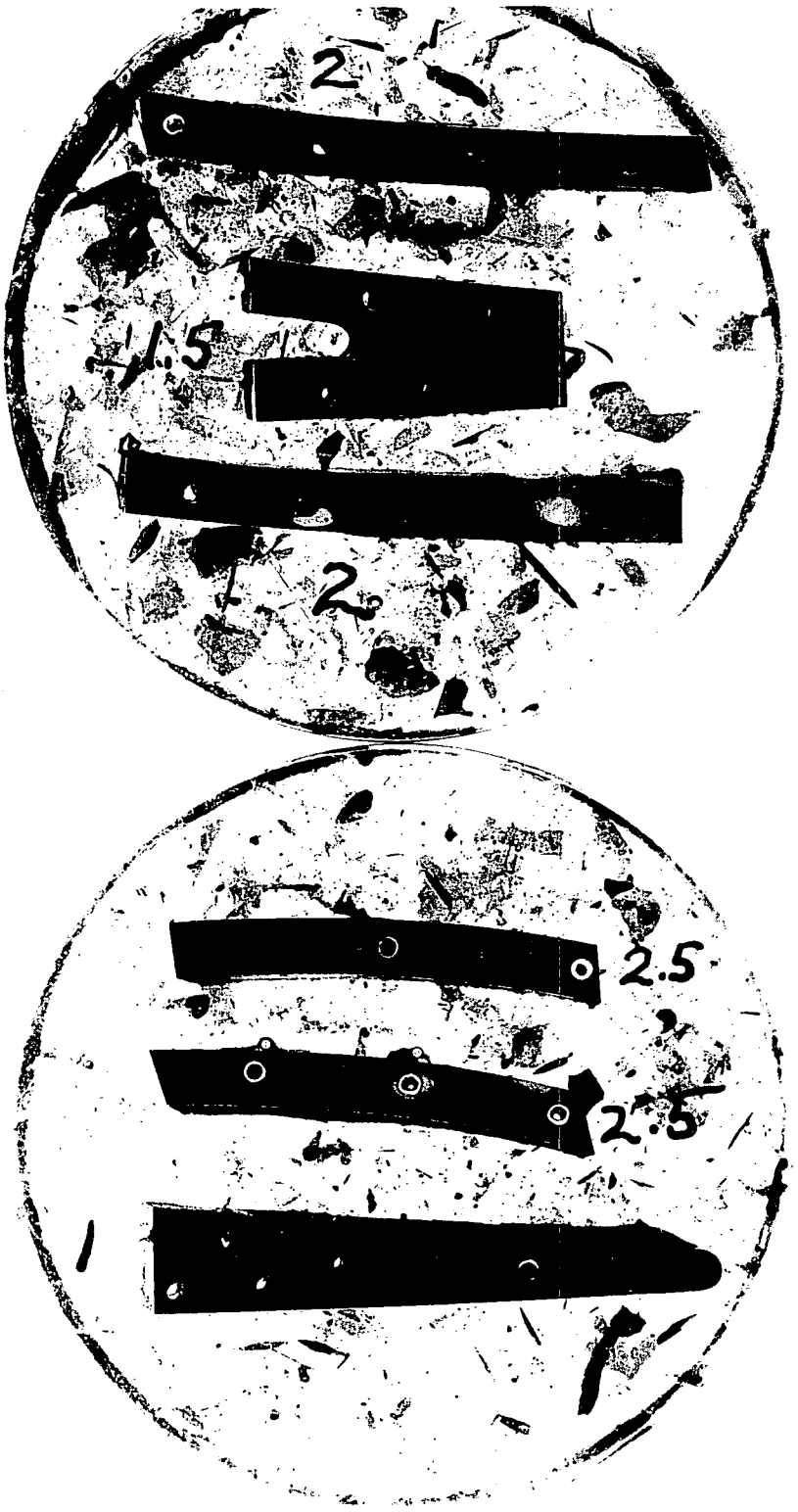

Figure 3-50. **Airfoil cross sections taken near the outer endwall of the second-stage nozzle.**

Figure 3-51. Leading edge airfoil cross section taken near the outer endwall of the second-stage nozzle

have caused any significant deviations in their temperature indications. As can be seen in Figure 3-54, the thermocouples are ungrounded and the junction is not alloyed with the high thermal conductivity material installation. The high thermal conductivity material is well attached to the shield around the thermocouple, and the shield does not touch the walls of the hole through which it was placed.

- **Braze Joints**

  An examination of the braze joints contained in these sections was performed. Figures 3-55 and 3-56 show typical braze joint conditions found in this tested nozzle. The braze joint between the outer endwall manifold and airfoil shaped cover is shown in Figure 3-55(a). The width of the braze joint varies from 0.006 to 0.025 inch. Braze joint integrity is good, with only minor porosity and nichrome particles visible in the braze joint. (The nichrome was added to aid in brazing these wide gaps). This demonstrates the effectiveness of the wide gap brazing procedures used with the gold, nickel, and palladium braze alloys.

  The ability of the braze alloy to flow into large relatively narrow gaps is shown on Figure 3-56. The braze alloy flowed more than 0.160 inch into a gap which ranged from 0.002 to 0.007 inch wide. A minimal amount of porosity can be seen in the braze joint.

  The wide-gap brazing addition of nichrome powder can be clearly seen in Figure 3-55(b). This joint is between the outer endwall manifold and airfoil shaped cover. Essentially, no diffusion zone can be seen between the nichrome

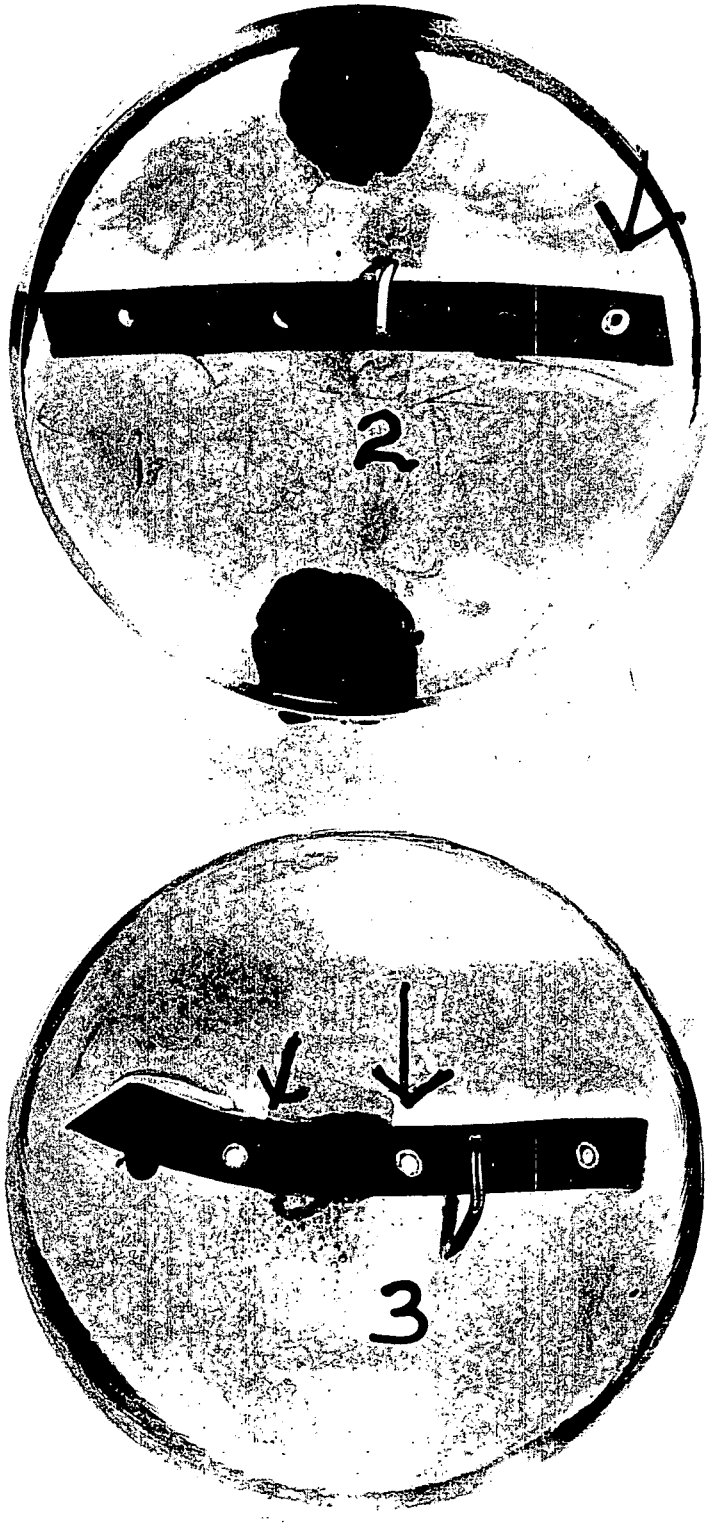

Figure 3-52. Cross sections of the surface thermocouples from the second-stage nozzle

Figure 3-53. Cross sections taken through the outer endwall of the second-stage nozzle

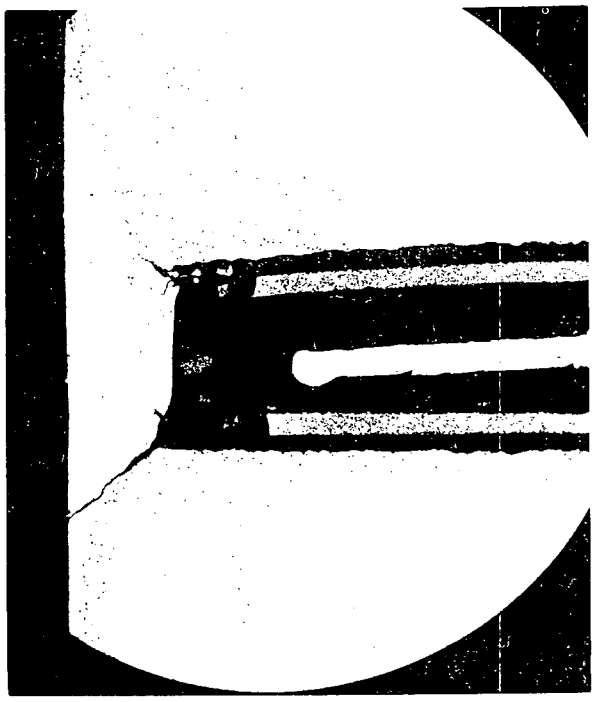

Figure 3-54. Surface thermocouple cross section from area 3 of the second-stage nozzle (magnification 22.5X)

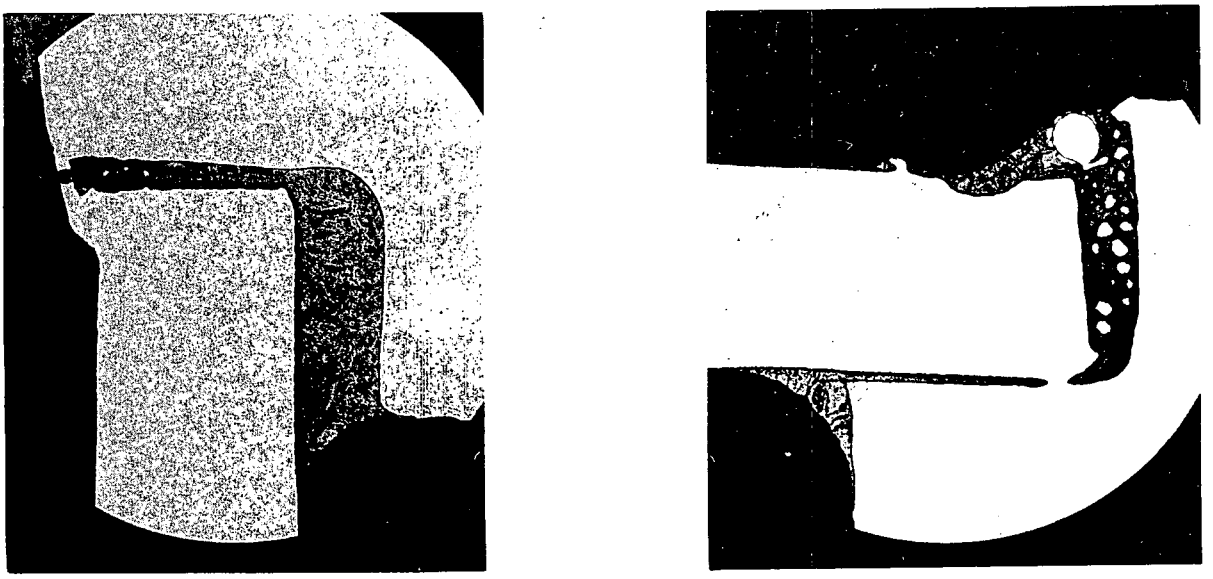

(a) (b)

Figure 3-55. Second-stage nozzle braze joint in outer endwall airfoil-shaped manifold (magnification 22.5X)

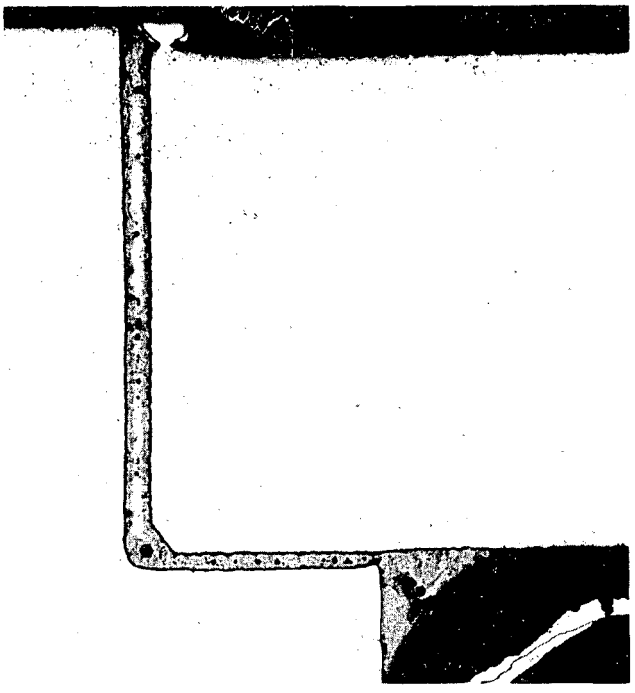

Figure 3-56. Second-stage nozzle braze joint in outer endwall trailing edge manifold (magnification 20X)

particles and braze alloy. A slight diffusion zone can be seen around the stainless steel wire at the top of the braze joint. Slight porosity can be seen in the joint.

No signs of cracking, tearing, or other problems could be seen in any of the braze joints examined. All the braze joints appear in excellent condition and no leakage from any braze joint was detected.

- **Casting Defects**
  The metallographic sections were also examined for casting defects. Two typical casting defects found in the nozzle are shown in Figures 3-57 and 3-58. A linear oxide cluster near the gas path surface is shown in Figure 3-57, and an oxide inclusion extending in from the gas path surface is shown in Figure 3-58. These casting defects are typical of those observed in investment castings. No cracking or signs of distress around any casting defect in this nozzle was observed.

- **Repair Weld**
  A typical repair weld during nozzle fabrication is shown on Figure 3-59. This was the result of the removal of an oxide inclusion by grinding and rewelding of the casting using a tungsten inert gas welding technique with IN718 filler wire. The weld produced a micro-crack in the nozzle, which propagated approximately 0.005 inch into the casting and stopped. No sign of continued crack propagation during nozzle testing was found.

- **Micro-Cracking**
  Examination of the area around the cooling passages revealed numerous cracks originating from the inside of the cooling passages. These cracks were primarily observed in the airfoil cross sections, with a larger number of these found near

Figure 3-57. Casting defect, linear oxide cluster type, found near the gas path surface of the second-stage nozzle (magnification 45X)

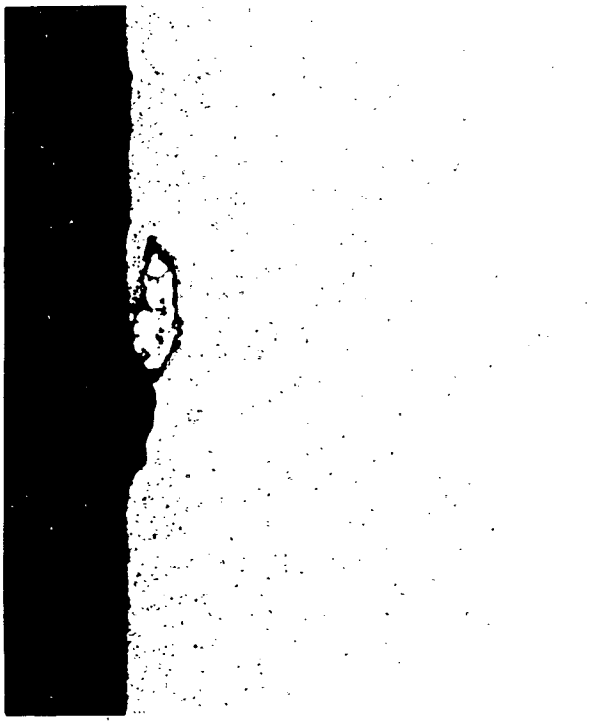

Figure 3-58. Casting defect, oxide inclusion type, found extending in from the gas path surface of second-stage nozzle (magnification 45X)

Figure 3-59. Typical weld repair of the second-stage nozzle showing a microcrack (magnification 90X)

the pitch section of the airfoil as shown on Figure 3-60. Etching revealed that all of these cracks were propagating along the IN718 grain boundaries, some toward the hot-gas path surface and some toward the cored surface of the nozzle. All the passages containing cracks had internal deposits, as described earlier.

The sections containing cracks were repolished and etched to look for slip lines and twinning. No indications of this kind were observed, indicating a lack of plastic deformation around the cracks.

Scanning Electron Microscopy.

A section was removed from the trailing edge to investigate the cause of water leakage associated with the two pinpoint indications as found by fluorescent penetrant inspection. The section was ground down parallel to the trailing edge cooling passage from the side opposite the two indications, until one half of the passage was removed. This allowed an examination of the inside of the trailing edge passage by scanning electron microscopy (SEM). In a similar fashion, the fifth cooling passage in the airfoil section of the nozzle was also prepared for examination. This passage was selected for examination because the design analysis had predicted that the maximum strains in the nozzle would occur in this region.

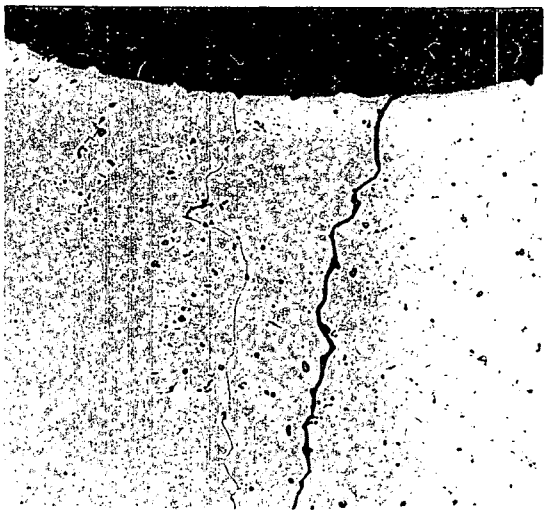

(a) Magnification 90X

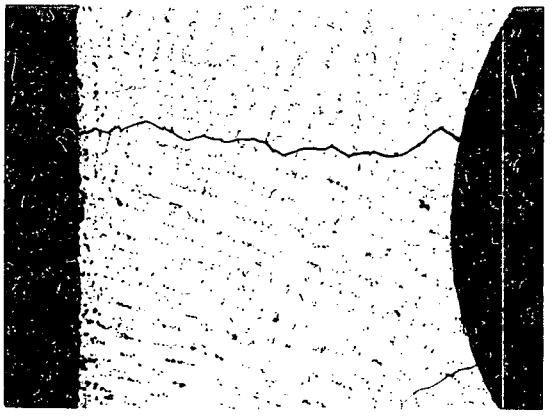

(b) Magnification 45X

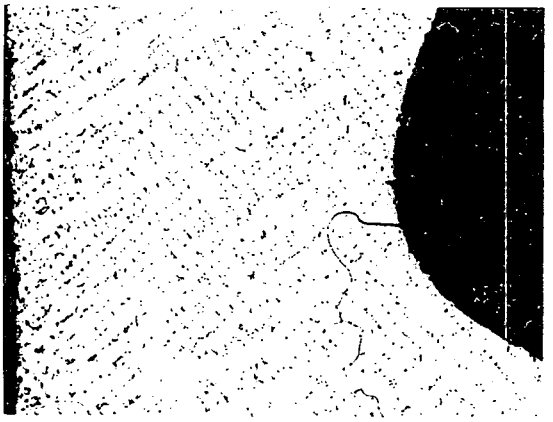

(c) Magnification 45X

Figure 3-60. Cracking from the inside of a cooling passage in the second-stage nozzle (magnification 90X)

A porous white deposit was found to line both the trailing edge and the fifth cooling passage. To reveal the metal surface beneath this deposit, the sample of the fifth cooling passage was immersed in a dilute (~50%) hydrochloric acid solution and heated to 150-200 °F. After about 15 hours, the sample was removed and examined. Most of the deposit was chemically removed, however, there was still a white film on portions of the inside surface of the cooling passage. Exposed portions were macro-etched in the process.

Dispersive x-ray energy spectra taken of the deposit inside the trailing edge passage is shown in Figure 3-61. The deposit was found to be rich in calcium, magnesium and silicon. Cracks could be seen in areas where the deposit had been removed during grinding (Figure 3-62). In these SEM photographs, the long dimension of the picture is parallel to the cooling passage direction. Figure 3-62(c) is the crack which was found to be associated with the pin-point indications observed on the exterior of the nozzle by fluorescent penetrant inspection.

To explore the fracture surface of the crack shown in Figure 3-62(c), two precision diamond saw cuts were made perpendicular to the trailing edge cooling passage direction, and the sample was carefully broken apart. Intergranular fractures are shown in SEM Figures 3-63 and 3-64. A crack can be seen propagating from the main fissure in Figure 3-63, while in Figure 3-64 a small portion of the sample showing the freshly fractured (during opening of the crack) surface is visible in the lower portion of the photograph. This freshly fractured area exhibits a transgranular mode compared to

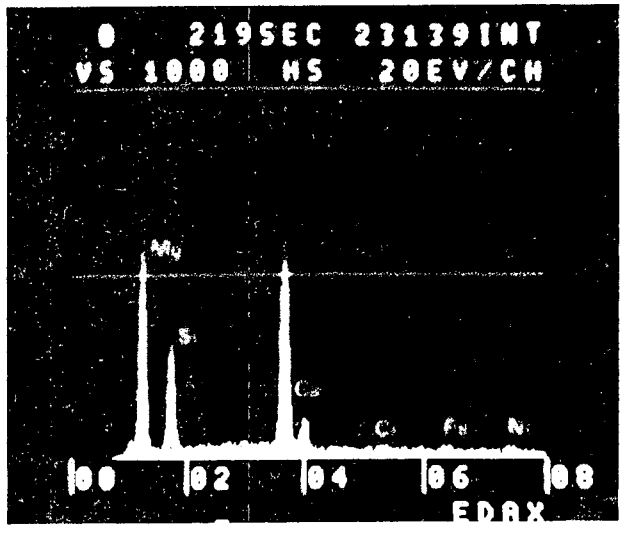

Figure 3-61. Dispersive x-ray energy spectra of the white deposit inside the trailing edge passage of the second-stage nozzle

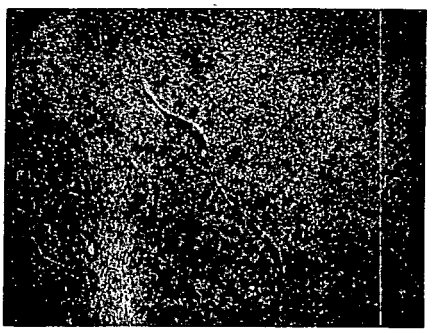

(a)

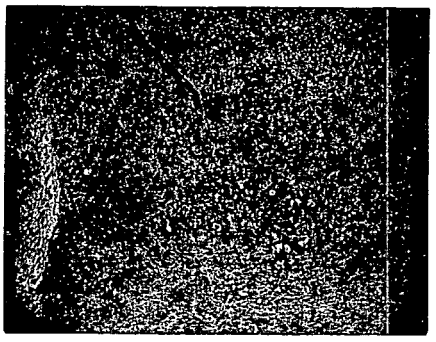

(b)

(c)

Figure 3-62. Cracking from the inside of the trailing edge cooling passage of the second-stage nozzle (magnification 100X)

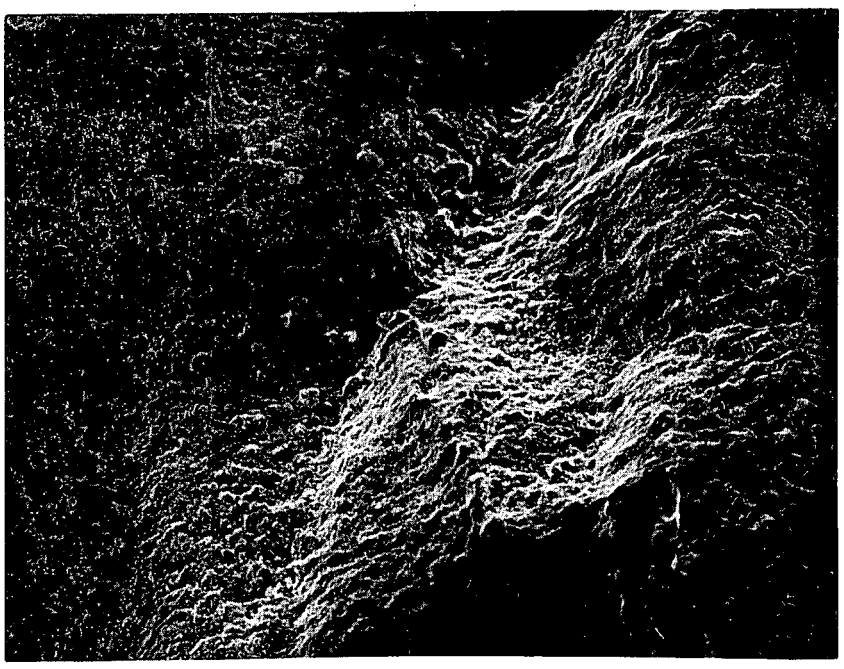

Figure 3-63. Trailing edge crack fracture surface of the second-stage nozzle (magnification 200X)

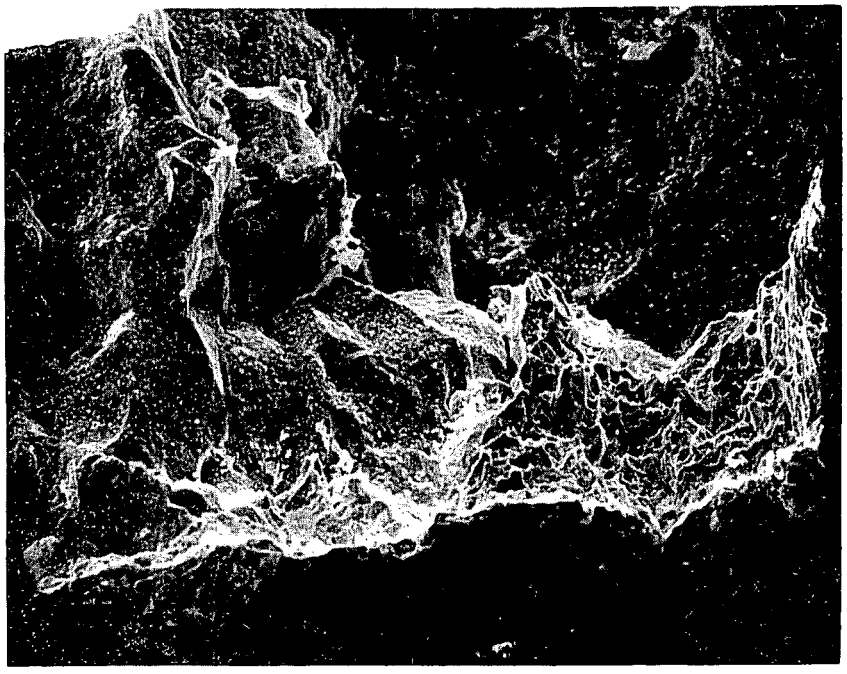

Figure 3-64. Trailing edge crack fracture surface and freshly fractured area of the second-stage nozzle (magnification 500X)

the intergranular crack propagation mode. Dispersive x-ray energy spectra analysis of the oxide film on the fracture surface identified sodium as being present along with the normally present constituents of IN718.

The fifth cooling passage showed etched grain boundaries (Figure 3-65) and fissures in the remaining oxide scale (Figure 3-66). These grain boundaries were most probably etched during chemical attempts to remove the deposits from this passage. The fissures in the oxide may or may not have been associated with cracks in the nozzle. However, no definitive cracking of the nozzle was observed in areas which had been chemically cleaned.

The sample fractured from the trailing edge cooling passage was subjected to replica cleaning in an attempt to remove the oxide from the fracture surface. This technique did appear successful in several areas, but not uniformly across the sample. The sample was then re-examined by SEM to look for fatigue markings on the fracture surface. None could be found.

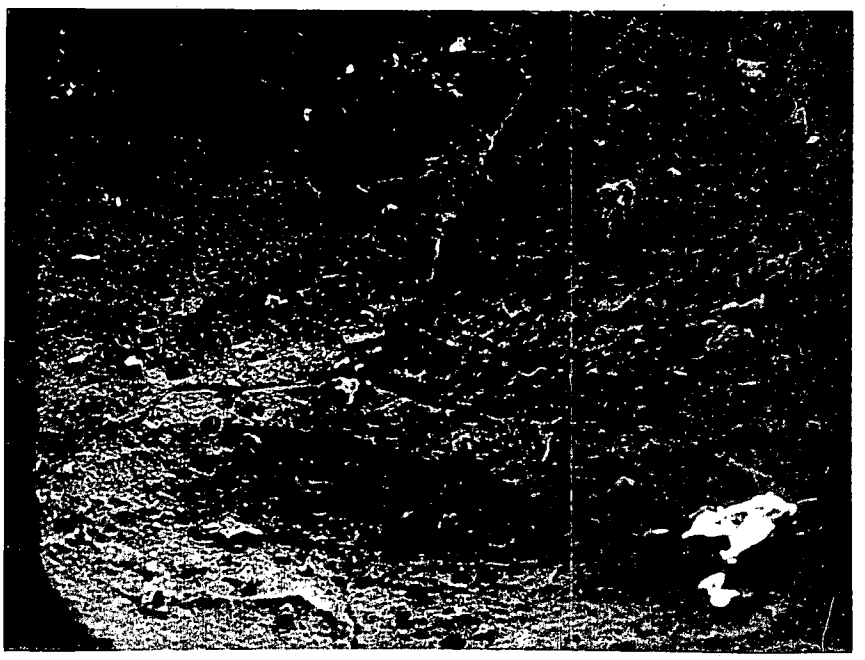

Figure 3-65. Second-stage nozzle fifth cooling passage internal surface showing etched grain boundary (magnification 200X)

Micro-Probe.

A section taken near the pitch line through the airfoil was examined by a combination of SEM/Micro-Probe to obtain distribution maps of the atomic elements in selected areas surrounding the cracks observed in the nozzle. A region in one of the cracks containing a corrosion product inside the crack is shown in Figure 3-67. The crack is running through a carbide which is just below another carbide in the IN718 matrix. The corrosion product appears within the carbide through which the crack is running. Preliminary dispersive x-ray energy anlysis showed that this corrosion prod-

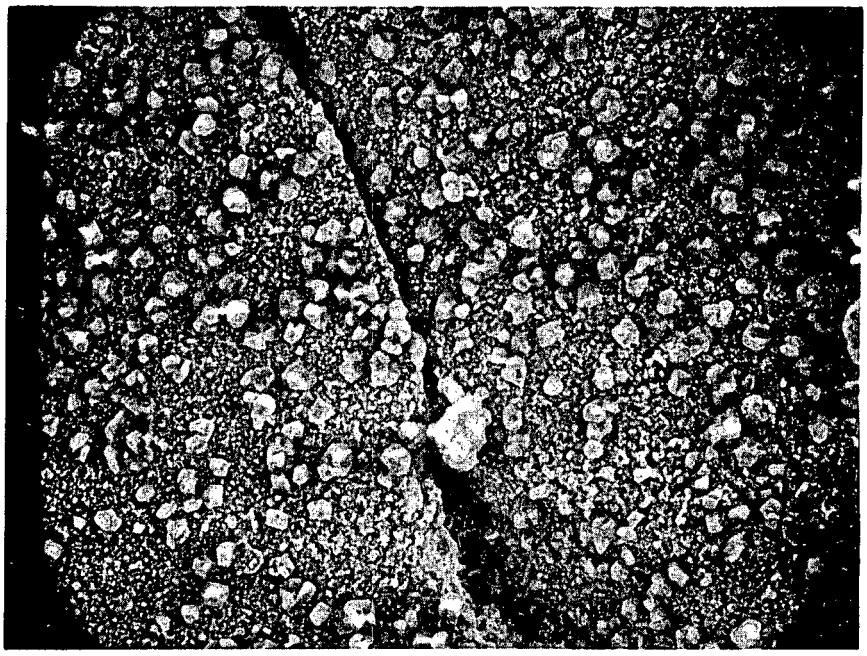

Figure 3-66. Second-stage nozzle fifth cooling passage inside surface showing fissure in the oxide layer inside the passage (magnification 500X)

uct was richer in Cb and Na than was the carbide. Based on this analysis, a series of x-ray back scatter images were taken. Figures 3-68, 3-69, 3-70, and 3-71 are scans taken from this area for the elements Cr, Cb, 0, and Na, respectively. As expected, the corrosion product and carbides are deficient in chromium (Figure 3-68), and they are rich in columbium (Figure 3-69), compared to the alloy 718 matrix. The corrosion product appears somewhat less rich in columbium than the carbides. The oxygen backscatter image (Figure 3-70) clearly shows the crack path. The corrosion product, as well as the crack, are rich in oxygen compared to the surrounding alloy matrix and carbides. The sodium backscatter image (Figure 3-71) shows a concentration of sodium in the corrosion product, but essentially none in the remainder of the region.

Another area of the same crack near the tip was similarly examined, and x-ray backscatter maps showing oxygen and sodium were taken. Figures 3-72, 3-73, and 3-74 show these results, and generally indicate the same pattern as the previously examined area. The crack appears rich in oxygen, particularly at corrosion product sites, and also appears rich in sodium at corrosion product sites.

Secondary Ion Mass Spectometry.

The sample used in the microprobe examination was also examined using secondary ion mass spectrometry (SIMS). This examination was done to confirm the presence of sodium in the crack by an independent technique. Figure 3-75 shows two different regions of a crack in this specimen where sodium was detected (in white). A faint indication of hydrogen was also detected in one of these regions. This confirmed the presence of sodium in the cracks.

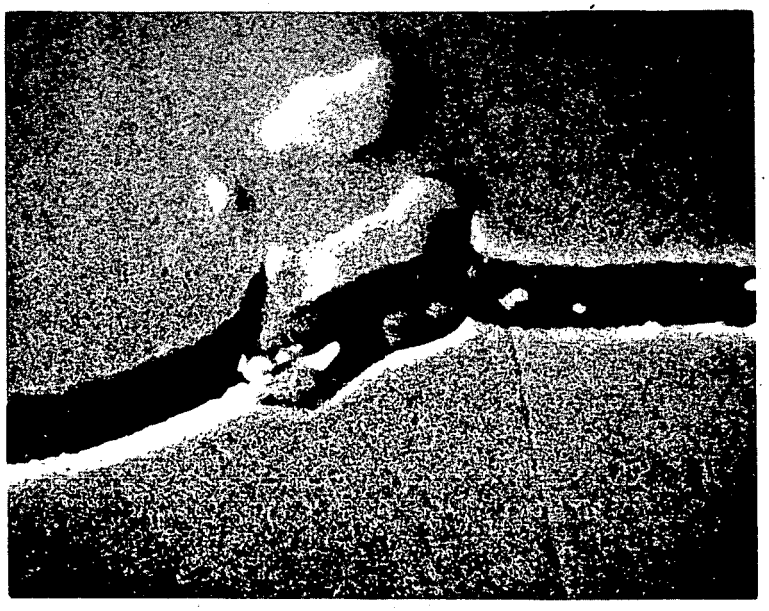

Figure 3-67. SEM of the crack in the second-stage nozzle showing carbides and corrosion product in area 1 (magnification 4000X)

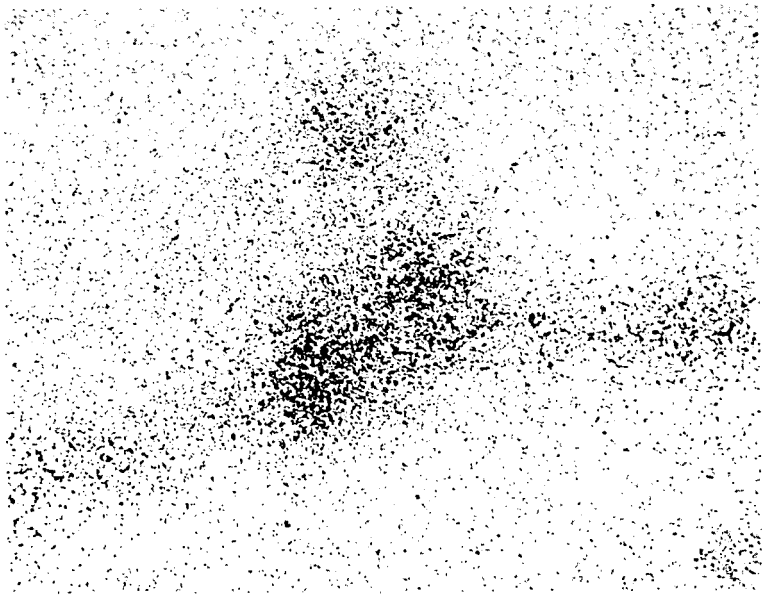

Figure 3-68. X-ray backscatter of chromium in area 1 of the second-stage nozzle (magnification 4000X)

Figure 3-69. X-ray backscatter of columbium in area 1 of the second-stage nozzle (magnification 4000X)

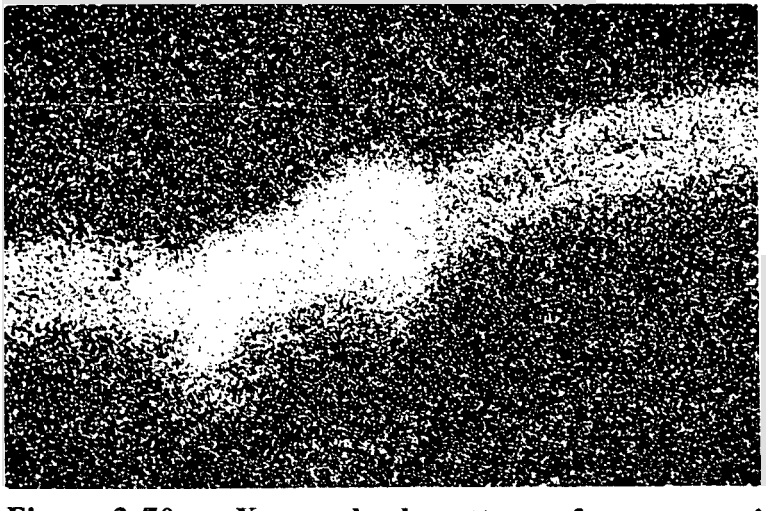

Figure 3-70. X-ray backscatter of oxygen in area 1 of the second-stage nozzle (magnification 4000X)

Figure 3-71. X-ray backscatter of sodium in area 1 of the second-stage nozzle (magnification 4000X)

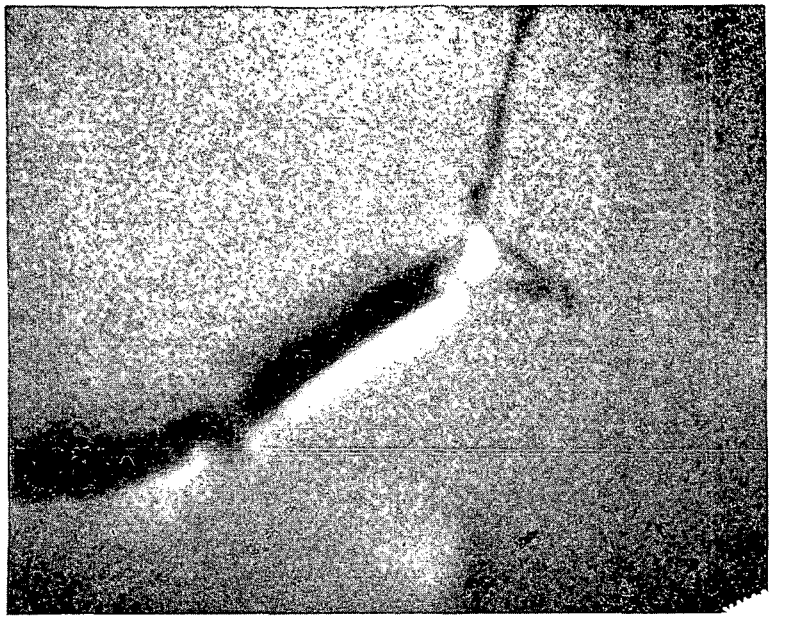

Figure 3-72. SEM of crack near tip, area 2, in the second-stage nozzle (magnification 4000X)

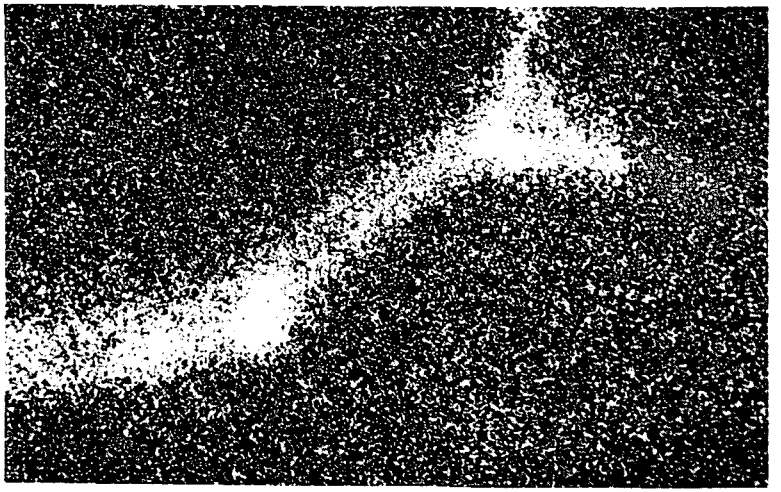

Figure 3-73. X-ray backscatter of oxygen in area 2 of the second-stage nozzle (magnification 4000X)

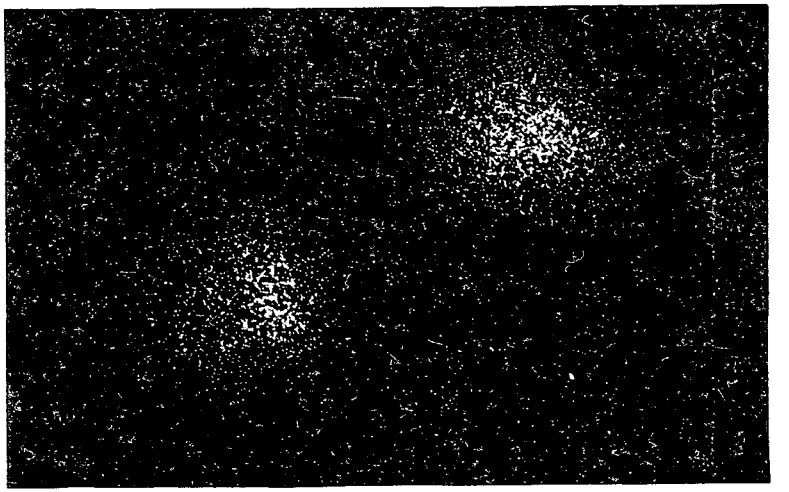

Figure 3-74. X-ray backscatter of sodium in area 2 of the second-stage nozzle (magnification 4000X)

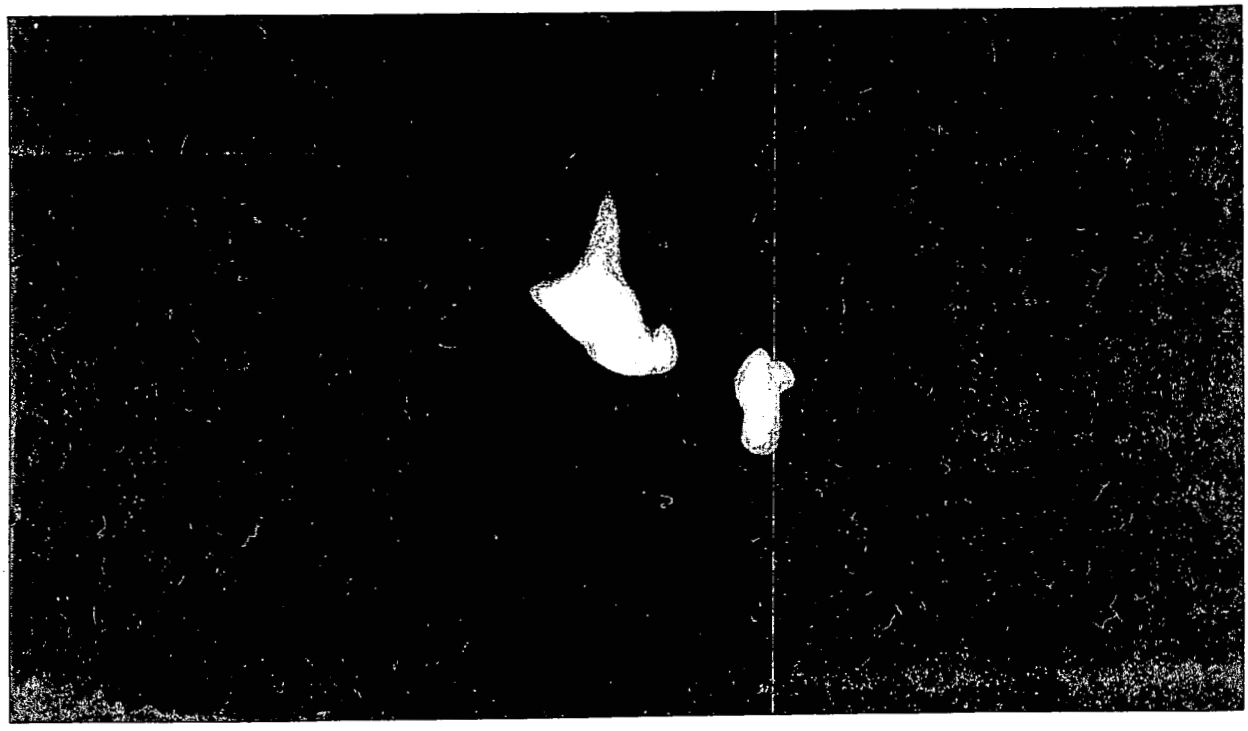

(a)

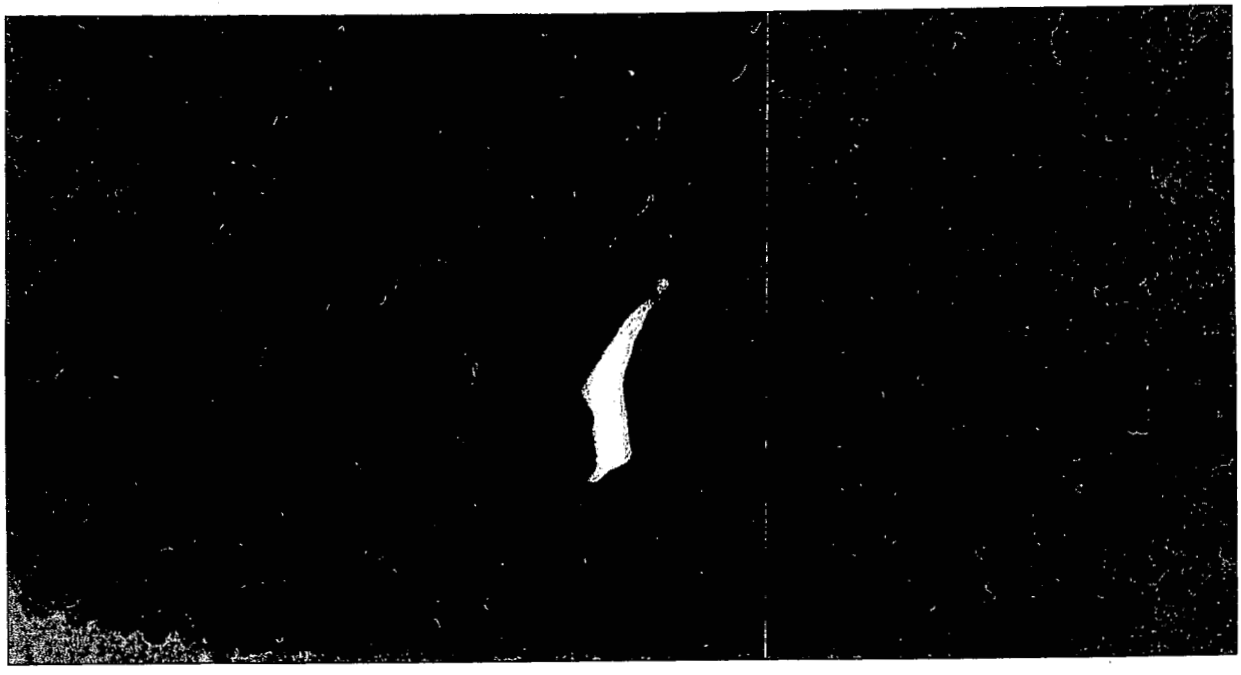

(b)

Figure 3-75. Secondary ion mass spectrometry image of sodium in a crack taken from the second-stage nozzle (magnification ~1000X)

Electron Microscopy.

A sample taken near the pitch line through the airfoil was etched using a solution of 50 parts HCl, 50 parts methanol, and 10 parts H_2O_2. A replica was then stripped for examination in an electron microscope. Figure 3-84 shows a typical area of this sample. The normally observed grain boundary substructure can be observed along with the extremely fine gamma double-prime precipitate. Comparison of this structure with control sample replicas of cast, hot isostatically pressed, and aged IN718 show no significant differences in microstructure.

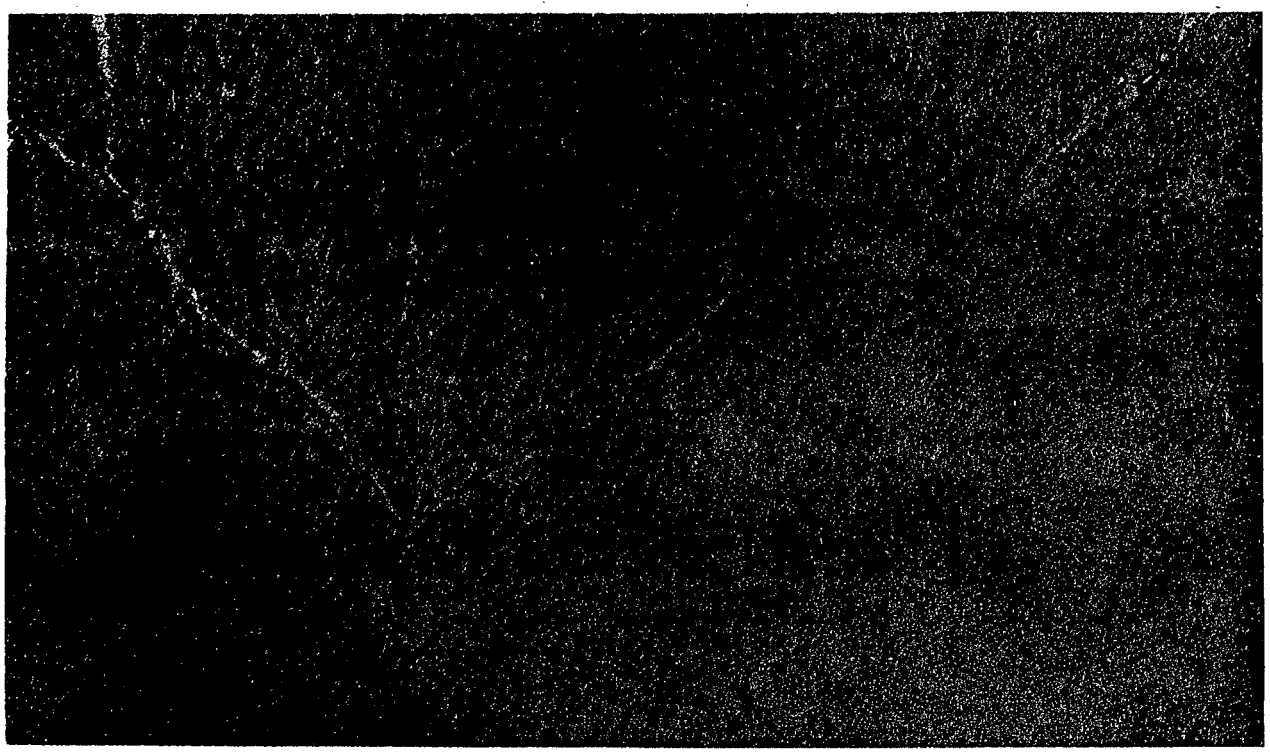

Figure 3-76. Electron microscopy replica of typical section in the second-stage nozzle showing grain boundary substructure and extremely fine gamma double prime (magnification 10,000 X)

Hardness.

Both macro (Rockwell C) and micro (Knoop) hardness impressions were taken. The average of the Rockwell C hardness measurements taken on the nozzle was Rc-39. The specification requires a minimum of Rc-34.

A micro hardness traverse was made across a typical airfoil cross section. Values ranged from 455 to 520 Knoop with an averge of 480. This is the equivalent of Rc-44 to Rc-49 with an average of Rc-46.

3.8.4 Analysis

3.8.4.1 Cooling Water Quality

Analysis of the deposits inside the cooling passages of the sectioned test nozzle suggest that the cooling water circuit had become contaminated with raw makeup water during the extended cyclic testing. A review of the test logs revealed several factors which contributed to this contamination. During the extended cyclic test, one of the two main circulating pumps in the closed-loop cooling water system experienced seal leakage and was turned off. After 160 extended cycles, leakage from the seals of the main pressurizing pump was noted. Testing was interrupted until plunger seals in the main pressurizing pump were replaced. Testing then continued until a total of 361 extended cycles were accumulated, with each cycle taking approximately ten minutes to complete.

Fault condition test points were also run for several hours during this period. Significant nozzle metal temperature increases (from 20 to 70% higher than at the start of extended testing) were observed to occur around the 312th cycle. After fault condition testing, a non-recoverable reduction was observed in the coolant flow obtainable through the nozzles (from 20 to 36% decrease). At the end of testing, the main pressurizing pump was leaking badly. Because of this leakage, water was continually being made up during testing. The makeup system processed makeup water through ion exchange resins (to remove all anions and cations), a pH control station where sodium hydroxide was added to the water to maintain a nominal pH of 9, into a de-aerating device to remove oxygen, and finally into a 1000-gallon holding tank.

A check of the ion exchange resins after completion of the extended test period revealed that the resins were totally saturated and no longer effective in removing anions and cations. The resins were then regenerated, and the holding tank and cooling loop system was filled the remainder of the way with makeup water. At this point, a mixture of old water and makeup water was in the closed loop. A sample of this mixed water was analyzed by Environment One Corporation and the results appear in Table 3-15. Results show that even after the addition of quality makeup water, the coolant loop water was not within required specification for hardness or dissolved solids.

3.8.4.2 Effect of Cooling Water Quality On Test Nozzles

The inverse solubility of the compounds generally found in hard water (e.g., $CaCO_3$,$MgCO_3$) causes these compounds to precipitate on hot surfaces – in this case, the cooling passages of the nozzles. These deposits were observed to be heavier in the nozzle cooling passages which comprise the second leg of the flow path through the nozzle, where the nozzle metal temperatures and water temperatures are highest. As these deposits increased in thickness, the resistance to heat flow from the nozzle into the cooling water increased. This caused the nozzle's metal temperatures to increase and caused a corresponding reduction in the bulk water cooling temperature.

Table 3-15

POST-TEST COOLANT LOOP WATER ANALYSIS

Parameter	Measured (ppm)	Specified (ppm)
Total Organic Carbon	1	-
Hardness	21	0
Total Dissolved Solids	49	1
Fe	0.020	0.007
Cu	0.0057	0.005
CO_2	0.9	-
Ca	4.3	-
Mg	2.5	-
Na	9.3	-
pH	8.6	9 to 9.3

3.8.4.3 Crack Formation Mechanism

Considering the effect of these deposits on the cooling passage surface temperature and the data from the microscopy and microprobe analyses, a highly probable mode of crack formation can be deduced. Microscopy revealed the lack of any plastic deformation around the cracks. This observation indicates that these cracks were not caused by classical low-cycle fatigue (LCF). The observation that the cracks are all propagating intergranularly (not transgranularly, as in LCF tested samples) and not in a consistent direction, supports a crack formation mechanism which is primarily environmentally induced.

The presence of sodium and oxygen inside the cracks shows that corrosion was definitely occurring. The only source of sodium is from the sodium hydroxide pH additive used in the coolant loop. The presence of the sodium hydroxide in the water, in combination with the deposits observed inside the cooling passages, caused the following mechanisms to occur:

- During the low-power portion of the extended cyclic testing, water wetted the surface of the cooling passages through the porous deposit.
- As the hot gas temperature increased during the cycle, the water between the porous deposit and the surface of the cooling passage reached a temperature high enough to boil (> 572 °F at the cooling system operating pressure of 1250 psia).
- The water boiled off between the deposit and the cooling hole surface leaving behind a deposit of sodium hydroxide on the surface of the cooling passage.
- As the cycle was repeated, and the low-power conditions were again established, the same concentration mechanism was repeated, resulting in the rapid buildup of an extremely caustic water solution at the metal surfaces of the cooling passages.

A.J. Sedriks et al.[1] have demonstrated the susceptibility of Fe-Cr-Ni alloys to caustic stress corrosion cracking. Although they did not specifically test IN718, testing on alloys of similar composition shows that rapid stress corrosion cracking may occur in deaerated 50% NaOH at 600 °F, under a nominal stress of 65 ksi. These conditions are very similar to those encountered in the monometallic nozzle test.

The lack of any difference in nozzle material microstructure, as observed both optically and through the electron microscope, and the normal hardness values indicate that no change in microstructure occurred which could have contributed to the cracking observed in the nozzle.

3.8.4.4 Corrective Actions

The cracking observed in the cooling passages of the monometallic nozzles is the result of caustic stress corrosion cracking and not low-cycle fatigue. Conditions favorable to caustic stress corrosion cracking were created in the test nozzles by loss of water chemistry control. Deposits were created in the nozzles as a result of resin depletion. These deposits allowed the sodium hydroxide pH control additive to be concentrated on the surface of the cooling passages, thereby producing highly caustic local water solutions, and higher than normal nozzle metal temperatures. No evidence was found of any other failure modes, such as fatigue cracking or braze joint cracking.

If the cooling water chemistry had remained within specification, the nozzles would not have shown any significant change as a result of this testing. Provisions for continuous in-line cooling water quality monitoring should be made in future testing. Use of a volatile pH control agent, such as ammonium hydroxide, will prevent concentrations of pH control agent from occurring.

3.9 CONCLUSIONS

The major conclusion of the second-stage, water-cooled, nonmetallic nozzle testing is that the "technology readiness"* of the nozzle design and fabrication has been demonstrated. After successful completion of steady-state, cyclic, and fault condition tests for a total of 20 hours of fired testing at 2082 °F, and 413 thermal cycles, the following additional conclusions are drawn:

- Water cooling in conjunction with a monometallic structure is effective in maintaining desired nozzle metal temperatures in a high heat flux environment.
- Lack of test-related distress in the nozzles after completion of several hundred simulated turbine startup/shutdown cycles demonstrates their mechanical resistance to low-cycle fatigue. The nozzle response to transients was such that the maximum thermal strain occurred at the steady-state design point conditions, and strain reversals did not occur.

* "Technology readiness" is defined as "that stage of system, subsystem, or component development where all major problems associated with the performance specification goals have been solved, and where the solutions to these problems have been demonstrated successfully. At that stage, no major risks remain for an agency or contractor in scaling up the technology (if full-scale demonstration has not been performed) and in proceeding with mission (or commercial) development of the system, subsystem, or component."

- Fabrication methods for constructing a monometallic second-stage nozzle were validated. No fabrication related deficiencies were exposed during the tests, or during post-test inspections.
- Hydraulically, the second-stage monometallic nozzle water cooling system is well balanced. Measured flows through all portions of the nozzle cooling circuit meet design criteria.
- Subcooled nucleate boiling occurred in some return cooling passages at the 50% design cooling flow test point. However, a large margin to critical heat flux was maintained.

A goal of the HTTT program is to demonstrate the growth capability to 3000 °F firing temperature, which results in a second-stage nozzle inlet gas temperature of 2400 °F. Figures 3-26 and 3-27 show plots of critical nozzle temperatures as a function of gas temperature. Extrapolation of these results to 2400 °F gas temperature shows that critical metal temperatures remain less than 1000 °F. These temperatures show that the present design can survive at a 3000 °F firing temperature, and if required, cooler metal temperatures and an added margin to the onset of nucleate boiling can be obtained by reducing the coolant inlet temperature and/or by increasing the coolant flowrate. This extrapolation demonstrates that the required growth capability has been achieved.

Section 4

HOT-GAS PATH DEVELOPMENT TESTING CONCLUSIONS

The successful completion of full-scale, water-cooled nozzle testing in a simulated turbine environment has demonstrated the thermal performance and durability of both the composite, water-cooled, first-stage nozzle and the monometallic, water-cooled, second-stage nozzle. Testing and post-test inspection results have verified the mechanical, thermal, and hydraulic capabilities of these components at full GE-TRV turbine operating conditions.

A three-throat, two-nozzle cascade of the first-stage nozzle was tested at a measured average nozzle inlet gas temperature of 2730 °F, a nozzle inlet gas pressure of 11.3 atmospheres, and a gas flow rate of 6.37 lbm/sec/throat. In addition to steady-state operation at the design firing temperature, the nozzle cascade was exposed to extensive thermal cyclic testing. The relationships of important parameters such as coolant temperature, coolant flow rate, hot-gas temperature, and hot-gas mass flow rate were determined. A total of 42 hours at the design point and 617 thermal cycles were accumulated through the test period. This number of cycles is equivalent to approximately twelve years of cyclic life at utility base load service.

First-stage nozzle test results show that measured metal and coolant temperatures correspond well with predicted design values. This nozzle design is fully satisfactory for TRV application, and this design has been shown to have growth capability to 3000 °F firing temperature.

A post-test metallurgical examination of sectioned portions of the first stage test nozzles shows a totally bonded structure, confirming the post-test nondestructive inspection results and attesting to the excellent performance of water-cooled composite nozzle hardware.

A three-throat, two-nozzle cascade of the second-stage nozzle was tested at a measured average nozzle inlet gas temperature of 2082 °F, a nozzle inlet gas pressure of 5.4 atmospheres, and a gas flow rate of 8.07 lbm/sec/throat. In addition to steady-state operation, the nozzle was exposed to thermal cyclic testing. As with the first-stage nozzle test, parameter variation testing was also conducted. Parameters that were varied included coolant temperature, coolant flow rate, hot-gas temperature, and hot-gas mass flow rate. A total of 20 hours of testing at the design point and 413 thermal cycles were accumulated through the test period.

Second-stage nozzle test results show that measured metal and coolant temperatures correspond well with predicted design values. This nozzle design is fully satisfactory for TRV application, and the design has growth capability to 3000 °F firing temperature.

A post-test metallurgical examination of sectioned portions of a tested nozzle airfoil and endwall showed a substantial amount of calcium/magnesium rich deposits in the return leg of the cooling circuit passages, and intergranular cracks emanating from several of the cooling passages. Microscopy and microprobe analyses revealed that the

damage observed was the result of caustic stress corrosion cracking and not low cycle fatigue. Conditions favorable to caustic stress corrosion cracking in IN718 material were created in the test nozzles by loss of water chemistry control during the extended test period. If the water chemistry control had remained within specifications, the monometallic nozzles would not have shown any significant change as a result of testing. Continuous in-line cooling water quality monitoring and use of a volatile pH agent, such as ammonium hydroxide, will preclude caustic stress corrosion cracking in future applications.

The "technology readiness"* of water-cooled first-stage and second-stage nozzles has been demonstrated. After successful completion of steady-state, cyclic, and fault condition tests, the following conclusions are drawn:

- Water cooling in both a composite and a monometallic structure is effective in maintaining desired nozzle metal temperatures in a high heat flux environment.
- Lack of low-cycle fatigue (LCF) related distress in either structure after completion of several hundred simulated turbine startup/shutdown cycles demonstrates their mechanical resistance to LCF.
- Fabrication methods for constructing both a composite and a monometallic nozzle were validated. No fabrication-related deficiencies were exposed during the tests.
- Hydraulically, both the first-stage and the second-stage nozzles are well balanced. Measured flows through all positions of these nozzles meet design criteria.
- At reduced cooling flows, a large margin to critical heat flux was maintained.
- Both nozzle designs have growth capability to 3000 °F firing temperature.

* "Technology readiness" is defined as "that stage of system, subsystem, or component development where all major problems associated with the performance specification goals have been solved, and where the solutions to these problems have been demonstrated successfully. At that stage, no major risks remain for an agency or contractor in scaling up the technology (if full-scale demonstration has not been performed) and in proceeding with mission (or commercial) development of the system, subsystem, or component."

Section 5

REFERENCES

(1) A.J. Sedriks et al., "The Effect of Nickel Content on The Stress Corrosion Resistance of Fe-Cr-Ni Alloys in an Elevated Temperature Caustic Environment," *Corrosion 32* (4), April 1976.

Appendix A

INFRARED OPTICAL PYROMETRY

I. INTRODUCTION

The measurement of metal surface temperatures on the trailing edge area of the composite and monometallic test nozzles was required for the engineering evaluation of the water-cooled nozzle concept. The restriction of not disturbing the gas flow past the nozzles made the use of a non-contacting technique necessary. Infrared pyrometry provided a method for measuring these temperatures. The nozzle surface design temperature range of 600 to 800 °F is below the measuring range usually assumed for infrared pyrometry measurements. A development effort was undertaken to produce an instrument capable of accurate measurements in the 600 to 800 °F metal temperature range. The metal temperatures were to be measured through hot combustion gases with temperatures from 1200 to 2600 °F containing high levels of carbon dioxide (CO_2) and water vapor (H_2O).

II. PHYSICAL ENVIRONMENT OF THE MEASUREMENT

The test stand containing the test nozzles is approximately 96 inches in diameter. The optical path required for a pyrometer is in excess of 48 inches to the outside laboratory environment. This path covers the distance from the test nozzle suction side trailing edges through the mixing chamber end cover. The instrument must be capable of scanning the trailing edge region in two dimensions to produce a thermal map of the nozzle surface temperatures. The scanning pyrometer must not disturb the hot gas flow field, and must withstand the 500 °F, 50 psia environment into which 100 gallons/minute of water are being released for test stand cooling purposes.

III. INSTRUMENT DESIGN

The amount of infrared energy available from a metal surface, as specified by Plank's Radiation Law, limited the choice of detectors. The total amount of radiation from a black body surface varies with the fourth power of the absolute temperature. This property of radiating surfaces is expressed as the Stephen Boltzman Law:

$$E = \sigma T^4$$

where σ is the Stephen Boltzman constant,

$$\sigma = 5.6687 \times 10^{-12}\ watts \cdot cm^{-2} \cdot (\text{deg K})^{-4}$$

Thus, a comparatively large change in measured radiation is the main basis for the successful application of optical radiation techniques for accurate temperature measurements. The emissivity of the nozzle material ranges from 0.4 to 0.8 depending on surface condition, roughness, and oxidation (see Reference 1).

The pyrometer was designed as a "single color" instrument, i.e., a narrow spectral band near the wavelength of maximum radiance was selected as the primary optical excitation for the instrument. Proper choice of the wavelength band can improve the thermal sensitivity of the instrument as long as the detector signal to noise ratio is relatively large.

The sensor was designed with a compatible infrared light collecting and transmitting system. The harsh environment of the test stand required the detector sensor to be placed on the outside of the test stand. The radiant energy (Figure A-1) of a 750 °F surface peaks at approximately 4μ. There is very little radiant energy available below 2μ. The emission/absorption bands of the hot combustion gases indicates large water vapor bands at 1.875μ and 2.75μ (Reference 2). A smaller CO_2 band exists at 2.05μ, and a larger band is located at 4.0μ.

The function of the optical system is to collect a defined part of the nozzle surface radiation and convert this to an electrical signal which can be correlated with temperature. The optical system has a defined field of view. It is necessary to fully fill this field of view by the radiating surfaces during the measurement and reference calibration measurements. In this specific case, the surface radiation spot size was anticipated to be 0.250 inch in diameter.

The optical measurement is best described as target energy starting at the nozzle surface, proceeding through the hot gas into a light receiving hole in the pyrometer probe end; then reflecting from a gold first surface mirror through a sapphire lens assembly which is focused on the end of a special quartz fiber optical bundle which channels the energy to the detector. The fiber optics is connected to the detector housing with an end cap fiber assembly. A band pass filter and 400 Hz chopper and driver are imposed in front of the optical detector and preamplifier. The maximum operating temperature range of the detector components is 50 to 122 °F. Reliable measurements with a solid state detector require nearly constant temperatures. In this case the detector housing temperature was not allowed to change more than 5 °F, which is equivalent to a ±35 °F error in pyrometer readout.

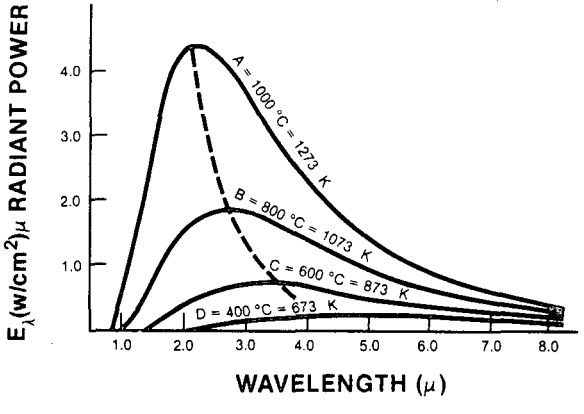

Figure A-1. Radiant power vs wavelength

There are three distinct infrared transmission windows in the atmosphere. These three windows relate to three possible detectors that could be used as infrared detectors.

- Silicon: 1.1μ
- Lead Sulphide: 2 to 2.5μ
- Lead Selenide: 3.4 to 4.0μ

The vanishingly small amount of radiant energy available at 1.1μ eliminated the silicon detector. The transmission characteristics of the quartz fiber optic tended to rule out lead selenide. Lead sulphide was the best commercially available detector compatible with the fiber optical system.

The effect of high-temperature and pressure combustion gases (constituted primarily of air) on the transmission properties of infrared radiation was not readily available in the literature. A calculation of the effect of temperature and pressure was completed by R.D. Lillquist of GE Corporate Research and Development (Reference 3) using a model developed by D.K. Edwards (Reference 4). Figure A-2 describes the transmission window central wavelength as a function of temperature and pressure for a propane-air combustion gas. Figure A-3 describes the transmission window width as a function of temperature and pressure for a propane-air combustion gas.

The pyrometer assembly was constructed as a double wall cylinder 72 inches long with a fiber optical bundle encased in a thin stainless steel tube and connected to a lens assembly. The lens assembly contained three sets of optical baffles to focus the

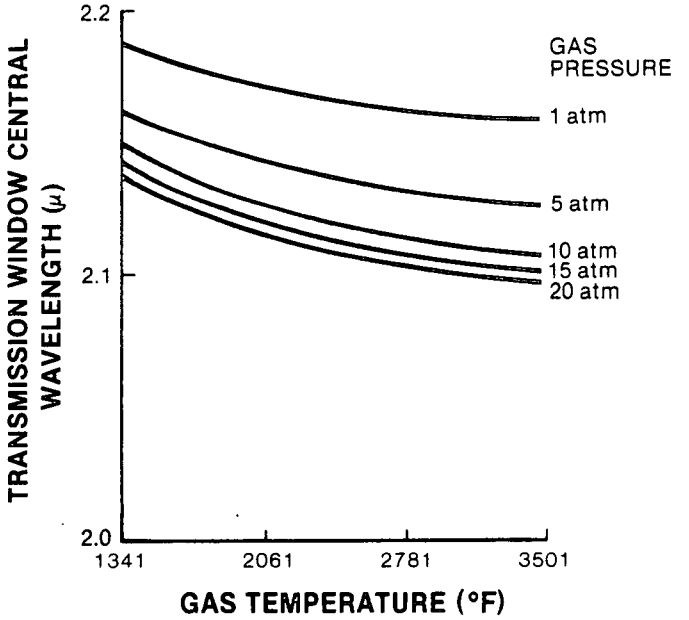

Figure A-2. Transmission window central wavelength

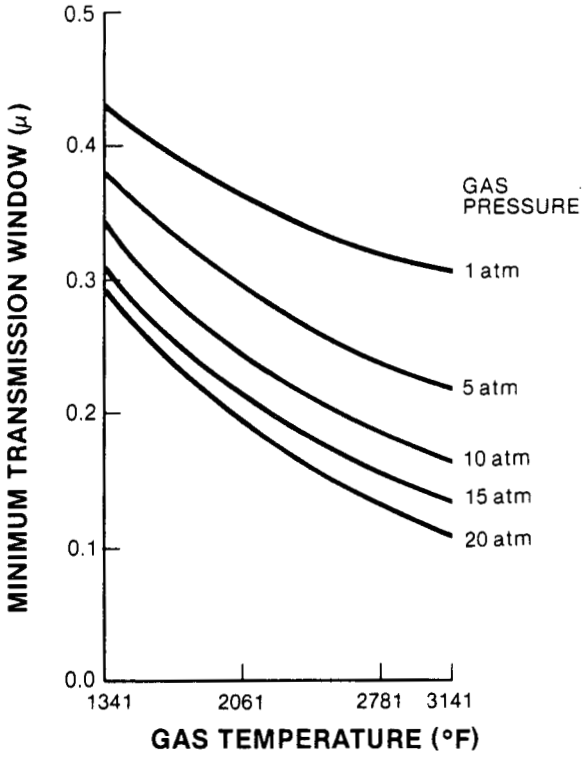

Figure A-3. Transmission window width

output of the lens directly on the end of the fiber bundle. The lens assembly was rigidly attached to the thin stainless steel tube containing the quartz fiber (Figure A-4). A gold first surface mirror with a 67.5 degree angle to the probe axis allowed scanning at nearly right angles to the probe axis. This angle was chosen to be perpendicular to the nozzle suction side surfaces, one inch from the trailing edge of the nozzle. The double wall cylinder design allowed water cooling the entire length of the probe. A purge line was attached to the central cavity near the quartz fiber bundle. The standoffs on the lens assembly permitted circulation past the lens and out the exit hole. Nitrogen was used as the purge gas for the majority of tests.

IV. LABORATORY CALIBRATION

The pyrometer as received did not contain a band pass filter. Since 72 inches of the quartz fiber permits only about 10% transmission beyond 2.0μ, a sharp cutoff filter cutting off all radiation below 2.0μ was used. To test the low-temperature accuracy of the instrument, a bench test using a 3-inch plug burner and a standard black body radiation furnace was used with the pyrometer looking through a methane flame into an oxidized copper target on the black body furnace. The methane flame contained 10% of the water vapor expected in a high-pressure propane combustion flame used in the nozzle tests. The initial tests with flame on/off conditions indicated the instrument could not detect low temperatures in the presence of water vapor. A double thickness of the 2.0μ sharp cutoff improved the low-temperature performance only marginally. A band pass filter (2.1 to 2.2μ) centered on the window improved the optical performance to better than 1%. See Figure A-5 for results.

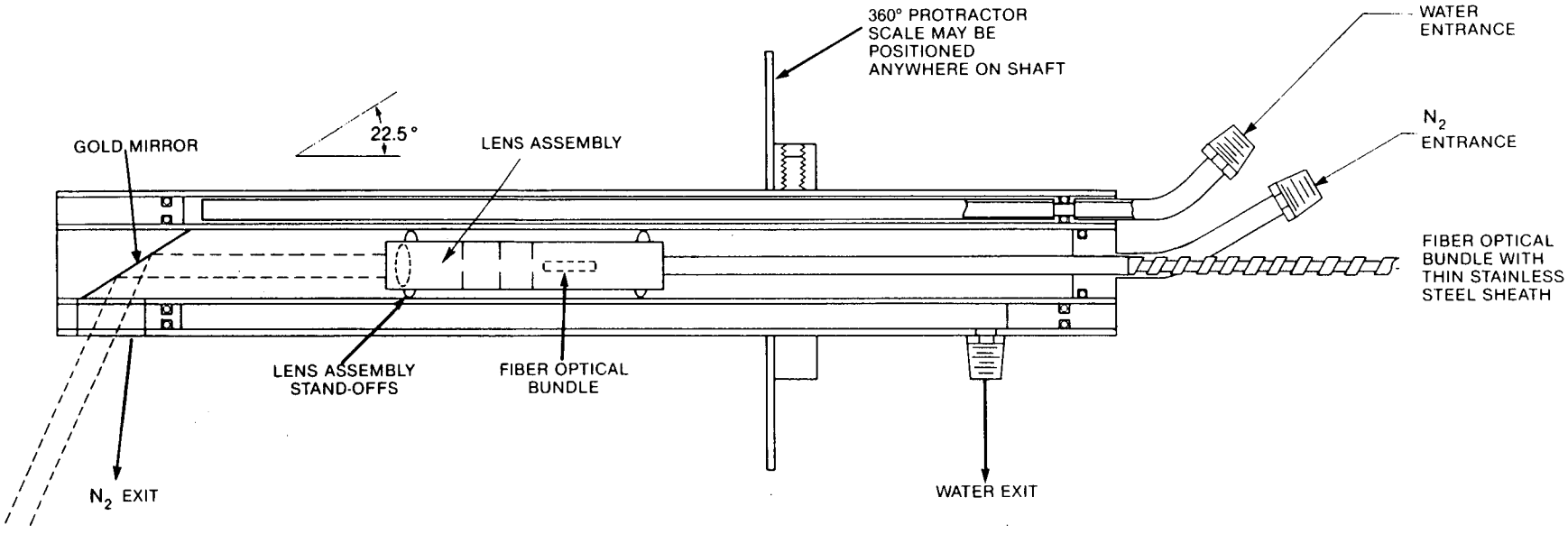

Figure A-4. Pyrometer assembly

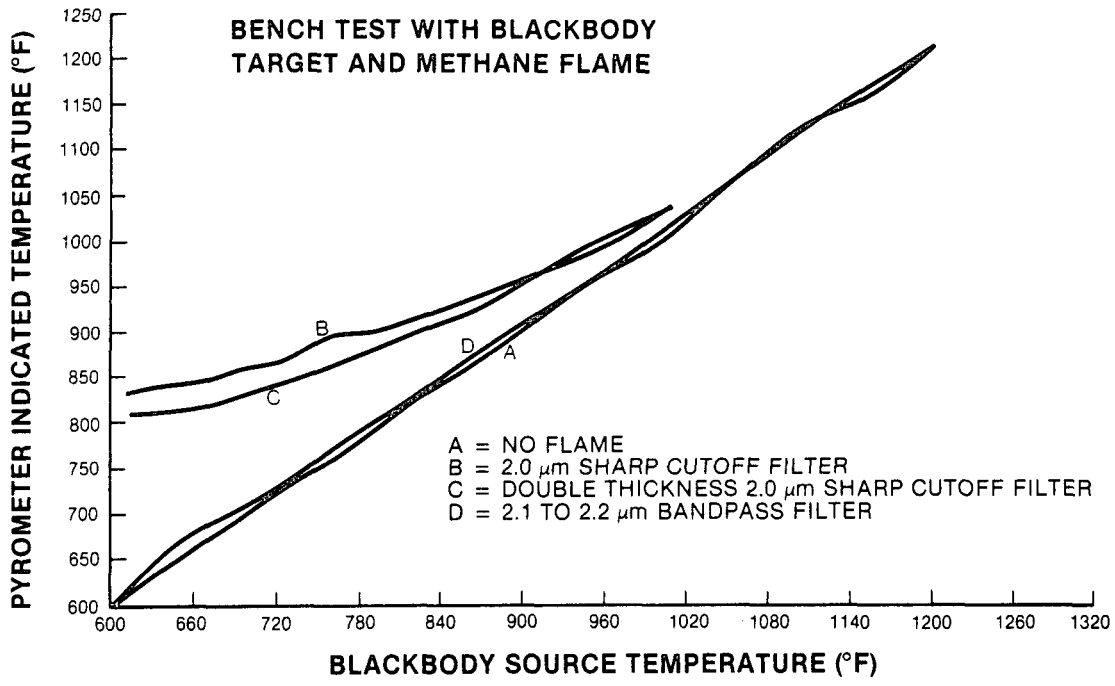

Figure A-5. Laboratory calibration of pyrometer

V. IN SITU CALIBRATION

To ensure the measure accuracy within the test stand during the nozzle tests, small embedded thermocouples were placed on the suction slave segments. The pyrometer was traversed in such a manner as to spot each thermocouple location. Adjustment of the pyrometer emissivity control to agree with the thermocouple reading provided an in situ calibration procedure.

VI. PHYSICAL ARRANGEMENT OF THE PYROMETER AND NOZZLES

The pyrometer probe was contained in a telescoping pipe arrangement. The unit is pictured in Figure A-6. The system resembles a periscope able to traverse in and out of the outer pipe. The outer pipe was threaded into the mixing chamber end cover and supported at midspan. There was concern for the thermal expansion of the pyrometer causing inaccuracies in locating the instrument during hot test conditions. The mixing chamber walls made of steel are rated for a 500 °F soak temperature. The pyrometer probe made of stainless steel with double the thermal expansion characteristic of the vessel wall would experience only a 250 °F nominal soak temperature. The two components expand in opposite directions by nominally the same amount, thus cancelling any thermally generated misalignment.

Figure A-7 illustrates the traversing and rotational motions allowing for two dimensional mapping of the nozzle suction surfaces, especially in the trailing edge region. For the composite nozzle, the distance from the pyrometer mirror opening to the nozzle surfaces varied from 10-7/8 to 13 inches. For the monometallic nozzle, the distance from the pyrometer mirror opening to the nozzle surface was 9-3/4 to

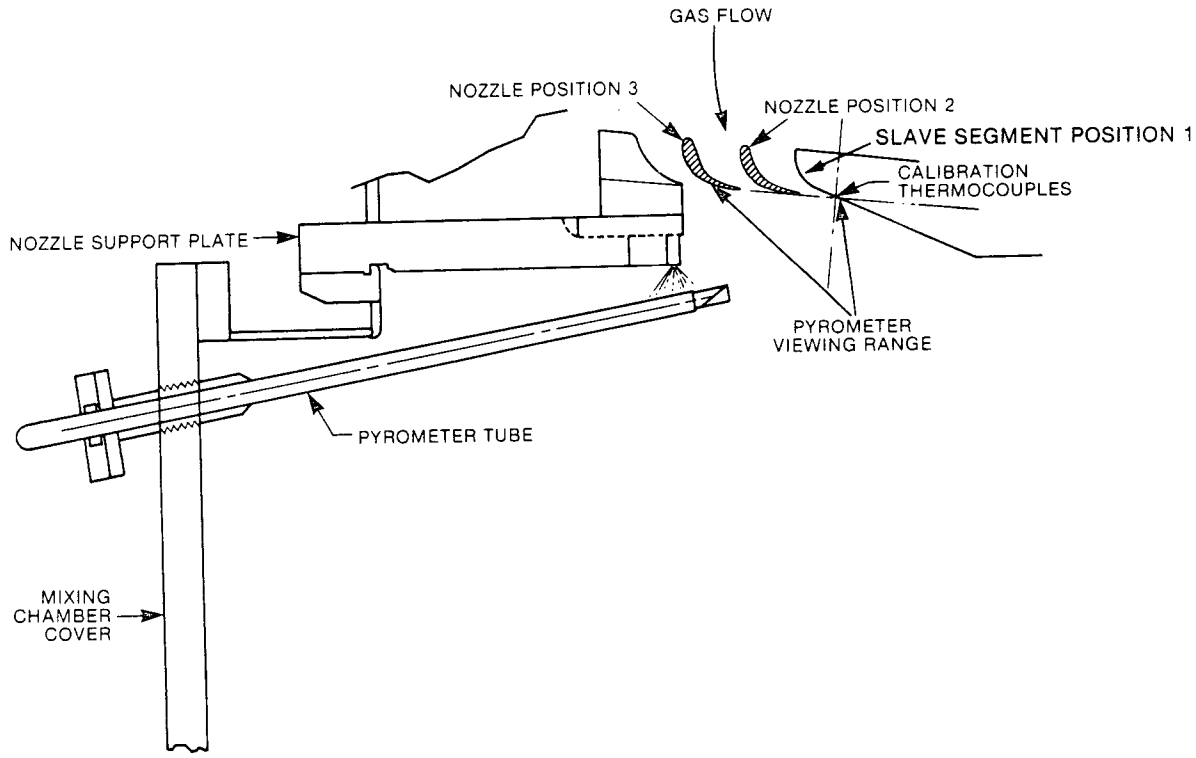

Figure A-6. Top view of pyrometer tube relative to nozzle cascade

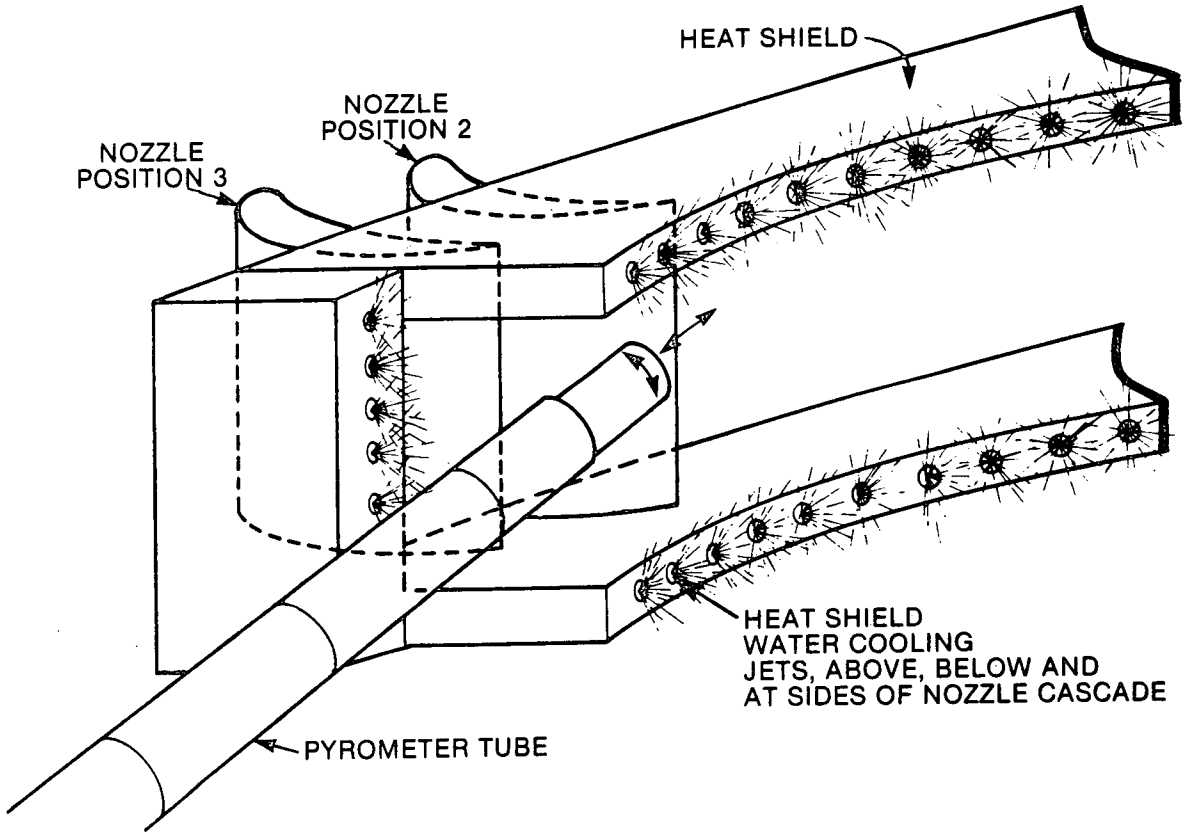

Figure A-7. Side view of pyrometer tube relative to nozzle cascade

12 inches. This had a minor effect on the spot size of the measured area on the nozzle surfaces. Spot size extremes were 0.330 to 0.275 inch. Of greater importance was the angle of the pyrometer scan to the normal surface of the nozzle. Exceeding a solid angle of 30° may cause reflections of hotter (or colder) infrared energy to be detected as a surface temperature. The physical arrangement of the nozzles in relation to the pyrometer indicate that a limitation would exist near the extreme leading edge position of the nozzles. The system was designed to be exactly normal to the surface of the nozzle one inch from the trailing edge.

VII. INITIAL TESTS

Several initial tests were made on the monometallic nozzle. A typical scan is shown in Figure A-8. The scan is a traverse from the trailing edge of nozzle position #3 across nozzle position #2 to the suction slave segment position #1. The pyrometer output exhibits a wide fluctuation of approximately 150°F. It was assumed that the trailing edge temperature of nozzle position #3 should be the same as nozzle position #2. It was suggested that the nearly choked flow through the two nozzle throats would cause an aspirating suction pulling tremendous amounts of water droplets back into the combustion gas stream. The hard water carbonate crusts on the top and bottom of the heat shield tended to confirm the presence of large amounts of water between the pyrometer and the nozzles.

An investigation of particle scattering from water droplets indicated that droplets near 2.0μ could efficiently scatter the spot infrared energy by a Mie Scattering mechanism, since the nozzles are the hottest surface within the cavity with the top, bottom and side heat shields cooled by water. Since the maximum embedded shield thermocouple was ~430°F, the scattering effect was thought to decrease the actual surface temperature of the nozzles. Figure A-9 describes the suggested two-layer conditions with the thicker water droplet layer on the extreme left. Four potential solutions are listed below:

1. Divert as much shield water as possible away from the cavity by installing right angle elbows in the shield water orifices.
2. Place a partition on one side of the nozzle cavity, thereby impeding the suction flow of the droplet laden air into the nozzle cavity.
3. Equalize the pressure on the nozzle side of the partition with compressor discharge air.
4. Place a pipe extension on the end of the pyrometer tube.

Elbows installed on the heat shield adjacent to the pyrometer were helpful. Placing compressor discharge air inside the partition, however, diverted the hot combustion gases into the far side of the heat shield on the vessel wall. The partition was removed.

A pipe extension (Figure A-9) was then placed on the end of the pyrometer tube matching the angle of the pyrometer optical beam. The pipe extended through the droplet layer into the hot, dry combustion gases. The end of the tube was of sufficient size that it could not intercept any part of the pyrometer infrared beam.

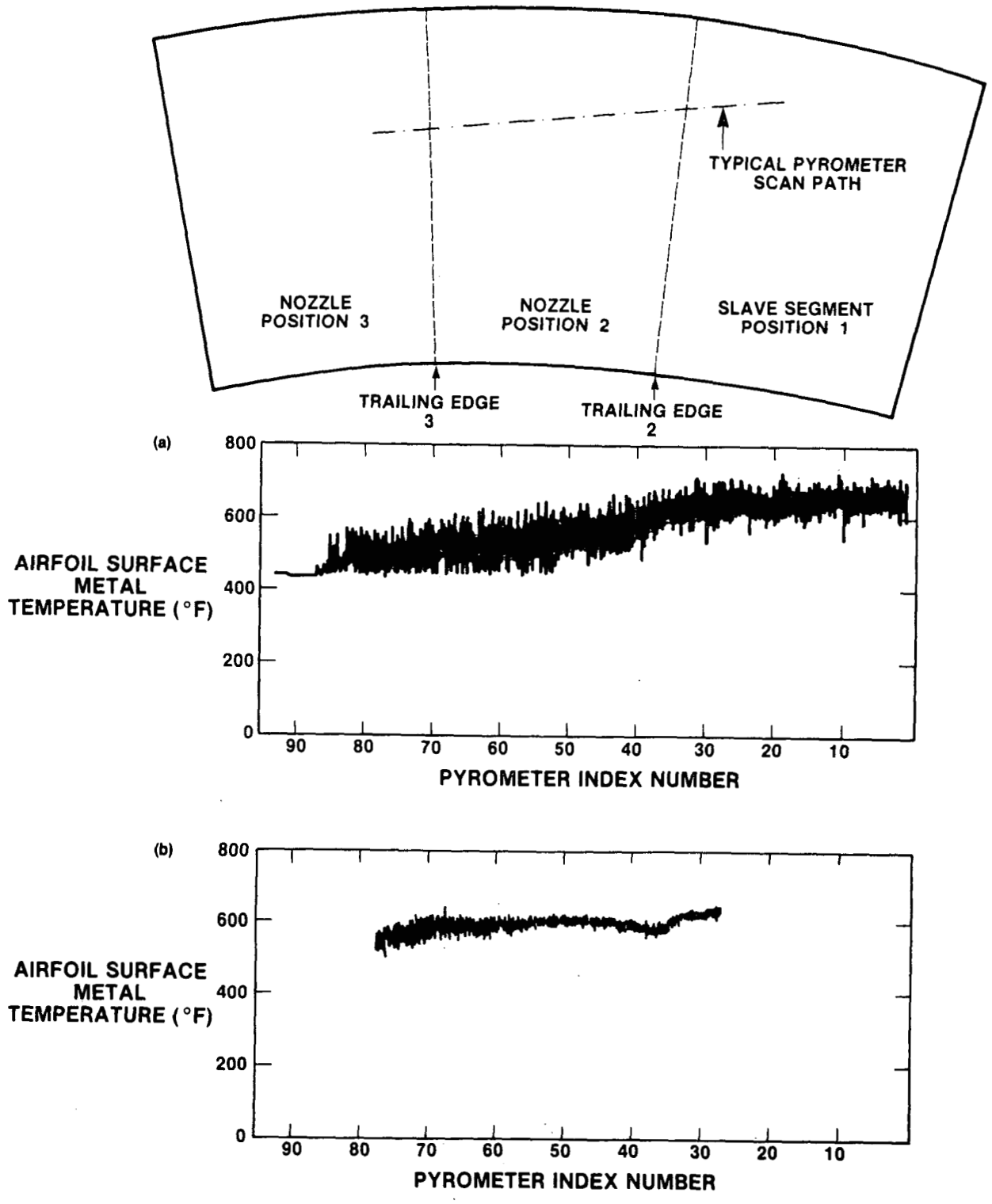

Figure A-8. (a) Second-stage nozzle test—initial pyrometer scan
(b) Second-stage nozzle test—pyrometer scan with extension pipe installed

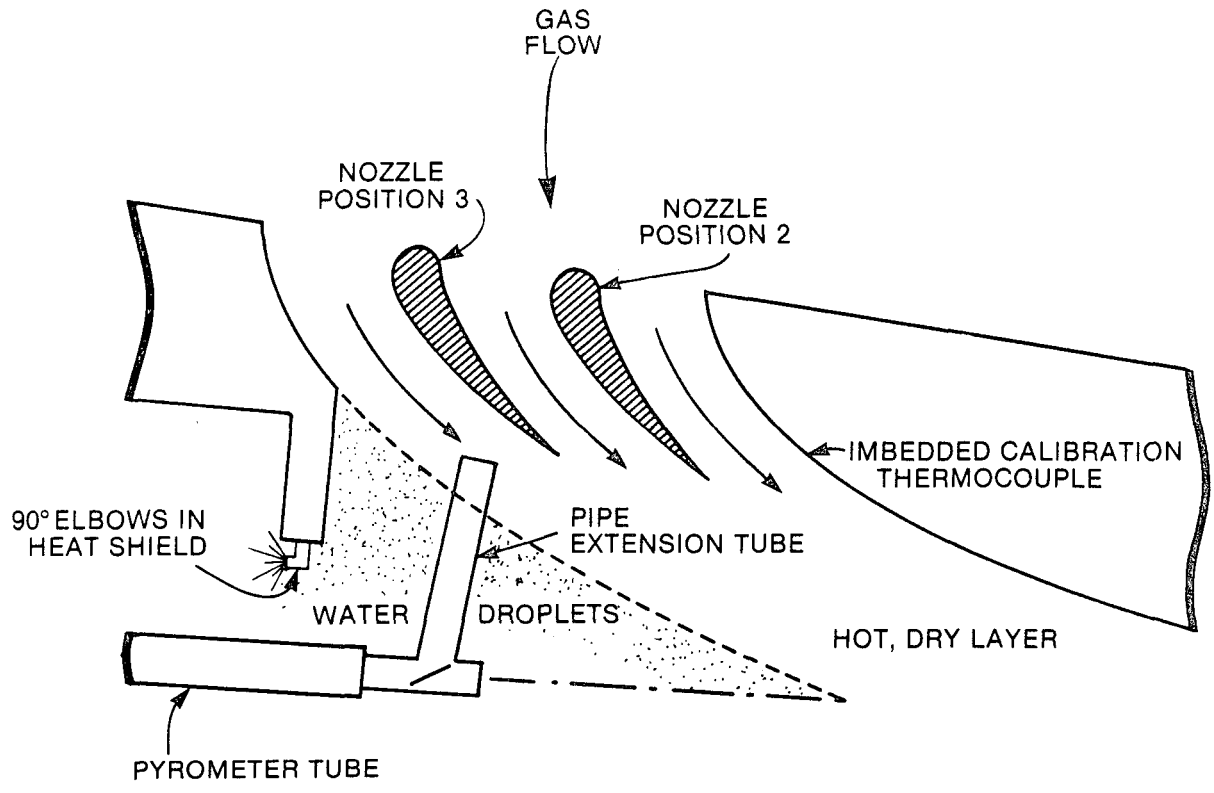

Figure A-9. Two-layer scheme of combustion gases

VIII. FINAL TESTS

With these hardware improvements, a series of tests were undertaken with extension tubes from 6 to 10 inches long mounted on the pyrometer. Prior to every series of tests, the pyrometer was cleaned and mounted in the test stand with the actuator mechanism and a rotational indexing vernier. The beam location was recorded, thus allowing repositioning of the instrument to a specific nozzle spot by recalling a specific digital location on the traversing actuator and rotational vernier scale. A typical scan with an extension tube installed is shown in Figure A-8b.

The traversing scans of the first stage nozzles are shown in Figure A-10. Surface temperatures of the trailing edge regions of the nozzle were 200 °F hotter than the central regions of the nozzles. The surface temperatures were also hotter near the top of the nozzles. This may have been caused by a higher heat transfer coefficient near the upper portion of the nozzle.

Time scans of the nozzle were made at various stationary locations when the combustion system was operated at steady-state conditions. The maximum temperatures observed confirmed the traversing scan data. Maximum temperatures observed on the trailing edge regions were 940 to 985 °F. Surface temperatures in the nozzle center, typically 2.5 to 3 inches from the trailing edges were 770 to 830 °F. The forward region temperatures, typically 3.5 to 4.5 inches from the trailing edge, varied from 720 to 760 °F.

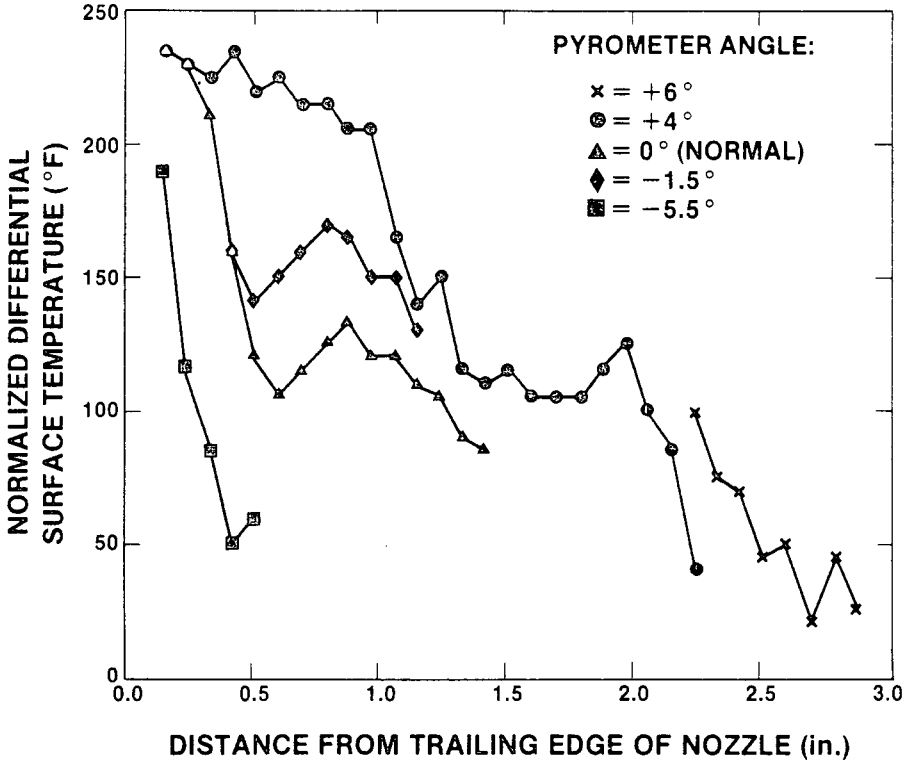

Figure A-10. First-stage nozzle test—pyrometer scans at steady-state design point

The traversing scans of the second stage nozzles indicate surface temperatures varied from 680 to 750 °F on the trailing edge region to 660 to 680 °F in the center region of the nozzle (2.5 to 3 inches from the trailing edge). The forward region temperatures, typically 4.5 to 5.5 inches from the trailing edge, varied from 630 to 660 °F. The surface temperature profile was nearly constant across most of the nozzle, with an average temperature of 670 to 680 °F. Water flow reductions did not affect the surface temperature to a significant degree as shown in Figure A-11. The time scans on the second stage nozzles confirmed the surface temperatures observed on the traversing scans.

The ambient temperature and the temperature of the detector cooling water affect pyrometer results. The detector housing temperature varied from a low of 72 °F for the initial test series to 89 °F during the extended test series. This variation caused absolute temperature variations of 40 to 60 °F in the pyrometer readout. An emissivity value of 0.8 was maintained for all tests.

IX. CONCLUSIONS

The environment of the test stand mixing chamber required several pyrometer design iterations to successfully measure surface temperatures on the nozzles. The

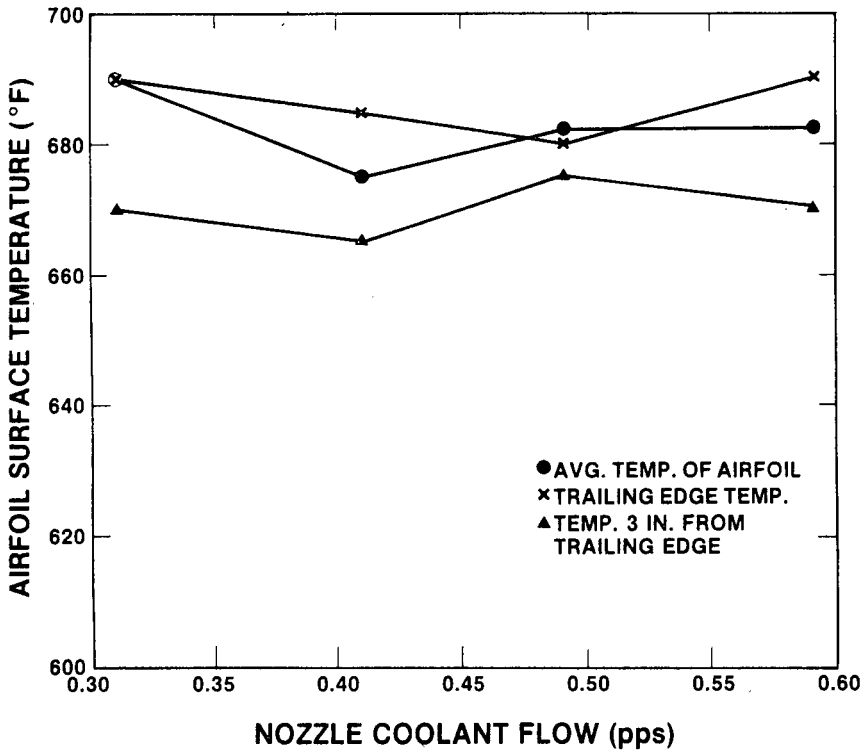

Figure A-11. Second-stage nozzle coolant flow reduction test—pyrometer pitchline airfoil scan coolant flow versus vane surface temperature, nozzle position 2

pyrometer measurements made during extended testing of the monometallic nozzles were confirmed by independent surface thermocouple measurements. The use of an in-situ calibration target proved to be necessary to set proper emissivity values. The success of the pyrometer measurements in the test stand may allow for critical monitoring, alarm, and control/trip functions for the TRV.

X. REFERENCES

1. D.P. Dewitt, R.S. Hernicz, "Theory and Measurement of Immittance Properties for Radiation Thermometry Applications, Temperature, Measurement and Control" in *Science and Industry,* Vol. 4, Part 1, p. 478, ISA, 1972.

2. Sources of Infrared Radiation, Figure 11-14, page 11-33, *Optical Engineering Handbook,* Dr. J.A. Mauro, ed., General Electric Company, 1966.

3. R.D. Lillquist, "An Infrared Pyrometer for Measuring 700-900 Kelvin Surface Temperatures in a Combustion Gas Background Environment," ASME Publication No. 80-HT-5, ASME/AIChE National Heat Transfer Conference, Orlando, Fla. July 27-30, 1980.

4. Edwards, D.K., "Molecular Gas Band Radiation," *Advances in Heat Transfer,* Vol. 12, pp. 115-193, Academic Press, New York, 1976.

Appendix B

BOILING PHENOMENA IN WATER-COOLED GAS TURBINE NOZZLES

The purpose of this appendix is to define the terms used in discussing the boiling which may occur when flow is reduced in a water-cooled nozzle. The discussion applies to boiling in a coolant passage (second-stage nozzle) as well as at the inner surface of a cooling tube (first-stage nozzle).

The heat transfer in the cooling tubes can be conveniently separated into the following regimes:

1. Single phase
2. Two-phase subcooled nucleate boiling
3. Two-phase saturated nucleate boiling (bulk boiling)

Regime 1: Single-phase heat transfer occurs when the wall temperature is below fluid saturation temperature. The cooling circuit design was targeted to operate in this regime, where heat transfer is purely by turbulent forced convection.

Regime 2: When the wall temperature reaches saturation temperature plus wall superheat, ΔT, nucleate boiling commences. This is referred to as the onset of nucleate boiling (ONB). Wall superheat depends on system pressure and wall heat flux according to the Jens-Lottes relationship (Reference 1) shown in Equation 1.

$$\Delta T = 1.9\, \Phi_w^{0.25}\, e^{-(P/900)} \qquad (1)$$

where ΔT is in °F, Φ_w in Btu/hr-ft^2, and P is in psia. For a typical nozzle cooling tube, ΔT is on the order of 20 °F. Since the bulk fluid temperature is below saturation, i.e., subcooled, and there is steam formed at the walls, this regime is called two-phase subcooled nucleate boiling. This regime is characterized by high heat transfer rates, constant wall temperature, and the formation of steam bubbles at nucleation sites along the wall. These bubbles quickly condense as they move away from the wall because the mixed mean temperature is below saturation (Reference 2). Although this flow and heat transfer regime is not detrimental in itself, an increase in wall heat flux or a drop in system pressure could cause a transition to unstable saturated nucleate boiling. The cooling design avoids this regime.

Regime 3: Two-phase saturated nucleate boiling occurs when the liquid mixed mean temperature reaches saturation. This regime is characterized by net formation of steam, slug flow, and constant wall temperature. In spite of high heat transfer rates, this regime must be avoided because pressure drop increases dramatically and instability of the nozzle coolant flow is likely to occur.

As the tube wall heat flux increases, a flux level is eventually reached at which there is sufficient vapor formation at the wall to cause a sharp reduction in heat transfer. This flux level is called critical heat flux (CHF). Reaching CHF results in a large sudden increase in metal temperature to a point where physical burnout may occur (Reference 2). CHF may occur in Regimes 2 and 3. If the airfoil cooling tubes are considered to be uniformly heated, CHF can be calculated from the Macbeth

Correlation (Reference 3). The important variables in this correlation are:

1. System pressure
2. Subcooling of tube inlet water
3. Tube geometry
4. Water flow rate per unit area

Both Φ_{ONB} and Φ_{CHF} are a function of the coolant flux *(G)*. These relationships have been calculated for the particular tube sizes in the first-stage nozzle and are plotted in Figures 2-39, 2-40, and 2-41 of Section 2.

REFERENCES

1. R.T. Lahey, F.J. Moody, *The Thermal-Hydraulics of a Boiling Water Nuclear Reactor,* American Nuclear Society, Hinsdale, Ill., 1977.
2. J.G. Collier, *Convective Boiling and Condensation,* McGraw-Hill Book Company (UK) Limited, London, 1972.
3. B. Thompson, R.V. Macbeth, "Boiling Water Heat Transfer – Burnout in Uniformly Heated Round Tubes: A compilation of World Data with Accurate Correlations," AEEW-R356, United Kingdom Atomic Energy Authority, 1964.

Appendix C

FIRST-STAGE NOZZLE TEST EXTERNAL HEAT TRANSFER CORRELATIONS

The purpose of this appendix is to document the calculation procedure used in determining the heat transfer correlations summarized in Section 2 on Figure 2-29. Refer to Table 2-3 in Section 2 for the nomenclature involved.

The following calculation procedure was used to calculate the Reynolds number, $Re^*_{c,REF}$, and Nusselt number, $Nu^*_{c,REF}$. These calculations were performed at each fired and unfired point run during the testing.

1. From the throat flow function, $\frac{W^*\sqrt{T^*}}{P_T\,(A^*C_q)}$, determine $\left(\frac{T^*_\infty}{T^*}\right)$, $\gamma = 1.4$ or $\gamma = 1.33$. Tables were used for air (unfired) tests and propane/air (fired) tests, respectively.

2. Calculate $T^*_\infty = T^*\left(\frac{T^*_\infty}{T^*}\right)$.

3. Calculate $r = Pr^{1/3}$. Since Pr varies very little with temperature, constant values of r were used for the fired and unfired tests, 0.884 and 0.880, respectively.

4. Calculate $T^*_{as} = r\,(T^* - T^*_\infty) + T^*_\infty$.

5. Calculate $T^*_{REF} = T^*_\infty + 0.5\,(T_s - T^*_\infty) + 0.22\,(T^*_{as} - T^*_\infty)$.

   Average surface temperature, T_s, and gas side heat transfer coefficient, h_g, were calculated from the heat load and copper temperature as discussed in Section 2.7.4.2. Due to the large temperature difference across the boundary layer, the Eckert reference temperature, T^*_{REF}, was used to determine gas properties μ and k.

6. Calculate Reynolds number and Nusselt number.

$$Re^*_{c,REF} = \frac{(\rho V)c}{\mu}$$

$$(\rho V) = W^*/(A^*C_q)$$

$$Nu^*_{c,REF} = \frac{h_g\,c}{k}$$

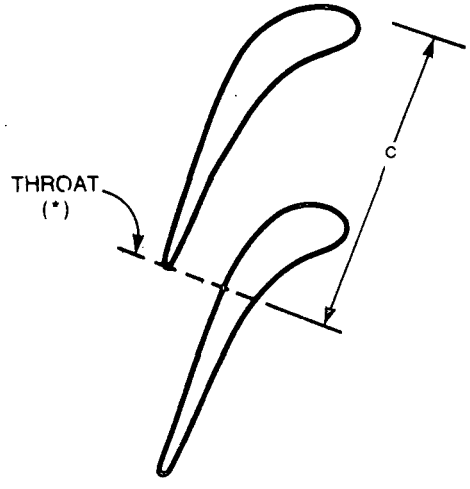

The correlation, labeled in Figure 2-29 as "Average Turbulent Flat Plate," was calculated according to the following equation:

$$Nu^{*}_{c,REF} = 0.036\ (Re^{*}_{c,REF})^{0.8}\ (Pr^{*}_{REF})^{0.33}$$

This curve is plotted for reference only and does not reflect on the validity of the data points or the design point. The design point located in Figure 2-29 was based on an average airfoil h_g of 386 Btu/hr-ft^2-°F.

Appendix D

FIRST STAGE NOZZLE TEST GAS TEMPERATURE PROFILE MEASUREMENT

The first-stage composite nozzle test combustor exit gas temperature profile was determined using data obtained from the water cooled gas sampling probes located in the combustor transition piece. See Appendix E for gas sampling probe design details. Full and partial traverses of the hot gas stream were taken at 2000°F, 2400°F, and 2600°F average bulk gas temperatures.

Results from these traverses are as follows:

2000°F Traverse

This traverse provided a checkout of all instrumentation including the gas sampling probes, and provided data at a bulk gas temperature of approximately 2000°F.

The four traversing probes were used independently to obtain the data. The four probes were labeled A, B, C, and D circumferentially across the gas path as shown on Figure D-1. At each of the five probe radial positions a temperature and gas sample was measured.

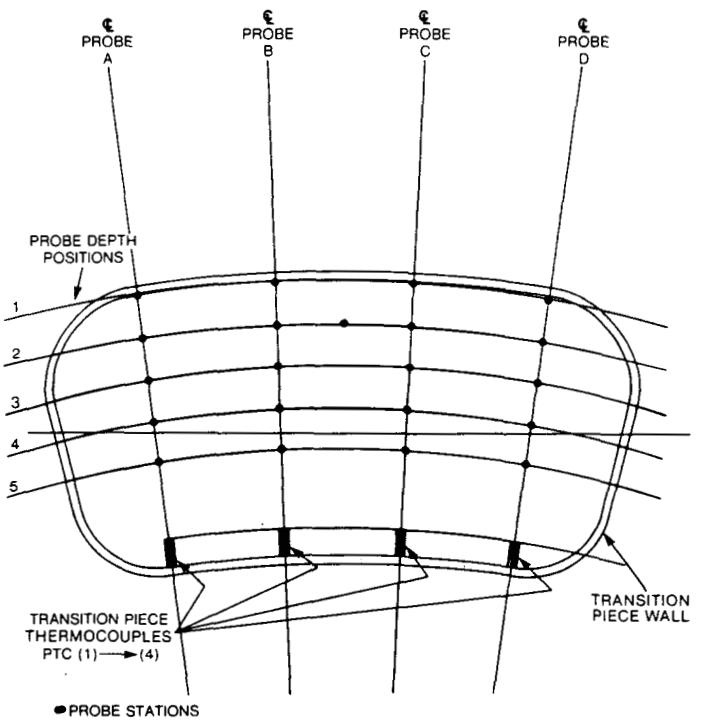

Figure D-1. Gas sample probe reading locations (looking with gas flow)

The probe position is given in inches measured from the innerwall of the transition piece. A gas temperature at a given probe position was measured using a thermocouple mounted on the probe and an O_2 emissions samples. The O_2 emissions measurement was related to temperature by using the plot shown on Figure D-2. This plot was generated by using the NASA Mass Equilibrium Program (NASA SP-273). This plot shows the adiabatic flame temperature plotted against the fuel to air ratio for inlet air temperatures of 500°F and 650°F. This plot also shows volume percent of O_2 plotted against the fuel to air ratio.

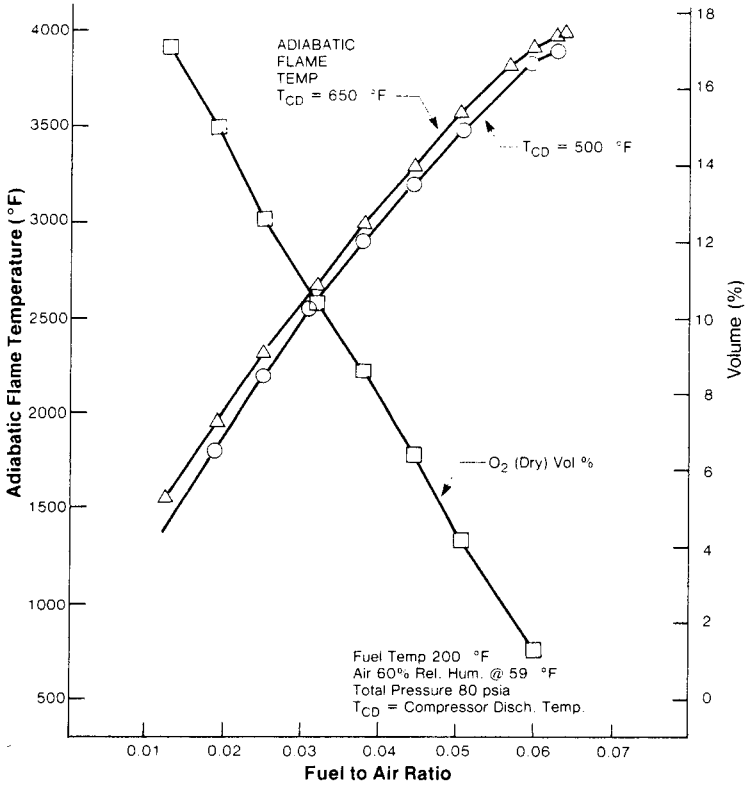

Figure D-2. Adiabatic flame temperature and volume percentage of O_2 vs fuel-to-air ratio, propane fuel

From these two curves, knowing the O_2 emissions, an adiabatic flame temperature can be estimated for a given fuel to air ratio. These estimates are compared to the thermocouple measured temperatures in Table D-1. The temperature measurements are circumferentially averaged at each probe position and plotted on Figure D-3. The bulk temperature is then calculated by averaging all the measurements including those from the four platinum-rhodium thermocouples immersed in the hot gas stream. The O_2 emissions derived profile is nearly identical to the thermocouple measured profile. The bulk temperature for the O_2 derived and measured temperature profiles were 1879°F and 1861°F respectively.

Table D-1

TRAVERSE PROBE DATA

Probe Position	MEASURED TEMPERATURES A	B	C	D	O_2 DERIVED TEMPERATURE A	B	C	D
	2000 °F TRAVERSE							
1	1595	1773	1676	467*	--	1710	--	--
2	1703	1861	1829	1841	1720	1882	1850	1650
3	1827	1870	1951	2039	1875	1905	1980	2035
4	1932	1939	2000	2065	1957	1978	2045	2093
5	1952	1943	1987	1949	1975	1997	2032	2012
PTC	1759	1741	1957	1820	--	--	--	--
	2400 °F TRAVERSE							
1	2122	2251	2168	624*	1400*	1470*	--	--
2	2301	2371	2325	2292	2285	2290	2355	2305
3	2379	2406	2460	2518	2397	2391	2433	2384
4	2404	2391	2500	2435	2405	2402	2433	2406
5	2444	2413	2485	2423	2466	2468	2501	2467
PTC	2209	2214	2441	2278	--	--	--	--
	2600 °F TRAVERSE							
1	2543	2635	2569	--	--	2600	--	--
2	2750	2782	2750	2726	2640	2783	2773	2723
3	2779	2813	2842	2846	2670	2796	2765	2716
4	2791	2810	2827	2715	2882	2820	2879	2852
5	2857	2807	2812	2810	2885	2854	2909	2875
PTC	2511	2557	2812	2597	--	--	--	--

LEGEND:

[ ] Data estimated from profile trends established during 2000 °F and 2400 °F traverses

-- No data

* Temperatures boundary-layer affected

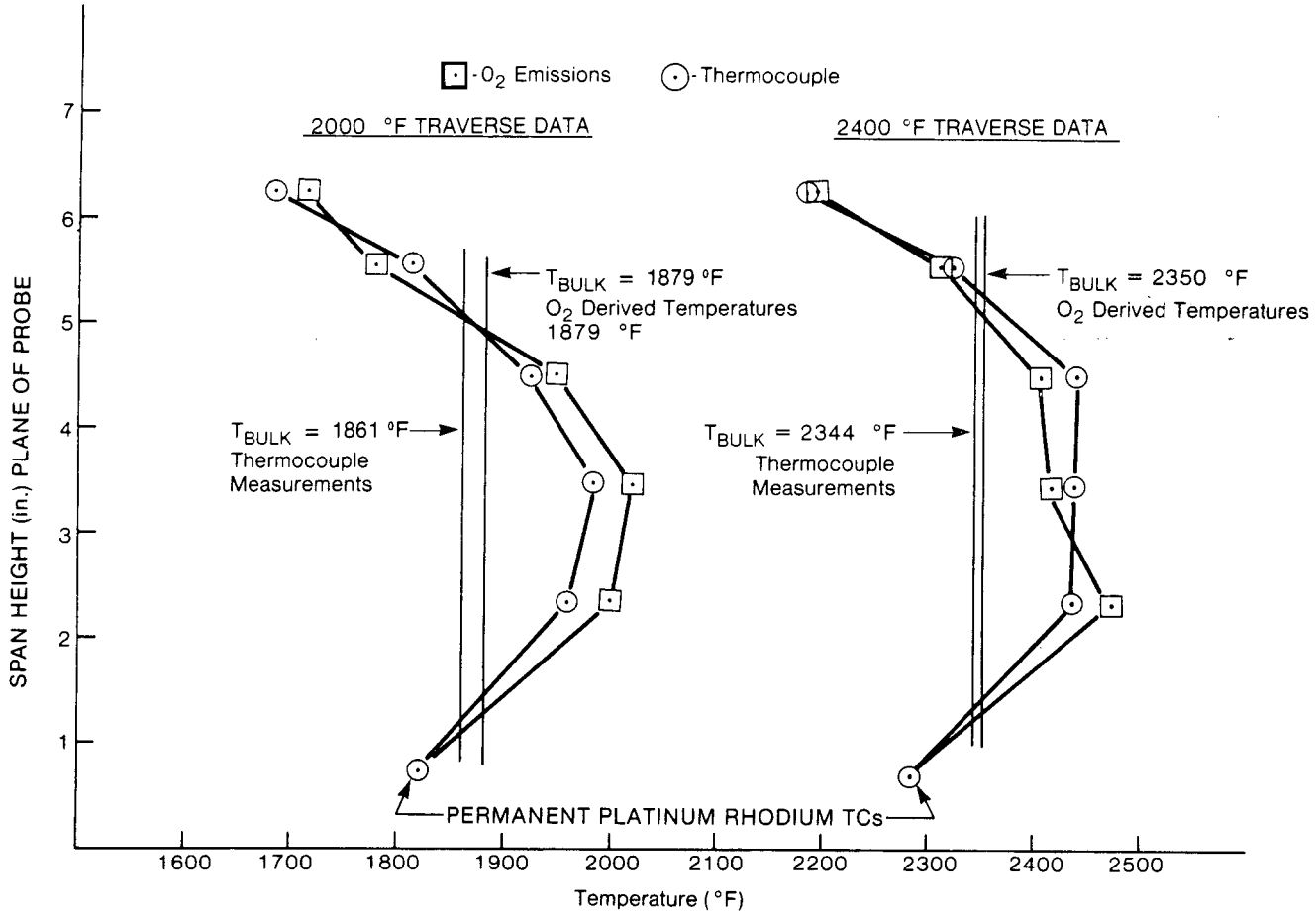

Figure D-3. Circumferentially averaged emission and measured temperature profiles

2400°F and 2600°F Traverses

Partial traverses were taken at bulk temperatures of approximately 2400°F and 2600°F. The data is listed in Table D-1. During the 2400°F traverse probe C could not be actuated. Temperatures were estimated for the probe not functioning by comparison with a full set of data recorded at the 2000°F traverse and symmetry considerations. The estimated temperatures are indicated in Table D-1. The four permanently fixed thermocouples (labelled PTC) were radiation corrected. Profiles of the gas path are shown for the 2400°F traverse on Figure D-3. The profiles are circumferential averages of the measured temperatures. Probe data obtained very near the outer wall of the transition piece were not used in calculating the traverse bulk temperature. In these instances the probe was too near the transition piece wall and revealed boundary layer effects. Temperature estimates were made in these instances using thermocouple data. This data is indicated in Table D-1.

A partial traverse was taken at 2600°F. Traverse data was taken over half the gas path. System time constraints and failure of a probe actuator prevented the taking of traverse data from all the probes. The probe thermocouples were not operating, since they were reading temperatures below those of the 2400°F traverse. The four permanent platinum-rhodium thermocouples were measuring temperatures much higher.

The emissions data, however, revealed temperatures consistent with the four platinum-rhodium thermocouples mentioned above. Table D-1 lists the O_2 emissions derived temperatures along with the other traverse data. Since the traverse was made over half the gas path, efforts were made to estimate the entire combustor temperature map at 2600°F by profile temperature trends established during the 2000°F and 2400°F traverses. Prior testing of this combustion system in addition to test experience with similar combustion systems suggests this may be done. The estimated temperatures are indicated in Table D-1. The estimated profiles are shown on Figure D-4. These profiles are a circumferential average of the O_2 emissions temperature and the estimated thermocouple temperatures of Table D-1.

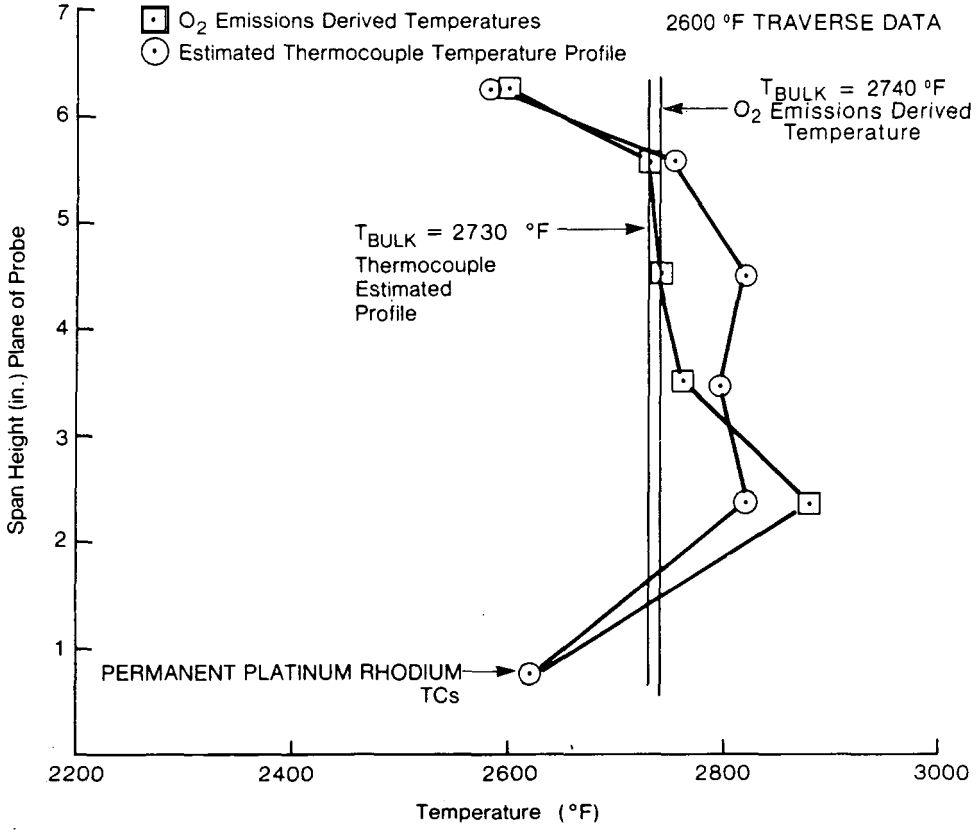

Figure D-4. Estimated temperature profile at 2600 °F traverse

Appendix E

FIRST-STAGE NOZZLE TEST HOT-GAS SAMPLING PROBES

I. PURPOSE

The hot-gas sampling probes were used to obtain measurements of the hot gas characteristics at the exit of the combustor and upstream of the nozzle. The probes were designed to:

- Measure gas temperature with an aspirated thermocouple
- Measure total pressure on the same line as aspirated thermocouple
- Measure static pressure
- Provide a quenched gas sample for:
  - Combustor exhaust temperature and efficiency determination
  - Emission compliance determination

The probe design was such that actuators could be used to traverse each of the four probes independently across the combustor exit. This provided data for determination of the gas profile.

II. DESIGN CONSIDERATION

The following criteria must be satisfied to accomplish the desired measurements:

- There must be a sonic pressure drop across the sampling probe tip in order to freeze all reactions.
- The probe tip opening must be sized to provide adequate sample flow for the gas analysis system at all operating conditions.
- The sample must be maintained above its dew point throughout the probe.
- The probe must be capable of traversing the combustor exit height.
- The probe must include an aspirated thermocouple.
- The probe must include provisions for measurement of total pressure.

III. SYSTEM DESIGN

The hot-gas sampling probe system consists of three major components, these are:

- Probes (manufactured by H&B Tooling Co.)
- Actuators (manufactured by L.C. Smith Co.)
- Actuator controllers (manufactured by L.C. Smith Co.)

Four sets of probes, actuators, and controllers were used to measure the gas characteristic upstream of the first-stage nozzle.

Each probe is 56.35 inches long overall and consists of a thermocouple, pressure tube, and sampling tube, all housed in an outer cylindrical case 1.315 inches in diameter. The cylindrical case also houses the cooling water. The gas stream end of the probe is elliptical for a length of 5.03 inches (Figure E-1). The shield for the platinum-rhodium aspirated thermocouple is at the lower end of the probe. The gas sample intake is located directly above the thermocouple shield. The sample intake has a nozzle shape to expand the gas, thereby quenching any combustion. One of the two static pressure taps can be seen on the side of the probe in line with the thermocouple shield tube. A second static pressure tap is located on the opposite side of the probe. The upper end of the probe is shown in Figure E-2. This figure shows the various connections needed for the multiple functions of the probe.

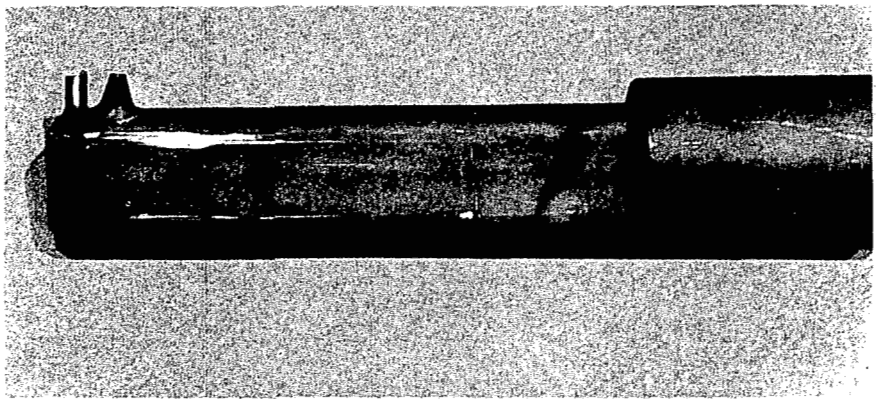

Figure E-1. Hot gas path end of probe

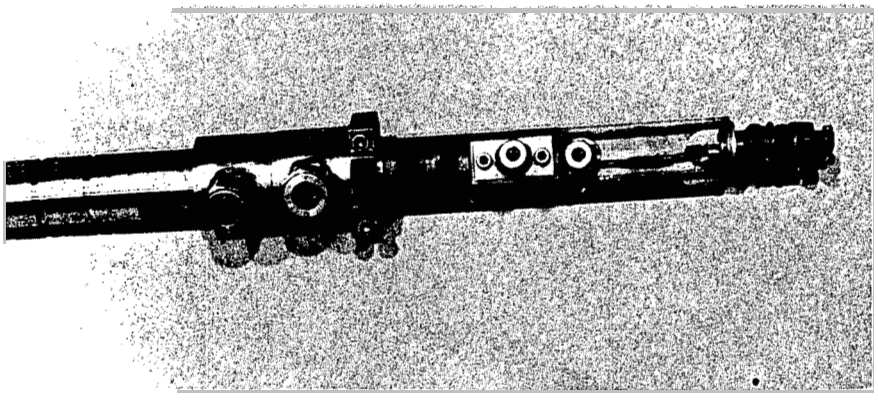

Figure E-2. Atmospheric end of probe

Viewing from left to right, the connections are:

1. Cooling water inlet
2. Cooling water outlet
3. Static pressure #1
4. Static pressure #2
5. Gas sample
6. Total pressure/TC aspiration
7. Thermocouple connector

Cooling water is required to protect the end of the probe in the hot gas stream. The closed loop probe cooling water system is described in Part I of this report. The gas sample must be maintained above 300 °F to prevent precipitation of the constituents; therefore, water at 300 °F was used for cooling.

The probe actuator is shown in Figure E-3. The actuator consists of two lead screws and recirculating ball followers attached to the movable platform which connects to the probe. The two lead screws are driven by a single dc motor via two worm screws and gears. The drive system is capable of producing 650 pounds of force. This is adequate to move against an internal test stand pressure of up to 16 atmospheres and also overcome friction of the seals and guides. The actuator is equipped with adjustable limit switches and a potentiometer whose output is proportional to platform position. The total travel of the movable platform is 9.5 inches.

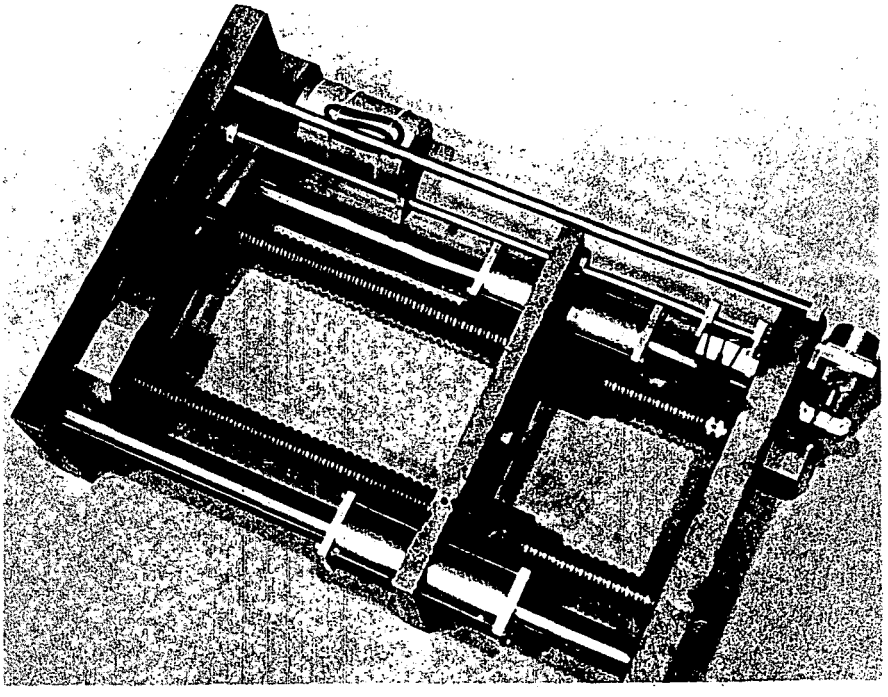

Figure E-3. Probe actuator

Figure E-4 is a photograph of the probe assembled to the actuator. Also shown in this figure is the probe guide tube and the pressure sealing ring. This ring contains two Teflon® "C"-shaped seals in series, which provide for motion of the probe and at the same time seal against the test stand pressure. The four L.C. Smith Model TP-P025-HD actuator controllers are located in the Control room of the Gas Turbine Development Lab and are pictured in Part I of this report.

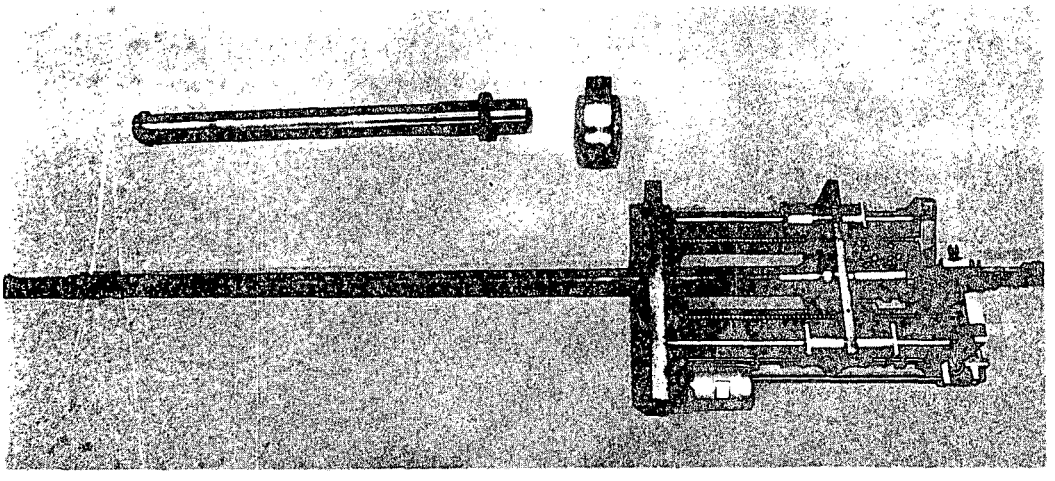

Figure E-4. Probe actuator assembly

The controller can control the actuator in either a manual or pre-position mode. In the pre-position mode, a sequence of discrete actuator traverse motion stopping positions can be programmed into the control. This control system is closed loop. A desired actuator position is set by the manual control located on the front panel or pre-programmed on a patch panel located at the rear of the controller. The desired actuator position is compared to the actual actuator position as read by the actuator potentiometer feedback voltage. If the actuator position does not match the desired position, a motor drive signal to the actuator is initiated to drive the actuator to the desired position. The actuator potentiometer position is read out on a digital voltmeter on the front panel of the controller. This output is also available to the data logger in the Gas Turbine Development Lab Control Room.

IV. SYSTEM OPERATION

The four hot-gas sampling probe assemblies were installed in ports provided in the instrument dutchman section of the Hot-Gas Path Test Stand (Figure E-5). The water inlet and outlet are visible as well as the thermocouple to measure the outlet water temperature. The insulation is around the hot gas sampling line. This line is also electrically heat traced to maintain the desired gas sample temperature. The gas sample is conducted into the control room via permanently installed electrically heated

® Registered trademark of E.I. duPont de Nemours & Co., Wilmington, Delaware.

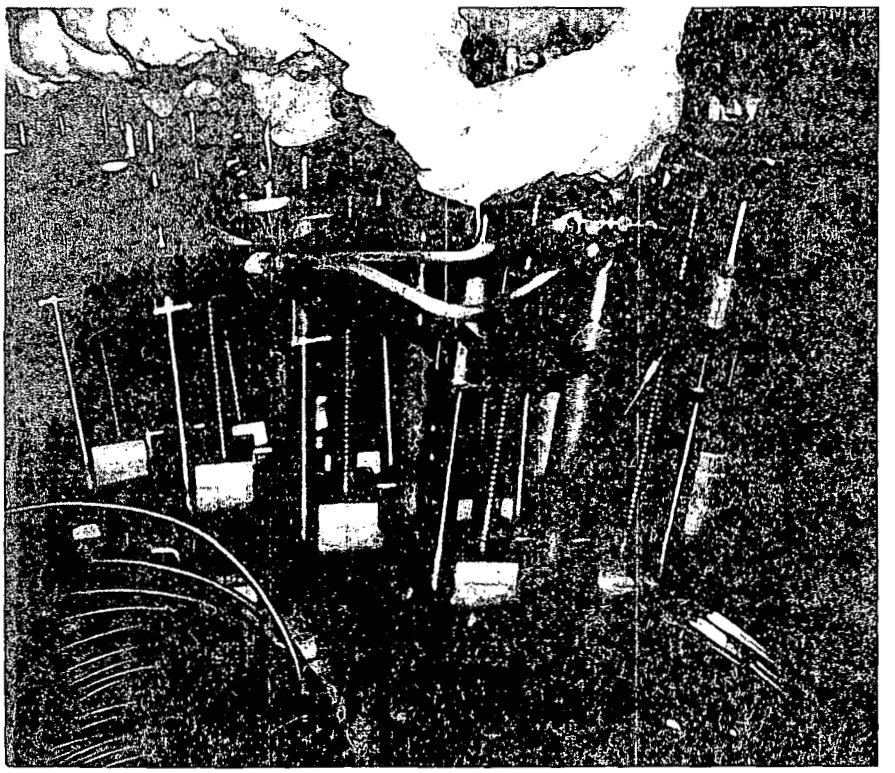

Figure E-5. Probe actuator assembly installed

sample lines. The control room is equipped with on-line gas analysis equipment to measure the characteristics of the gas sample. This is described in detail in Part I of this report.

The actuator controllers were operated in a pre-programmed mode, i.e., a set of six positions was programmed for each controller. Each probe would be positioned, a gas sample obtained and measured, the probe would then be advanced to the next position, and another measurement taken. This procedure was repeated for each probe. The temperature from the aspirated thermocouple and static pressure profiles were obtained in the same manner. Data obtained from these probes is presented in Appendix D of this report.

☆ U.S. GOVERNMENT PRINTING OFFICE: 1982-546-085/3244